NEUROSTEREOLOGY

EDITED BY: Bente Pakkenberg, Mikkel Vestergaard Olesen,
Sanne Simone Kaalund and Karl-Anton Dorph-Petersen

PUBLISHED IN: Frontiers in Neuroanatomy

frontiers Research Topics

frontiers

ISSN 1664-8714
ISBN 978-2-88945-880-6
DOI 10.3389/978-2-88945-880-6

About Frontiers

Frontiers is more than just an open-access publisher of scholarly articles: it is a pioneering approach to the world of academia, radically improving the way scholarly research is managed. The grand vision of Frontiers is a world where all people have an equal opportunity to seek, share and generate knowledge. Frontiers provides immediate and permanent online open access to all its publications, but this alone is not enough to realize our grand goals.

Frontiers Journal Series

The Frontiers Journal Series is a multi-tier and interdisciplinary set of open-access, online journals, promising a paradigm shift from the current review, selection and dissemination processes in academic publishing. All Frontiers journals are driven by researchers for researchers; therefore, they constitute a service to the scholarly community. At the same time, the Frontiers Journal Series operates on a revolutionary invention, the tiered publishing system, initially addressing specific communities of scholars, and gradually climbing up to broader public understanding, thus serving the interests of the lay society, too.

Dedication to Quality

Each Frontiers article is a landmark of the highest quality, thanks to genuinely collaborative interactions between authors and review editors, who include some of the world's best academicians. Research must be certified by peers before entering a stream of knowledge that may eventually reach the public - and shape society; therefore, Frontiers only applies the most rigorous and unbiased reviews.
Frontiers revolutionizes research publishing by freely delivering the most outstanding research, evaluated with no bias from both the academic and social point of view. By applying the most advanced information technologies, Frontiers is catapulting scholarly publishing into a new generation.

What are Frontiers Research Topics?

Frontiers Research Topics are very popular trademarks of the Frontiers Journals Series: they are collections of at least ten articles, all centered on a particular subject. With their unique mix of varied contributions from Original Research to Review Articles, Frontiers Research Topics unify the most influential researchers, the latest key findings and historical advances in a hot research area! Find out more on how to host your own Frontiers Research Topic or contribute to one as an author by contacting the Frontiers Editorial Office: researchtopics@frontiersin.org

NEUROSTEREOLOGY

Topic Editors:
Bente Pakkenberg, Bispebjerg-Frederiksberg Hospital, Denmark
Mikkel Vestergaard Olesen, Bispebjerg-Frederiksberg Hospital, Denmark
Sanne Simone Kaalund, Bispebjerg-Frederiksberg Hospital, Denmark
Karl-Anton Dorph-Petersen, Aarhus University, Denmark

Citation: Pakkenberg, B., Olesen, M. V., Kaalund, S. S., Dorph-Petersen, K.-A., eds. (2019). Neurostereology. Lausanne: Frontiers Media.
doi: 10.3389/978-2-88945-880-6

Table of Contents

frontiers in Neuroanatomy

EDITORIAL
published: 16 April 2019
doi: 10.3389/fnana.2019.00042

Editorial: Neurostereology

Bente Pakkenberg[1,2]*, *Mikkel Vestergaard Olesen*[1], *Sanne Simone Kaalund*[1] and *Karl-Anton Dorph-Petersen*[3,4,5]

[1] Research Laboratory for Stereology and Neuroscience, Bispebjerg Hospital, Copenhagen, Denmark, [2] Department of Clinical Medicine, Faculty of Health Sciences, University of Copenhagen, Copenhagen, Denmark, [3] Translational Neuropsychiatry Unit, Department of Clinical Medicine, Aarhus University, Aarhus, Denmark, [4] Centre for Stochastic Geometry and Advanced Bioimaging, Aarhus University, Aarhus, Denmark, [5] Translational Neuroscience Program, Department of Psychiatry, University of Pittsburgh, Pittsburgh, PA, United States

Keywords: brain, stereological methods, disector, fractionator, cavalieri volume

Editorial on the Research Topic

Neurostereology

Quantification of cells in a three-dimensional (3-D) structure requires robust estimates based on unbiased principles. Studies using two-dimensional methods (2-D) to report data of 3-D structures are still frequently used. However, these methods do not consider the irregular nature of biological structures in terms of shape and distribution of the target features. Consequently, they make assumptions about the 3-D structure of interest and the results do not refer to the complete structure. These limitations reduce the sensitivity and accuracy of the methods as well as increase the risk of errors. This can be avoided by the application of design-unbiased stereology. Stereology is based on a set of statistical and mathematical principles and provides efficient tools for estimation of volume, surface area, length, and number of objects in 3-D structures by sampling in 2-D sections. Because stereology relies on statistical sampling principles and stochastic geometric theory, it is guaranteed that no methodological biases are introduced to the analysis. Thus, in principle, it allows one to obtain accurate and precise quantitative data of structural changes in biological tissue.

In this special volume, the papers will focus on the application of different stereological methods and their practical aspects. The papers are introduced and explained by prominent neurostereologists and reported in the order by which *the method* was first introduced.

The first paper (Basler et al.) deals with the precision of the Cavalieri estimator of volume. If correctly applied, the resulting sampling-generated variability should not be able to mask significant group differences. To provide tentative answers to the question if sampling has been "good enough," the authors discuss the influence of sampling frequency, smoothness factor and section orientation on the Gundersen-Jensen coefficient of error (CE). Using the layers of the mouse hippocampal dentate gyrus as an example they found that the CE provided reasonable estimates of the precision obtained using different sample sizes. The data are presented, allowing the reader to approximate sampling intervals in frontal, horizontal, or sagittal sections that provide CE's of specified sizes.

The second paper by Fichtl et al. uses intact, macro- and microscopically well-preserved postnatal human cerebellar hemispheres allowing for high-precision morphologic investigations. The study identifies anatomically distinct cerebellar fissures and delineate functionally relevant regions. It also describes how to estimate the volume of regions of interest and quotes the literature for proven sampling schemes. The paper is richly illustrated.

The physical disector method and its use in the industry is described in the paper by Fabricius et al. The study describes how automated alignment of microscopic images allows for efficient stereological analysis of specific dopaminergic neurons in the substantia nigra of hemiparkinsonian rats. The authors conclude that the automated physical disector provides a useful and efficient tool for unbiased estimation of selected cell types in regions of interest in the rat brain.

OPEN ACCESS

Edited and reviewed by:
Javier DeFelipe,
Cajal Institute (CSIC), Spain

***Correspondence:**
Bente Pakkenberg
bente.pakkenberg@regionh.dk

Received: *25 February 2019*
Accepted: *27 March 2019*
Published: *16 April 2019*

Citation:
Pakkenberg B, Olesen MV, Kaalund SS and Dorph-Petersen K-A (2019) Editorial: Neurostereology. Front. Neuroanat. 13:42. doi: 10.3389/fnana.2019.00042

Napper describes the use of the optical disector and its application to the rodent brain using immunohistochemistry. It emphasizes that estimates of numerical density can result in misleading data, most often in an unknown direction. The author shows how new developments in electron microscopy enable the application of design-based stereology, particularly the disector method, to this type of sections. In the study serial block-face scanning electron microscopy is used to efficiently obtain total number data at an ultrastructural level.

The study by Larsen describes the use of the optical fractionator applied to the human fetal brain. Simple estimates of cell volumes and densities may be unreliable due to unpredictable shrinking artifacts, and the fragility of e.g., the fetal brain requires particular care in histological handling and processing. Aiming at just total numbers, the optical fractionator design is especially useful and offers direct, robust, and reliable estimates.

Kreutz and Barger gives an example of the optical fractionator using immunofluorescence techniques. Improvements in immunohistochemistry and fluorescence imaging technologies have facilitated easy application of immunofluorescence protocols, allowing for visualization of multiple target proteins in one tissue sample. Combining immunofluorescence labeling with stereological data collection can thus provide a powerful tool to maximize explanatory power and efficiency, while minimizing tissue use. The paper provides a protocol for reliably integrating the optical fractionator technique and multiple immunofluorescence techniques.

Parker and Sweet provide a review of dendritic spine density, number of cells, and application of the nucleator to provide pyramidal cell somal volume in auditory cortex. They identify and describe potential neural substrates for auditory impairment and gray matter loss in the auditory cortex in schizophrenia. The review highlights how stereology has been crucial for obtaining proper data collection, reporting and, ultimately, interpretation of the complex relationship between the target estimates.

West describes the practical application of the space ball probe and reviews its use in a number of studies focusing on axon, dendrite, and capillary length in the nervous system. The review provides a discussion of the salient features of the methodology of length, the validity of the method and details potential difficulties in its application to histological tissue.

Finally, Boyce and Gundersen complete this special volume on neurostereology by describing the application of the automatic proportionator for estimation of a sparse cell populations. The proportionator, an estimator based on non-uniform sampling theory, marries automated image analysis with stereological principles. It provides a highly efficient and precise method to address the challenge of quantitating e.g., sparse cell populations in the central and peripheral nervous system in situations where traditional stereological methods based upon systematic, uniformly random sampling are impractical. The power of the proportionator as a stereological tool is illustrated.

AUTHOR CONTRIBUTIONS

BP, MVO, SSK, and K-AD-P collaborated together in initiating this Topic, and in writing the editorial.

ACKNOWLEDGMENTS

We sincerely thank all the authors for their most valuable contribution to the Neurostereological Research Topic in Frontiers in Neuroanatomy, and the many referees who substantially improved the papers and protocols. We hope that this summary of examples may encourage scientists to consider the application of stereological methods on their own studies.

Conflict of Interest Statement: The authors declare that the research was conducted in the absence of any commercial or financial relationships that could be construed as a potential conflict of interest.

frontiers in Neuroanatomy

ORIGINAL RESEARCH
published: 12 December 2017
doi: 10.3389/fnana.2017.00123

Sampling the Mouse Hippocampal Dentate Gyrus

Lisa Basler[1,2], *Stephan Gerdes*[1], *David P. Wolfer*[1,3,4] *and Lutz Slomianka*[1,4*]

[1] *Division of Functional Neuroanatomy, Institute of Anatomy, University of Zürich, Zürich, Switzerland,* [2] *Department of Pulmonology, University Hospital Zürich, Zürich, Switzerland,* [3] *Neuroscience Center Zürich, University of Zürich, ETH Zürich, Zürich, Switzerland,* [4] *Department of Health Sciences and Technology, ETH Zürich, Zürich, Switzerland*

Sampling is a critical step in procedures that generate quantitative morphological data in the neurosciences. Samples need to be representative to allow statistical evaluations, and samples need to deliver a precision that makes statistical evaluations not only possible but also meaningful. Sampling generated variability should, e.g., not be able to hide significant group differences from statistical detection if they are present. Estimators of the coefficient of error (*CE*) have been developed to provide tentative answers to the question if sampling has been "good enough" to provide meaningful statistical outcomes. We tested the performance of the commonly used Gundersen-Jensen *CE* estimator, using the layers of the mouse hippocampal dentate gyrus as an example (molecular layer, granule cell layer and hilus). We found that this estimator provided useful estimates of the precision that can be expected from samples of different sizes. For all layers, we found that a smoothness factor (*m*) of 0 generally provided better estimates than an *m* of 1. Only for the combined layers, i.e., the entire dentate gyrus, better *CE* estimates could be obtained using an *m* of 1. The orientation of the sections impacted on *CE* sizes. Frontal (coronal) sections are typically most efficient by providing the smallest *CE*s for a given amount of work. Applying the estimator to 3D-reconstructed layers and using very intense sampling, we observed *CE* size plots with $m = 0$ to $m = 1$ transitions that should also be expected but are not often observed in real section series. The data we present also allows the reader to approximate the sampling intervals in frontal, horizontal or sagittal sections that provide *CE*s of specified sizes for the layers of the mouse dentate gyrus.

Keywords: dentate gyrus, stereology, volume, Cavalieri estimator, CE estimators, C57BL/6 mice

OPEN ACCESS

Edited by:
Bente Pakkenberg, Research Laboratory for Stereology and Neuroscience, Denmark

Reviewed by:
Hans J. Gundersen, Retired, Denmark
Karl Daniel Murray, University of California, Davis, United States

***Correspondence:**
Lutz Slomianka
slomianka@anatom.uzh.ch

Received: *06 June 2017*
Accepted: *29 November 2017*
Published: *12 December 2017*

Citation:
Basler L, Gerdes S, Wolfer DP and Slomianka L (2017) Sampling the Mouse Hippocampal Dentate Gyrus. Front. Neuroanat. 11:123. doi: 10.3389/fnana.2017.00123

INTRODUCTION

Design-based stereological methods provide easily interpretable and statistically valid estimates on the volumes, surfaces, lengths or numbers of regions or objects of interest in the brain. These methods have however been rather resilient to automation (e.g., Schmitz et al., 2014). They therefore often require more time to perform than methods that generate less reliable, more difficult to interpret, but, alas, just as publishable data. To minimize the time/workload one can adjust the

precision of the estimates to the requirements of a study. It does not make sense to generate very precise estimates in the individual subjects that form, e.g., control and experimental groups, if the biological variability between subjects is high. Aside from the difference in the group means, group variances and the number of subjects determine the outcomes of statistical comparisons. If a high precision of estimates has little impact on the group variance, it may be less laborious to detect a group difference by relaxing precision but instead increasing the number of subjects in the groups (Gundersen and Østerby, 1981; West, 2012). To decide on the most efficient investment of work, one needs to be able to numerically assess the impact of estimate precision on group variance. While the group variance is part of the output of standard statistics, estimate precision is not. There are two ways to obtain it.

The estimation procedure can be replicated multiple times in a subject. The variance of the replicates, often expressed as the coefficient of variation (*CV*; standard deviation of the replicates divided by the mean of the replicates) would be an expression of precision of the estimates. While it may not be feasible to independently resample a structure, which would, e.g., require re-sectioning, an oversampling-subsampling approach can be used (Gundersen and Jensen, 1987). A very large or even exhaustive sample can be split into subsamples using multiple sampling intervals. This approach is quite labor intensive, and it has been used mostly to provide real life examples (Gundersen and Jensen, 1987; Roberts et al., 1993; McNulty et al., 2000; Slomianka and West, 2005) for the usefulness of the second way in which estimates of sampling induced variance can be obtained, i.e., mathematical estimators of precision.

Mathematical estimators of the coefficient of error (*CE*) of an estimate (e.g., Gundersen-Jensen estimator: Gundersen and Jensen, 1987; Gundersen et al., 1999; split-sample estimator: Cruz-Orive, 1990; Cruz-Orive and Geiser, 2004) can be based on the data from just one estimate, i.e., without the necessity of multiple replications of each estimate. The mean *CE* of the estimates should equal the *CV* of replicates. The facility of the *CE* calculation comes at a price. One needs to know or judge a variable critical to the calculation of the *CE*, the smoothness (*m*) of the dataset. Stereology software packages typically provide *CE* calculations for *m* values of 0 or 1. An *m* of 0 will provide a conservative estimate of precision, rarely exceeded in applications (Slomianka and West, 2005; Azim et al., 2012), but it may also be many-fold larger than the estimate provided by an *m* of 1. A second disadvantage is that precision can only be judged retrospectively, i.e., after datasets have been collected from the subjects.

While the labor associated with an oversampling-subsampling approach may not appear justified for one-off studies, our group has had a long-standing interest in the quantitative morphology of the hippocampus region and, in particular, the dentate gyrus (e.g., van Dijk et al., 2016). The work described here was performed to allow us to prospectively choose sampling intervals that provide *CE*s of a specified size. We here share the outcomes to allow readers to improve their qualified guesses at sampling schemes that provide the precision of estimates necessary in their studies and/or to select the *m* appropriate for the calculation of *CE* estimates.

MATERIALS AND METHODS

Tissue Preparation

Two 17-weeks old female C57/Bl6 mice were used in this study. Animals were deeply anaesthetized with sodium pentobarbital (50 mg/kg) and perfused transcardially with 100 ml 4% paraformaldehyde in 0.13 M phosphate buffer (pH 7.4). All procedures were conducted in accordance with the Swiss animal welfare guidelines and approved by the cantonal veterinarian office of Zürich, Switzerland. The brains were dissected, split into left and right hemispheres using a razor blade, and post-fixed overnight.

Hemispheres were dehydrated in a graded series of alcohols and embedded in glycolmethacrylate (GMA; Technovit 7100, Heraeus Kulzer GMBH, Wehrheim, Germany) following the manufacturer's instructions, but using infiltration times of one day for each infiltration step. Sections were cut at a nominal thickness of 20 μm on a rotary microtome using steel knives. Prior to the cutting of each section, the block surface was wetted with water to soften the GMA. Care was taken to work as uniformly as possible and without interruption of the cutting of each hemisphere. One hemisphere from each brain was cut frontally; the remaining two hemispheres were cut either sagittally or horizontally. All sections were individually collected in well-plates, mounted on clean glass slides and oven-dried at 70°C for 1 h prior to staining.

Sections were Giemsa stained following the protocol of Iñiguez et al. (1985) by immersion in 25 ml stock solution (Merck, Darmstadt, Germany) diluted in 225 ml 67 mM KH_2PO_4 buffer for 40 min. After staining, sections were differentiated for 10 s in 1% acetic acid, dehydrated for 10 s in 96% ethanol followed by 10 min each in 99% and 100% ethanol. Sections were cleared in Histoclear and mounted with Histomount (Amresco, Solon, OH).

Quantitative Procedures on Real Sections

The Cavalieri estimator (Gundersen, 1986; Gundersen et al., 1988) was used to generate the point counts in the datasets to be analyzed. Grids of points separated by 35 μm along the x- and y-axes were overlaid each section that contained the dentate gyrus using Stereoinvestigator software (MBF Bioscience, Williston. VT). Using this grid we obtained counts of around 10,000 points for the dentate granule cell layer, and the same grid was used for the hilus and molecular layer. The number of points in all three layers of the dentate gyrus is much higher than recommendations (up to a few hundred) but does not require much effort using modern stereological software. The high number of points in each section also minimizes the within-section variance, S^2, that originates from slight variations in the placement of the grid and, therefore, slight differences in the counts that can be obtained in a section. The definitions of the dentate layers corresponded to those used by, e.g., (Haug, 1974), West et al. (1978) or Slomianka and Geneser (1993) and are illustrated along the septotemporal axis of the horizontal series in **Figure 1**.

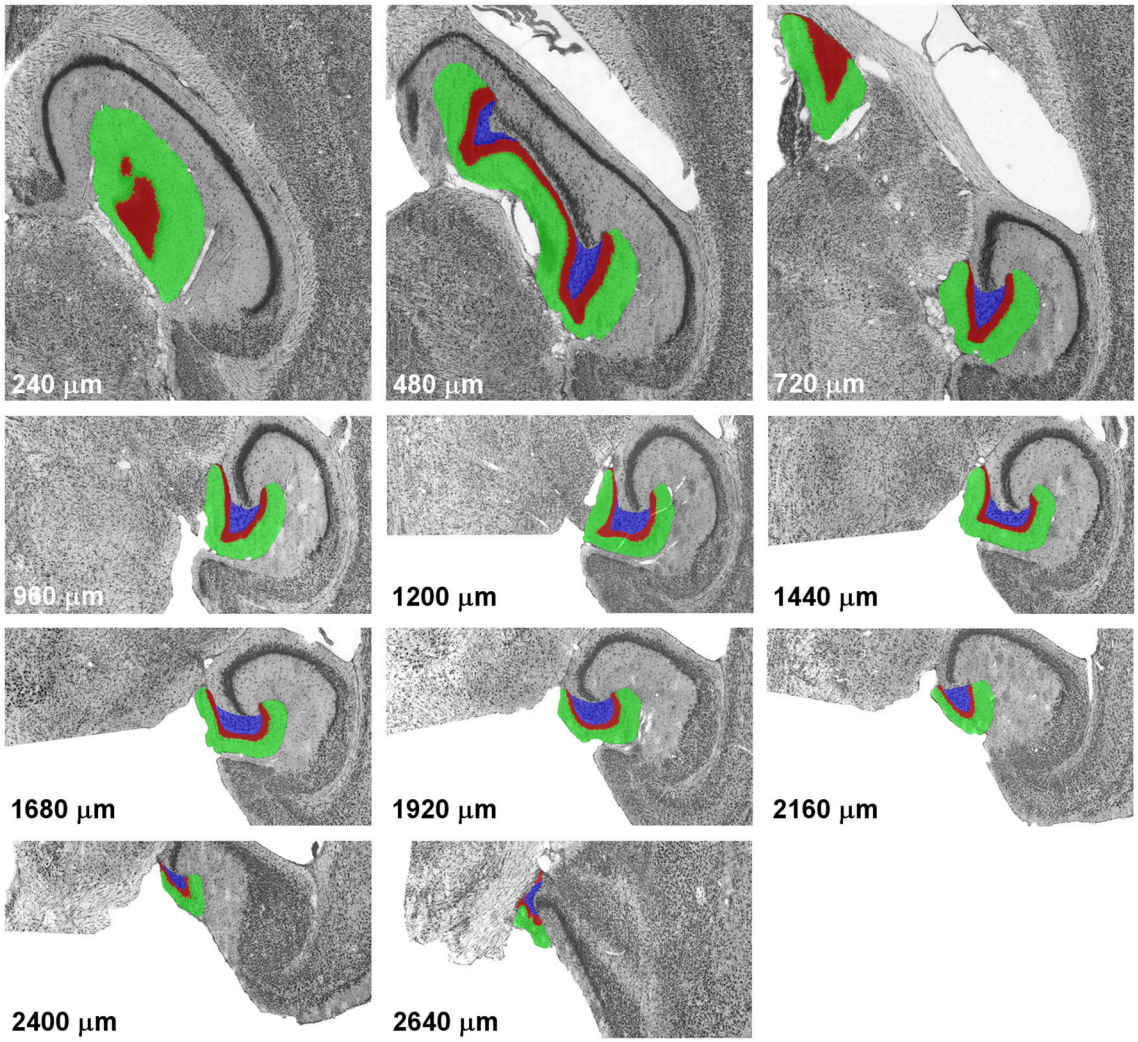

FIGURE 1 | Definitions of the dentate gyrus layers. Illustrations represent a complete sample of every 12th section of a horizontal series passing through the mouse dentate gyrus from dorsal to ventral. With the exception of the last image, alignment is maintained, with the images of levels from 960 to 2,400 µm corresponding to the lower half of the images of more dorsal levels. The dentate molecular layer is highlighted in green, the granule cell layer in red and the hilus in blue.

3D Modeling and Analysis

An exhaustive series of horizontal sections of the entire hemisphere was digitized at a resolution of 3 µm/pixels. Images were aligned manually using gross features of the hemisphere and thereafter cropped to only include the hippocampal formation. The cropped images were manually fine-aligned using landmarks within the hippocampus at high magnification (Autoaligner 6.0.0, Bitplane, Schweiz). Thereafter, the layers of the dentate gyrus were highlighted in red, green or blue. Color channels were exported, and the dentate layers were reconstructed in 3D using Imaris 6.3.1 (Bitplane AG, Switzerland). A Gauss filter with a filter width of 20 µm was applied to the model to smoothen the edges representing individual section. While the very mild filtering did not remove all edges, wider filter settings did obliterate anatomical detail by, e.g., filling in part of the narrow space between the blades of the granule cell layer occupied by the hilus septally or by blunting the narrow extensions of the hilus beneath the ends of the blades of the granule cell layer. The surface of the model was calculated using a walking cubes algorithm and saved for further analysis.

Point counts were generated from the 3D models using the Imaris extensions and interface to Matlab. Models were sectioned frontally, horizontally and sagittally using sections of 1 µm thickness. Points were spaced at x- and y-distances that corresponded to the resolution of the original scans and/or the distance between the sections that were used to generate the models, i.e., 3 µm along the x- and y-axes when the models were sliced horizontally and 3 and 20 µm when the models were sliced frontally or sagittally.

CE Estimation

The Gundersen-Jensen *CE* estimator (Gundersen et al., 1999; see formula below) was used to estimate the *CE*s for all possible samples up to sampling intervals of 20 for the real sections and up to 400 for the virtual sections of the 3D models. The maximum spacing between samples was therefore 400 µm for both real and virtual sections. *CE*s were calculated for an m of 0 and 1.

$$CE := \frac{\sqrt{\left(3(A - S^2) + C - 4B\right) \times \alpha + S^2}}{\sum P}$$

in which

$A = \sum_{i=0}^{n} (P_i{}^2)$, i.e., the sum, across all sections of the sample, of the counts in each individual section (P_i) squared

$B = \sum_{i=0}^{n} (P_i \times P_{i+1})$ i.e., the sum, across all sections of the sample, of P_i, multiplied by the counts in the following section of the sample, i.e., P_{i+1}, and

$C = \sum_{i=0}^{n} (P_i \times P_{i+2})$ i.e., the sum, across all sections of the sample, of P_i multiplied by the counts obtained in the next to the following section, i.e., P_{i+2}

α is 1/12 for an $m = 0$ and 1/240 for $m = 1$

ΣP is the sum of the points counted in all section.

$$S^2 := 0.0724 \times \frac{\bar{b}}{\sqrt{\bar{a}}} \times \sqrt{n \times \sum P}$$

in which

$\frac{\bar{b}}{\sqrt{\bar{a}}}$ is a shape factor that can be calculated from the boundary length, b, and area, a, of the dentate layers. In that the contribution of S^2 (also referred to as noise, local error or nugget variance) to the *CE* is minimal using the point counts obtained in this study, we did not estimate the shape factor, but used the nomogram in Gundersen and Jensen (1987) to select 10 as a conservative estimate of $\frac{\bar{b}}{\sqrt{\bar{a}}}$,

n is the number of sections contained in the sample, and

ΣP is the sum of the points counted in all sections.

The *CE*s were estimated empirically by calculating, for each sampling interval from 2 to 20, the coefficient of variation of all samples belonging to a sampling interval. E.g., for the sampling interval 17, 17 samples are generated. Sample 1 contains sections 1, 18, 35, 52 … etc., sample 2 containing sections 2, 19, 36, 53 … etc., continuing up to sample 17 which contains section 17, 34, 51, 68 etc. A volume estimate is calculated for each of the 17 samples. The coefficient of variation for the sampling interval 17 is finally calculated by dividing the standard deviation of the 17 possible estimates by the mean of the 17 estimates.

Estimates of the *CE* for both m values and empirical estimates were plotted against sampling intervals.

RESULTS

Empirical *CE*s and Estimator *CE*s Obtained from the Sectioned Dentate Gyrus

113 (frontal series), 130 (horizontal series), or 107 (sagittal series) sections containing the dentate gyrus were obtained for analysis. No sections were missing. In these series, we obtained point counts of 5,284 to 5,589 for the hilus, 9,956 to 11,927 for the granule cell layer, and 28,854 to 30,674 for the molecular layer.

The volume distributions of three layers of the dentate gyrus along the direction of cutting are illustrated in **Figure 2**. The empirical *CE*s (*CV*s of replicates), belonging to subsamples up to a sampling interval of 20 (i.e., using every 20th section), are illustrated in **Figure 3** together with the *CE* estimates of each subsample of each sampling interval using an $m = 0$ or an $m = 1$. In addition, **Figure 3** provides these data for the entire dentate gyrus, i.e., the collated data of the hilus, granule cell layer and molecular layer.

For the layers of the dentate gyrus, *CE* estimates using both m values typically provide upper and lower bounds for the empirical *CE*s obtained. Exceptions were found for sampling intervals around 14 for the granule cell layer and around 18 for the molecular layer in the sagittal series and sampling intervals around 14 for the hilus in the horizontal series. Around these intervals, the empirical *CE*s exceeded the estimates. At sampling intervals larger than 10, the empirical *CE*s of the hilus and granule cell layer were usually found within the scatter of *CE* estimates that used an $m = 0$, i.e., *CE* estimates using an $m = 0$ are better predictors of the empirical *CE*s. For lower sampling intervals, the small differences between the *CE* estimates resulting from different m values and the limited number of subsamples available to calculate empirical *CE*s make it difficult to evaluate which m would result in a better *CE* estimation.

The entire dentate gyrus behaved somewhat differently from its layers. For all sampling intervals used in frontal sections and most sampling intervals smaller than 15 in horizontal sections, *CE*s that were estimated using an $m = 1$ were better predictors of the empirical CEs. In sagittal series, an $m = 0$ again provided better predictions.

We did not estimate the shape factors that are needed to estimate the contribution within-section variance, S^2, to the *CE* estimates, but instead used a conservative shape factor of 10. The high number of points counted in each section should result in a minimal contribution of S^2 to the *CE*s. We also calculated *CE*s using an unrealistically high shape factor of 50, which barely generated perceptible changes in the graphs (data not shown).

Empirical *CE*s and Estimator *CE*s Obtained from Reconstructions

Figure 4 illustrates the 3D models that were obtained after reconstructing the dentate layers from a horizontal series of sections. The volume distributions obtained from virtually sectioning the models frontally and sagittally largely corresponded to the volume distributions seen in the real sections.

The comparison of empirical and estimated CEs was performed analogous to the comparison in real sections, but using much thinner, 1 µm thick virtual sections. Sampling intervals up to 400 were assessed, at which interval the distance between the virtual sections corresponded to the distance between the 20 µm thick real section and a sampling interval of 20 ($20 \times 20\,\mu m = 400\,\mu m$)—the maximum used to assess the real sections. The decrease in section thickness provided larger

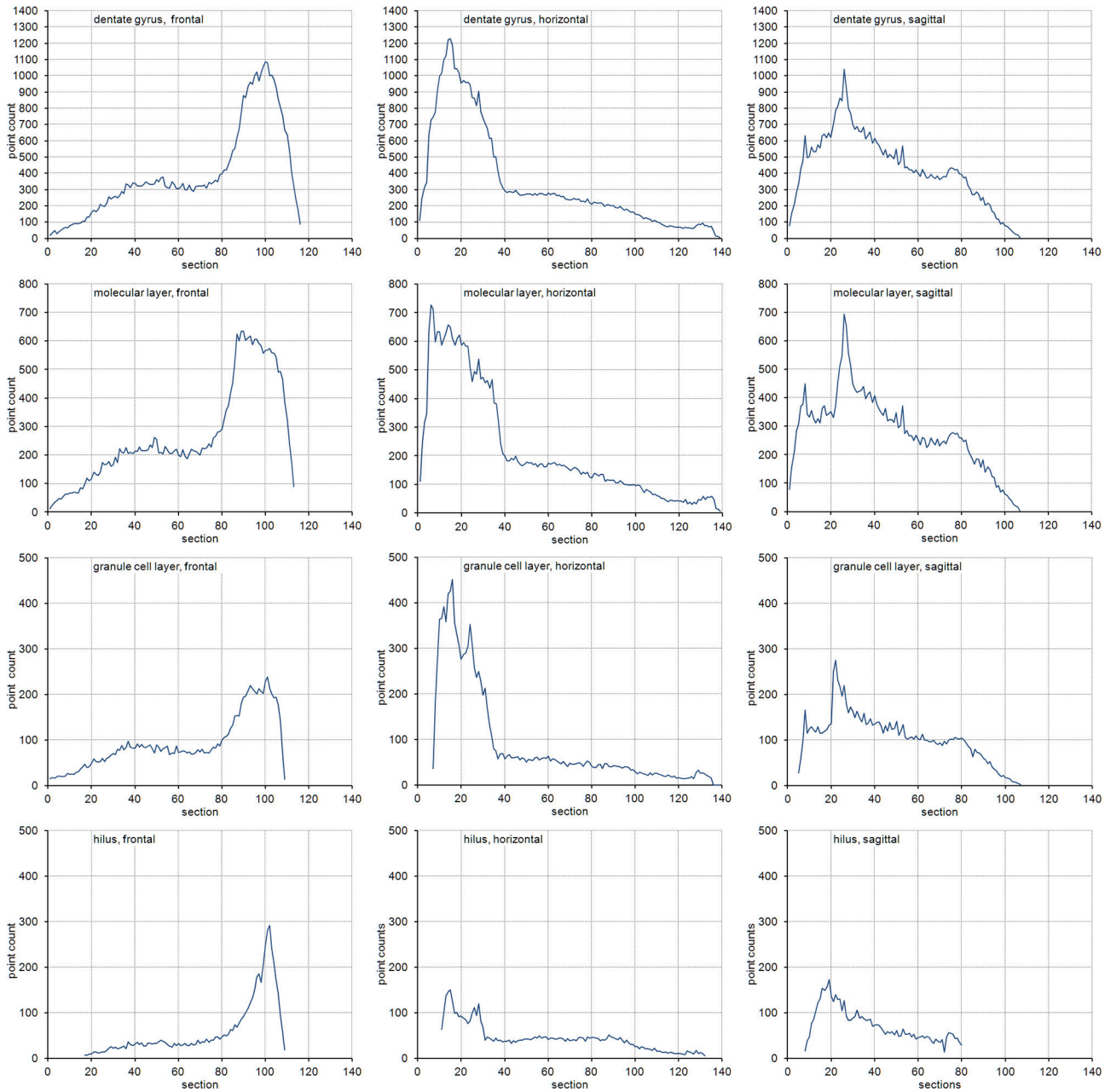

FIGURE 2 | Volume distributions of the dentate gyrus and its layers. Volume distributions are illustrated by the point count obtained in each section. Cutting directions are anterior to posterior for frontal sections, dorsal to ventral for horizontal sections and medial to lateral for sagittal sections.

numbers of subsamples for sampling intervals with low section to section distances.

Figure 5 illustrates the empirical *CE*s obtained from the virtual sections together with the means of the *CE* estimates obtained from the subsamples of each sampling interval using an $m = 0$ or an $m = 1$. Again, the empirical *CE*s are typically bounded by the estimated *CE*s that were calculated for the two m values. For sampling intervals above 200, corresponding to sampling every 10th real section, the outcomes of sampling virtual sections largely correspond to the sampling of real sections. Instead, for sampling intervals lower than 120, corresponding to the sampling of every 6th section, *CE*s are usually better predicted by an $m = 1$. For the intervening intervals, the quality of the prediction of different m values depends on the layer of the dentate gyrus and the orientation of the sections.

In addition, we observed the Zitterbewegung of the empirical *CE* estimates, i.e., oscillating changes in the size of the *CE* estimate that increase in amplitude and period with increasing sampling intervals (best seen in the frontally sectioned hilus in **Figure 5**).

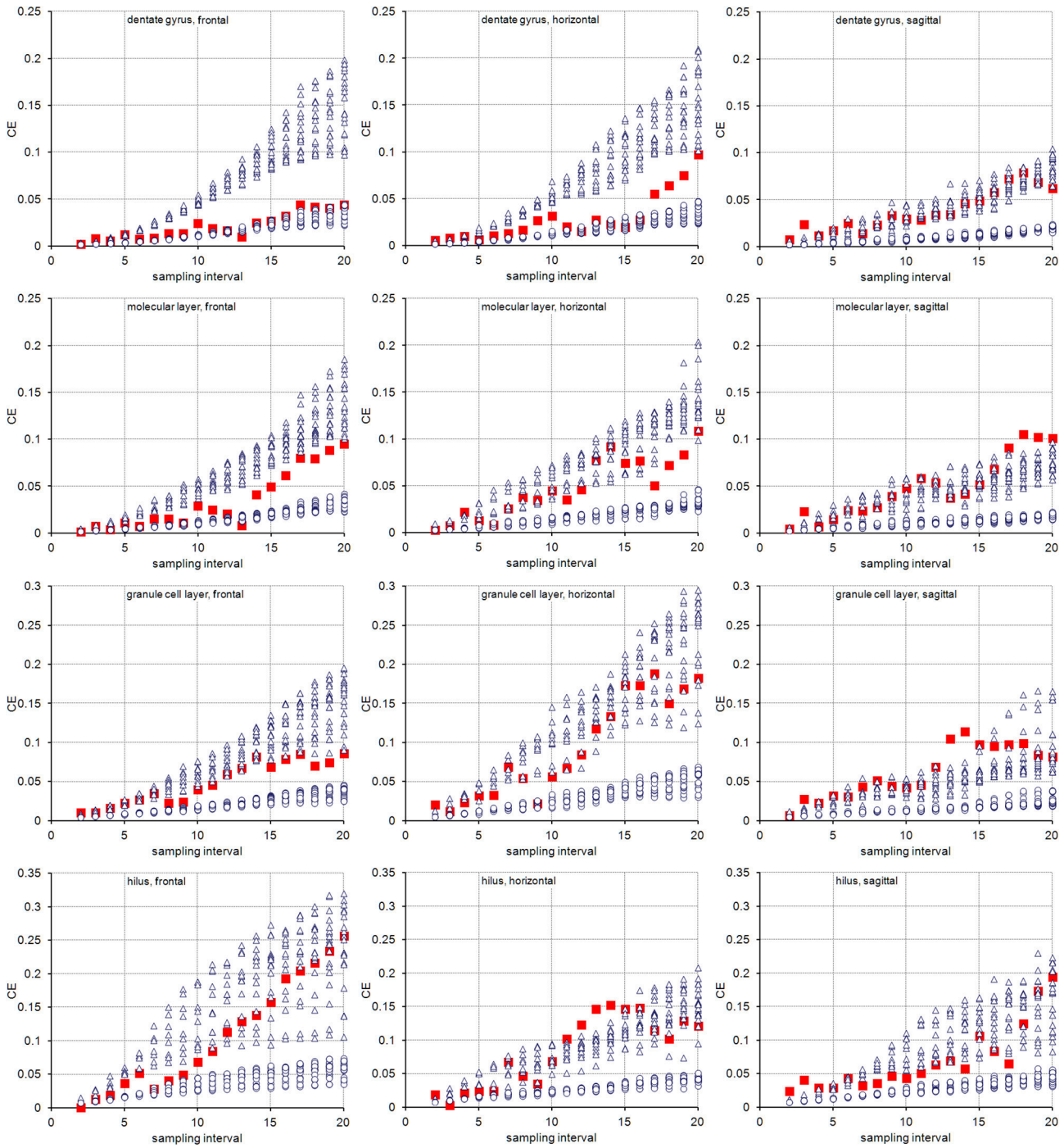

FIGURE 3 | Measurement precision vs. sampling frequency. *CE*s are plotted for increasing intervals between the sampled sections. Empirical estimates of the *CE*s (filled squares) are typically bounded by Gundersen-Jensen *CE* estimates for $m = 0$ (open triangles) and $m = 1$ (open circles). Sampling intervals at which the empirical *CE* exceeds the range of estimated *CE*s correspond to intervals between peaks in the volume distributions of the layers (**Figure 2**). How many sections will be analyzed depends on the size of the structure of interest along the direction of the cutting. E.g., about 110 frontal 20 μm thick sections would contain the granule cell layer (see **Figure 2**). Series sampled using an interval of 10, i.e., every 10th section is collected (200 μm between sections), would contain 11 sections to be analyzed. If sections are cut, e.g., 40 μm thick, a series of every 5th section (200 μm between sections) would generate a similar number of sections.

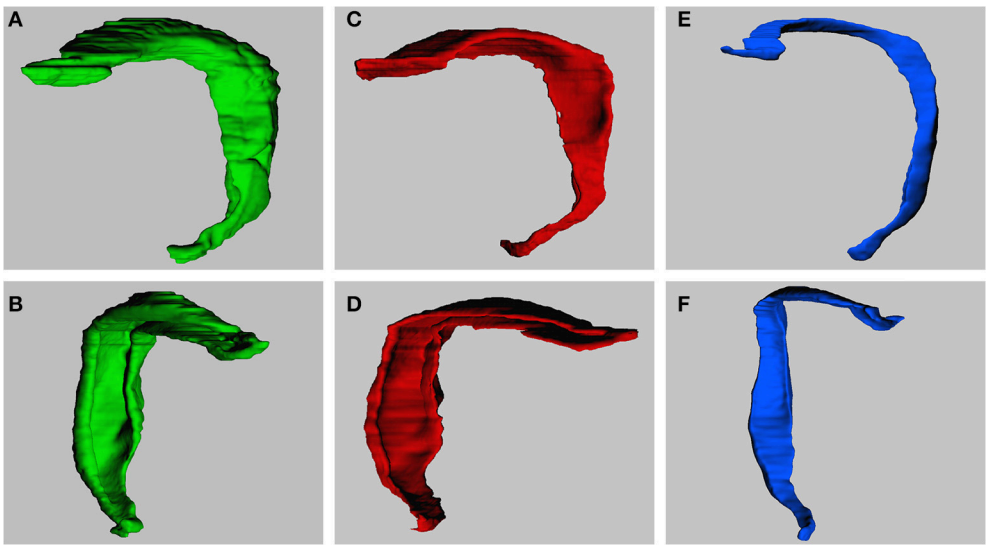

FIGURE 4 | 3-Dimensional models of dentate gyrus layers. Models are constructed based on the horizontal series of real sections. Models represent the dentate molecular layer **(A,B)**, the granule cell layer **(C,D)** and hilus **(E,F)**. Views are from medial to lateral **(A,C,E)** or into the concavity of the dentate layers from anterior to posterior (**B,D,F**; slight variations between exact angles).

DISCUSSION

In summary, frontal sections of the dentate gyrus are the most efficient way to generate quantitative estimates of the volumes of its layer. For a given sampling interval, *CE* values are generally lower for the granule cell layer and molecular layer in frontal sections than those obtained from sagittal or horizontal sections. Also, the number of sections to be cut frontally is lower than those that need to be cut horizontally. Finally, the layers are quantitatively "better behaved" in frontal than in sagittal sections, in which the *CE* for some sampling intervals may be difficult to predict using the Gundersen-Jensen estimator (see also below). An *m* of 0 would be the appropriate choice for *CE* estimations. If the entire dentate gyrus is the region of interest, frontal sampling is exceedingly efficient and provides volume estimates with *CE*s of less than 5% assessing as few as 5 to 6 sections. Efficiency is, of course, not the only factor to be considered when a direction to section the material is chosen. Another factor would be the ability to define interregional and interlaminar boundaries (Slomianka and West, 2005).

Extrapolation to Other Estimators

With some caution, it should be possible to extrapolate the efficiencies seen for volume estimates to estimators of number, length and surface. Although differences in the densities and morphologies of cells are present in the dentate gyrus, changes along the hippocampal axes are generally modest and gradual (Gaarskjaer, 1978; Jinno et al., 1998; Uchida et al., 2005; Jinno and Kosaka, 2010; Jinno, 2011; Amrein et al., 2015; Buckmaster et al., 2017). Estimators of parameters other than volume are therefore likely to generate distributions along the direction of cutting that resemble the volume distributions shown here. Note that the contribution of within-section variance, S^2, to the *CE* is calculated very differently from that of point counts used in volume estimations. It equals the sum of interactions between stereological probe and the parameter of interest (Gundersen et al., 1999), e.g., the number of intersections between a test area and capillaries or cell processes in estimations of their lengths (Løkkegaard et al., 2001; Nykjær Nikolajsen et al., 2011; Gondré-Lewis et al., 2016) or the number of intersections between test lines and cortical or neuronal surface (Acer et al., 2010; Loesch et al., 2010). The contribution of S^2 to the *CE* (CE_{S^2}) would be $\sqrt{sum\ of\ interactions}/sum\ of\ the\ interactions$, i.e., 0.1 (or 10%) for a count of 100. While point counts for volume estimates can be easily increased to make S^2 negligible, this may not be the case for other types of probe-feature interactions. Using our data on volume estimate precision, a rough guesstimate of the *CE*s to be expected from estimators of number, length or surface, could be $\sqrt{CE_{vol}{}^2 + CE_{S^2}{}^2}$. If, e.g., the granule cell layer is sampled in frontal sections spaced at 200 µm intervals (sampling interval 10, $CE_{vol} \sim 0.04$) and if, e.g., a total of 200 cells is counted in this sample of sections, one may expect a *CE* of $\sim \sqrt{0.04^2 + 0.07^2}$ or 0.08. The small increase of from 0.07 to 0.08 may suggest that the selection of sections does not have a major impact on the final *CE*, but it actually contributes one quarter to the variance generated by the sampling (0.04^2 / $0.08^2 = 0.25$). Also note that counting very many cells does not guarantee a small *CE*. One may decide to count 10,000 granule cells in a sample of every 20th section. Even though the CE_{S^2} only amounts to 0.01, one would still have to expect a final *CE* ranging from ~0.08 (sagittal or frontal sections) to 0.18 (horizontal sections) because of the selection of only every 20th section. Clearly, counting 200 cells in samples from every 10th section is a massively more efficient way to obtain a *CE* of 0.08.

A rough guesstimate of the *CE* will provide a starting point for a study. Once a data set is available, *CE*s should, of course,

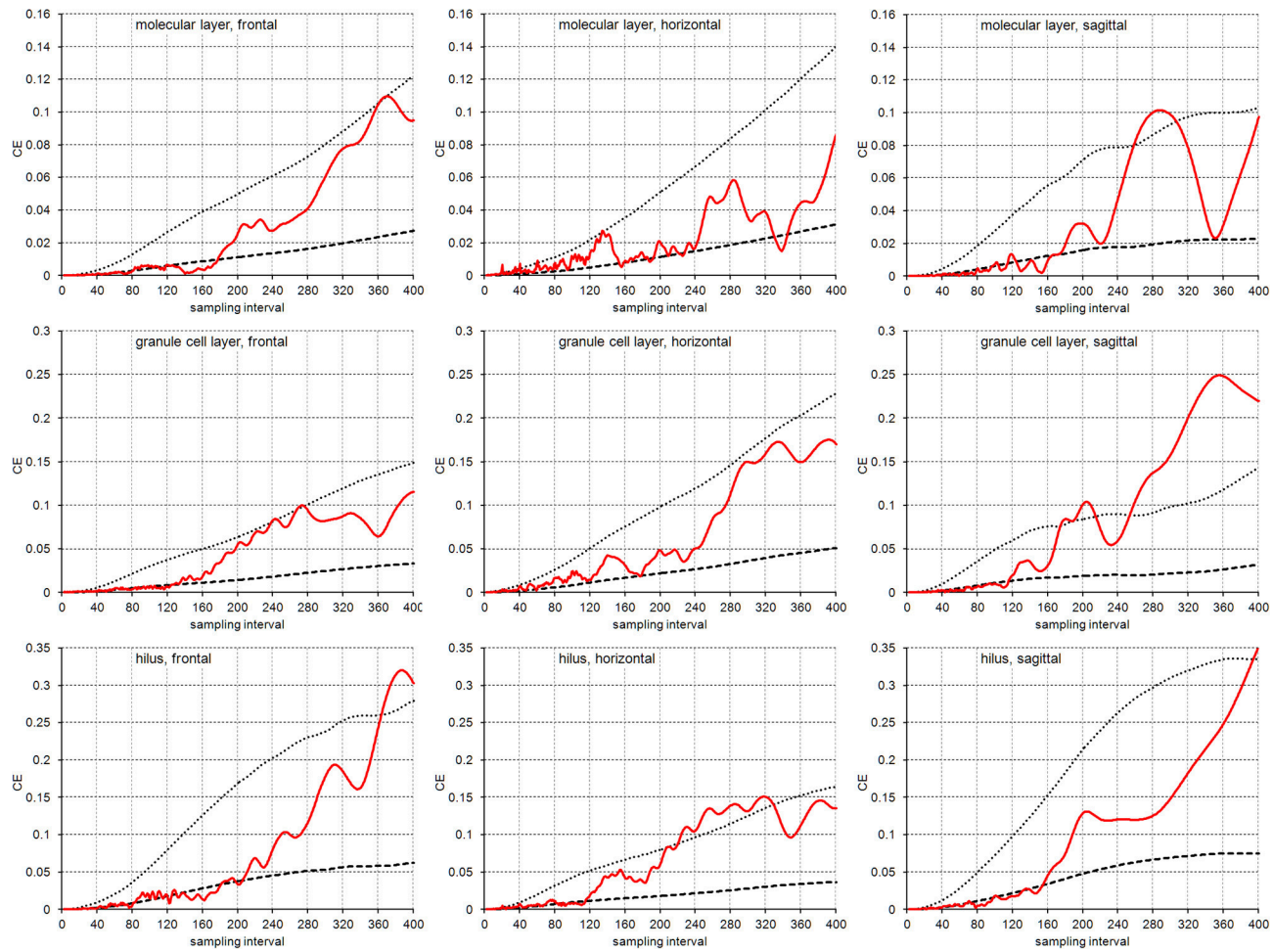

FIGURE 5 | CE estimates based on virtual sectioning of 3D models**.** Empirical *CE* estimates (solid lines) are typically bounded by the means of the Gundersen-Jensen *CE* estimates for $m = 0$ (dotted lines) and $m = 1$ (broken lines) and exceed *CE* estimates for sampling intervals that correspond to the distance between peaks in the volume distributions (**Figure 2**). The very intense sampling (1 μm sections) and higher subsample numbers for low sampling intervals show transitions in the behavior of the empirical *CE* from following an $m = 1$ at low sampling intervals to an $m = 0$ at high sampling intervals. In addition, empirical *CE*s now oscillate with increasing amplitude and period for increasing sampling intervals (Zitterbewegung; best seen in the frontally sectioned hilus).

be estimated using the approaches appropriate for the method that has been selected. Such estimates are typically provided by stereological software packages. Calculated examples of *CE* estimations can be found in, e.g., West et al. (1991) and (West, 2012) for estimates based on fractionator sampling or in West and Gundersen (1990) if estimates are based on separate density and volume estimates.

Which Smoothness Factor to Choose?

While an estimate of the smoothness factor, *m*, also can be calculated (Kiêu et al., 1999), datasets available from typical applications are too small to provide robust estimates (Cruz-Orive, 1999; Gundersen et al., 1999; García-Fiñana and Cruz-Orive, 2004). The selection of a smoothness factor *m* is therefore often a matter of investigator judgment. The original form of the Gundersen-Jensen *CE* estimator used an *m* of 0 (Gundersen and Jensen, 1987), while the later revision made an argument for the use of an *m* of 1 (Gundersen et al., 1999). We previously found that an *m* of 0 provided better estimates for the hippocampal CA1 pyramidal cell layer (Slomianka and West, 2005) and here confirm this observation for the layers of the dentate gyrus. The smoothing of the 3D models in excess of 20 μm filter width did hide anatomical detail. Even exhaustive series of 20 μm thick sections do not appear to provide sufficient resolution to predict all anatomical features from section to section, which would be a justification for the choice of an *m* of 0. Another possible explanation for larger than expected *CE*s at low sampling intervals are sources of variance not accounted for by the Gundersen-Jensen *CE* estimator. One source may be observer error, i.e., variations in counts that result from observer uncertainty about the location of the boundary of the structure that is being assessed. Another source may be variance of the exact distances between the sections and their thicknesses (Baddeley et al., 2006; Ziegel et al., 2010). Both types of error have

the potential to significantly increase *CE*s, in particular when sampling intervals are small. In contrast, one µm thick virtual sections of 3D models, which retained the anatomical detail, do provide the necessary resolution and provide some sampling intervals that allow the use of an *m* of 1 also for the dentate layers. Such sampling intervals would, however, be prohibitive in terms of the workload required in the real world. Also, *CE*s that are generated by such intervals are so low (usually 0.02 or less) that the workload is unlikely to be justified considering that animal to animal variation is usually much higher. In statistical comparisons, the chances to observe group differences would be more efficiently increased by increasing the number of subjects (Gundersen and Østerby, 1981; West, 2012).

Cases of Poor *CE* Estimates

Most stereological protocols encompass the selection of sampling sites at regular intervals along the x- and y-axes of the section. *CE* estimators may perform poorly if there is a match of sampling intervals with periodic changes in anatomy. Such changes may relate to repeated units in the organization of the brain, e.g., cortical barrels or columns. Even though a perfect match is unlikely to occur, it is relatively easy to avoid in the plane of the section by the random application (including rotation) of the grid of sampling sites. There is no similar way to alter sampling positions along the z-axis, and matches between sampling interval and periodic changes in morphology will result in poor *CE* estimates. When empirical *CE*s exceeded *CE* predictions, the associated section sampling intervals were close matches to the distance between two prominent peaks in the volume distribution the dentate layers. The peaks in turn reflect sagittal or horizontal sections that pass through large parts of the suprapyramidal and, once again, the infrapyramidal blades of the dentate gyrus layers. "Crest-on" frontal sections avoid this from happening. If horizontal or sagittal sections are preferred for reasons unrelated to estimate precision, the respective intervals should be avoided.

With these few and avoidable exceptions, the Gundersen-Jensen *CE* estimator provides useful bounds for the precision to be expected from sampling schemes of the mouse dentate gyrus.

AUTHOR CONTRIBUTIONS

LB and SG performed the practical work under the supervision of DW and LS. LS wrote the first draft of the manuscript, which was revised in collaboration with all co-authors.

DISCLOSURE

The data presented in this manuscript were part of theses written by LB and SG in fulfillment of the requirements to obtain the degree Dr. med. at the University of Zürich.

REFERENCES

Acer, N., Çankaya, M. N., Işçi, Ö., Baş, O., Çamurdanoglu, M., and Turgut, M. (2010). Estimation of cerebral surface area using vertical sectioning and magnetic resonance imaging: a stereological study. *Brain Res.* 1310, 29–36. doi: 10.1016/j.brainres.2009.11.017

Amrein, I., Nosswitz, M., Slomianka, L., Van Dijk, R. M., Engler, S., Klaus, F., et al. (2015). Septo-temporal distribution and lineage progression of hippocampal neurogenesis in a primate (*Callithrix jacchus*) in comparison to mice. *Front. Neuroanat.* 9:85. doi: 10.3389/fnana.2015.00085

Azim, K., Fiorelli, R., Zweifel, S., Hurtado-Chong, A., Yoshikawa, K., Slomianka, L., et al. (2012). 3-Dimensional examination of the adult mouse subventricular zone reveals lineage-specific microdomains. *PLoS ONE* 7:e49087. doi: 10.1371/journal.pone.0049087

Baddeley, A., Dorph-Petersen, K.-A., and Vedel Jensen, E. B. (2006). A note on the stereological implications of irregular spacing of sections. *J. Microsc.* 222, 177–181. doi: 10.1111/j.1365-2818.2006.01585.x

Buckmaster, P. S., Abrams, E., and Wen, X. (2017). Seizure frequency correlates with loss of dentate gyrus GABAergic neurons in a mouse model of temporal lobe epilepsy. *J. Comp. Neurol.* 525, 2592–2610. doi: 10.1002/cne.24226

Cruz-Orive, L. M. (1990). On the empirical variance of a fractionator estimate. *J. Microsc.* 160, 89–95. doi: 10.1111/j.1365-2818.1990.tb03050.x

Cruz-Orive, L. M. (1999). Precision of Cavalieri sections and slices with local errors. *J. Microsc.* 193, 182–198. doi: 10.1046/j.1365-2818.1999.00460.x

Cruz-Orive, L. M., and Geiser, M. (2004). Estimation of particle number by stereology: an update. *J. Aerosol Med.* 17, 197–212. doi: 10.1089/jam.2004.17.197

Gaarskjaer, F. B. (1978). Organization of the mossy fiber system of the rat studied in extended hippocampi I. terminal area related to the number of granule and pyramidal cells. *J. Comp. Neurol.* 178, 49–72. doi: 10.1002/cne.901780104

García-Fiñana, M., and Cruz-Orive, L. M. (2004). Improved variance prediction for systematic sampling on R. *Statistics* 38, 243–272. doi: 10.1080/0233188032000158826

Gondré-Lewis, M. C., Darius, P. J., Wang, H., and Allard, J. S. (2016). Stereological analyses of reward system nuclei in maternally deprived/separated alcohol drinking rats. *J. Chem. Neuroanat.* 76, 122–132. doi: 10.1016/j.jchemneu.2016.02.004

Gundersen, H. J. G., and Østerby, R. (1981). Optimizing sampling efficiency of stereological studies in biology: or "Do more less well!". *J. Microsc.* 121, 65–73. doi: 10.1111/j.1365-2818.1981.tb01199.x

Gundersen, H. J. G. (1986). Stereology of arbitrary particles. *J. Microsc.* 143, 3–45. doi: 10.1111/j.1365-2818.1986.tb02764.x

Gundersen, H. J. G., Bendtsen, T. F., Korbo, L., Marcussen, N., Møller, A., Nielsen, K., et al. (1988). Some new, simple and efficient stereological methods and their use in pathological research and diagnosis. *APMIS* 96, 379–394. doi: 10.1111/j.1699-0463.1988.tb05320.x

Gundersen, H. J. G., and Jensen, E. B. (1987). The efficiency of systematic sampling in stereology and its prediction. *J. Microsc.* 147, 229–263. doi: 10.1111/j.1365-2818.1987.tb02837.x

Gundersen, H. J. G., Jensen, E. B. V., Kieu, K., and Nielsen, J. (1999). The efficiency of systematic sampling in stereology – reconsidered. *J. Microsc.* 193, 199–211. doi: 10.1046/j.1365-2818.1999.00457.x

Haug, F.-M. S. (1974). Light microscopical mapping of the hippocampal region, the pyriform cortex and the corticomedial amygdaloid nuclei of the rat with Timm's sulphide silver method I. Area dentata, hippocampus and subiculum. *Z. Anat. Entwickl-Gesch* 145, 1–27. doi: 10.1007/BF00519123

Iñiguez, C., Gayoso, M. J., and Carreres, J. (1985). A versatile and simple method for staining nervous tissue using Giemsa dye. *J. Neurosci. Methods* 13, 77–86.

Jinno, S. (2011). Regional and laminar differences in antigen profiles and spatial distributions of astrocytes in the mouse hippocampus, with reference to aging. *Neuroscience* 180, 41–52. doi: 10.1016/j.neuroscience.2011.02.013

Jinno, S., Aika, Y., Fukuda, T., and Kosaka, T. (1998). Quantitative analysis of GABAergic neurons in the mouse hippocampus, with optical disector using confocal laser scanning microscope. *Brain Res.* 814, 55–70. doi: 10.1016/S0006-8993(98)01075-0

Jinno, S., and Kosaka, K. (2010). Stereological estimation of numerical densities of glutamatergic principal neurons in the mouse hippocampus. *Hippocampus* 20, 829–840. doi: 10.1002/hipo.20685

Kiêu, K., Souchet, S., and Istas, J. (1999). Precision of systematic sampling and transitive methods. *J. Stat. Plan. Inference* 77, 263–279. doi: 10.1016/S0378-3758(98)00193-1

Loesch, A., Mayhew, T. M., Tang, H., Lobo Ladd, F. V., Lobo Ladd, A. A. B., et al. (2010). Stereological and allometric studies on neurons and axo-dendritic synapses in the superior cervical ganglia of rats, capybaras and horses. *Cell Tissue Res.* 341, 223–237. doi: 10.1007/s00441-010-1002-8

Løkkegaard, A., Nyengaard, J. R., and West, M. J. (2001). Stereological estimates of number and length of capillaries in subdivisions of the human hippocampal region. *Hippocampus* 11, 726–740. doi: 10.1002/hipo.1088

McNulty, V., Cruz-Orive, L. M., Roberts, N., Holmes, C. J., and Gual-Arnau, X. (2000). Estimation of brain compartment volume from MR Cavalieri slices *J. Comput. Assist. Tomogr.* 24, 466–477. doi: 10.1097/00004728-200005000-00021

Nykjær Nikolajsen, G., Skovgaard Jensen, M., and West, M. J. (2011). Cholinergic axon length reduced by 300 meters in the brain of an Alzheimer mouse model. *Neurobiol. Aging* 32, 1927–1931. doi: 10.1016/j.neurobiolaging.2011.05.006

Roberts, N., Cruz-Orive, L. M., Reid, N. M. K., Brodie, D. A., Bourne, M., and Edwards, R. H. T. (1993). Unbiased estimation of human body composition by the Cavalieri method using magnetic resonance imaging. *J. Microsc.* 171, 239–253. doi: 10.1111/j.1365-2818.1993.tb03381.x

Schmitz, C., Eastwood, B. S., Tappan, S. J., Glaser, J. R., Peterson, D. A., and Hof, P. R. (2014). Current automated 3D cell detection methods are not a suitable replacement for manual stereologic cell counting. *Front. Neuroanat.* 8:27. doi: 10.3389/fnana.2014.00027

Slomianka, L., and Geneser, F. A. (1993). Distribution of acetylcholinesterase in the hippocampal region of the mouse: III. the area dentata. *J. Comp. Neurol.* 331, 225–235.

Slomianka, L., and West, M. J. (2005). Estimators of the precision of stereological estimates: an example based on the CA1 pyramidal cell layer of rats. *Neuroscience* 136, 757–767. doi: 10.1016/j.neuroscience.2005.06.086

Uchida, K., Nakamura, S., Kobayashi, T., and Machida, T. (2005). Topographic analysis of cell proliferation in the hippocampus of the adult mouse. *Neuroreport* 16, 2033–2036. doi: 10.1097/00001756-200512190-00013

van Dijk, R. M., Huang, S.-H., Slomianka, L., and Amrein, I. (2016). Taxonomic separation of hippocampal networks: principal cell populations and adult neurogenesis. *Front. Neuroanat.* 10:22. doi: 10.3389/fnana.2016.00022

West, M. J. (2012). The precision of estimates in stereological analyses. *Cold Spring Harb. Protoc.* 2012, 937–949. doi: 10.1101/pdb.top071050

West, M. J., Danscher, G., and Gydesen, H. (1978). A determination of the volumes of the layers of the rat hippocampal region. *Cell Tissue Res.* 188, 345–359. doi: 10.1007/BF00219777

West, M. J., and Gundersen, H. J. G. (1990). Unbiased stereological estimation of the number of neurons in the human hippocampus. *J. Comp. Neurol.* 296, 1–22. doi: 10.1002/cne.902960102

West, M. J., Slomianka, L., and Gundersen, H. J. G. (1991). Unbiased stereological estimation of the total number of neurons in the subdivisions of rat hippocampus using the optical fractionator. *Anat. Rec.* 231, 482–497. doi: 10.1002/ar.1092310411

Ziegel, J., Baddeley, A., Dorph-Petersen, K.-A., and Vedel Jensen, E. B. (2010). Systematic sampling with errors in sample locations. *Biometrika* 97, 1–13. doi: 10.1093/biomet/asp067

Conflict of Interest Statement: The authors declare that the research was conducted in the absence of any commercial or financial relationships that could be construed as a potential conflict of interest.

frontiers in Neuroanatomy

ORIGINAL RESEARCH
published: 08 January 2018
doi: 10.3389/fnana.2017.00134

Delineation of Subregions in the Early Postnatal Human Cerebellum for Design-Based Stereologic Studies

Anna Fichtl[1], Andreas Büttner[2], Patrick R. Hof[3], Christoph Schmitz[1] and Maren C. Kiessling[1]*

[1] Chair of Neuroanatomy, Faculty of Medicine, Institute of Anatomy, Ludwig-Maximilians-Universität München, Munich, Germany, [2] Institute of Forensic Medicine, University of Rostock, Rostock, Germany, [3] Fishberg Department of Neuroscience and Friedman Brain Institute, Icahn School of Medicine at Mount Sinai, New York, NY, United States

Recent design-based stereologic studies have shown that the early postnatal (<1 year of age) human cerebellum is characterized by very high plasticity and may thus be very sensitive to external and internal influences during the first year of life. A potential weakness of these studies is that they were not separately performed on functionally relevant subregions of the cerebellum, as was the case in a few design-based stereologic studies on the adult human cerebellum. The aim of the present study was to assess whether it is possible to identify unequivocally the primary, superior posterior, horizontal, ansoparamedian, and posterolateral fissures in the early postnatal human cerebellum, based on which functionally relevant subregions could be delineated. This was tested in 20 human post mortem cerebellar halves from subjects aged between 1 day and 11 months by means of a combined macroscopic and microscopic approach. We found that the superior posterior, horizontal, and posterolateral fissures can be reliably identified on all of the specimens. However, reliable and reproducible identification of the primary and ansoparamedian fissures was not possible. Accordingly, it appears feasible to perform subregion-specific investigations in the early postnatal human cerebellum when the identification of subregions is restricted to crus I (bordered by the superior posterior and horizontal fissures) and the flocculus (bordered by the posterolateral fissure). As such, it is recommended to define the entire cerebellar cortex as the region of interest in design-based stereologic studies on the early postnatal human cerebellum to guarantee reproducibility of results.

Keywords: cerebellum, design-based stereology, humans, postnatal, reproducibility of results, subregions

OPEN ACCESS

Edited by:
Bente Pakkenberg, Research Laboratory for Stereology and Neuroscience, Denmark

Reviewed by:
Michela Ferrucci, University of Pisa, Italy
Salvador Martinez, Universidad Miguel Hernández de Elche, Spain

****Correspondence:***
Christoph Schmitz
christoph_schmitz@med.uni-muenchen.de

Received: *26 June 2017*
Accepted: *20 December 2017*
Published: *08 January 2018*

Citation:
Fichtl A, Büttner A, Hof PR, Schmitz C and Kiessling MC (2018) Delineation of Subregions in the Early Postnatal Human Cerebellum for Design-Based Stereologic Studies. Front. Neuroanat. 11:134. doi: 10.3389/fnana.2017.00134

INTRODUCTION

The cerebellum is connected to the cerebrum, the brainstem, and the spinal cord by several fiber pathways (e.g., Paxinos, 1990; Roostaei et al., 2014; Witter and De Zeeuw, 2015). It is critically involved in motor and sensory function as well as higher cognitive and emotional functions that can be assigned to different subregions of the cerebellum (e.g., Stoodley and Schmahmann, 2009; Buckner, 2013; Witter and De Zeeuw, 2015). The human cerebellum can be examined at different levels. For example, its function can be studied *in vivo* using positron emission tomography (PET; e.g., Petacchi et al., 2010) and functional magnetic resonance imaging (fMRI; e.g., Schraa-Tam et al., 2012). Structural studies comprise MRI *in vivo* (Schmahmann et al., 1999) and various

approaches to understand its microscopic anatomy. In this context, Stoodley and Schmahmann (2009) performed a meta-analysis of more than 50 functional neuroimaging studies of the human cerebellum and found the following: (i) sensorimotor tasks activate the anterior lobe (lobule V) and adjacent lobule VI, with additional foci in lobule VIII; (ii) motor activation is found in lobule VIIIA/B, while somatosensory activation is confined to lobule VIIIB; (iii) the posterior lobe is involved in higher-level tasks; (iv) lobule VI and Crus I are involved in language and verbal working memory, lobule VI in spatial tasks, lobules VI, Crus I and VIIB in executive functions, and lobules VI, Crus I and medial lobule VII in emotional processing; (v) language is heavily right-lateralized and spatial tasks left-lateralized, reflecting crossed cerebro-cerebellar projections; and (vi) emotional processing involves vermal lobule VII, implicated in cerebellar-limbic circuitry. Furthermore, language and executive tasks activate regions of Crus I and lobule VII proposed to be involved in prefronto-cerebellar loops.

Several studies have shown that quantitative-histologic investigations using design-based stereology provide more reliable insight into the normal and pathologic microscopic structure of the human cerebellum than related studies that were not performed with these techniques. In this regard it is of note that Sparks and Hunsaker (2002) hypothesized that the cerebellum plays an important role in the pathogenesis of sudden infant death syndrome (SIDS). This hypothesis is related to the role of the cerebellum in respiratory and cardiovascular control (Cruz-Sánchez et al., 1997; Harper et al., 2000), as well as the hypothesis that in SIDS affected children may suffer from prolonged apnea and suddenly stop breathing (Steinschneider, 1972; Guilleminault et al., 1975). Most probably Gadsdon and Emery (1976) first called attention to the possible involvement of the cerebellum in SIDS. In the following years, additional post mortem studies on the cerebellum of SIDS patients were published, yielding conflicting results. Some of these studies reported no differences between SIDS and control cases (Oehmichen et al., 1989; Riedel et al., 1989). Other studies proposed a developmental delay of the cerebellum in SIDS (Cruz-Sánchez et al., 1997) or reported several changes in the cerebellar cortex in SIDS (Lavezzi et al., 2006, 2007). However, none of these studies were performed using a rigorous design-based stereologic approach. This was performed more recently by Kiessling et al. (2013) who found no alterations in mean total numbers of Purkinje cells and granule cells in the cerebellum of SIDS patients and age- and sex-matched controls. Moreover, using the design-based stereologic probe "space balls" (Calhoun and Mouton, 2000; Mouton et al., 2002), Müller-Starck et al. (2014) found no differences either in mean microvessel length density in the cerebellar layers between the same SIDS cases and controls investigated by Kiessling et al. (2013) or between controls with a low likelihood of hypoxia and those with a higher likelihood of hypoxia. These data did not support the hypothesis of hypoxia in the cerebellum in SIDS.

A potential weakness of the studies by Kiessling et al. (2013) and Müller-Starck et al. (2014) is that they were not performed in functionally relevant subregions in the cerebellum (see Stoodley and Schmahmann, 2009), as had been done in a few other studies applying design-based stereology. For instance, Andersen et al. (2003) found an age-related neuron loss in the human cerebellum starting at ∼65 years of age when investigating post mortem brains from subjects without neurological disorders aged between 19 and 84 years. By determining total neuron numbers, these authors investigated four different cerebellar subregions. The greatest neuron loss was reported in the anterior lobe, namely a loss of 40.6% of Purkinje cells and granule cells. In contrast, neuron loss in the posterior lobe, vermis, and flocculonodular lobe was not as remarkable. As a result, Andersen et al. (2003) reported an overall age-related decrease by 11.7% in the total number of Purkinje cells and 12.7% in the total number of granule cells in the human cerebellum. This study demonstrated that design-based stereologic investigations focusing on cerebellar subregions may in fact come to different conclusions than studies performed on the entire human cerebellum.

Accordingly, it appears attractive to study quantitative parameters such as total numbers of cells and microvessel length densities in a subregion-specific manner in SIDS and neurodevelopmental disorders affecting the cerebellum (e.g., Steinlin, 2008; Stoodley, 2016; Stoodley and Limperopoulos, 2016) using design-based stereology. However, the latter would require unequivocal and reproducible identification of subregions that can serve as regions of interest (ROIs) in such studies. In this regard, it is critical to note that the human cerebellum has a much higher structural and functional plasticity during the first year of life than previously thought (Kiessling et al., 2014), and may respond very sensitively to internal and external influences during this time. Specifically, ∼85% of the cerebellar granule cells are generated postnatally in humans, and the mean number of granule cells per Purkinje cell in the human cerebellum increases from approximately 480 in the first postnatal month to ∼2,700 in the 11th month of life (Kiessling et al., 2014). These data may have important implications for several neuropsychiatric conditions in which cerebellar involvement has been demonstrated, including its potential role in autism (Palmen et al., 2004; Fatemi et al., 2012), autistic characteristics associated with changes of the cerebellar vermis (Hashimoto et al., 1995; Christakou et al., 2013), schizophrenia (Martin and Albers, 1995; Joyal et al., 2004; Andreasen and Pierson, 2008), attention deficit hyperactivity disorder (Berquin et al., 1998; Mostofsky et al., 1998; Castellanos et al., 2001; Durston et al., 2011), mood swings and bipolar disorders (Strakowski et al., 2005; Baldaçara et al., 2011), and impairment in cognitive functions (Gasbarri et al., 2003).

The development of the human cerebellum begins approximately in the fourth week of gestation with the formation of the cerebellar territory in the hindbrain. Cell proliferation and migration provide the basis for further differentiation and foliation of the cerebellar surface. The occurrence of cerebellar fissures dates to the 12th week of gestation (Donkelaar et al., 2003). The human cerebellar development results in a densely folded cerebellar cortex subdivided into 10 lobules and 13 sublobules, separated by 11 fissures (Schmahmann et al., 1999) until birth (Larsell, 1947). Most importantly, within the first year of life, the human cerebellum still undergoes considerable

modification. Specifically, the cortical thickness of different cerebellar subregions shows different rates of growth in neo- and archi-cerebellum, presumably depending on their origin (Tsekhmistrenko, 1996). Nevertheless, the exact dynamics of cellular and volumetric growth of different cerebellar subregions within archi- and neo-cerebellum are not fully understood. It is quite conceivable that certain cerebellar subregions, and, thus, subregion-specific cerebellar functions, develop faster than others. In any case, such potential differences in subregion-specific developmental velocity would have to be considered when investigating the developing human cerebellum in a subregion-specific manner.

Based on widely accepted macroscopic (Nieuwenhuys et al., 1980), microscopic (Skefos et al., 2014), and MRI-based (Schmahmann et al., 1999) delineations of the adult human cerebellar cortex, five different ROIs were determined in the present study for the early postnatal (<1 year of age) human cerebellum. The first ROI comprises lobules IV–VI of the cerebellar hemisphere (blue area in **Figure 1**) and is bordered by the superior posterior fissure (red in **Figure 1**). The second ROI comprises crus I (red area in **Figure 1**) and is bordered by the superior posterior fissure and the horizontal fissure (green in **Figure 1**). The third ROI comprises crus II (green area in **Figure 1**) and is bordered by the horizontal fissure and the ansoparamedian fissure (yellow in **Figure 1**). The fourth ROI comprises lobules VIIB–VIIIB (yellow area in **Figure 1**) and is bordered by the ansoparamedian fissure and the posterolateral fissure (dark gray in **Figure 1**). The fifth ROI comprises the flocculus (gray area in **Figure 1**).

We proposed that unequivocal identification of these ROIs is possible in the early postnatal (<1 year of age) human cerebellum, comparable to the situation in the adult human cerebellum based on the descriptions by Nieuwenhuys et al. (1980), Schmahmann et al. (1999), and Skefos et al. (2014). This was tested in the present study.

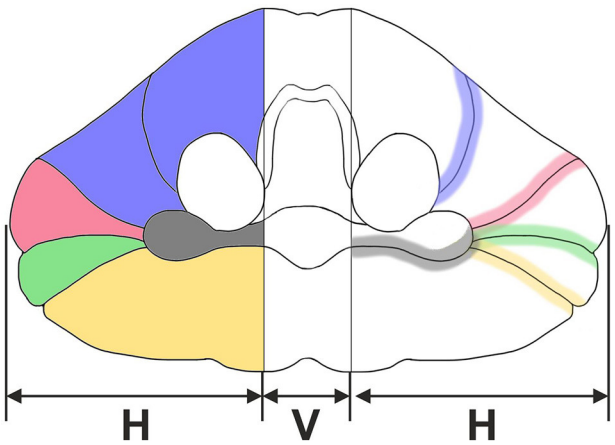

FIGURE 1 | Sketch of an adult human cerebellum in ventral view. Vermis (V) and hemispheres (H) are indicated. Five regions of interest are depicted on the **left:** lobules IV-VI (blue), crus I (red), crus II (green), lobules VIIB-VIIIB (yellow), and flocculus (dark gray). Furthermore, four anatomically distinct fissures representing important landmarks on the cerebellar surface are depicted on the **right:** primary fissure (blue), superior posterior fissure (red), horizontal fissure (green), ansoparamedian fissure (yellow), and posterolateral fissure (dark gray).

MATERIALS AND METHODS

The present study was performed on post mortem cerebellar halves obtained from 20 children aged between 1 day and 11 months with known clinical records (**Table 1**). The cerebellar halves were collected at the Institute of Legal Medicine, Faculty of Medicine, LMU Munich (Munich, Germany) between 1999 and 2001. The mean post mortem interval (time between death and autopsy was 32.5 ± 4.8 h (mean ± standard error of the mean) (range, 7–76). The use of these autopsy cases for scientific investigations was approved by the Institutional Review Board of the University of Rostock (Rostock, Germany) under registration number A 2012-0053. Further consent to be obtained from the next of kin was not needed as per German regulations and was also waived by the ethics committee that approved the study.

During autopsy the cerebella were divided mediosagittally. Either the left or the right hemisphere was available for each case, and was immersion-fixed with 10% formaldehyde for 15–17 years (details are provided in Kiessling et al., 2013, 2014). Accordingly, only one hemisphere per cerebellum was investigated in the present study. Histological processing was performed at the Chair of Neuroanatomy, Institute of Anatomy, Faculty of Medicine, LMU Munich (Munich, Germany).

Six cerebellar halves (identified as A in **Table 1**) were rinsed in tap water for 1 week prior to being immersed in sucrose solution in Tris-buffered saline (10, 20, and 30%) at 4°C until they sank to the bottom of the jar containing the sucrose solution. Then, cerebellar halves were swabbed with paper tissue to remove fluid on the surface, meninges and vessels were carefully removed, and photographs of the cerebellar halves from different perspectives (dorsal, ventral, cranial, caudal, lateral, and medial) were taken with a Canon EOS 5D Mark III camera and Canon EF 24–105 mm 1:4.0 L IS USM objective (Canon, Tokyo, Japan).

The surface of these six cerebellar halves were scanned to document macroscopic features including the primary, superior posterior, horizontal, ansoparamedian, and posterolateral fissures (**Figure 1**, right) in order to identify the following regions of interest (**Figure 1**, left): lobules IV–VI, crus I, crus II, lobules VIIB–VIIIB, and flocculus. Identification of fissures strictly followed the description by Schmahmann et al. (1999) based on the criteria summarized in **Table 2**. A representative example is shown in **Figure 2**. Identified fissures were filled with artist acrylics of different colors (distributed by Aldi, Mülheim an der Ruhr, Germany) mixed with tap water (3/1 v/v) (same colors as in **Figure 1**). In some cases, individual fissures could not be unequivocally identified and more than one fissure were filled with the same acrylic color (see **Figure 3**). After filling identified fissures with acrylic colors the cerebellar halves were again photographed from the same perspectives.

Afterwards, the cerebellar halves were frozen in dry ice for 1 h and were cut into 100 µm-thick serial sagittal sections using a cryostat (Type CM 1950; Leica Microsystems, Wetzlar,

TABLE 1 | Characteristics of the cases investigated in the present study.

Case no.	P	Age [m]	G	BoL [cm]	BoW [kg]	BrW [g]	Cause of death	H
1	B	0.03	F	49	2.7	335	Suffocation	R
2	B	0.03	F	50	3.3	n.d.	Strangling	L
3	B	0.83	M	54	4.3	540	Suffocation (crime)	L
4	A	1	F	47	2.5	387	Infection	L
5	B	1.5	M	61	5.4	594	Heart defect	L
6	A	2.5	M	62	5.6	583	SIDS	L
7	B	3	M	63	5.5	721	Infection	R
8	B	3	M	55	5.4	539	WFS	L
9	A	4	F	65	6.3	723	SIDS	L
10	B	4	M	64	6.6	826	Unknown	R
11	A	6	M	69	6.7	859	SIDS	L
12	B	7	M	70	6.8	751	Suffocation (crime)	L
13	A	8	F	73	7.0	798	SIDS	R
14	B	8	M	72	9.7	1239	Otitis media	L
15	B	9	F	75	7.8	911	MCAD deficiency/AGS	L
16	A	10	F	81	11.5	1229	Suffocation (peanut)	L
17	B	10	M	74	8.9	956	Sepsis	L
18	B	10	F	65	5.5	836	Carbon monoxide intoxication	L
19	B	10	F	73	8.6	967	Myocarditis	L
20	B	11	M	73	8.8	960	Heart defect	L

P, processing; A, processing of cerebellar halves as described in the present study; B, processing of cerebellar halves as described in Kiessling et al. (2013, 2014); m, months; G, gender; F, female; M, male; BoL, body length; BoW, body weight; BrW, brain weight; H, hemisphere; R, right; L, left; n.d., not determined; SIDS, sudden infant death syndrome; WFS, Waterhouse-Friedrichsen syndrome; MCAD, medium-chain acyl-CoA dehydrogenase; AGS, adrenogenital syndrome.

TABLE 2 | Criteria used for identification of fissures in the early postnatal human cerebellum according to Schmahmann et al. (1999).

Fissure	Description
Horizontal	Separates lobule VIIAf from lobule VIIAt in the vermal region, and crus I from crus II in the hemispheres
Superior posterior	Separates lobule VI from lobule VII in the vermis and lobule VI from crus I (of the ansiform lobule) in the hemisphere
Posterolateral	Forms the boundary between the posterior lobe of the cerebellum and the flocculonodular lobe, separating lobule IX from lobule X (in older terminology–nodulus at the vermis; flocculus at the hemisphere)
Primary	Distinguishes the anterior lobe of the cerebellum (lobules I through V) from the posterior lobe (lobules VI through IX), and specifically it separates lobule V from lobule VI, both in the vermis and the hemisphere
Ansoparamedian	Is submerged on the ventral surface of the "tuber," separating lobules VIIAt from VIIB (previously termed the paramedian or gracile lobule)

Germany) equipped with C35 blades (Feather Safety Razor, Osaka, Japan). Five subsequent series of every 24th section each (with random starting points determined by a random number generator) encompassing the entire cerebellar half (distance between sections: 24 $\times$100 µm, which equals 2.4 mm) were collected. Four of these series of sections were stored at −20°C; one series of every 24th section per cerebellar half was randomly selected for further processing and mounted on either Superfrost plus glass slides (Menzel, Braunschweig, Germany) or gelatin-coated glass slides (Menzel). Sections were placed on a light box (Prolite Basic; Kaiser Fototechnik, Buchen, Germany) and photographed with the camera mentioned above (**Figure 4**). Fissures filled with acrylic colors were identified and marked by scratches on the lower surface of the glass slides. Then, sections were stained with cresyl violet, coverslipped with Malinol (Waldeck Division Chroma, Münster, Germany) and photographed again (**Figure 4**).

The other 14 cerebellar halves (identified as B in **Table 1**) had already been processed and were used in previous studies (Kiessling et al., 2013, 2014). Processing of these 14 cerebellar halves was identical to the description above except for the filling of fissures with acrylic colors and marking of the glass slides.

The final figures were assembled using Corel Photo-Paint X8 and Corel Draw X8 (both versions 18.1.0.661; Corel, Ottawa, Canada). Only minor adjustments of contrast and brightness were made, without altering the appearance of the original images.

RESULTS

Identification of Anatomically Distinct Fissures in the Early Postnatal Human Cerebellum

Tables 3, **4** summarize the findings of the present study with regard to the identification of anatomically distinct fissures in early postnatal human cerebella based on combined macroscopic and microscopic investigation. The superior posterior, horizontal, and posterolateral fissures could be

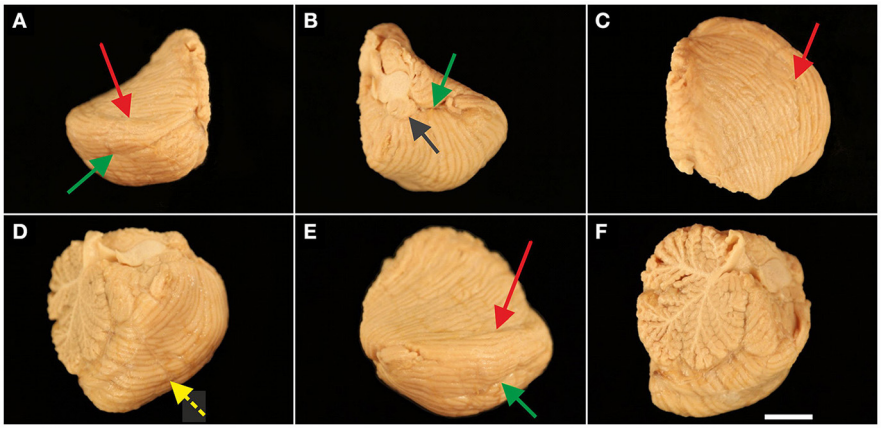

FIGURE 2 | Representative left cerebellar half from a 6-month-old child (case no. 11 in **Table 1**). The cerebellar half is shown from dorsal **(A)**, ventral **(B)**, cranial **(C)**, caudal **(D)**, lateral **(E)**, and medial **(F)** views. The arrows indicate prominent, macroscopically visible fissures (colors of the arrows are the same as those used in **Figure 1**): superior posterior fissure (red arrow in **A,C,E)**, horizontal fissure (green arrow in **A,B,E**), and posterolateral fissure (dark gray arrow in **B**). Identification of prominent, macroscopically visible fissures was less obvious in caudal view [the dotted yellow arrow in **(D)** points to the ansoparamedian fissure] and was not unequivocally possible in medial view. The scale bar in **(F)** represents 1 cm in **(A–F)**.

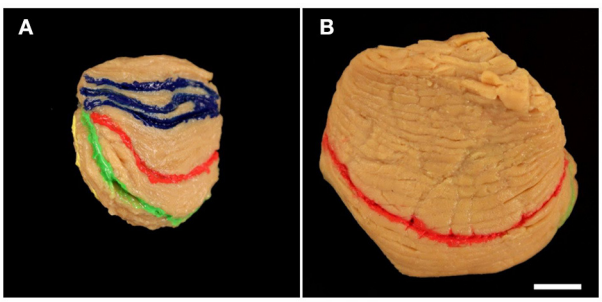

FIGURE 3 | Representative right cerebellar half from a 2.5-month-old child (**A**; case no. 6 in **Table 1**) and left cerebellar hemisphere from a 10-month-old child (**B**; case no. 16 in **Table 1**) viewed from cranial. Fissures marked in blue **(A)** represent three likely positions of the primary fissure (colors are the same as those used in **Figure 1**). In **(B)** more than three neighboring fissures where likely to represent the primary fissure; therefore blue acrylic color was not applied. Other colored fissures are the superior posterior fissure (red in **A,B**), horizontal fissure (green in **A,B**), and ansoparamedian fissure (yellow in **A**). The scale bar in **(B)** represents 1 cm in **(A,B)**.

unequivocally identified on all six cerebellar halves that were macroscopically investigated in the present study, irrespective of age ("A" cases in **Table 1**). In contrast, the primary and ansoparamedian fissures could not be reliably identified because, at the macroscopic level, they did not differ from neighboring fissures.

The histologic sections of five out of the six "A" cases did not allow the unequivocal identification of 10 cerebellar lobules subdivided into 13 sublobules and separated by 11 fissures. Because of a variable number of folia, the total number of lobules and sublobules differed among the cases (**Figure 5**). The superior posterior fissure and horizontal fissure could be readily identified on all histologic sections, but the primary and ansoparamedian fissures were not reliably identifiable. According to several references (see for example Paxinos, 1990), the primary fissure directly abuts the superior posterior fissure, and together they define the borders of crus I. However, other studies described a different localization of the primary fissure. For instance, Schmahmann et al. (1999) described that crus I includes an additional fissure. In addition, the ansoparamedian fissure was described in the literature as directly adjoining the horizontal fissure (Paxinos, 1990). However, on the histologic sections of the cerebellar halves of the "A" cases the exact position of the ansoparamedian fissure could not be identified because of slight morphologic differences in lobule VIIIA. Specifically, lobule VIIIA appeared V-shaped in cases no. 7, 12, 13, and 14 (the latter is depicted in **Figure 5A**) and apparently consisted of two folia. However, these two folia were not completely separated by a fissure and converged in one shared tail of white matter, which ended in the central white matter (case no. 14 in **Figure 5A**). In contrast, at the corresponding position on histologic sections of the other four cerebellar halves, there were two single folia, fully separated by a fissure (case no. 17 in **Figure 5B**).

In all "A" cases, small-sized accessory folia were found at the bottom of fissures, particularly of the superior posterior fissure (**Figure 6A**). These folia could not be unequivocally related to the regions of interest shown in **Figure 1** because of their position below the surface of the cerebellar halves.

Histologic Identification of Anatomically Distinct Fissures in the Early Postnatal Human Cerebellum without Prior Macroscopic Assessment

In "B" cases (**Table 1**), in which a macroscopic evaluation of fissures was not available, microscopic identification of the superior posterior and horizontal fissures on sagittal sections of the cerebellum was as reliable as in the "A" cases. In

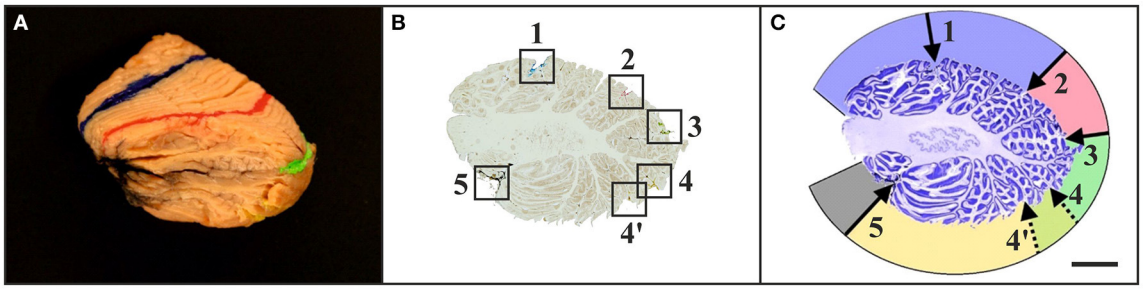

FIGURE 4 | Representative left cerebellar half from a 6-month-old child (case no. 11 in **Table 1**) after filling identified fissures with acrylic colors **(A)** (colors as in **Figure 1**), cutting the cerebellar half into 100 μm-thick sagittal sections **(B)**, and staining the sections with cresyl violet **(C)**. The squares in **(B)** indicate the positions where the acrylic colors were clearly visible on unstained sections. Marking the positions of the acrylic colors by scratches on the lower surface of the glass slides facilitated recognizing of identified fissures on sections after staining with cresyl violet **(C)** [the numbers in **(C)** correspond to the numbers in **(B)**]. This allowed identification of regions of interest on histological sections of early postnatal (<1 year of age) human cerebella based on macroscopic identification of fissures representing important landmarks on the cerebellar surface. Numbers in **(B,C)**: 1, primary fissure (blue in **A,B**); 2, superior posterior fissure (red in **A,B**); 3, horizontal fissure (green in **A,B**); 4, ansoparamedian fissure (yellow in **A,B**); 5, posterolateral fissure (dark gray in **A,B**). Colors in **(C)** indicate lobules IV–VI (blue), crus I (red), crus II (green), lobules VIIB-VIIIB (yellow), and flocculus (dark gray). Note that in this example two neighboring fissures were likely to represent the ansoparamedian fissure (indicated by 4 and 4′). Therefore, both fissures were labeled with yellow acrylic color **(A,B)**, and the border between crus II and lobules VIIB-VIIIB could not unequivocally be determined **(C)**. The scale bar in **(C)** represents 1 cm in **(A–C)**.

TABLE 3 | Summary of the findings of the present study based on macroscopic and microscopic investigation.

Fissure	Criteria for macroscopic investigation	Criteria for microscopic investigation
	(1) Unequivocal, reproducible identification possible	
Horizontal	- Courses along the cerebellar equator - Dorsal: rather oblique course toward the vermis - Ventral: ending in the flocculus	- Bottom of the fissure nearby the tapering part of the white matter - Characteristic triangular shape of crus II
Superior posterior	- Prominent and uniform position at the cerebellar surface	- Proximal fissure next to the horizontal fissure in cranial direction
Posterolateral	- Unique cerebellar localization and structure, considerably differing from other cerebellar regions	- First fissure next to the cerebellar peduncle in caudal direction
	(2) Unequivocal, reproducible identification not possible	
Primary	- No characteristic traits compared to surrounding fissures	- Proximal fissure next to the superior posterior fissure in cranial direction
Ansoparamedian	- Morphological variability of the bordering lobules crus II and VIIB	- Proximal fissure next to the horizontal fissure in caudal direction - Fifth fissure next to the flocculus in cranial direction

contrast, in two out of the 14 "B" cases the ansoparamedian fissure could only be approximated due to V-shaped areas in lobule VIIIA (as described in the "A" cases). Also, it was not possible to identify the posterolateral fissure of two "B" cases with certainty (cases no. 5 and 15). Because of the clear structure of the flocculus, the posterolateral fissure could be identified in macroscopic investigations. However, this was not possible when fissures and lobules could only be evaluated two-dimensionally at the histologic level. Specifically, it was not possible to identify the posterolateral fissure unequivocally on sections showing the transition zone from the flocculus to lobule VIIIB (**Figure 6B**).

As such, reproducible delineation of the regions of interest shown in **Figure 1** based on isolated inspection of histologic sections was not possible because of confounding fissures that were found particularly in lateral sections. **Table 3** summarizes the findings in regard to identification of anatomically distinct fissures on histologic sections of early postnatal human cerebella without macroscopic examination. This approach yielded less reliable results than when a macroscopic evaluation was conducted before histologic processing. None of these observations were restricted to either the left or the right cerebellar hemisphere.

DISCUSSION

Validity of the Results

The use of intact, macroscopically and microscopically well-preserved human cerebellar halves allowed for high-precision morphologic investigations such as the identification of anatomically distinct fissures and delineation of functionally relevant regions of interest. The cerebellar halves investigated in the present study represented a sample throughout the first year of life, which is a critical period of time with regard to the early postnatal development of the human cerebellum (Kiessling et al., 2014). The investigation of only one cerebellar half per case can be considered valid because biologically relevant

TABLE 4 | Summary of the findings of the present study with regard to identification of anatomically distinct fissures in early postnatal (<1 year of age) human cerebella of the cases summarized in **Table 1**.

Case no.	P	Age [m]	H	PF	SPF	HF	APF	PLF	N-F	R
1	B	0.03	R	(+)	+	+	(+)	+	11–12	
2	B	0.03	L	(+)	+	+	(+)	+	10–11	
3	B	0.83	L	(+)	+	+	(+)	+	12–13	
4	A	1	L	–	+	+	(+)	+	7–8	†
5	B	1.5	L	–	–	–	–	–	n.d	‡
6	A	2.5	L	(+)	+	+	(+)	+	9–10	‡
7	B	3	R	(+)	+	+	(+)	+	10–11	
8	B	3	L	(+)	+	+	(+)	(+)	10–11	‡
9	A	4	L	(+)	+	+	(+)	+	9–10	
10	B	4	R	(+)	+	+	(+)	+	11–12	
11	A	6	L	(+)	+	+	(+)	+	8–9	‡
12	B	7	L	–	+	+	(+)	+	9–10	‡
13	A	8	R	(+)	+	+	(+)	+	9–10	
14	B	8	L	(+)	+	+	–	+	11–12	
15	B	9	L	(+)	+	+	(+)	–	9–10	‡
16	A	10	L	(+)	+	+	(+)	+	11–12	
17	B	10	L	–	+	+	(+)	+	11–12	
18	B	10	L	(+)	+	+	(+)	+	9–10	
19	B	10	L	–	+	+	(+)	+	11–12	‡
20	B	11	L	(+)	+	+	(+)	+	10–11	

P, Processing; A, processing of cerebellar halves as described in the present study; B, processing of cerebellar halves as described in Kiessling et al. (2013, 2014); m, months; H, hemisphere; R, right; L, left; PF, primary fissure; SPF, superior posterior fissure; HF, horizontal fissure; APF, ansoparamedian fissure; PLF, posterolateral fissure; n.d., not definable; +, unequivocal identification possible; (+), identification only approximately possible because two neighboring fissures were equally likely; –, identification not possible; N-F number of fissures; R, remarks; †, abnormal/missing fissures; ‡, minor foliation within the anterior lobe compared to the adult human cerebellum.

asymmetry in the gross anatomy of the left and right halves of the human cerebellum has not been reported (Gocmen-Mas et al., 2009). Besides, the results of the present study are not influenced by the inclusion of cerebella from children who died from SIDS. Some studies postulated differences within other parts of the central nervous system between SIDS cases and matched controls. For example, Hunt et al. (2017) found altered protein expression in pontine neurons in SIDS cases. However, Kiessling et al. (2013) demonstrated using a rigorous design-based stereologic approach that there are no differences in mean volumes of the different layers within the cerebellum as well as in mean total numbers of cerebellar Purkinje cells and granule cells between SIDS cases and age- and sex-matched controls. Consequently, it is reasonable to assume that the formation and anatomical location of cerebellar fissures in SIDS cases and age- and sex-matched controls do not significantly differ from each other (as was corroborated by the findings on the "B" cases outlined in **Table 4**).

A potential limitation of the present study is that only cerebellar halves were investigated. As a result, the vermis was not available at full-size as it is located in-between the hemispheres, and was therefore excluded from investigation. It should however be noted that according to Schmahmann et al. (1999), there is no true "vermis" in the anterior lobe. Rather, application of this term to the paramedian sectors of the anterior lobe is an extension of the Latin term "vermis" (meaning "worm") used by Malacarne (1776) to denote the structure visible in the posterior and inferior aspect of the cerebellum. The vermis (as such) is present from lobules VI through X. The use of the term vermis to indicate "midline" has become in time fully entrenched, and has brought with it the problem of defining what is the lateral extent of the anterior lobe "vermis" (Schmahmann et al., 1999). It has been suggested that the paravermian sulcus limits the vermis laterally. However, in many brains there is no paravermian sulcus and where one appears to be present, it may simply reflect the indentation produced by the course of the medial branch of the superior cerebellar artery (Schmahmann et al., 1999). Furthermore, the findings of the present study cannot be directly transferred to the adult human cerebellum as the definite formation of different cerebellar regions is still in process after the first year of life (Tsekhmistrenko, 1996).

Another potential issue is that the cerebellar halves investigated in the present study were not uniformly randomly sampled, e.g., by the flip of a coin, to decide whether the left or the right half of a given cerebellum was sampled and analyzed. However, the results summarized in **Table 4** clearly demonstrate that the main finding of the present study (impossibility to identify reliably and reproducibly the primary and ansoparamedian fissures in the early postmortem human cerebellum) did not depend on whether the left or the right hemispheres were investigated.

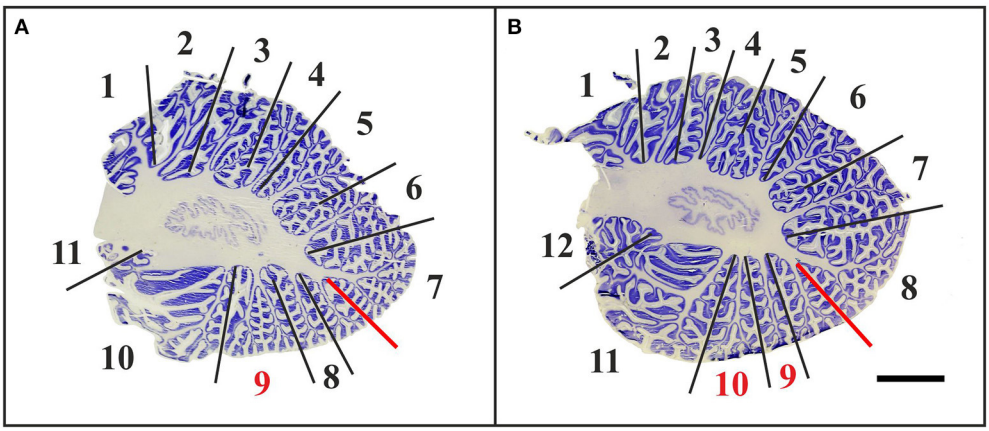

FIGURE 5 | Representative 100-μm-thick parasagittal, cresyl violet-stained sections of the left cerebellar hemisphere from an 8-month-old child (**A**; case no. 14 in **Table 1**) compared to the left cerebellar hemisphere of a 10-month-old child (**B**; case no. 17 in **Table 1**). Dividing the cerebellar cortex into subregions is based on fissures reaching the central white matter (continuous lines). The red lines indicate uncertain subdivisions. When counting these in-between lobules, the total number of lobules extends to at least 11 in the cerebellum of the 8-month-old child (numbers in **A**), whereas the cerebellum of the 10-month-old child displays 12 lobules (numbers in **B**). The red numbers in **(A,B)** indicate morphologically variable regions that are part of lobule VIIIA. The scale bar in **(B)** represents 1 cm in **(A**,**B)**.

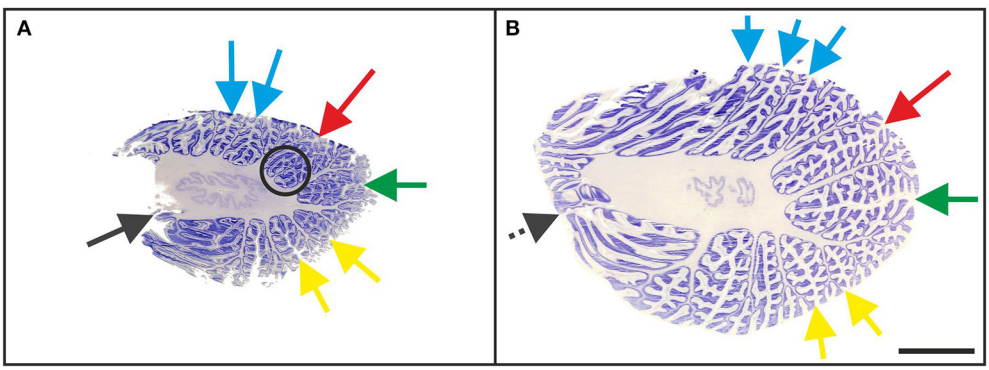

FIGURE 6 | Representative 100-μm-thick parasagittal, cresyl violet-stained sections of the left cerebellar hemisphere from a 3-month-old child (**A**; case no. 7 in **Table 1**) and an 11-month-old child (**B**; case no. 20 in **Table 1**). The arrows indicate prominent visible fissures (colors as in **Figure 1**) as follows: primary fissure (blue), superior posterior fissure (red), horizontal fissure (green), and ansoparamedian fissure (yellow). Parasagittal sections were most suitable for microscopic identification of the posterolateral fissure (dark gray arrow in **A**), while on more lateral sections the posterolateral fissure could not be unequivocally identified because of the fusion of the flocculus with the surrounding cerebellar tissue (dotted dark gray arrow in **B**). The circled area represents accessory folia at the bottom of the superior posterior fissure. The scale bar in **(B)** represents 1 cm in **(A,B)**.

Identification of Subregions of Interest in the Early Postnatal Human Cerebellum

The key result of the present study was that identification of the regions of interest shown in **Figure 1** based on the criteria established by Schmahmann et al. (1999) is only partially possible in the early postnatal (<1 year of age) human cerebellum. Division of the human cerebellum into five subregions of interest as outlined in **Figure 1** represents a combination of functional and morphologic aspects. Indeed, the superior posterior, horizontal, and posterolateral fissures could be reliably detected on the 20 human cerebella that were investigated in the present study. In contrast, reliable and reproducible identification of the primary and ansoparamedian fissures was not possible. In this regard, Schmahmann et al. (1999) noted that the primary fissure and other fissures within the anterior lobe are progressively more difficult to discern on parasagittal sections as one moves laterally away from the midline. Specifically, the primary fissure is unmistakable on midsagittal sections but it is continuous with an undistinguished small fissure in the intermediate sectors of the hemispheres.

Accordingly, it appears feasible to perform subregion-specific investigations on early postnatal human cerebella when the identification of subregions is restricted to crus I (bordered by the superior posterior and horizontal fissures) and the flocculus (bordered by the posterolateral fissure). These subregions could be unequivocally and reliably identified on all 20 human cerebella that were investigated in the present study.

Considering the functional relevance of crus I and the flocculus, only isolated investigations of the latter would be likely to provide biologically relevant results. This is due to the fact that control of eye movements is specifically represented in the flocculonodular lobe whereas crus I cannot be functionally separated from lobulus VI and crus II (Timmann, 2012). As a consequence, isolated investigations of the flocculus would be superior to investigations of crus I taken out of context. Separate investigations of the other regions of interest shown in **Figure 1** appear not possible because the associated fissures cannot be reliably identified.

The present study is the first to address whether the five regions of interest shown in **Figure 1** can be reliably delineated on early postnatal human cerebella. Validity and suitability of the criteria for identification of cerebellar fissures of the early postnatal human cerebellum as summarized in **Tables 2**, **3** requires further investigation. These criteria were derived from reports on delineation of subregions of the adult human cerebellum using a variety of methods. Specifically, Schmahmann et al. (1999) generated an atlas of the adult human cerebellum using high-resolution MRI images. Concerning the identification of fissures, these authors mentioned that the exact delineation of the ansoparamedian fissure in the adult human cerebellum had already led to controversies in the past. It should be mentioned that Schmahmann et al. (1999) indicated the precise position of the ansoparamedian fissure on their MRI scans. On the other hand, these authors did not provide reproducible criteria for identification that could be used in design-based stereologic studies of the early postnatal human cerebellum at the microscopic level. Moreover, one cannot exclude that the discrepancies between the results of the present study and the atlas of Schmahmann et al. (1999) are at least in part due to the fact that the latter was established on MRI scans obtained from a single subject. It seems important to repeat the work of Schmahmann et al. (1999) on a larger sample, also including early postnatal (<1 year of age) subjects.

Skefos et al. (2014) determined Purkinje cell densities in the cerebellum of eight cases with autism aged 5–56 years and eight controls aged 4–52 years with design-based stereology. The authors divided the cerebellum into four different subregions, using the primary, horizontal, ansoparamedian, and posterolateral fissures as landmarks. Skefos et al. (2014) found the mean overall Purkinje cell density to be lower in the cases with autism compared to controls, with this effect being most prominent in crus I and II. As outlined above, reliable and reproducible identification of subregions of the human cerebellum as proposed by Skefos et al. (2014) was not possible in the present study. In this regard, it is worth noting that Skefos et al. (2014) did not investigate early postnatal human cerebella, and illustrated their procedure for identifying subdivisions of the human cerebellum on a single histologic section without providing the age of the corresponding subject. Accordingly, it remains unclear whether the discrepancy between the results by Skefos et al. (2014) and the results of the present study may be related to the age of the investigated subjects. In any case, we found no correlation between the age of the subjects and the number of distinct cerebellar fissures (as well as the ability to identify them unequivocally, see **Table 4**). It should also be mentioned that Skefos et al. (2014) stated that in some cases as much as 10% of the tissue had been lost during processing. In addition, some sections demonstrated fraying at the edge of the folia. These complications prevented Skefos et al. (2014) from estimating total numbers of Purkinje cells, and in some cases not all regions of interest could be completely sampled and analyzed.

Relevance of Design-Based Stereologic Investigations of the Entire Early Postnatal Human Cerebellum

As outlined above it is not feasible to perform design-based stereologic studies on functionally relevant subregions in the early postnatal human cerebellum, except for the flocculus and crus I. However, this does not imply that design-based stereologic studies of the early postnatal human cerebellum, with the entire cerebellum as region of interest, are of inferior significance, as in fact demonstrated by a number of studies.

Kiessling et al. (2014) investigated 14 cerebellar halves (with different causes of death other than SIDS) aged between 1 day and 11 months after birth with design-based stereology. These authors determined total numbers of cerebellar Purkinje cells and granule cells, as well as volumes of the different cerebellar layers. The total number of Purkinje cells was stable across the investigated age span, and the mean total number of Purkinje cells (13.0×10^6; Kiessling et al., 2014) was similar to the mean total number of Purkinje cells in the adult human cerebellum reported in the literature: 15.3×10^6 Purkinje cells were reported by Andersen et al. (1992) as well as by Korbo and Andersen (1995), 14.3×10^6 by Andersen and Pakkenberg (2003) and Andersen et al. (2003), 14.9×10^6 by Andersen (2004), and 11.2×10^6 by Agashiwala et al. (2008). It should be noted that in all of these studies—except Kiessling et al. (2014)—estimated mean total bilateral numbers of cerebellar Purkinje cells were reported, which were divided by two in the present study to compare them to the estimated mean total unilateral number of cerebellar Purkinje cells reported by Kiessling et al. (2014). In contrast to the adult human cerebellum, total numbers of cerebellar granule cells yielded very different results. Specifically, compared to the adult human cerebellum, only ∼15% of the cerebellar granule cells were found at their final position in the inner granule cell layer by the time of birth (Kiessling et al., 2014), indicating that about 85% of the final numbers of these cells are yet to be generated postnatally. These data were supported by an age-related increase of the volume of the cerebellar molecular layer, inner granule cell layer, and white matter. Kiessling et al. (2014) concluded that the human cerebellum, based on its high plasticity, might be remarkably sensitive to external and internal influences during the first year of life. In addition, these authors proposed a very high plasticity of the early human postnatal cerebellum to be related to acquisition of novel skills. In this context, Knickmeyer et al. (2008) examined the cerebellum of healthy humans in the course of the first 2 years of life with MRI, and found a volumetric increase of 240%

of the cerebellum during the investigated period, suggesting that the early postnatal cerebellar growth may be directly linked to motor learning. Consistent with this hypothesis, Johnson (2001) emphasized the relevance of behavioral tests on children for a better understanding of functional brain development including the cerebellum. It should also be mentioned that Groszer et al. (2008) found abnormal cerebellar foliation and deficits in motor learning of mice carrying a mutation associated with speech impairments in humans.

Based on earlier reports in the literature that the cerebellum could be involved in the neuropathology of autism (for review see, Palmen et al., 2004), Whitney et al. (2009) investigated 10 cerebellar halves (six cases with autism and four controls aged between 17 and 54 years) with design-based stereology. Whitney et al. (2009) examined volumes of cerebellar layers and densities of cerebellar Purkinje cells, basket cells, and stellate cells. No statistically significant difference was found between the cases with autism and controls. The biological significance of these data arises from the fact that numerical matching between the cerebellar Purkinje cells and their associated interneurons provides an indication of the developmental time span for characteristic impairments related to autism. Synaptic contacts to the Purkinje cells are essential for survival of basket and stellate cells during cerebellar development, and basket and stellate cells undergo cell death if Purkinje cells are not present at the time when interneurons could establish synaptic contacts (Sotelo and Triller, 1979; Feddersen et al., 1992). Thus, in case of early Purkinje cell loss (or developmental disturbance of the formation of Purkinje cells) basket and stellate cells are also reduced in number (Whitney et al., 2009), resulting in severe defects in the development of the mouse cerebellum with impact on both foliation and size (Feddersen et al., 1992; Smeyne et al., 1995). In contrast, loss of Purkinje cells after formation of synaptic contacts with basket and stellate cells does not cause obvious malformations of the cerebellum (Feddersen et al., 1992) as Purkinje cell death does no longer affect the survival of basket and stellate cells at that time (Sotelo and Triller, 1979; Jeong et al., 2000; Duchala et al., 2004).

Practical Recommendations for Design-Based Stereologic Investigations of Total Numbers of Cells in the Early Postnatal Human Cerebellum

Use Human Cerebella to Investigate Normal and Pathological Human Cerebellar Development

There are important differences in the development of the cerebellum between humans and rodents. For example, the formation of the internal granule cell layer starts prenatally in humans (Rakic and Sidman, 1970; Sidman and Rakic, 1973) but only postnatally in mice (Shimada et al., 1977; Huard et al., 1999). With regard to microvessels, capillary branching is not obvious in the rat cerebellar external granule cell layer until postnatal day 18 (Yu et al., 1994). In contrast, in the comparable stage of development in humans (1 year postnatal) branching of microvessels was observed in all cerebellar layers between the first postnatal day and 11 months of age (Müller-Starck et al., 2014). As a result, pathologic alterations of cerebellar development in mice and rats may not accurately model alterations of cerebellar development in humans. This must be considered when using animal models for research into normal and pathologic development of the cerebellum.

Determine the Entire Cerebellar Cortex as ROI

It may be possible to identify reliably and delineate functionally relevant subregions in the adult human cerebellum. As outlined in the present study, this appears not to be possible in the case of the early postnatal human cerebellum, except for the flocculus and crus I. Accordingly, the entire cerebellar cortex should be determined as the ROI in order to guarantee reproducibility of results.

Apply Different Sampling Schemes for Counting Purkinje and Granule Cells

At the age of 1 year there are ∼2,700 times more granule cells than Purkinje cells in the human cerebellum (Kiessling et al., 2014). It is obvious that this will require two different sampling schemes, one for counting Purkinje cells and one for counting granule cells.

Use Dynamic Instead of Static Sampling Schemes for Counting Purkinje and Granule Cells

This represents the most important difference in design-based stereologic sampling between the early postnatal and the adult human cerebellum. In the normal human cerebellum, the total number of Purkinje cells is stable during the first year of life (Kiessling et al., 2014). However, the region of interest (entire cerebellar cortex) undergoes a substantial increase in volume during this time, from ∼5 cm^3 (combined molecular layer, Purkinje cell layer, and internal granule cell layer per cerebellar half) on the first postnatal day to ∼30 cm^3 at 11 months of age (Kiessling et al., 2014). In consequence, the global Purkinje cell density (total number of Purkinje cells divided by the volume of the entire cerebellar cortex) is approximately six times higher on the first postnatal day than at 1 year of age in the human cerebellum. A static sampling scheme [i.e., an Optical Fractionator sampling scheme (West et al., 1991, 1996; Schmitz and Hof, 2005) with constant section sampling fraction and constant area sampling fraction] would not be practical to determine total number of Purkinje cells under these conditions.

Furthermore, the total number of granule cells in the internal granule cell layer increases from ∼5×10^9 on the first postnatal day to ∼40×10^9 at 11 months of age per cerebellar half (Kiessling et al., 2014). During the same time the volume of the cerebellar internal granule cell layer per cerebellar half increases from ∼4 cm^3 on the first postnatal day to ∼15 cm^3 at 11 months of age (Kiessling et al., 2014). As a result, both the global granule cell density and the total number of granule cells in the internal granule cell layer of the human cerebellum show substantial alterations during the first year of life, and a static sampling scheme would not be practical to determine total number of granule cells in the internal granule cell layer under these conditions.

Table 5 summarizes examples of proven sampling schemes for determining total numbers of Purkinje cells and granule cells in the internal granule cell layer using the Optical Fractionator method for some of the cases listed in **Table 1** (taken from Kiessling et al., 2014). These exemplary sampling schemes were developed for 100-μm-thick frozen sagittal sections of the human cerebellum stained with cresyl violet (as investigated in the present study), and may serve as basis for developing reasonable dynamic sampling schemes in future design-based stereologic studies on the early postnatal human cerebellum.

Consider Counting Other Cell Types in the Early Postnatal Human Cerebellum

It could be of interest also to investigate other types of cells in the early postnatal human cerebellum with design-based stereologic methods, among them the unipolar brush cells. These cells are interneurons situated in the cerebellar internal granule cell layer and the dorsal cochlear nucleus and characterized by a small (10–20 μm) soma, a single short dendritic shaft and brush-like dendritic processes (reviewed in Víg et al., 2005). They give rise to glutamatergic axons terminating on dendrites of granule cells and Golgi cell in the cerebellar glomeruli (reviewed in Mugnaini et al., 2011). The unipolar brush cells are suggested to exert feedforward amplification of single mossy fiber afferent signals that would reach the overlying Purkinje cells via ascending granule cell axons and their parallel fibers (reviewed in Mugnaini et al., 2011). These cells are intermediate in size between granule cells and Golgi cells in the mammalian cerebellar cortex (Mugnaini and Floris, 1994) which allows to distinguish them from granule cells in Nissl-stained sections. In the mouse cerebellar cortex there are at least three distinct subsets of unipolar brush cells, expressing the calcium-binding protein calretinin, the metabotropic glutamate receptor (mGluR)1α and phospholipase C (PLC) β4, and PLCβ4 but not mGluR1α (Chung et al., 2009).

So far, the unipolar brush cells in the human cerebellum were only examined in a few studies (Víg et al., 2005; Wegiel et al., 2013). Notably, Víg et al. (2005) found that in human, calretinin-immunoreactive unipolar brush cells are present in the cerebellar vermis at birth and their number increases at least until the first postnatal year. This is in line with the finding of Kiessling et al. (2014) that ∼85% of the cerebellar granule cells are generated postnatally in human. Furthermore, Wegiel et al. (2013) reported a potential role of the unipolar brush cells in the neuropathology of autism.

However, neither the present study nor the previous studies by Kiessling et al. (2013, 2014) addressed the unipolar brush cells. Accordingly, the data provided in **Table 5** cannot be used to develop sampling schemes for determining total number of unipolar brush cells in the early postnatal human cerebellum using the Optical Fractionator. Furthermore, neither Víg et al. (2005) nor Wegiel et al. (2013) investigated total number or density of the unipolar brush cells with stereologic methods. Accordingly, investigating these cells in the early postnatal human cerebellum would require first a pilot study to assess their regional density (note that the data provided by Víg et al., 2005 and Wegiel et al., 2013 are not sufficient in this regard), followed by a stereologic pilot study to determine their age-dependent total number. With that information, detailed stereologic studies of the unipolar brush cells and their potential role in the neuropathology of neurodevelopmental, neuropsychiatric, and neurodegenerative disorders could then be performed.

CONCLUSION

Design-based stereologic studies of the early postnatal (<1 year of age) human cerebellum are required to understand better its normal and pathologic development and its role in various neurodevelopmental disorders. However, unlike for the adult

TABLE 5 | Examples of proven sampling schemes (taken from Kiessling et al., 2014) for determining total numbers of Purkinje cells and granule cells in the early postnatal (<1 year of age) human cerebellum using the Optical Fractionator method (West et al., 1991, 1996; Schmitz and Hof, 2005).

CN	A [m]	∑ s	ssf^{-1}	sl-g [μm]	sl-ucf [μm]	asf^{-1} [10^3]	h [μm]	t [μm]	tsf^{-1}	∑ uvcs	∑ n	CE
DETERMINATION OF TOTAL NUMBERS OF PURKINJE CELLS												
1	0.03	8	36	1,300	130	0.100	25	35.4	1.42	1,435	2,377	0.021
10	4	8	48	2,800	150	0.348	45	56.0	1.24	853	720	0.037
12	7	9	48	2,900	150	0.374	45	58.7	1.30	943	744	0.037
20	11	8	48	3,100	150	0.427	45	49.7	1.14	925	573	0.042
DETERMINATION OF TOTAL NUMBERS OF GRANULE CELLS IN THE INTERNAL GRANULE CELL LAYER												
1	0.33	8	36	1,300	10	16.9	5	35.4	7.1	1,393	793	0.036
10	4	8	48	2,800	8	122.5	5	56.0	11.2	829	467	0.046
12	7	9	48	2,900	10	84.1	5	58.7	11.7	933	592	0.041
20	11	8	48	3,100	8	150.2	5	49.7	9.9	914	489	0.045

*CN, case number in **Table 1**; ∑ s, number of analyzed 100-μm thick frozen sagittal sections stained with cresyl violet; ssf^{-1}, reciprocal value of the section sampling fraction; sl-g, side length in XY directions of the grid used to determine the systematic, uniformly random (SRS) positions of unbiased virtual counting spaces; sl-ucf, side length in XY directions of unbiased counting frames that serve as basis for the unbiased virtual counting spaces; asf^{-1}, reciprocal value of the area sampling fraction; h, height of unbiased virtual counting spaces; t, measured actual average section thickness after histological processing; tsf^{-1}, reciprocal value of the thickness sampling fraction; ∑ uvcs, number of unbiased virtual counting spaces used; ∑n, number of counted Purkinje cells or granule cells; CE, predicted coefficient of error of estimated total neuron numbers using the prediction method described by Schmitz (1998) and Schmitz and Hof (2005). Note that the sampling parameters ∑ s (and thus, ssf^{-1}), sl-g, sl-ucf (and thus, asf^{-1}), and h (and thus, tsf^{-1}) were individually adjusted because of substantial interindividual differences in the size of the cerebella and the total number of granule cells in the internal granule cell layer (details are provided in the main text).*

human cerebellum, it is not feasible to identify reliably and delineate functionally relevant subregions in the early postnatal cerebellum, except for the flocculus and crus I. Accordingly, it is recommended to define the entire cerebellar cortex as the ROI in design-based stereologic studies and use of dynamic rather than static sampling schemes to guarantee reproducibility and reliability of results. Beyond this, it seems important to repeat the work by Schmahmann et al. (1999) who developed a MRI atlas of the human cerebellum in proportional stereotaxic space on a larger sample than a single specimen, including early postnatal subjects.

AUTHOR CONTRIBUTIONS

AF, AB, PH, CS, and MK: Made substantial contributions to the conception and design of the work, and to the acquisition, analysis, and interpretation of data for the work; AF, AB, PH, CS, and MK: Drafted the work, approved the final version to be published, and agreed to be accountable for all aspects of the work in ensuring that questions related to the accuracy or integrity of any part of the work are appropriately investigated and resolved.

FUNDING

This work was supported in part by the Simons Foundation Grant FA #345922 (PH).

ACKNOWLEDGMENTS

The authors thank B. Aschauer, A. Baltruschat, and S. Tost for expert technical assistance. This work contains data from AF's German MD thesis.

REFERENCES

Agashiwala, R. M., Louis, E. D., Hof, P. R., and Perl, D. P. (2008). A novel approach to non-biased systematic random sampling: a stereologic estimate of Purkinje cells in the human cerebellum. *Brain Res.* 1236, 73–78. doi: 10.1016/j.brainres.2008.07.119

Andersen, B. B. (2004). Reduction of Purkinje cell volume in cerebellum of alcoholics. *Brain Res.* 1007, 10–18. doi: 10.1016/j.brainres.2004.01.058

Andersen, B. B., Gundersen, H. J. G., and Pakkenberg, B. (2003). Aging of the human cerebellum: a stereological study. *J. Comp. Neurol.* 466, 356–365. doi: 10.1002/cne.10884

Andersen, B. B., Korbo, L., and Pakkenberg, B. (1992). A quantitative study of the human cerebellum with unbiased stereological techniques. *J. Comp. Neurol.* 326, 549–560. doi: 10.1002/cne.903260405

Andersen, B. B., and Pakkenberg, B. (2003). Stereological quantitation in cerebella from people with schizophrenia. *Br. J. Psychiatry* 182, 354–361. doi: 10.1192/bjp.182.4.354

Andreasen, N. C., and Pierson, R. (2008). The role of the cerebellum in schizophrenia. *Biol. Psychiatry* 64, 81–88. doi: 10.1016/j.biopsych.2008.01.003

Baldaçara, L., Nery-Fernandes, F., Rocha, M., Quarantini, L. C., Rocha, G. G., Guimarães, J. L., et al. (2011). Is cerebellar volume related to bipolar disorder? *J. Affect. Disord.* 135, 305–309. doi: 10.1016/j.jad.2011.06.059

Berquin, P. C., Giedd, J. N., Jacobsen, L. K., Hamburger, S. D., Krain, A. L., Rapoport, J. L., et al. (1998). Cerebellum in attention-deficit hyperactivity disorder: a morphometric MRI study. *Neurology* 50, 1087–1093. doi: 10.1212/WNL.50.4.1087

Buckner, R. L. (2013). The cerebellum and cognitive function: 25 years of insight from anatomy and neuroimaging. *Neuron* 80, 807–815. doi: 10.1016/j.neuron.2013.10.044

Calhoun, M. E., and Mouton, P. R. (2000). Length measurement: new developments in neurostereology and 3D imagery. *J. Chem. Neuroanat.* 20, 61–69. doi: 10.1016/S0891-0618(00)00074-0

Castellanos, F. X., Giedd, J. N., Berquin, P. C., Walter, J. M., Sharp, W., Tran, T., et al. (2001). Quantitative brain magnetic resonance imaging in girls with attention-deficit/hyperactivity disorder. *Arch. Gen. Psychiatry* 58, 289–295. doi: 10.1001/archpsyc.58.3.289

Christakou, A., Murphy, C. M., Chantiluke, K., Cubillo, A. I., Smith, A. B., Giampietro, V., et al. (2013). Disorder-specific functional abnormalities during sustained attention in youth with attention deficit hyperactivity disorder (ADHD) and with autism. *Mol. Psychiatry* 18, 236–244. doi: 10.1038/mp.2011.185

Chung, S. H., Sillitoe, R. V., Croci, L., Badaloni, A., Consalez, G., and Hawkes, R. (2009). Purkinje cell phenotype restricts the distribution of unipolar brush cells. *Neuroscience* 164, 1496–1508. doi: 10.1016/j.neuroscience.2009.09.080

Cruz-Sánchez, F. F., Lucena, J., Ascaso, C., Tolosa, E., Quintò, L., and Rossi, M. L. (1997). Cerebellar cortex delayed maturation in sudden infant death syndrome. *J. Neuropath. Exp. Neur.* 56, 340–346. doi: 10.1097/00005072-199704000-00002

Donkelaar, H. J., ten Lammens, M., Wesseling, P., Thijssen, H. O., and Renier, W. O. (2003). Development and developmental disorders of the human cerebellum. *J. Neurol.* 250, 1025–1036. doi: 10.1007/s00415-003-0199-9

Duchala, C. S., Shick, H. E., Garcia, J., Deweese, D. M., Sun, S., Stewart, V. J., et al. (2004). The toppler mouse: a novel mutant exhibiting loss of Purkinje cells. *J. Comp. Neurol.* 476, 113–129. doi: 10.1002/cne.20206

Durston, S., van Belle, J., and de Zeeuw, P. (2011). Differentiating frontostriatal and fronto-cerebellar circuits in attention-deficit/hyperactivity disorder. *Biol. Psychiatry* 69, 1178–1184. doi: 10.1016/j.biopsych.2010.07.037

Fatemi, S. H., Aldinger, K. A., Ashwood, P., Bauman, M. L., Blaha, C. D., Blatt, G. J., et al. (2012). Consensus paper: pathological role of the cerebellum in autism. *Cerebellum* 11, 777–807. doi: 10.1007/s12311-012-0355-9

Feddersen, R. M., Ehlenfeldt, R., Yunis, W. S., Clark, H. B., and Orr, H. T. (1992). Disrupted cerebellar cortical development and progressive degeneration of Purkinje cells in SV40 T antigen transgenic mice. *Neuron* 9, 955–966. doi: 10.1016/0896-6273(92)90247-B

Gadsdon, D. R., and Emery, J. L. (1976). Quantitative morphological studies of developing human cerebellar cortex in various disease states. *Arch. Dis. Child.* 51, 964–967. doi: 10.1136/adc.51.12.964

Gasbarri, A., Pompili, A., Pacitti, C., and Cicirata, F. (2003). Comparative effects of lesions to the ponto-cerebellar and olivo-cerebellar pathways on motor and spatial learning in the rat. *Neuroscience* 116, 1131–1140. doi: 10.1016/S0306-4522(02)00780-7

Gocmen-Mas, N., Pelin, C., Canan, S., Yazici, A. C., Zagyapan, R., Senan, S., et al. (2009). Stereological evaluation of volumetric asymmetry in healthy human cerebellum. *Surg. Radiol. Anat.* 31, 177–181. doi: 10.1007/s00276-008-0424-4

Groszer, M., Keays, D. A., Deacon, R. M. J., de Bono, J. P., Prasad-Mulcare, S., Gaub, S., et al. (2008). Impaired synaptic plasticity and motor learning in mice with a point mutation implicated in human speech deficits. *Curr. Biol.* 18, 354–362. doi: 10.1016/j.cub.2008.01.060

Guilleminault, C., Peraita, R., Souquet, M., and Dement, W. C. (1975). Apneas during sleep in infants: possible relationship with sudden infant death syndrome. *Science* 190, 677–679. doi: 10.1126/science.1188364

Harper, R. M., Woo, M. A., and Alger, J. R. (2000). Visualization of sleep influences on cerebellar and brainstem cardiac and respiratory control mechanisms. *Brain Res. Bull.* 53, 125–131. doi: 10.1016/S0361-9230(00)00317-8

Hashimoto, T., Tayama, M., Murakawa, K., Yoshimoto, T., Miyazaki, M., Harada, M., et al. (1995). Development of the brainstem and cerebellum in autistic patients. *J. Autism Dev. Disord.* 25, 1–18. doi: 10.1007/BF02178163

Huard, J. M., Forster, C. C., Carter, M. L., Sicinski, P., and Ross, M. E. (1999). Cerebellar histogenesis is disturbed in mice lacking cyclin D2. *Development* 126, 1927–1935.

Hunt, N. J., Waters, K. A., and Machaalani, R. (2017). Promotion of the unfolding protein response in orexin/dynorphin neurons in sudden infant death syndrome (SIDS): elevated pPERK and ATF4 expression. *Mol. Neurobiol.* 54, 7171–7185. doi: 10.1007/s12035-016-0234-3

Jeong, Y. G., Hyun, B. H., and Hawker, R. (2000). Abnormalities in cerebellar Purkinje cells in the novel ataxic mutant mouse, pogo. *Brain Res. Dev. Brain Res.* 125, 61–67. doi: 10.1016/S0165-3806(00)00114-0

Johnson, M. H. (2001). Functional brain development in humans. *Nat. Rev. Neurosci.* 2, 475–483. doi: 10.1038/35081509

Joyal, C. C., Pennanen, C., Tiihonen, E., Laakso, M. P., Tiihonen, J., and Aronen, H. J. (2004). MRI volumetry of the vermis and the cerebellar hemispheres in men with schizophrenia. *Psychiatry Res.* 131, 115–124. doi: 10.1016/j.pscychresns.2003.09.003

Kiessling, M. C., Büttner, A., Butti, C., Müller-Starck, J., Milz, S., Hof, P. R., et al. (2013). Intact numbers of cerebellar Purkinje and granule cells in sudden infant death syndrome: a stereologic analysis and critical review of neuropathologic evidence. *J. Neuropathol. Exp. Neurol.* 72, 861–870. doi: 10.1097/NEN.0b013e3182a31c31

Kiessling, M. C., Büttner, A., Butti, C., Müller-Stark, J., Milz, S., Hof, P. R., et al. (2014). Cerebellar granule cells are generated postnatally in humans. *Brain Struct. Funct.* 219, 1271–1286. doi: 10.1007/s00429-013-0565-z

Knickmeyer, R. C., Gouttard, S., Kang, C., Evans, D., Wilber, K., Smith, J. K., et al. (2008). A structural MRI study of human brain development from birth to 2 years. *J. Neurosci.* 28, 12176–11218. doi: 10.1523/JNEUROSCI.3479-08.2008

Korbo, L., and Andersen, B. B. (1995). The distributions of Purkinje cell perikaryon and nuclear volume in human and rat cerebellum with the nucleator method. *Neuroscience* 69, 151–158. doi: 10.1016/0306-4522(95)00223-6

Larsell, O. (1947). The development of the cerebellum in man in relation to its comparative anatomy. *J. Comp. Neurol.* 87, 85–129. doi: 10.1002/cne.900870203

Lavezzi, A. M., Ottaviani, G., and Matturri, L. (2007). Ontogenesis of human cerebellar cortex and biopathological characterization in sudden unexplained fetal and infant death. *Virchows Arch.* 450, 31–40. doi: 10.1007/s00428-006-0311-5

Lavezzi, A. M., Ottaviani, G., Terni, L., and Matturri, L. (2006). Histological and biological developmental characterization of the human cerebellar cortex. *Int. J. Dev. Neurosci.* 24, 365–371. doi: 10.1016/j.ijdevneu.2006.06.002

Malacarne, M. V. G. (1776). *Nuova Esposizione Della Vera Struttura del Cerveletto Umano*. Torino: Briolo.

Martin, P., and Albers, M. (1995). Cerebellum and schizophrenia: a selective review. *Schizophr. Bull.* 21, 241–250. doi: 10.1093/schbul/21.2.241

Mostofsky, S. H., Reiss, A. L., Lockhart, P., and Denckla, M. B. (1998). Evaluation of cerebellar size in attention-deficit hyperactivity disorder. *J. Child Neurol.* 13, 434–439. doi: 10.1177/088307389801300904

Mouton, P. R., Gokhale, A. M., Ward, N. L., and West, M. J. (2002). Stereological length estimation using spherical probes. *J. Microsc.* 206, 54–64. doi: 10.1046/j.1365-2818.2002.01006.x

Mugnaini, E., and Floris, A. (1994). The unipolar brush cell: a neglected neuron of the mammalian cerebellar cortex. *J. Comp. Neurol.* 339, 174–180. doi: 10.1002/cne.903390203

Mugnaini, E., Sekerková, G., and Martina, M. (2011). The unipolar brush cell: a remarkable neuron finally receiving deserved attention. *Brain Res. Rev.* 66, 220–245. doi: 10.1016/j.brainresrev.2010.10.001

Müller-Starck, J., Büttner, A., Kiessling, M. C., Angstman, N. B., Császár, N., Haeussner, E., et al. (2014). No changes in cerebellar microvessel length density in sudden infant death syndrome: implications for pathogenetic mechanisms. *J. Neuropath. Exp. Neur.* 73, 312–323. doi: 10.1097/NEN.0000000000000055

Nieuwenhuys, R., Voogd, J., and Lange, W. (1980). *Das Zentralnervensystem des Menschen*. Berlin: Springer-Verlag.

Oehmichen, M., Wullen, B., Zilles, K., and Saternus, K. S. (1989). Cytological investigations on the cerebellar cortex of sudden infant death victims. *Acta Neuropathol.* 78, 404–409. doi: 10.1007/BF00688177

Palmen, S. J., van Engeland, H., Hof, P. R., and Schmitz, C. (2004). Neuropathological findings in autism. *Brain* 127, 2572–2583. doi: 10.1093/brain/awh287

Paxinos, G. (1990). *The Human Nervous System*. San Diego, CA: Academic Press.

Petacchi, A., Kaernbach, C., Ratnam, R., Robin, D. A., and Bower, J. M. (2010). Enhanced activation of cerebellar regions during pitch discrimination in humans: a PET study. *BMC Neurosci.* 11:P84. doi: 10.1186/1471-2202-11-S1-P84

Rakic, P., and Sidman, R. L. (1970). Histogenesis of cortical layers in human cerebellum, particularly the lamina dissecans. *J. Comp. Neurol.* 139, 473–500. doi: 10.1002/cne.901390407

Riedel, A., Klekamp, J., Harper, C., and Kretschmann, H. J. (1989). Morphometric study on the postnatal growth of the cerebellum of Australian aborigines and Caucasians. *Brain Res.* 499, 333–343. doi: 10.1016/0006-8993(89)90782-8

Roostaei, T., Nazeri, A., Sahraian, M. A., and Minagar, A. (2014). The human cerebellum: a review of physiologic neuroanatomy. *Neurol. Clin.* 32, 859–869. doi: 10.1016/j.ncl.2014.07.013

Schmahmann, J. D., Doyon, J., McDonald, D., Holmes, C., Lavoie, K., Hurwitz, A. S., et al. (1999). Three-dimensional MRI atlas of the human cerebellum in proportional stereotaxic space. *Neuroimage* 10, 233–260. doi: 10.1006/nimg.1999.0459

Schmitz, C. (1998). Variation of fractionator estimates and its prediction. *Anat. Embryol.* 198, 371–397. doi: 10.1007/s004290050191

Schmitz, C., and Hof, P. R. (2005). Design-based stereology in neuroscience. *Neuroscience* 130, 813–831. doi: 10.1016/j.neuroscience.2004.08.050

Schraa-Tam, C. K., Rietdijk, W. J., Verbeke, W. J., Dietvorst, R. C., van den Berg, W. E., Bagozzi, R. P., et al. (2012). fMRI activities in the emotional cerebellum: a preference for negative stimuli and goal-directed behavior. *Cerebellum* 11, 233–245. doi: 10.1007/s12311-011-0301-2

Shimada, M., Yamano, T., Nakamura, T., Morikawa, Y., and Kusunoki, T. (1977). Effect of maternal malnutrition on matrix cell proliferation in the cerebrum of mouse embryo: an autoradiographic study. *Pediatr. Res.* 11, 728–732. doi: 10.1203/00006450-197706000-00006

Sidman, R. L., and Rakic, P. (1973). Neuronal migration, with special reference to developing human brain: a review. *Brain Res.* 62, 1–35. doi: 10.1016/0006-8993(73)90617-3

Skefos, J., Cummings, C., Enzer, K., Holiday, J., Weed, K., Levy, E., et al. (2014). Regional alterations in Purkinje cell density in patients with autism. *PLoS ONE* 9:e81255. doi: 10.1371/journal.pone.0081255

Smeyne, R. J., Chu, T., Lewin, A., Bian, F., Crisman, S. S., Kunsch, C., et al. (1995). Local control of granule cell generation by cerebellar Purkinje cells. *Mol. Cell. Neurosci.* 6, 230–251. doi: 10.1006/mcne.1995.1019

Sotelo, C., and Triller, A. (1979). Fate of presynaptic afferents to Purkinje cells in the adult nervous mutant mouse: a model to study presynaptic stabilization. *Brain Res.* 175, 11–36. doi: 10.1016/0006-8993(79)90511-0

Sparks, D. L., and Hunsaker, J. C. (2002). Neuropathology of sudden infant death (syndrome): literature review and evidence of a probable apoptotic degenerative cause. Childs. *Nerv. Syst.* 18, 568–592. doi: 10.1007/s00381-002-0629-5

Steinlin, M. (2008). Cerebellar disorders in childhood: cognitive problems. *Cerebellum* 7, 607–610. doi: 10.1007/s12311-008-0083-3

Steinschneider, A. (1972). Prolonged apnea and the sudden infant death syndrome: clinical and laboratory observations. *Pediatrics* 50, 646–654.

Stoodley, C. J. (2016). The cerebellum and neurodevelopmental disorders. *Cerebellum* 15, 34–37. doi: 10.1007/s12311-015-0715-3

Stoodley, C. J., and Limperopoulos, C. (2016). Structure-function relationships in the developing cerebellum: evidence from early-life cerebellar injury and neurodevelopmental disorders. *Semin. Fetal Neonatal Med.* 21, 356–364. doi: 10.1016/j.siny.2016.04.010

Stoodley, C. J., and Schmahmann, J. D. (2009). Functional topography in the human cerebellum: a meta-analysis of neuroimaging studies. *Neuroimage* 44, 489–501. doi: 10.1016/j.neuroimage.2008.08.039

Strakowski, S. M., Delbello, M. P., and Adler, C. M. (2005). The functional neuroanatomy of bipolar disorder: a review of neuroimaging findings. *Mol. Psychiatry* 10, 105–116. doi: 10.1038/sj.mp.4001585

Timmann, D. (2012). "Kleinhirn und exekutive funktionen, sprache sowie visuell-räumliche funktionen," in *Kognitive Neurowissenschaften*, eds H. O. Karnath and P. Thier (Berlin; Heidelberg: Springer Verlag), 609–617.

Tsekhmistrenko, T. A. (1996). Structural transformations in the human cerebellar cortex from birth to the age of three years. *Neurosci. Behav. Physiol.* 26, 579–583. doi: 10.1007/BF02359503

Víg, J., Takács, J., Abrahám, H., Kovács, G. G., and Hámori, J. (2005). Calretinin-immunoreactive unipolar brush cells in the developing human cerebellum. *Int. J. Dev. Neurosci.* 23, 723–729. doi: 10.1016/j.ijdevneu.2005.10.002

Wegiel, J., Kuchna, I., Nowicki, K., Imaki, H., Wegiel, J., Ma, S. Y., et al. (2013). Contribution of olivofloccular circuitry developmental defects to atypical gaze in autism. *Brain Res.* 1512, 106–122. doi: 10.1016/j.brainres.2013.03.037

West, M. J., Østergaard, K., Andreassen, O. A., and Finsen, B. (1996). Estimation of the number of somatostatin neurons in the striatum: an in situ hybridization study using the optical fractionator method. *J. Comp. Neurol.* 370, 11–22. doi: 10.1002/(SICI)1096-9861(19960617)370:1<11::AID-CNE2>3.0.CO;2-O

West, M. J., Slomianka, L., and Gundersen, H. J. (1991). Unbiased stereological estimation of the total number of neurons in the subdivisions of the rat hippocampus using the optical fractionator. *Anat. Rec.* 231, 482–497. doi: 10.1002/ar.1092310411

Whitney, E. R., Kemper, T. L., Rosene, D. L., Bauman, M. L., and Blatt, G. J. (2009). Density of cerebellar basket and stellate cells in autism: evidence for a late developmental loss of Purkinje cells. *J. Neurosci. Res.* 87, 2245–2254. doi: 10.1002/jnr.22056

Witter, L., and De Zeeuw, C. I. (2015). Regional functionality of the cerebellum. *Curr. Opin. Neurobiol.* 33, 150–155. doi: 10.1016/j.conb.2015.03.017

Yu, B. P., Yu, C. C., and Robertson, R. T. (1994). Patterns of capillaries in developing cerebral and cerebellar cortices of rats. *Acta Anat.* 149, 128–133. doi: 10.1159/000147567

Conflict of Interest Statement: The authors declare that the research was conducted in the absence of any commercial or financial relationships that could be construed as a potential conflict of interest.

frontiers in Neuroanatomy

ORIGINAL RESEARCH
published: 08 December 2017
doi: 10.3389/fnana.2017.00109

Application of the Physical Disector Principle for Quantification of Dopaminergic Neuronal Loss in a Rat 6-Hydroxydopamine Nigral Lesion Model of Parkinson's Disease

Katrine Fabricius, Pernille Barkholt, Jacob Jelsing and Henrik H. Hansen*

Gubra, Hoersholm, Denmark

Stereological analysis is the optimal tool for quantitative assessment of brain morphological and cellular changes induced by neurotoxic lesions or treatment interventions. Stereological methods based on random sampling techniques yield unbiased estimates of particle counts within a defined volume, thereby providing a true quantitative estimate of the target cell population. Neurodegenerative diseases involve loss of specific neuron types, such as the midbrain tyrosine hydroxylase-positive dopamine neurons in Parkinson's disease and in animal models of nigrostriatal degeneration. Therefore, we applied an established automated physical disector principle in a fractionator design for efficient stereological quantitative analysis of tyrosine hydroxylase (TH)-positive dopamine neurons in the substantia nigra pars compacta of hemiparkinsonian rats with unilateral 6-hydroxydopamine (6-OHDA) lesions. We obtained reliable estimates of dopamine neuron numbers, and established the relationship between behavioral asymmetry and dopamine neuron loss on the lesioned side. In conclusion, the automated physical disector principle provided a useful and efficient tool for unbiased estimation of TH-positive neurons in rat midbrain, and should prove valuable for investigating neuroprotective strategies in 6-OHDA model of parkinsonism, while generalizing to other immunohistochemically-defined cell populations.

Keywords: physical disector, autodisector, stereology, 6-OHDA rat model, substantia nigra, Parkinson Disease

OPEN ACCESS

Edited by:
Sanne Simone Kaalund, Research Laboratory for Stereology and Neuroscience, Denmark

Reviewed by:
Miguel Angel García-Cabezas, Boston University, United States
Hans J. Gundersen, Retired, Maribo, Denmark

****Correspondence:***
Katrine Fabricius
kf@gubra.dk

Received: *01 August 2017*
Accepted: *06 November 2017*
Published: *08 December 2017*

Citation:
Fabricius K, Barkholt P, Jelsing J and Hansen HH (2017) Application of the Physical Disector Principle for Quantification of Dopaminergic Neuronal Loss in a Rat 6-Hydroxydopamine Nigral Lesion Model of Parkinson's Disease. Front. Neuroanat. 11:109. doi: 10.3389/fnana.2017.00109

INTRODUCTION

Application of basic principles of stereology can be applied to the task of estimating the total number of particles in a three-dimensional object; these particles can be neurons, glial cells, or organelles. The stereological technique now known as the physical disector (meaning "two-sections") was first described in 1984 (Sterio, 1984), and has since become an established tool in quantitative neurobiology (e.g., Kristiansen and Nyengaard, 2012).We emphasize that stereological techniques are based on unbiased principles, which means that estimations, when obtained according to geometrically-defined rules, are "without systematic deviation from the true value." For quantification of the number and volume of three-dimensional objects, e.g., neuron numbers and sizes, stereology offers a variety of probes that are geometric structures with mathematical properties designed for application in the tissue under investigation. More specifically, the *disector*

probe is a three-dimensional physical or optical probe used to estimate the total number of particles. The physical disector procedure uses pairs of neighboring sections lying some distance (h) apart, which must be close enough to infer what lies between the two sections and thus insure that all particles are counted (Sterio, 1984; Gundersen et al., 1988).

The two sections for the physical disector are designated the reference section and the lookup section. If a particle appears in the reference section, but not in the lookup section, the particle is counted, such that each particle has an equal probability of being counted, irrespective of its size, shape, or orientation in the tissue (Gundersen et al., 1988; **Figure 1**). In applications of the optical disector, counting of particles requires moving the focal plane of the microscope in the z-axis at intervals within relatively thick tissue sections (e.g., 40 μm). Thus, a stack of thin focal planes is analyzed proceeding through the depth of the section. All unique identifiers (e.g., the nucleolus or nucleus of a neuron) within the disector height (h) are counted, after exclusion of guard zones above and below the disector, so as to avoid ambiguous identification or loss of cells at the end plane (West, 1999; Boyce et al., 2010; Tschanz et al., 2011). Here, the counting-frame consists of a square with one finite line (the inclusion line, green) and one infinite line (the exclusion lines, red lines) (**Figure 1**). The rule is that all particles inside or touching the unbiased counting frame are counted provided they do not touch the exclusion line. The frames are placed at equidistant X,Y-step within the region of interest on each section, and the volume is calculated knowing the frame area, h, and the magnification (Gundersen, 1977; Gundersen et al., 1988). Systematic uniform random sampling (SURS) gives a true representation of the whole population, providing that the first sampling step is chosen at random within the sampling frequency.

Recent years have seen increasing use of the stereological methods, notably for applications in the study of neurodegenerative diseases (Pakkenberg et al., 1991, 2003; Pakkenberg, 1993; Pakkenberg and Gundersen, 1997; Cabello et al., 2002; Stroeven and Hu, 2007; Eriksen et al., 2009; Boyce et al., 2010). Use of the physical disector can be rather time-consuming compared to the optical disector, due to the requirement that the experimenter must align the sections manually on a computer screen. This obstacle is circumvented by automated systems, which obtain an operator-independent alignment of microscopic images from the reference and lookup sections e.g., the Visiopharm newCast Autodisector system (Visiopharm, Denmark). Estimates can then be obtained off-line, with a considerable economy of effort due to the robust automatic alignment of images rather than manual alignment of tissue sections. The optical disector is often used for neuron counts, but the physical disector method is more suited for the thinner sections typically used in immunohistochemical staining protocols.

Parkinson's disease (PD) is a chronic and progressive neurodegenerative disorder with cardinal motor symptoms of tremor, rigidity and bradykinesia, which are largely attributed to the loss of dopamine (DA-ergic) neurons located in the *substantia nigra pars compacta* (SNc) of the mesencephalon (reviewed in Thomas and Flint Beal, 2007; Kalia and Lang, 2015). Animal models of PD have proved to be helpful in gaining an understanding of the underlying pathophysiology, and have also been instrumental in the discovery of novel treatments (e.g., Deumens et al., 2002; Eslamboli et al., 2003; Schober, 2004; Yuan et al., 2005; Blesa et al., 2012; Peoples et al., 2012; Torres and Dunnett, 2012). The classic PD model is obtained by infusion of the neurotoxin 6-hydroxydopamine (6-OHDA) to the medial forebrain bundle (MFB) or directly to SNc, which can induces a near ablation of the DA-ergic neurons (Jeon et al., 1995; Walsh et al., 2011). However, it is difficult in practice to obtain reproducible partial lesions of the nigrostriatal pathway with 6-OHDA infusions. The degeneration of nigrostriatal fibers leads to depletion of striatal dopamine content, but the associated effects on numbers of midbrain DA-ergic neurons are quantified in relatively few studies, generally without using stereological methods (e.g., Monville et al., 2006; Bertilsson et al., 2008; Torres and Dunnett, 2012; Hansen et al., 2016), although there are some stereological analyses in the 6-OHDA model (e.g., Petroske et al., 2001; Ma et al., 2009; Blesa et al., 2012; Peoples et al., 2012). We suppose that innovative stereological tools such as the autodisector and the use of digital slides can significantly simplify the procedure for quantitation of immunohistochemically-identified dopamine neurons (Keller et al., 2013). In this paper, we tested the applicability and efficiency of the physical disector design for the stereological evaluation of the number of midbrain TH-positive DA-ergic neurons in a conventional 6-OHDA model. Since results of this study have been presented elsewhere (Hansen et al., 2016), our present aim is to give a detailed technical account of the issues arising in the application of the autodisector and digital slides in a rat 6-OHDA model of PD. Others have previously reported on the effects of intoxication of Göttingen minipigs with methylenedioxymethamphetamine (MDMA) on the abundance of serotonin neurons of the dorsal raphe nucleus (Cumming et al., 2007). To our knowledge, the present 6-OHDA study is the first stereological study in a neurodegeneration model that combines the use of digital images of immunohistologically-stained brain sections using the automated aligning of images for the physical disector set-up.

Abbreviations: 6-OHDA, 6-hydroxydopamine; asf, area sampling fraction; DA, dopaminergic; hsf, height sampling fraction; i.p., intraperitoneal; MFB, medial forebrain bundle; PD, Parkinson's disease; ROI, region of interest; s.c., subcutaneous; SEM, standard error of the mean; SNc, substantia nigra pars compacta; SPD, Sprague-Dawley; ssf, section sampling fraction; SURS, systematic uniform random sampling; TBS, Tris-buffered saline; TH, tyrosine hydroxylase.

METHODS AND MATERIALS

6-OHDA Lesion

All animal experiments were conducted in accordance with Gubra bioethical guidelines (internal ethics committee), which are fully compliant to internationally accepted principles for the care and use of laboratory animals. The described experiments were covered by personal licenses for Jacob Jelsing (2013-15-2934-00784) issued by the Danish Ethical Committee for animal

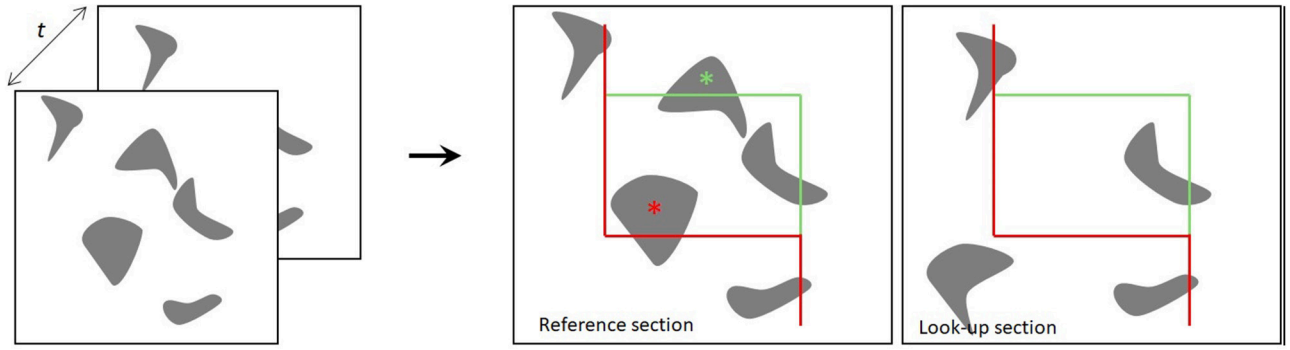

FIGURE 1 | The principle of the physical disector. The distance t indicates the separation between the two sections. Two neighboring sections are superimposed, and the particles present within a counting frame in one section (reference section) but not the other (lookup section) are counted. The red lines of the counting frame are exclusion lines, and particles touching these boundaries are not counted. The green lines are inclusion lines (Gundersen, 1977; Gundersen et al., 1988).

research. A total of 40 male Sprague-Dawley rats (300–340 g, 7–8 weeks. Taconic DK) were used, in groups of 8–12 per treatment group. Four animals died during the study giving a total of 36 animals used for stereology. Rats were anesthetized with a mixture of 1.25 mg/ml midazolam, 2.5 mg/ml fluanisone and 0.079 mg/ml fentanyl (hypnorm/dormicum) at a dose of 2.7 ml/kg (s.c.). Animals were kept on a heating pad maintained on 36–37°C throughout surgery. A minimum of 20 min prior to 6-OHDA injection, animals were pre-treated with pargyline (a monoamine oxidase inhibitor; 5 mg/kg, i.p.) and desipramine (a noradrenaline uptake inhibitor; 25 mg/kg, i.p.) to prevent collateral damage to noradrenergic neurons. Animals were placed in a stereotaxic apparatus and (following sinus calibration for the lateral coordinates) received infusions of 6-OHDA (Cat# H116, Sigma- Aldrich, DK) in 0.01% ascorbic acid vehicle into the right medial forebrain bundle (MFB) using a Hamilton syringe with the tip placed at the following coordinates according to the atlas of Paxinos and Watson (1997); for partial nigral lesions (3 μg 6-OHDA in 2 μl), anterior-posterior (AP) −2.8 mm, lateral (L) −1.9 mm and ventral (V) −8.2 mm (relative to dura mater); full nigral lesion (total of 13.5 μg in 4.5 μl, delivered at two injection coordinates), AP = −4.4 mm L = 1.2 mm, DV = 7.8 mm (7.5 μg in 2.5 μl) and AP = −4.0 mm, L = 0.8 mm, DV = 8.0 mm (6 μg in 2 μl). The 6-OHDA infusions were made over 2 min, and the needle was left in place for another 5 min before being slowly retracted. Fresh 6-OHDA solutions were made from stock immediately prior to surgery and kept on ice until use. Intraoperative analgesia was obtained with carprofen (s.c., 0.1 ml/100 g body-weight of rimadyl 50 mg/ml, diluted 1:9 in isotonic NaCl) immediately prior to surgery. Rats received 4 ml NaCl i.p. post-surgically to restore fluid balance, and received daily post-surgical analgesia treatments with Baytril (5 mg/ml in 1 ml, s.c.) and Rimadyl (50 mg/ml in 1 ml) for at least 2 days post-surgery. Following the surgical procedures, all animals were monitored closely for signs of distress.

Behavioral Testing

R-(-)-Apomorphine hydrochloride hemihydrate (sigma-aldrich, DK Cat# A4393) and D-amphetamine (Sigma-aldrich, DK) induced rotations were assessed on weeks 1, 2, and 3 post-surgery. Rotations were counted using a Rotometer system (AccuScan Product Line, Omnitech Electronics Inc, USA). Following administration of r-(-)-apomorphine hydrochloride hemihydrate (0.05 mg/kg, s.c.) or D-amphetamine (5 mg/kg, s.c.), animals were placed in plastic bowls (diameter ∼50 cm). The number of turns completed over a period of 15 min was counted, beginning at 10 min after apomorphine injection or 30 min after amphetamine injection, to accommodate the slower pharmacodynamics of amphetamine. Unilateral 6-OHDA-lesioned rats exhibit behavior super-sensitivity to dopaminergic agonists, which is reflected by amphetamine and apomorphine induced rotations (Ungerstedt and Arbuthnott, 1970), and is marked by upregulation of striatal dopamine D2/3 receptors on the lesioned side (Palner et al., 2011). The dopaminergic agonist apomorphine evokes contralateral turning, due to the direct stimulation of supersensitive dopamine D_2-like and D_1 receptors in the denervated striatum. In contrast, ipsiversive rotations is induced by indirect dopamine agonists such as amphetamine, due to their attenuated effect on dopamine release on the lesioned side (Ungerstedt and Arbuthnott, 1970; Hefti et al., 1980; Carman et al., 1991; Schwarting and Huston, 1996). Of the two agents, amphetamine is the stronger evoker of behavioral asymmetry. Thus, rats with more restricted lesions of the SNc do not show rotational asymmetry in response to apomorphine, such that animals with rotation exclusively after amphetamine administration exhibit a partial nigral lesion.

Collection of Brain Tissue and Storage

Animals were killed by decapitation while under acute CO_2/O_2 anesthesia. Brains were carefully removed and fixed by immersion in 4% parformaldehyde (PFA) for a minimum of 24 h at room temperature), followed by 48 h at t 4°C, whereupon brains were transferred to a 1% PFA solution and stored at 4°C until further processing.

Collection of Slides

The brains were bisected in the coronal plane posterior of the optic chiasm at the level of bregma −3.3 mm according to the

rat brain atlas of Paxinos and Watson (1997) (see **Figure 2**). The superior cortical areas were trimmed away. The caudal part was weighted (formalin weight) and paraffin-infiltrated overnight and then reweighed (paraffin weight). The difference between the wet formalin and paraffin weights is taken as an index of shrinkage upon paraffin embedding. Hemi-brains were then embedded in pairs in paraffin blocks.

To evaluate the precision of section thickness and shrinkage, a caliper was used to measure dimensions of the paraffin block before sectioning was begun. The paraffin block was cut on a microtome (Microm HM340E, Thermo Fisher Scientific, UK) until landmarks of the following coordinates were observed: interaural 4.84 mm; bregma −4.16 mm (just caudal to the disconnection of the tuberoinfundibular stem) (Paxinos and Watson, 1997). The height of the block was then measured with the caliper. In this study, we only used the calculated section thickness to inform about the total volume of the selected brain region.

After re-mounting the block onto the microtome base, a series of adjacent serial sections of 5 µm thickness was cut in the coronal plane using SURS throughout the entire rostro-caudal extent of the SNc. A predetermined sampling fraction was applied (every 50th section), allowing for a sufficient number of section pairs (10–15) to be sampled along the rostrocaudal extent of the SNc. Sections were collected pair-wise onto FLEX IHC slides (DAKO, cat# K802021-2, Agilent technologies, Denmark (DK)) such that two neighboring sections were on each slide. After the last section pair was sampled, the paraffin block was measured again with the caliper and the total number of cut sections was recorded. Thus, the mean section thickness (t) could be calculated by subtraction of the two caliper measurements followed by division by the total number of cut sections (sampled and discarded), see also calculation section below. Slide-mounted sections were dried overnight at 37°C.

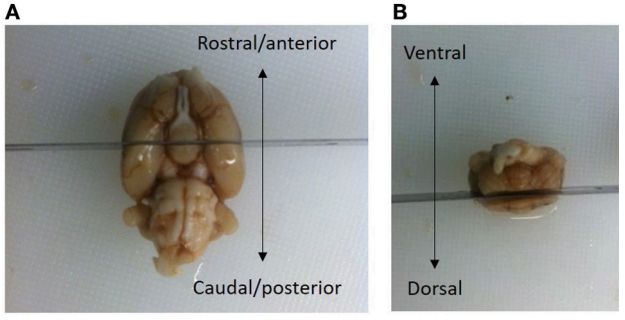

FIGURE 2 | The brains were bisected in the coronal plane at a level posterior to the optic chiasm, i.e., −3.3 mm relative to bregma (Paxinos and Watson, 1997). **(A)** The superior cortical areas were trimmed away. **(B)** The brain in **(A)** is viewed from the ventral aspect, with the rosto-caudal axis indicated by an arrow. The brain in **(B)** is viewed in the caudal aspect with the dorsal/ventral axis indicated by an arrow. The frontal part of the cerebral hemispheres was discarded. A small vertical fiducial incision can be made in the top right brain hemisphere to confirm that the correct orientation at the time of sampling. After fixation, the part of the brain containing mesencephalon was weighed and embedded in pairs overnight in paraffin-blocks.

Immunohistochemical Staining

Slides were deparaffinized by dipping the slides successively for 15 min in xylene, 2 × 3 min in 99% ethanol, 1 × 2 min in 96% ethanol, 1 × 2 min in 70% ethanol and finally running tap water for 5 min. Sections were subjected to antigen retrieval by immersion of the slides in a TEGTris EGTA pH 9 (TEG) buffer (90°C) for 15 min followed by a TBS buffer wash for 5 min. After antigen retrieval, sections were immunostained using a DAKO automated autostainer (Link 48, Agilent Technologies, DK) according to an optimized protocol. In brief, endogenous peroxidase activity was blocked for 10 min in 1% H_2O_2 in TBS + 0.25% Tween-20 (buffer) followed by blocking of unspecific binding by incubation for 20 min in 5% normal swine serum in TBS + 1% BSA + 0.25% Tween-20. Next, the slides were incubated in primary mouse antibody (TH 1:16000, Sigma T2928, lot 110M477, Sigma-Aldrich, DK) diluted in TBS + 1% BSA + 0.25% Tween-20 for 30 min. After a rinse in TBS + 0.25% Tween-20, slides were incubated for 30 min in HRP coupled Envision Polymer rabbit anti-mouse (ready to use DAKO, K4004, Agilent Technologies, DK). After rinsing in buffer, slides were incubated with diaminobenzidine (DAB; 3,3′-diaminobenzidine) 2 component system with chromogen (DAKO, K3468, Agilent technologies, DK). Development was stopped by immersion in water after 10 min. For counterstaining, we used a specialized Mayers Hematoxylin stain (DAKO, Cat# S330930, Agilent technologies, DK), diluted 1:3 in distilled water, with treatment for 1 min. Slides were then dehydrated by brief immersion three times in distilled water, three times in 96% ethanol, 1 × 2 min in 99% ethanol, and 2 × 2 min in xylene, followed by mounted with cover slips using Pertex mounting media (Histolab Products AB, cat#0801). Slides were then dried overnight in a fume head. All slides were scanned on a digital scanner at 20X objective corresponding to 40X magnification (resolution 50,000 pixels per inch, ScanScope AT, Aperio) and saved as Scanscope virtual slides (svs), which is a format compatible with the CAST visiopharm system (Visiopharm, DK) and Image scope software.

Counting and Estimation of Tyrosine Hydroxylase-Positive Neurons

Estimates of total TH-positive neuron numbers in the SNc (separately for left and right hemisphere) were performed using the automated physical disector in a fractionator design on virtual slides. All slide images were loaded onto the CAST Autodisector (Visiopharm, DK) system and an automated alignment and sampling was performed at 10 X magnification. In rare cases where the automatic alignment was not perfect, the researcher performed a manual alignment of the sections. This proved necessary only for sections that were not optimally cut and stained. The region of interest (ROI) was defined on each section using ROI delineation applied to the SNc (see **Figure 3**). The criterion for delineating the SNc from the ventral tegmental area (VTA) was the localization of the oculomotor nerve root; Whereas the VTA is medial to the root, the SNc is laterally located. SNc was defined extending from anterior-posterior level −5.3 mm with respect to bregma to −6.3 mm according to Paxinos and Watson (1997). The disector counting frame and

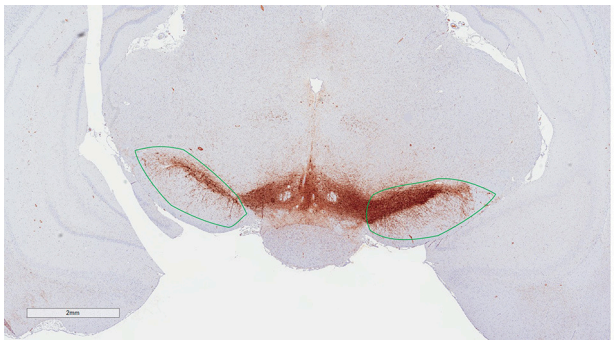

FIGURE 3 | Region of interest (substantia nigra) delineated on a TH immunohistological stained section counterstained with modified Meyer hematoxylin. The section is at the level of bregma −5.6 mm according to the rat atlas of Paxinos and Watson (1997).

sampling frequency were adjusted to allow for counting of 150–200 neurons ($\sum Q^-$) in each of approximately 100 disectors (**Figure 4** for counting example).

Estimation of the Total Neuron Number Using the Physical Disector, N

Knowing the section sampling fraction (ssf, every 50th sections), the area of the disector counting frame and the relation between the total number of neurons in each subdivision ($\sum Q^-$), the total number of TH-positive neurons (N) was estimated as:

$$N = \left(1/ssf \times 1/asf \times \sum Q^-\right)$$

where asf = a (frame)/X (step) × Y step. The result was divided by two, since the two sections can be compared both ways in a physical fractionator" i.e., with alternating use of the sections in the pair as sampling section and lookup section, respectively" (see **Table 1** for calculation examples) (Gundersen, 1986; Dorph-Petersen et al., 2001; Boyce et al., 2010).

Error Predictions

Stereology is a reliable method that provides unbiased quantitative results so long as the experimental design meets the necessary critera. In biological sciences there are two primary sources of variation in a dataset: biological coeffecient of variance (CV_{biol}) and a sampling variance, which is usually called the coefficient of error (CE) (Gundersen and Jensen, 1987). There will always be a natural variation between animals and a high CV_{biol} can only be compensated by increasing the group size. Sampling variance, on the other hand, can be controlled by the design of the sampling protocol. Thus, CE declines in magnitude if the number of counted objects is increased. In our design, a CE value was considered acceptable if its contribution was less than 50% of the total variance, such that variance due to stereological sampling is less important than the biological variance. In general, a stereological design with 150–200 counting events is usually sufficient to obtain data meeting this criterion for acceptable CE (Gundersen and Jensen, 1987; West, 1999). Knowing the CE is critical for determining whether the sampling protocol can in fact be optimized. This is a crutial point because stereological estimates are non-independent due to the use of systematic uniform random sampling (SURS) in the sampling scheme. This consideration led to the development of a set of equations to calculate the modified CE, which is the sum of two factors, the variance from the point-counting (noise) and the variance from the area sampling ($Var_{(SURS)}$)(Gundersen et al., 1999). The $Var_{(SURS),}$ is the systematic uniformly random sampling variance, which is calculated from:

$$VAR_{SURS} = \frac{\sqrt{(3\ (A - noise) - 4B + C)}}{240} \quad where \begin{matrix} A = \sum Q_i^- Q_i^- \\ B = \sum Q_i^- Q_{i+1}^- \\ C = \sum Q_i^- Q_{i+2}^- \end{matrix}$$

Where noise is, in the case of number estimates, equal to the sum of all cells ($\sum Q^-$). 240 is a constant appropriate for the current stereological design. The modified CE estimate for volumes include a different noise calculation, which is not presented in this paper.

From the two parameters Noise and VAR_{SURS}, $CE_{\sum Q^-}$ can be calculated as:

$$CE_{\sum Q^-} = \frac{\sqrt{Noise + VAR_{SURS}}}{\sum Q^-}$$

See **Table 2** for calculation example.

When estimating the mean CE for e.g., a treatment group, the following formula is applied

$$\overline{CE} = \sqrt{\frac{CE_1^2 + CE_2^2 \ldots\ldots CE_n^2}{n}}$$

Where *n* is the number of subjects in the group.

Statistics

All data were fed into Excel spread sheets and subsequently subjected to relevant statistical analyses using GraphPad Prism (GraphPad Software, La Jolla, CA) or SigmaStat (Systat Software, San Jose, CA), where applicable. Results are presented as mean ± standard error of the mean (S.E.M.). Turning behavior data were analyzed using a two-way repeated measurement analysis of variance (ANOVA). Stereological data were evaluated statistically by an unpaired *t*-test (partial lesion model), or a one-way ANOVA followed by Dunnett's *post-hoc* test (full lesion model). Spearman's correlation test was applied to evaluate the relationship between individual TH neuron number by side and corresponding apomorphine and amphetamine-induced rotations. A *p*-value less than 0.05 was considered statistically significant.

RESULTS

In the partial lesion model, the number of TH-positive neurons in the lesioned (ipsilateral to 6-OHDA infusion) SNc was reduced by 55%, as compared to the contralateral SNc (ipsilateral 4,754 ± 667, mean CE = 0.05; contralateral, 10,321 ± 527, mean

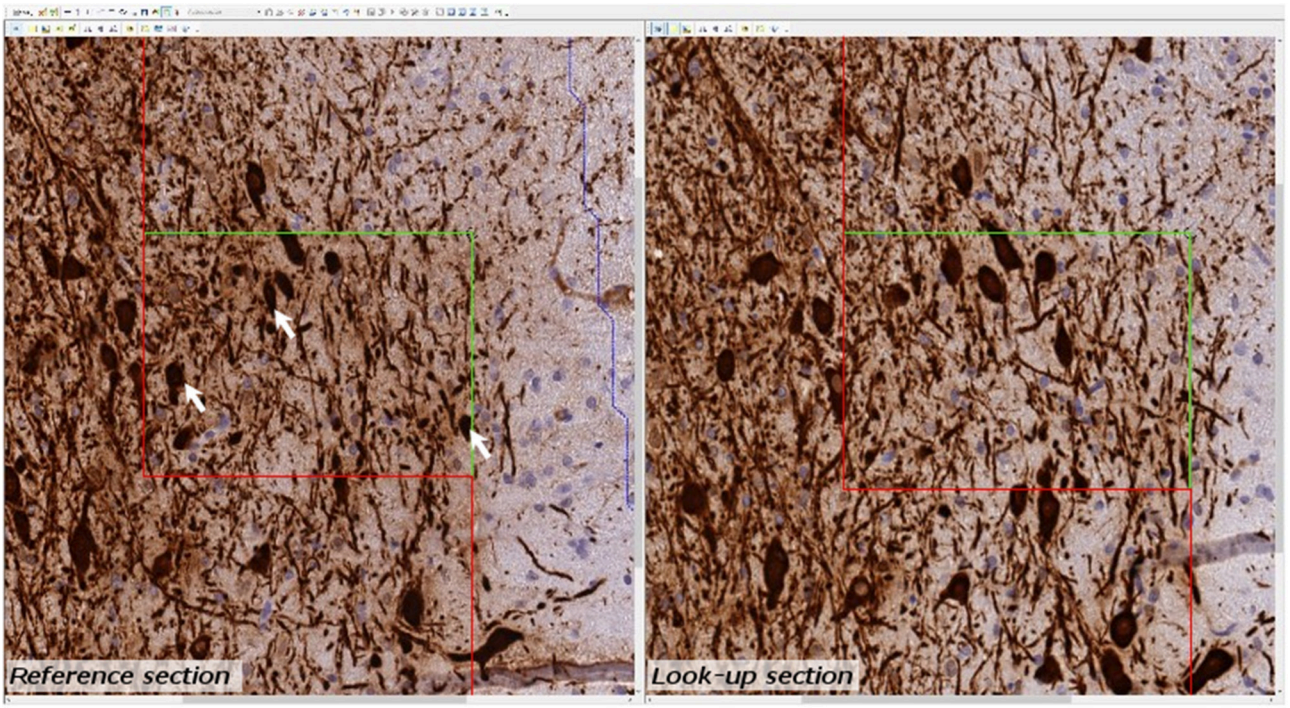

FIGURE 4 | Example of micrograph used for stereological quantification with the physical disector. TH positive neurons (arrow) are counted if they appear in one section (reference section) but not the other (lookup section).

TABLE 1 | Calculation example for estimation of TH-positive neurons.

Animal No	Region	$\sum Q^-$	$\sum P$	a(frame) (μm^2)	X-Y step (μm)	1/asf	1/ssf	N	V (mm^3)
1	SNc control	159	190	60000	387.29	2.50	50	9,938	7.13
2	SNc control	180	181	60000	387.29	2.50	50	11,250	6.79
3	SNc control	172	147	60000	387.29	2.50	50	10,750	5.51

asf = a(frame)/X ×Y step ssf = section sampling fraction, $\sum Q^-$ = sum of TH positive neurons, $\sum P$ = sum of points hitting the SNc.

CE = 0.31) (**Figure 5**). Volume estimates showed a reduction in ipsilateral SNc volume by 27% (4.80 + 0.32 mm^3), as compared to the corresponding contralateral SNc volume (6.60 ± 0.27 mm^3) (data not shown). A correlation analysis of the number of ipsilateral nigral TH-positive neurons and corresponding D-amphetamine induced rotations showed a strong inverse linear relationship of mean nigral TH-positive neuron numbers vs. rotation numbers ($n = 26$, spearman $r = -0.61$, $p = 0.0009$, see **Figure 6**).

In the full nigral lesion model, the number of TH-positive neurons was reduced by 85% (mean ± SEM, ipsilateral 1,020 ± 438, mean CE = 0.09; contralateral: 6,946 ± 1,282, mean CE = 0.44; **Figure 5**). Comparison with the parital lesion results suggest that there was a 30% reduction in the number of TH-positive neurons on the side contralateral to the repeated 6-OHDA infusion (data not shown). Volume estimates showed a 59% reduction in ipsilateral SNc volume (0.64 ± 0.20 mm^3), as compared to corresponding contralateral SNc volume (1.58 ± 0.22 mm^3). There were no significant correlations between apomorphine-induced rotations and TH-positive cell numbers (data not shown). Volume data in this data-set should only be evaluated when compared to the non-infused side.

DISCUSSION

The physical fractionator method is widely accepted as the current best practice for accurate estimation of total cell numbers in thin tissue sections. This rigorous estimator of object number is based on an unbiased design that minimizes or avoids all known sources of stereological and methodological bias. The primary drawback of the manual fractionator is its low efficiency (low throughput) due to the requirement for manual alignment of pairs of adjacent sections. The automatic method described here allows for an automatic and digital approach to incorporate the unbiased principles of the physical fractionator method. The routine use of digital images in the field of pathology

TABLE 2 | Example of CE calculation.

CE (N)	Q_i^-	A:$Q_i^- Q_i^-$	B:$Q_i^- Q_{i+1}^-$	C:$Q_i^- Q_{i+2}^-$
1	9	81	270	207
2	30	900	690	360
3	23	529	276	322
4	12	144	168	72
5	14	196	84	154
6	6	36	66	90
7	11	121	165	165
8	15	225	225	210
9	15	225	210	105
10	14	196	98	28
11	7	49	14	
12	2	4		
13	0			
14				
sum	158	2,706	2,266	1,713
Noise		158		
Var(SURS)	1.22			
CE (N)=	0.08			

Q^-, number of counted TH neurons in a disector section pair.

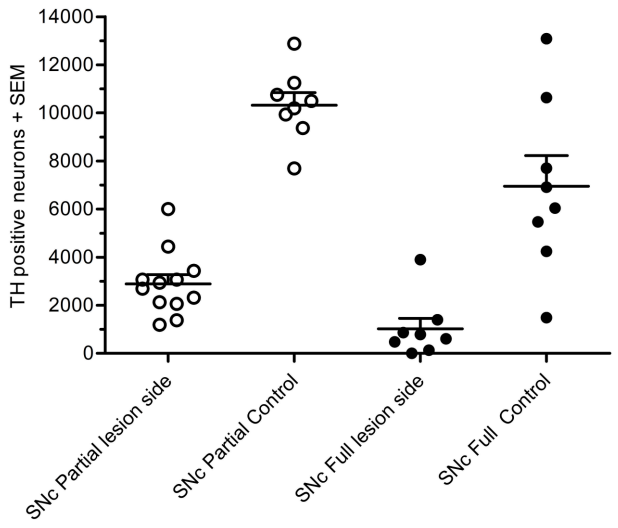

FIGURE 5 | Total number of TH-positive cells in substantial nigra of 6-OHDA-lesioned rats, showing results for the partial lesion model (open symbols) and the full lesion model (filled symbols). Adapted from Hansen et al. (2016), with permission from Brain Research.

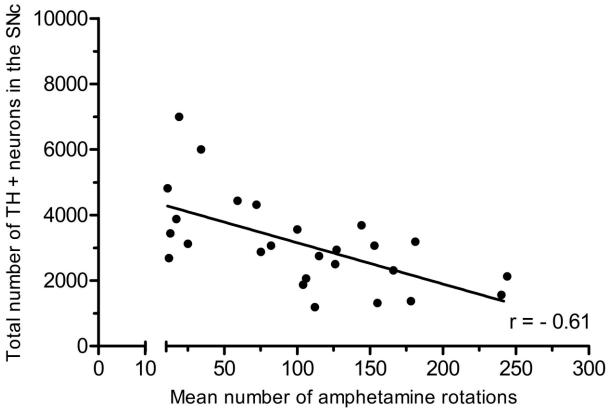

FIGURE 6 | Positive correlation of amphetamine-induced rotations and TH-positive neuron numbers in the SNc. Adapted from Hansen et al. (2016), with permission from Brain Research.

has considerable potential, but has hitherto found scant use. However, this is changing in recent years due to improvement of the technique and wider availability of slide scanners (Taylor, 2011). To minimize the time needed for cell counting, a software system using virtual slides and automated alignment is ideal for physical disector estimation. When using a software-based system, the counting of particles (cells) can be performed off-line from the microscope, and an autodisector on virtual slides combines automatic generation of disector pairs through the use of digital images. When tissue slides are scanned in a digital slide scanner and the autodisector is applied, each slide is partitioned into fields of view, and cells are counted in all fields. Although we have not rigorously compared the time saved with the autodisector system compared to a manual system in the present study of TH-positive neurons, one study by Keller et al. (2013) found that the autodisector on virtual slides was 55–104% faster than the manual physical disector. Although this did not take into account the time expended in scanning, the Aperio scanner used in the present study can process up to 400 microscope slides at a time. Thus, one can initiate scanning in the afternoon, and the process will be completed overnight. In this study, we applied the autodisector on virtual slides, but the autodisector can also be applied directly on tissue slides on a standard microscope equipped for stereology. However, in this event the efficiency will be lower because the image generation is bound to be slower. In addition, acquiring slide images of sufficient quality is time-consuming as a manual process. The use of virtual slides can also be implemented for stereological estimates of volume (as in the present study) and also length and surface areas. However, the time spared by automation of those procedures would probably be less because the time required for microscope stage movement would be almost identical in the two setups. In the present study, the main economy of time was gained by the fast and automatic generation of the disector image pairs. When using virtual slides, it is a matter of concern whether the image quality of the virtual slides is degraded relative to the original tissue slides (Treanor, 2009), and especially important that the plane of focus be acceptable. In general, we found the quality of the virtual slides to be sufficient for evaluation in the stereological setup, but this may depend on the avidity of the particular antibody or staining procedure.

The automated alignment, however, requires optimization of the section sampling technique. Importantly, no cracks or folds should be visible on the sections. Since the digital alignment is based on self-similarity of two image files, high-quality tissue

sections are therefore required for obtaining the full benefit of this automatic methodology. In our experience, an experience histologist can undertake manual neuron counting of up to five different ROI per day. However, with a slightly larger initial expenditure of effort, the quality and quantity of the stereological analyses can be improved substantially by applying an automated physical disector principle in a fractionator design for quantitative analysis of immunophenotyped neurons. Compared to optical disectors, the physical disector does not require optimization of shrinkage artifacts, which can be quite challenging for paraffin-embedded material. Further, the use of immunohistologically-stained sections allows for more specific estimations of define cell populations, such as the TH-containing midbrain dopamine neurons estimated in this study. A recent study applied a fully automated optical fractionator design to the counting of NeuN-positive neurons in a mouse neurodegenerative disease model (Mouton et al., 2017), but the present is, to our knowledge, the first study describing the use of the automated physical disector design in a neurodegenerative disease model.

Rats with a partial or full unilateral 6-OHDA nigral lesion showed a 55% or 85% reduction of TH-positive neurons in the ipsilateral SNc, respectively, as compared to the corresponding contralateral SNc, which contained approximately 7000 TH-positive neurons. This is to be compared with estimages of 550,000 pigmented neurons in the human nigra, which is reduced by 66% in patients dying with idiopathic PD (Pakkenberg et al., 1991).

While the severity of motor deficits (amphetamine-induced rotations) in the present study was highly correlated with the extent of DA-ergic neuron loss in rats with a partial nigral lesion, we saw no significant correlation between motor deficits in the apomorphine challenge test and loss of nigral DA-ergic neurons in rats with a more aggressive ("full") nigral lesion. This could be due to a carry over effect of the 6-OHDA to the contralateral side, leading to a partial sensitization in the "unlesioned" side. Rotational behavior is therefore an imperfect index of the progressive partial nigral 6-OHDA lesion model. On the other hand, the extent of neuronal loss and the proportional rotational responsiveness to a D-amphetamine challenge in the partial nigral 6-OHDA lesion model is in agreement with previous findings using conventional quantification methods of lesion size and rotation (Hefti et al., 1980; Carman et al., 1991; Hudson et al., 1993). However, as the present stereological approach considers the total number of DA-ergic neurons within the complete rostro-caudal extension of the SNc, we contend that it provides an inherently more accurate estimate of DA-containing neurons in the SNc in the partial nigral lesion model, which help to improve the correlation between behavioral and stereological findings. Previous stereological studies of TH-positive cells using an optical disector design in PD models of rodents correspond well with the findings in our study (Deumens et al., 2002; Aponso et al., 2008; Heuer et al., 2013; Boix et al., 2015). We have recently reported the application of this stereological method in the preclinical evaluation of a potential drug therapeutic strategy in PD (Hansen et al., 2016). In addition to neuron counting, the stereological approach can also provide data on volume changes in relevant brain regions. In the context of the present rat 6-OHDA model, partial and full nigral lesions reduced SNc volumes by 27 and 59%, respectively, thus showing that tissue loss being a direct consequence of neuronal loss. This result concurs with volumetric MR-based imaging results in 1-methyl-4 phenyl-1,2,3,6-tetrahydropyridine (MPTP)-treated marmosets (Modo et al., 2017). So long as this relationship holds, tissue volume changes might serve as a surrogate for neuronal loss, but neuron counts remain the gold standard for neurodegenerative disease models.

In conclusion, the automated physical disector provides a useful and effective tool for unbiased estimation of the total loss of nigral dopaminergic neurons in the unilateral 6-OHDA model. This stereological approach should thus prove instrumental in the preclinical evaluation of potential drug therapies for PD, but more generally also potentially extends to the evaluation of neurotoxic or development effects on the number of any cell phenotype ammenable for specific labeling by histology or immunohistochemistry.

AUTHOR CONTRIBUTIONS

KF: Wrote the manuscript, performed the *in vivo* experiments, performed the stereological work and interpreted the results, PB: Performed the histological and stereological experiments, interpreted the results and co-wrote the manuscript. HH: Revised and supervised the manuscript. JJ: Conceived and supervised the project and created **Figure 1**.

ACKNOWLEDGMENTS

The authors thank Prof. Paul Cumming for critical reading of the manuscript.

REFERENCES

Aponso, P. M., Faull, R. L., and Connor, B. (2008). Increased progenitor cell proliferation and astrogenesis in the partial progressive 6-hydroxydopamine model of Parkinson's disease. *Neuroscience* 151, 1142–1153. doi: 10.1016/j.neuroscience.2007.11.036

Bertilsson, G., Patrone, C., Zachrisson, O., Andersson, A., Dannaeus, K., Heidrich, J., et al. (2008). Peptide hormone exendin-4 stimulates subventricular zone neurogenesis in the adult rodent brain and induces recovery in an animal model of Parkinson's disease. *J. Neurosci. Res.* 86, 326–338. doi: 10.1002/jnr.21483

Blesa, J., Pifl, C., Sánchez-González, M. A., Juri, C., García-Cabezas, M. A., Adánez, R., et al. (2012). The nigrostriatal system in the presymptomatic and symptomatic stages in the MPTP monkey model: a PET, histological and biochemical study. *Neurobiol. Dis.* 48, 79–91. doi: 10.1016/j.nbd.2012.05.018

Boix, J., Padel, T., and Paul, G. (2015). A partial lesion model of Parkinson's disease in mice - Characterization of a 6-OHDA-induced medial forebrain bundle lesion. *Behav. Brain Res.* 284, 196–206. doi: 10.1016/j.bbr.2015.01.053

Boyce, R. W., Dorph-Petersen, K. A., Lyck, L., and Gundersen, H. J. (2010). Design-based stereology: introduction to basic concepts and practical

approaches for estimation of cell number. *Toxicol. Pathol.* 38, 1011–1025. doi: 10.1177/0192623310385140

Cabello, C. R., Thune, J. J., Pakkenberg, H., and Pakkenberg, B. (2002). Ageing of substantia nigra in humans: cell loss may be compensated by hypertrophy. *Neuropathol. Appl. Neurobiol.* 28, 283–291. doi: 10.1046/j.1365-2990.2002.00393.x

Carman, L. S., Gage, F. H., and Shults, C. W. (1991). Partial lesion of the substantia nigra: relation between extent of lesion and rotational behavior. *Brain Res.* 553, 275–283. doi: 10.1016/0006-8993(91)90835-J

Cumming, P., Møller, M., Benba, K., Minuzzi, L., Jakobsen, S., Jensen, S. B., et al. (2007). A PET study of effects of chronic 3,4-methylenedioxymethamphetamine (MDMA, "ecstasy") on serotonin markers in Göttingen minipig brain. *Synapse* 61, 478–487. doi: 10.1002/syn.20377

Deumens, R., Blokland, A., and Prickaerts, J. (2002). Modeling Parkinson's disease in rats: an evaluation of 6-OHDA lesions of the nigrostriatal pathway. *Exp. Neurol.* 175, 303–317. doi: 10.1006/exnr.2002.7891

Dorph-Petersen, K. A., Nyengaard, J. R., and Gundersen, H. J. (2001). Tissue shrinkage and unbiased stereological estimation of particle number and size. *J. Microsc.* 204, 232–246. doi: 10.1046/j.1365-2818.2001.00958.x

Eriksen, N., Stark, A. K., and Pakkenberg, B. (2009). Age and Parkinson's disease-related neuronal death in the substantia nigra pars compacta. *J. Neural Transm. Suppl.* 2009, 203–213. doi: 10.1007/978-3-211-92660-4-16

Eslamboli, A., Baker, H. F., Ridley, R. M., and Annett, L. E. (2003). Sensorimotor deficits in a unilateral intrastriatal 6-OHDA partial lesion model of Parkinson's disease in marmoset monkeys. *Exp. Neurol.* 183, 418–429. doi: 10.1016/S0014-4886(03)00139-0

Gundersen, H. J., Bagger, P., Bendtsen, T. F., Evans, S. M., Korbo, L., Marcussen, N., et al. (1988). The new stereological tools: disector, fractionator, nucleator and point sampled intercepts and their use in pathological research and diagnosis. *APMIS* 96, 857–81. doi: 10.1111/j.1699-0463.1988.tb00954.x

Gundersen, H. J. G. (1977). Notes on the estimation of the numerical density of arbitrary profile: the edge effect. *J. Microsc.* 111, 219–223.

Gundersen, H. J. (1986). Stereology of arbitrary particles. *J. Microsc.* 143, 3–45. doi: 10.1111/j.1365-2818.1986.tb02764.x

Gundersen, H. J., and Jensen, E. B. (1987). The efficiency of systematic sampling in stereology and its prediction. *J. Microsc.* 147, 229–263. doi: 10.1111/j.1365-2818.1987.tb02837.x

Gundersen, H. J., Jensen, E. B., Kieu, K., Nielsen, J., Kiêu, K., Nielsen, J., et al. (1999). The efficiency of systematic sampling in stereology – reconsidered. *J. Microsc.* 193, 199–211. doi: 10.1046/j.1365-2818.1999.00457.x

Gundersen, H. J., Bendtsen, T. F., Korbo, L., Marcussen, N., Møller, A., Nielsen, K., et al. (1988). Some new, simple and efficient stereological methods and their use in pathological research and diagnosis. *APMIS* 96, 379–94.

Hansen, H. H., Fabricius, K., Barkholt, P., Mikkelsen, J. D., Jelsing, J., Pyke, C., et al. (2016). Characterization of liraglutide, a glucagon-like peptide-1 (GLP-1) receptor agonist, in rat partial and full nigral 6-hydroxydopamine lesion models of Parkinson's disease. *Brain Res.* 1646, 354–365. doi: 10.1016/j.brainres.2016.05.038

Hefti, F., Melamed, E., Sahakian, B. J., and Wurtman, R. J. (1980). Circling behavior in rats with partial, unilateral nigro-striatal lesions: effect of amphetamine, apomorphine, and DOPA. *Pharmacol. Biochem. Behav.* 12, 185–188. doi: 10.1016/0091-3057(80)90353-6

Heuer, A., Smith, G. A., and Dunnett, S. B. (2013). Comparison of 6-hydroxydopamine lesions of the substantia nigra and the medial forebrain bundle on a lateralised choice reaction time task in mice. *Eur. J. Neurosci.* 37, 294–302. doi: 10.1111/ejn.12036

Hudson, J. L., van Horne, C. G., Strömberg, I., Brock, S., Clayton, J., Masserano, J., et al. (1993). Correlation of apomorphine- and amphetamine-induced turning with nigrostriatal dopamine content in unilateral 6-hydroxydopamine lesioned rats. *Brain Res.* 626, 167–174. doi: 10.1016/0006-8993(93)90576-9

Jeon, B. S., Jackson-Lewis, V., and Burke, R. E. (1995). 6-Hydroxydopamine lesion of the rat substantia nigra: time course and morphology of cell death. *Neurodegeneration* 4, 131–137. doi: 10.1006/neur.1995.0016

Kalia, L. V., and Lang, A. E. (2015). Parkinson's disease. *Lancet* 386, 896–912. doi: 10.1016/S0140-6736(14)61393-3

Keller, K. K., Andersen, I. T., Andersen, J. B., Hahn, U., Stengaard-Pedersen, K., Hauge, E. M., et al. (2013). Improving efficiency in stereology: a study applying the proportionator and the autodisector on virtual slides. *J. Microsc.* 251, 68–76. doi: 10.1111/jmi.12044

Kristiansen, S. L., and Nyengaard, J. R. (2012). Digital stereology in neuropathology. *APMIS* 120, 327–340. doi: 10.1111/j.1600-0463.2012.02889.x

Ma, J., Shaw, V. E., and Mitrofanis, J. (2009). Does melatonin help save dopaminergic cells in MPTP-treated mice? *Park. Relat. Disord.* 15, 307–314. doi: 10.1016/j.parkreldis.2008.07.008

Modo, M., Crum, W. R., Gerwig, M., Vernon, A. C., Patel, P., Jackson, M. J., et al. (2017). Magnetic resonance imaging and tensor-based morphometry in the MPTP non-human primate model of Parkinson's disease. *PLoS ONE* 10:e0180733. doi: 10.1371/journal.pone.0180733

Monville, C., Torres, E. M., and Dunnett, S. B. (2006). Comparison of incremental and accelerating protocols of the rotarod test for the assessment of motor deficits in the 6-OHDA model. *J. Neurosci. Methods* 158, 219–223. doi: 10.1016/j.jneumeth.2006.06.001

Mouton, P. R., Phoulady, H. A., Goldgof, D., Hall, L. O., Gordon, M., and Morgan, D. (2017). Unbiased estimation of cell number using the automatic optical fractionator. *J. Chem. Neuroanat.* 80, A1–A8. doi: 10.1016/j.jchemneu.2016.12.002

Pakkenberg, B. (1993). Total nerve cell number in neocortex in chronic schizophrenics and controls estimated using optical disectors. *Biol. Psychiatry* 34, 768–772. doi: 10.1016/0006-3223(93)90065-L

Pakkenberg, B., and Gundersen, H. J. (1997). Neocortical neuron number in humans: effect of sex and age. *J. Comp. Neurol.* 384, 312–320. doi: 10.1002/(SICI)1096-9861(19970728)384:2<312::AID-CNE10>3.0.CO;2-K

Pakkenberg, B., Møller, A., Gundersen, H. J., Mouritzen Dam, A., and Pakkenberg, H. (1991). The absolute number of nerve cells in substantia nigra in normal subjects and in patients with Parkinson's disease estimated with an unbiased stereological method. *J. Neurol. Neurosurg. Psychiatry* 54, 30–3. doi: 10.1136/jnnp.54.1.30

Pakkenberg, B., Pelvig, D., Marner, L., Bundgaard, M. J., Gundersen, H. J., Nyengaard, J. R., et al. (2003). Aging and the human neocortex. *Exp. Gerontol.* 38, 95–99. doi: 10.1016/S0531-5565(02)00151-1

Palner, M., Kjaerby, C., Knudsen, G. M., and Cumming, P. (2011). Effects of unilateral 6-OHDA lesions on [3H]-N- propylnorapomorphine binding in striatum *ex vivo* and vulnerability to amphetamine-evoked dopamine release in rat. *Neurochem. Int.* 58, 243–247. doi: 10.1016/j.neuint.2010.12.007

Paxinos, G., and Watson, C. (1997). *The Rat Brain in Stereotaxic Coordinates, 3rd Edn*. San Diego, CA: Academic Press.

Peoples, C., Spana, S., Ashkan, K., Benabid, A.L., Stone, J., Baker, G. E., et al. (2012). Photobiomodulation enhances nigral dopaminergic cell survival in a chronic MPTP mouse model of Parkinson's disease. *Parkinsonism Relat. Disord.* 18, 469–76. doi: 10.1016/j.parkreldis.2012.01.005

Petroske, E., Meredith, G. E., Callen, S., Totterdell, S., and Lau, Y. S. (2001). Mouse model of Parkinsonism: a comparison between subacute MPTP and chronic MPTP/probenecid treatment. *Neuroscience* 106, 589–601. doi: 10.1016/S0306-4522(01)00295-0

Schober, A. (2004). Classic toxin-induced animal models of Parkinson's disease: 6-OHDA and MPTP. *Cell Tissue Res.* 318, 215–224. doi: 10.1007/s00441-004-0938-y

Schwarting, R. K., and Huston, J. P. (1996). Unilateral 6-hydroxydopamine lesions of meso-striatal dopamine neurons and their physiological sequelae. *Prog. Neurobiol.* 49, 215–266. doi: 10.1016/S0301-0082(96)00015-9

Sterio, D. C., (1984). The unbiased estimation of number and sizes of arbitrary particles using the disector. *J. Microsc* 134, 127–136.

Stroeven, P., and Hu, J. (2007). Review paper – stereology: historical perspective and applicability to concrete technology. *Mater. Struct.* 39, 127–135. doi: 10.1617/s11527-005-9031-6

Taylor, C. R. (2011). From microscopy to whole slide digital images: a century and a half of image analysis. *Appl. Immunohistochem. Mol. Morphol.* 19, 491–493. doi: 10.1097/PAI.0b013e318229ffd6

Thomas, B., and Flint Beal, M. (2007). Parkinson's disease. *Hum. Mol. Genet.* 16, R183–R194. doi: 10.1093/hmg/ddm159

Torres, E. M., and Dunnett, S. B. (2012). "6-OHDA lesion models of Parkinson's disease in the rat," in *Animal Models of Movement Disorders*, eds S. B. Lane and E. L. Dunnet (Cardiff: Humana Press), 267–279. doi: 10.1007/978-1-61779-298-4

Treanor, D. (2009). Virtual slides: an introduction. *Diagn. Histopathol.* 15, 99–103. doi: 10.1016/j.mpdhp.2009.01.006

Tschanz, S. A., Burri, P. H., and Weibel, E. R. (2011). A simple tool for stereological assessment of digital images: the STEPanizer. *J. Microsc.* 243, 47–59. doi: 10.1111/j.1365-2818.2010.03481.x

Ungerstedt, U., and Arbuthnott, G. W. (1970). Quantitative recording of rotational behavior in rats after 6-hydroxy-dopamine lesions of the nigrostriatal dopamine system. *Brain Res.* 24, 485–493. doi: 10.1016/0006-8993(70)90187-3

Walsh, S., Finn, D. P., and Dowd, E. (2011). Time-course of nigrostriatal neurodegeneration and neuroinflammation in the 6-hydroxydopamine-induced axonal and terminal lesion models of Parkinson's disease in the rat. *Neuroscience* 175, 251–261. doi: 10.1016/j.neuroscience.2010.12.005

West, M. J. (1999). Stereological methods for estimating the total number of neurons and synapses: issues of precision and bias. *Trends Neurosci.* 22, 51–61. doi: 10.1016/S0166-2236(98)01362-9

Yuan, H., Sarre, S., Ebinger, G., and Michotte, Y. (2005). Histological, behavioural and neurochemical evaluation of medial forebrain bundle and striatal 6-OHDA lesions as rat models of Parkinson's disease. *J. Neurosci. Methods* 144, 35–45. doi: 10.1016/j.jneumeth.2004.10.004

Conflict of Interest Statement: The authors declare that the research was conducted in the absence of any commercial or financial relationships that could be construed as a potential conflict of interest.

frontiers in Neuroanatomy

REVIEW
published: 05 March 2018
doi: 10.3389/fnana.2018.00016

Total Number Is Important: Using the Disector Method in Design-Based Stereology to Understand the Structure of the Rodent Brain

Ruth M. A. Napper *

Brain Health Research Centre, Department of Anatomy, School of Biomedical Sciences, University of Otago, Dunedin, New Zealand

The advantages of using design-based stereology in the collection of quantitative data, have been highlighted, in numerous publications, since the description of the disector method by Sterio (1984). This review article discusses the importance of total number derived with the disector method, as a key variable that must continue to be used to understand the rodent brain and that such data can be used to develop quantitative networks of the brain. The review article will highlight the huge impact total number has had on our understanding of the rodent brain and it will suggest that neuroscientists need to be aware of the increasing number of studies where density, not total number, is the quantitative measure used. It will emphasize that density can result in data that is misleading, most often in an unknown direction, and that we run the risk of this type of data being accepted into the collective neuroscience knowledge database. It will also suggest that design-based stereology using the disector method, can be used alongside recent developments in electron microscopy, such as serial block-face scanning electron microscopy (SEM), to obtain total number data very efficiently at the ultrastructural level. Throughout the article total number is discussed as a key parameter in understanding the micro-networks of the rodent brain as they can be represented as both anatomical and quantitative networks.

Keywords: stereology, serial block-face scanning electron microscopy, total number, rodent brain, the disector method

OPEN ACCESS

Edited by:
Bente Pakkenberg, Research Laboratory for Stereology and Neuroscience, Denmark

Reviewed by:
Carlos Avendaño, Universidad Autonoma de Madrid, Spain
Lidia Alonso-Nanclares, Consejo Superior de Investigaciones Científicas (CSIC), Spain
John F. Bertram, Monash University, Australia

***Correspondence:**
Ruth M. A. Napper
ruth.napper@otago.ac.nz

Received: *31 May 2017*
Accepted: *15 February 2018*
Published: *05 March 2018*

Citation:
Napper RMA (2018) Total Number Is Important: Using the Disector Method in Design-Based Stereology to Understand the Structure of the Rodent Brain. Front. Neuroanat. 12:16. doi: 10.3389/fnana.2018.00016

INTRODUCTION

The first detailed drawings of the cells of the brain, by "Ramón y Cajal" indicated that the brain is a complex arrangement of many different types of cells (see Swanson and Lichtman, 2016). Modern imaging methods have shown that the complexity of this network spans from the nanoscale to axonal pathways (Bohland et al., 2009; Finlay, 2016). This network is formed by the connections between a series of nodes, at cellular and subcellular levels, each representative of a specific brain region and fundamental to functional interactions in the brain (Barbas, 2015; Li et al., 2016). Within each node there is a total number of cells and synapses and these numbers are crucial in understanding how a brain region interacts functionally with other regions. All anatomically connected brain regions are quantitative networks and models of normal and pathological brain function benefit from using estimates of total number

(for early descriptions of this idea see Mulders et al., 1997). The total number of neurons and/or synapses in each region, each node, in a quantitative network must be obtained without size or shape bias and within identifiable anatomical boundaries (Witter, 2010). The unbiased stereological estimator, the disector, combined with design-based stereological sampling can be used to obtain an estimate of total number within a defined volume of tissue (West et al., 1991; Oorschot, 1996).

Rodents, particularly rats and mice, are key animal models used to investigate many pathologies of the human brain (Nestler and Hyman, 2010) and thus it is essential to have quantitative models of the rodent brain networks to correlate with function. This review article will focus on the idea that total number, either of cells or synapses, obtained with the disector method, is crucial in enabling the rodent brain to be understood as a quantitative network that allows both function and dysfunction to be interpreted at a cellular basis. Finally, it will suggest that the disector method is poised along-side developments in electron microscopy to allow major advances in our understanding of the quantitative structure of the rodent brain at the subcellular level. Throughout the article total number is discussed as a key parameter in understanding the micro-networks of the rodent brain as they can be represented as both anatomical and quantitative networks.

THE DISECTOR METHOD—A REVOLUTION IN THE ESTIMATION OF TOTAL NUMBER

The brain is comprised of a number of component networks of individual cells and synapses that can be considered particles with a certain shape and size. These particles can be counted as long as any profile of the particle can be reliably identified in random sections through the particle. It has been well established that within the brain both cells and synapses rarely conform to simple geometric shapes and that the volume of particles may change with experimental treatment as noted in a number of studies (Kitahara et al., 2016). If number is estimated from the presence of particles in a single tissue section it is biased towards particles of larger volume and although a range of correction factors can be applied to single section estimates this is far from ideal (Calverley and Jones, 1987; Calverley et al., 1988; Park and Ahmad, 2014). The existence of a particle size bias should have been abolished with the publication of a seminal article describing the disector method in 1984 by Sterio. This method was a major breakthrough in quantitation. It requires that all profiles from a particle can be identified in a section, that each particle has a single "top" or "bottom", depending on the direction from which slices through the particle are viewed and that section thickness is known, preferably measured. The original disector method (Sterio, 1984), known as the physical disector used two adjacent sections a known distance apart, that was not greater than around one third of the height of the smallest particle to be counted. Particle profiles visible in one section, the reference section, are counted if they are not present in the parallel "lookup" section, meaning the profile counted must have been either the top or bottom of the particle. This method and how to apply it over a range of cell and synapse types are described in a number of excellent books, key stereological reviews and specific research publications (Geinisman et al., 1996; Howard and Reed, 2005; West, 2012, 2013a; Mouton, 2014). The disector method was rapidly adopted by neuroscientists estimating synapse number as serial physical sections are commonly used in transmission electron microscopy and it was well established that synapse size and shape varies with section orientation (Geinisman et al., 1992, 1996). It continues to be a key tool for estimating total synapse number and synapse number per neuron (da Costa et al., 2009; Jasinska et al., 2016).

The use of two parallel sections to form the disector was ideally suited to transmission electron microscopic studies of subcellular elements but was time consuming at a light microscope level. The optical disector method removed this constraint by using one relatively thick physical section and counting within it, through a series of optical sections (Gundersen, 1986). Essentially particle number is counted within an unbiased sampling frame as one focuses through a series of optical sections for a known distance that forms the z-dimension of the disector volume. In three dimensions the unbiased sampling frame is an unbiased sampling volume with either the upper or lower optical section forming an exclusion plane (Gundersen, 1986; Gundersen et al., 1988a; West et al., 1991; West, 2013a; Mouton, 2014). This method requires accurate measurement of the z-direction within the section and use of a high-quality objective lens to minimize the thickness of the focal plane. Optical section thickness can be minimized in the confocal microscope making it ideally suited for the optical disector method (Peterson, 1999; Kubínová and Janáček, 2015). Detailed explanations of the optical disector method can be found in key stereological articles (West, 2013a; Mouton, 2014) and examples of its use in specific brain regions are numerous (West et al., 1991; Oorschot, 1996; Bonthius et al., 2004; Ash et al., 2014).

The disector method provides an unbiased estimate of total number within the disector volume sampled within the structure of interest. This is a measure of density (N_v) within the known disector volume but if the total volume of the structure is not known this can be misleading (Oorschot, 1994; Coggeshall and Lekan, 1996; Dumitriu et al., 2012; Ash et al., 2014). The volume of the brain region within which density is estimated may change due to tissue processing or many other factors and this change may be differential across experimental groups and to an unknown extent. The relationship between density and total number is unknown, thus making density a potentially misleading quantitative measure. This is avoided by determining the volume of the region of interest, the reference volume (Vref), within which the density is determined. These parameters can then be used to estimate the total number (N) where $N = N_v \times$ Vref. These methods are described in detail in many excellent sources (Gundersen et al., 1988b; West, 2013a; Mouton, 2014).

The removal of potential bias but also efficiency have been important concerns as stereological methods have continued to be developed (Gundersen and Jensen, 1987;

Gundersen et al., 1999; West, 1999, 2012; Hosseini-Sharifabad and Nyengaard, 2007). The unbiased sampling design of stereology, based on application of a set of uniform random points, enabled concurrent estimation of Vref during a disector estimation of density. This had the advantage that the estimate of total number (*N*) is not affected by any change in tissue volume as all the measurements are relative, are fractions (Gundersen et al., 1988a; West, 1993, 2002). The disector method, following a random systematic sampling design, estimates particle number (*N*) from the number of particles counted ($\sum Q^-$) in a known volume of tissue that is a known fraction (f) of the volume of region of interest (the Vref). The total number (*N*) of particles within the Vref is determined from the number of particles counted ($\sum Q^-$) and the inverse of the fraction (f), $N = \sum Q^- \times (1/f)$. The original method used the physical disector but with use of the optical disector the method became known as the optical fractionator (West et al., 1991; West, 2002; Hosseini-Sharifabad and Nyengaard, 2007) and is very widely used. Despite the unbiased nature of the disector method and the major advantages of using an estimate of total number, the methodology still contains potential sources of systematic bias. With increased use of the optical disector over the last decades the type of sections within which a disector density estimate is made has changed and become more diverse. Tissue deformation during sectioning and the potential loss of particles from the section surface are long standing issues, addressed by assigning an upper and lower guard to each section where particles were not counted (Gundersen, 1986; West et al., 1991). However, there is evidence of uneven section shrinkage in frozen sections, an increasingly common choice for optical disector studies (Bonthius et al., 2004; Carlo and Stevens, 2011; Puigdellívol-Sánchez et al., 2015) and of variable density along the z-axis in sections from a range of sectioning methods (Hatton and von Bartheld, 1999; Dorph-Petersen et al., 2001; Gardella et al., 2003; von Bartheld, 2012; West, 2013b). These potential sources of systematic bias are important and solutions such as using smaller counting frames that vary in position in the Z-axis, have been suggested as ways of achieving higher precision (Puigdellívol-Sánchez et al., 2015). Investigators should publish information on the tissue processing, embedding and cutting protocols used, alongside details of stereological sampling parameters so that results can be compared across research studies. Neuroscientists would benefit if journals insisted these parameters be included in publications as it would allow data to be more easily compared between studies. Other sources of potential bias, such as differences between experimenters in object or boundary identification can be minimized by including specific criteria used and photographic evidence (West et al., 1991; Gondré-Lewis et al., 2016). Immuno-labeling to phenotype particles of interest, can help identification but antibody penetration and labeling success in the z-axis direction must be assessed and reported (Ash et al., 2014). Despite the potential of errors within individual estimates of total number, total number remains superior to density estimates and can be combined with our knowledge of brain networks to develop quantitative networks at both cellular and synaptic levels of anatomically connected regions within the rodent brain. This type of network will enhance our understanding of the rodent and thus the human brain (Gulley and Juraska, 2013 and see DeFelipe, 2015; DeFelipe et al., 2016 for more detailed discussion).

TOTAL NUMBER—NOT VOLUME OR DENSITY—THE PAST

It has been over three decades since the original description of the disector method and the demonstration that volume and density on their own were of limited value in understanding the number of structures within a brain region. One of the most influential studies that emphasized the importance of using total number within a defined volume, not density, was an early study undertaken by stereologists on human brain tissue. A 40% decrease in total neuron number was found in the mediodorsal thalamic nucleus from schizophrenic patients compared to controls despite numerous previous studies reporting no change in density (Pakkenberg and Gundersen, 1989). The potential effect of a volume change on density had been ignored and misleading data resulted. Total number via a disector estimation, not an unbiased density estimate alone, has been the key major advance in understating the rodent brain in health and disease. An understanding of the value of total number estimates within a defined brain region has provided understanding of a key neuroscience dogma; "that cells are lost from the brain as it ages", which contained the implication that this occurred throughout the brain. This view had arisen because density estimates, made within unknown tissue volumes, had resulted in misleading data. Although there was no significant decrease in the total number of neocortical neurons in the aging human brain (Pakkenberg and Gundersen, 1997) neuronal deficits have been found in some specific cortical regions and layers and for some neuronal phenotypes during aging (Shi et al., 2006; Stranahan et al., 2012). It has also been found that there is an age-related decrease in the total number of granule and Purkinje cells in the anterior, but not posterior lobe, of the cerebellum (Andersen et al., 2003). This study also found the volume of the Purkinje cell perikarya decreased with aging, emphasizing the importance of the disector method in determining density without bias from cell size (Andersen et al., 2003). The lack of neuronal loss in the hippocampus and key output regions stimulated alternative areas of investigation on cognitive decline in aging (Merrill et al., 2001). Stereological quantitation combined with immuno-labeling found a specific loss of GAD67- and SOM-positive neurons in the hilar region of memory impaired rats but no decline in total number of NeuN labeled cells. This finding was instrumental in associating a loss of protein expression in the labeled cells with dysfunction suggesting therapeutic intervention may be possible (Spiegel et al., 2013). Concurrently the total number of glial cells in specific brain nuclei increases during aging stimulating further research on the role of glial cells as causative rather than reflective of brain changes (Rubinow and Juraska, 2009). It is clear that aging can alter the total number of neurons within specific brain regions but the important point is that use of the disector method, ensures that the density estimate is not biased by age-related particle size changes, plus the conversion of sample density to total number, accommodating

unknown regional volume change, has enabled the generation of reliable findings (Pakkenberg and Gundersen, 1989, 1997). Total number estimates within design-based stereological studies have contributed in past decades over the breadth of neuroscience to advance our understanding of Parkinson's and Huntington's disease (Arcuri et al., 2016), ischemeic brain injury (Avendaño et al., 1995; Mestriner et al., 2013), epilepsy (Foresti et al., 2009; Ye et al., 2013), schizophrenia (Kaalund et al., 2013), depression (Allard et al., 2004) and traumatic brain injury (Bregy et al., 2012; Cope et al., 2016) to name a few. Understanding injury in the developing brain has also been advanced by the use of total number with studies of hypoxic/ischemeic brain damage (Cameron et al., 2015), fetal alcohol spectrum disorder (Napper and West, 1995; Klintsova et al., 1997), maternal stress (Oreland et al., 2010) and a range of other prenatal insults (Smith et al., 2008; Sadowski et al., 2014). The endpoint of the majority of this research is to understand brain function. Thus, investigation of the total number of synapses in a brain region or on a specific type of neuron is as important as total cell number in understanding how neuronal populations interact within a network (DeFelipe, 2015). As mentioned previously, estimation of the total number of synapses with the disector method was rapidly adopted (Geinisman et al., 1992, 1996). Numerous studies have used disector estimates of total synapse number to investigate changes resulting from a number of phenomena including protein undernutrition (Lukoyanov and Andrade, 2000), hypothyroidism (Madeira and Paula-Barbosa, 1993), aging (Poe et al., 2001), epilepsy (Thind et al., 2010; Yamawaki et al., 2015), diabetes (Zhao et al., 2016) and in some cases the reversibility of synapse change (Lukoyanov and Andrade, 2000; Yamawaki et al., 2015). Studies have also indicated that an increase in the number of synapses occurs with a change in behavior (Klintsova et al., 1997; Hajszan et al., 2009; Dalzell et al., 2011; Jasinska et al., 2016). An important aspect of a disector estimate of total synapse number is that values obtained from control animals within any study can be used, due to the unbiased nature of the estimator, by other investigators to model and understand connectivity in the rodent brain (da Costa et al., 2009; Ciccarelli et al., 2012). Other provisos do affect how comparable such data sets are but when provisos are noted, total number becomes valuable to the global neuroscience community in a way density cannot be, even if obtained with the disector method.

TOTAL NUMBER—THE PRESENT

As indicated above the ways in which design-based stereological estimates of total number have contributed to our understanding of the rodent brain is immense but this may be under threat due to considerable pressure to generate data as efficiently as possible. Efficiency has always been a key focus of the expert stereologists who have driven the ongoing development of stereological methods (Nava et al., 2014) with research publications also stressing the efficiency of design-based stereology (West et al., 1991; Johnson, 2001; Zhu et al., 2015; Kelly and Hawken, 2017). However, a more recent method to obtain total number estimates, the "isotropic fractionator" is gaining popularity as studies show that under certain conditions it generates data comparable to stereological based total number estimates but in less time (Herculano-Houzel and Lent, 2005; Herculano-Houzel et al., 2015). However, this method has major limitations. One mentioned by Herculano-Houzel (2017), is that the process of homogenization destroys all information about the structural arrangement of cells within the tissue which is extremely important in understanding how function emanates from a biological region. Another serious limitation is that the brain region of interest must be accurately dissected out, prior to homogenization precluding obtaining information from small brain regions, layers and at an ultrastructural level (Fu et al., 2013). This may also result in considerable inter-investigator variability. If we consider that a key use of total number, obtained using design-based stereology, is to understand the relationship between cells, the quantitative network of the brain, this method will not deliver.

Immuno-labeling methods have been an essential tool in design-based stereological studies and have provided total number data on specific cell types (Mokin and Keifer, 2006; Prasad and Richfield, 2010). The continual development of imaging technologies and the minimal thickness of confocal imaging planes combined with immuno-labeling allows precise identification of molecular species and quantitation with a precision previously only possible in the electron microscope (Peterson, 1999). The use of transgenic mice is also an opportunity where design-based stereological determinations of total number could make a major contribution to understanding the phenotype of these animals and changes in brain structure and function (Berlanga et al., 2011; Manaye et al., 2013; Manaye and Mouton, 2014). However, despite many publications highlighting the "reference trap", the volume within which the disector estimate was made is not always determined and data is presented as "densities" which may be misleading, as discussed above (Siucinska et al., 2014; Woeffler-Maucler et al., 2014). It is also important to note that many of these studies do not report the use of systematic random sampling, a requirement of design-based stereology to ensure the estimate is representative of the whole tissue region, not just the sample area, despite this capability existing in most confocal imaging platforms. Neuroscience has already seen that biased data can direct science down false avenues and waste considerable research resources (Pakkenberg and Gundersen, 1989; Mura et al., 2004). It is also important to emphasize that the use of unbiased stereology to estimate total number is not as time consuming as naïve investigators may think (Gundersen and Osterby, 1981; Gundersen and Jensen, 1987; West et al., 1991; Brasnjevic et al., 2013; Wang et al., 2014).

TOTAL NUMBER—THE FUTURE

Faced with trying to understand the rodent brain, many neuroscientists consider that the total number of neurons/synapses is important and that reliable estimates of such values are an essential requirement of quantitative neuroscience.

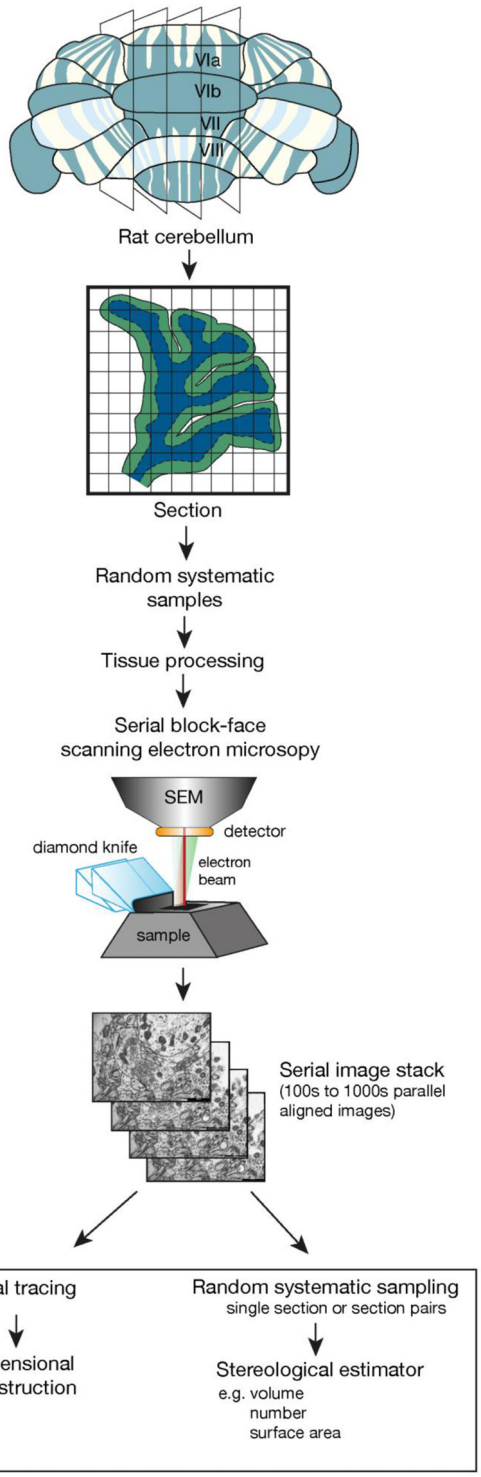

FIGURE 1 | The flow diagram outlines the essential steps involved in taking a tissue sample, using random systematic sampling methodology, to the final stage of using stereological sampling probes on sections or section pairs taken from a stack of sections imaged using serial block face scanning electron microscopy. This could also be accomplished using focused ion beam scanning electron microscopy (FIB-SEM). Key elements in this design (*Continued*)

FIGURE 1 | Continued
are the generation of parallel sections followed by random systematic sampling to obtain tissue samples for tissue processing and electron microscopic investigation. Random systematic sampling would then be used to obtain the sampling location within the scanning electron microscope. The cube of tissue and the number of samples imaged would be experiment dependent but each imaging location would generate a set of serial, perfectly aligned sections that could then be used with a range of stereological estimators.

Numerous studies have used design-based stereology to enable a better understanding of the correlation of structure with function (Hédou et al., 2002; Schmitz and Hof, 2005; Zhao et al., 2016). The rapidly growing area of connectomics, previously known as neuroanatomical connections, is focused on the production of a map of connections within a specific brain region at a cellular or subcellular level (Mikula, 2016; Swanson and Lichtman, 2016). However, whether specific network arrangements can be generalized to apply across an entire brain region or between species is an area of current debate and alternative methods of assessing brain networks need to be considered (Luebke, 2017). One potential method is to use estimates of total number, of either cells or synapses within defined brain regions, from unbiased stereological estimates to establish quantitative networks at macro and micro levels (for a wider discussion of understanding of the brain as circuits see DeFelipe et al., 2016). I have suggested that the rodent brain can be considered as a distributed network with many discrete regional networks interacting to produce an immense spectrum of behavior (Koob and Volkow, 2016; Herculano-Houzel, 2017) and at each level this network is a quantitative network at a cellular and synaptic level. If all neuroscientists produced unbiased total number estimates as the key quantitative parameter this data would form the basis of a valuable data set for the construction of quantitative networks.

Estimates of total synapse number obtained with the disector method have contributed to our understanding of network interactions in the rodent brain. This has always been technically demanding and time consuming but we are now poised with recent technical developments in electron microscopy to revolutionize the generation of quantitative synapse data. Serial block face scanning electron microscopy (SBF-SEM) and focused ion beam SEM (FIB-SEM) enable the collection of large three-dimensional data sets of nervous tissue components, at high resolution, in the electron microscope with an efficiency incomprehensible compared to conventional serial sectioning (Kim et al., 2013; Wu et al., 2017). In both SBF-SEM and FIB-SEM the high energy electrons originating in the electron beam reflected from the specimen volume (the tissue in the resin block) are captured to form the image. After each image is captured, a thin layer is removed from the block face, equivalent to or considerably less than the thickness of a conventional thin section, and the resulting new face is re-imaged. The direct imaging of the block face avoids the deformation and loss of sections that is common when images are collected from serial sections and images are sequentially built up in near perfect alignment. A set of

images can be collected in a fully automated manner that previously required several years of painstaking highly skilled work (Merchán-Pérez et al., 2009; Peddie and Collinson, 2014; Wu et al., 2017). This volume of tissue generated can then be sampled using unbiased stereological methods as if it were a physical tissue block, and quantitative estimates of a range of parameters can be obtained as outlined in **Figure 1** (Ferguson et al., 2017). An added value is that the three-dimensional reconstruction of components within the tissue volume enables the investigator to verify the appearance of a structure in single sections ensuring a high degree of accuracy in profile identification (see Harris et al., 2015 for further details). Validation of stereological estimates has always required comparisons with total number from reconstruction studies and this is now feasible on the ultrastructural level (Delaloye et al., 2009).

The potential use of stereological tools on SBF-SEM image stacks can be seen by considering a recent article that investigated the effects of a selective serotonin reuptake inhibitor on the dentate gyrus granule cells (Kitahara et al., 2016). It found a significant increase in extremely large spines, without an increase in spine density. The increase in spine size was accompanied by an increased postsynaptic density that correlated with an increase in volume of the presynaptic bouton and the volumes of mitochondria and synaptic vesicles within it. Potential evidence of a structural change supporting the enhanced glutamatergic neurotransmission was also detected.

Although this article used 3-dimensional reconstruction to obtain the data, stereological tools for estimating volume and surface area could be obtained in combination with the disector method for particle selection and provide data equivalent to that obtained via detailed reconstruction (Kitahara et al., 2016). It is important that we consider the use of SBF-SEM and FIB-SEM in combination with design-based stereology to advance our understanding of the ultrastructure of nervous tissue (Waworuntu et al., 2016). Ongoing developments in the capture of high resolution images and in the methods of reconstruction and optimization of images, will ensure that in the near future this is a very efficient process (Bellesi et al., 2015; Borrett and Hughes, 2016; Nguyen et al., 2016; Wernitznig et al., 2016).

CONCLUSION

In order to understand the information processing in the rodent brain that underlies behavior, it is essential to understand the connectivity between neurons and synapses across a huge number of different microcircuits (Dennis and Thompson, 2013; Kelly and Castellanos, 2014; Mátyás et al., 2014). Estimates of total number, obtained using the disector method within design based stereological studies, allows the brain to be viewed as a network composed of many nodes that are each a complex of subnetworks. We are making advances in understanding the complexity of brain networks with the 3-dimensional reconstruction studies undertaken for connectomic analysis but it is also apparent that networks are location specific. If all estimates of cell and synapse number were obtained as total number from design-based stereological studies this data could be used collectively to advance our understanding of the networks of the rodent brain that underlie function and dysfunction. We must always remember the seminal work that demonstrated density as a potentially misleading quantity and be aware that the quality of the imaging technology used to obtain density does not alter the fact that it is a density and is potentially misleading. Conversations about the merits of using total number estimates obtained within design-based stereological studies vs. other methods must be held within the neuroscience community and we should strive to produce the most reliable data possible. The generation of data that can be used universally, such as total number estimates will enable greater advances in understanding the rodent and subsequently the human brain to be made.

AUTHOR CONTRIBUTIONS

The author confirms being the sole contributor of this work and approved it for publication.

REFERENCES

Allard, J. S., Tizabi, Y., Shaffery, J. P., Trouth, C. O., and Manaye, K. (2004). Stereological analysis of the hypothalamic hypocretin/orexin neurons in an animal model of depression. *Neuropeptides* 38, 311–315. doi: 10.1016/j.npep.2004.06.004

Andersen, B. B., Gundersen, H. J., and Pakkenberg, B. (2003). Aging of the humancerebellum: a stereological study. *J. Comp. Neurol.* 466, 356–365. doi: 10.1002/cne.10884

Arcuri, L., Viaro, R., Bido, S., Longo, F., Calcagno, M., Fernagut, P. O., et al. (2016). Genetic and pharmacological evidence that endogenous nociceptin/orphanin FQ contributes to dopamine cell loss in Parkinson's disease. *Neurobiol. Dis.* 89, 55–64. doi: 10.1016/j.nbd.2016.01.016

Ash, J. A., Velazquez, R., Kelley, C. M., Powers, B. E., Ginsberg, S. D., Mufson, E. J., et al. (2014). Maternal choline supplementation improves spatial mapping and increases basalforebrain cholinergic neuron number and size in aged Ts65Dn mice. *Neurobiol. Dis.* 70, 32–42. doi: 10.1016/j.nbd.2014.06.001

Avendaño, C., Roda, J. M., Carceller, F., and Díez-Tejedor, E. (1995). Morphometric study of focal cerebral ischemia in rats: a stereological evaluation. *Brain Res.* 1995, 83–92. doi: 10.1016/0006-8993(94)01407-9

Barbas, H. (2015). General cortical and special prefrontal connections: principles from structure to function. *Annu. Rev. Neurosci.* 38, 269–289. doi: 10.1146/annurev-neuro-071714-033936

Bellesi, M., de Vivo, L., Tononi, G., and Cirelli, C. (2015). Effects of sleep and wake on astrocytes: clues from molecular and ultrastructural studies. *BMC Biol.* 13:66. doi: 10.1186/s12915-015-0176-7

Berlanga, M. L., Price, D. L., Phung, B. S., Giuly, R., Terada, M., Yamada, N., et al. (2011). Multiscale imaging characterization of dopamine transporter knockout micereveals regional alterations in spine density of medium spiny neurons. *Brain Res.* 1390, 41–49. doi: 10.1016/j.brainres.2011.03.044

Bohland, J. W., Wu, C., Barbas, H., Bokil, H., Bota, M., Breiter, H. C., et al. (2009). A proposal for a coordinated effort for the determination of brainwide neuroanatomicalconnectivity in model organisms at a mesoscopic scale. *PLoS Comput. Biol.* 5:e1000334. doi: 10.1371/journal.pcbi.1000334

Bonthius, D. J., McKim, R., Koele, L., Harb, H., Karacay, B., Mahoney, J., et al. (2004). Use offrozen sections to determine neuronal number in the murine hippocampus and neocortex using the optical disector and optical fractionator. *Brain Res. Protoc.* 14, 45–57. doi: 10.1016/j.brainresprot.2004.09.003

Borrett, S., and Hughes, L. (2016). Reporting methods for processing and analysis of data from serial block face scanning electron microscopy. *J. Microsc.* 263, 3–9. doi: 10.1111/jmi.12377

Brasnjevic, I., Lardenoije, R., Schmitz, C., Van Der Kolk, N., Dickstein, D. L., Takahashi, H., et al. (2013). Region-specific neuron and synapse loss in the hippocampus of Appsl/Ps1 knock-in mice. *Transl. Neurosci.* 4, 8–19. doi: 10.2478/s13380-013-0111-8

Bregy, A., Nixon, R., Lotocki, G., Alonso, O. F., Atkins, C. M., Tsoulfas, P., et al. (2012). Posttraumatic hypothermia increases doublecortin expressing neurons in the dentate gyrus after traumatic brain injury in the rat. *Exp. Neurol.* 233, 821–828. doi: 10.1016/j.expneurol.2011.12.008

Calverley, R. K. S., Bedi, K. S., and Jones, D. G. (1988). Estimation of the numerical density of synapses in rat neocortex. *J. Neurosci. Methods* 23, 195–205. doi: 10.1016/0165-0270(88)90003-9

Calverley, R. K. S., and Jones, D. G. (1987). Determination of the numerical density of perforated synapses in rat neocortex. *Cell Tissue Res.* 248, 399–407. doi: 10.1007/bf00218208

Cameron, S. H., Alwakeel, A. J., Goddard, L., Hobbs, C. E., Gowing, E. K., Barnett, E. R., et al. (2015). Delayed post-treatment with bone marrow-derived mesenchymal stemcells is neurorestorative of striatal medium-spiny projection neurons and improves motor function after neonatal rat hypoxia-ischemia. *Mol. Cell. Neurosci.* 68, 56–72. doi: 10.1016/j.mcn.2015.03.019

Carlo, C. N., and Stevens, C. F. (2011). Analysis of differential shrinkage in frozen brain sections and its implications for the use of guard zones in stereology. *J. Comp. Neurol.* 519, 2803–2810. doi: 10.1002/cne.22652

Ciccarelli, A., Calza, A., Panzanelli, P., Concas, A., Giustetto, M., and Sassoè-Pognetto, M. (2012). Organization of GABAergic synaptic circuits in the rat ventral tegmental area. *PLoS One* 7:e46250. doi: 10.1371/journal.pone.0046250

Coggeshall, R. E., and Lekan, H. A. (1996). Methods for determining numbers of cells andsynapses: a case for more uniform standards of review. *J. Comp. Neurol.* 364, 6–15. doi: 10.1002/(sici)1096-9861(19960101)364:1<6::aid-cne2>3.3.co;2-i

Cope, E. C., Morris, D. R., Gower-Winter, S. D., Brownstein, N. C., and Levenson, C. W. (2016). Effect of zinc supplementation on neuronal precursor proliferation in the rathippocampus after traumatic brain injury. *Exp. Neurol.* 279, 96–103. doi: 10.1016/j.expneurol.2016.02.017

da Costa, N. M., Hepp, K., and Martin, K. A. (2009). A systematic random sampling scheme optimized to detect the proportion of rare synapses in the neuropil. *J. Neurosci. Methods* 180, 77–81. doi: 10.1016/j.jneumeth.2009.03.001

Dalzell, L., Connor, S., Penner, M., Saari, M. J., Leboutillier, J. C., and Weeks, A. C. (2011). Fear conditioning is associated with synaptogenesis in the lateral amygdala. *Synapse* 65, 513–519. doi: 10.1002/syn.20869

DeFelipe, J. (2015). The anatomical problem posed by brain complexity and size: a potential solution. *Front. Neuroanat.* 9:104. doi: 10.3389/fnana.2015.00104

DeFelipe, J., Douglas, R. J., Hill, S. L., Lein, E. S., Martin, K. A., Rockland, K. S., et al. (2016). Comments and general discussion on "the anatomical problem posed by braincomplexity and size: a potential solution". *Front. Neuroanat.* 10:60. doi: 10.3389/fnana.2016.00060

Delaloye, S., Kraftsik, R., Kuntzer, T., and Barakat-Walter, I. (2009). Does the physicaldisector method provide an accurate estimation of sensory neuron number in rat dorsal root ganglia? *J. Neurosci. Methods* 176, 290–297. doi: 10.1016/j.jneumeth.2008.09.004

Dennis, E. L., and Thompson, P. M. (2013). Mapping connectivity in the developing brain. *Int. J. Dev. Neurosci.* 31, 525–542. doi: 10.1016/j.ijdevneu.2013.05.007

Dorph-Petersen, K. A., Nyengaard, J. R., and Gundersen, H. J. G. (2001). Tissue shrinkage and unbiased stereological estimation of particle number and size. *J. Microsc.* 204, 232–246. doi: 10.1046/j.1365-2818.2001.00958.x

Dumitriu, D., Berger, S. I., Hamo, C., Hara, Y., Bailey, M., Hamo, A., et al. (2012). Vamping: stereology-based automated quantification of fluorescent puncta size and density. *J. Neurosci. Methods* 209, 97–105. doi: 10.1016/j.jneumeth.2012.05.031

Ferguson, S., Steyer, A. M., Mayhew, T. M., Schwab, Y., and Lucocq, J. M. (2017). Quantifying Golgi structure using EM: combining volume-SEM and stereology for higher throughput. *Histochem. Cell Biol.* 147, 653–669. doi: 10.1007/s00418-017-1564-6

Finlay, B. L. (2016). Principles of network architecture emerging from comparisons of the cerebral cortex in large and small brains. *PLoS Biol.* 14:e1002556. doi: 10.1371/journal.pbio.1002556

Foresti, M. L., Arisi, G. M., Katki, K., Montañez, A., Sanchez, R. M., and Shapiro, L. A. (2009). Chemokine CCL2 and its receptor CCR2 are increased in the hippocampusfollowing pilocarpine-induced status epilepticus. *J. Neuroinflammation* 6:40. doi: 10.1186/1742-2094-6-40

Fu, Y., Rusznak, Z., Herculano-Houzel, S., Watson, C., and Paxinos, G. (2013). Cellular composition characterizing postnatal development and maturation of the mouse brain and spinal cord. *Brain Struct. Funct.* 218, 1337–1354. doi: 10.1007/s00429-012-0462-x

Gardella, D., Hatton, W. J., Rind, H. B., Rosen, G. D., and von Bartheld, C. S. (2003). Differential tissue shrinkage and compression in the z-axis: implications foroptical disector counting in vibratome-, plastic- and cryosections. *J. Neurosci. Methods* 124, 45–59. doi: 10.1016/s0165-0270(02)00363-1

Geinisman, Y., deToledo-Morrell, L., Morrell, F., Persina, I. S., and Rossi, M. (1992). Age- related loss of axospinous synapses formed by two afferent systems in the rat dentate gyrus as revealed by the unbiased stereological disector technique. *Hippocampus* 2, 437–444. doi: 10.1002/hipo.450020411

Geinisman, Y., Gundersen, H. J., van der Zee, E., and West, M. J. (1996). Unbiasedstereological estimation of the total number of synapses in a brain region. *J. Neurocytol.* 25, 805–819. doi: 10.1007/bf02284843

Gondré-Lewis, M. C., Darius, P. J., Wang, H., and Allard, J. S. (2016). Stereological analysesof reward system nuclei in maternally deprived/separated alcohol drinking rats. *J. Chem. Neuroanat.* 76, 122–132. doi: 10.1016/j.jchemneu.2016.02.004

Gulley, J. M., and Juraska, J. M. (2013). The effects of abused drugs on adolescent development of corticolimbic circuitry and behavior. *Neuroscience* 249, 3–20. doi: 10.1016/j.neuroscience.2013.05.026

Gundersen, H. J. G. (1986). Stereology of arbitrary particles. A review of unbiased number and size estimators and the presentation of some new ones, in memory of William R. Thompson. *J. Microsc.* 143, 3–45. doi: 10.1111/j.1365-2818.1986.tb02764.x

Gundersen, H. J. G., Bagger, P., Bendtsen, T. F., Evans, S. M., Korbo, L., Marcussen, N., et al. (1988a). The new stereological tools: disector, fractionator, nucleator and point sampled intercepts and their use in pathological research and diagnosis. *APMIS* 96, 857–881. doi: 10.1111/j.1699-0463.1988.tb00954.x

Gundersen, H. J. G., Bendtsen, T. F., Korbo, L., Marcussen, N., Møller, A., Nielsen, K., et al. (1988b). Some new, simple and efficient stereological methods and their use in pathological research and diagnosis. *APMIS* 96, 379–394. doi: 10.1111/j.1699-0463.1988.tb05320.x

Gundersen, H. J. G., and Jensen, E. B. (1987). The efficiency of systematic sampling in stereology and its predicition. *J. Microsc.* 147, 229–263. doi: 10.1111/j.1365-2818.1987.tb02837.x

Gundersen, H. J. G., Jensen, E. B. V., Kiêu, K., and Nielsen, J. (1999). The efficiency of systematic sampling in stereology—reconsidered. *J. Microsc.* 193, 199–211. doi: 10.1046/j.1365-2818.1999.00457.x

Gundersen, H. J. G., and Osterby, R. (1981). Optimizing sampling efficiency of stereologicalstudies in biology: of 'Do more less well!'. *J. Microsc.* 121, 65–73. doi: 10.1111/j.1365-2818.1981.tb01199.x

Hajszan, T., Dow, A., Warner-Schmidt, J. L., Szigeti-Buck, K., Sallam, N. L., Parducz, A., et al. (2009). Remodeling of hippocampal spine synapses in the rat learned helplessness model of depression. *Biol. Psychiatry* 65, 392–400. doi: 10.1016/j.biopsych.2008.09.031

Harris, K. M., Spacek, J., Bell, M. E., Parker, P. H., Lindsey, L. F., Baden, A. D., et al. (2015). Aresource from 3D electron microscopy of hippocampal neuropil for user training and tool development. *Sci. Data* 2:150046. doi: 10.1038/sdata.2015.46

Hatton, W. J., and von Bartheld, C. S. (1999). Analysis of cell death in the trochlear nucleus of the chick embryo: calibration of the optical disector countingmethod reveals systematic bias. *J. Comp. Neurol.* 409, 169–186. doi: 10.1002/(sici)1096-9861(19990628)409:2<169::aid-cne1>3.3.co;2-f

Hédou, G., Jongen-Rêlo, A. L., Murphy, C. A., Heidbreder, C. A., and Feldon, J. (2002). Sensitized Fos expression in subterritories of the rat medial prefrontal cortex and nucleus accumbens following amphetamine sensitization as revealed by stereology. *Brain Res.* 950, 165–179. doi: 10.1016/s0006-8993(02)03034-2

Herculano-Houzel, S. (2017). Numbers of neurons as biological correlates of cognitive capability. *Curr. Opin. Behav. Sci.* 16, 1–7. doi: 10.1016/j.cobeha.2017.02.004

Herculano-Houzel, S., and Lent, R. (2005). Isotropic fractionator: a simple, rapid methodfor the quantification of total cell and neuron numbers in the brain. *J. Neurosci.* 25, 2518–2521. doi: 10.1523/JNEUROSCI.4526-04.2005

Herculano-Houzel, S., von Bartheld, C. S., Miller, D. J., and Kaas, J. H. (2015). How to count cells: the advantages and disadvantages of the isotropic fractionator compared with stereology. *Cell Tissue Res.* 360, 29–42. doi: 10.1007/s00441-015-2127-6

Hosseini-Sharifabad, M., and Nyengaard, J. R. (2007). Design-based estimation of neuronal number and individual neuronal volume in the rat hippocampus. *J. Neurosci. Methods* 162, 206–214. doi: 10.1016/j.jneumeth.2007.01.009

Howard, V., and Reed, M. G. (2005). *Unbiased Stereology: Three-Dimensional Measurement in Microscopy*. New York, NY: Garland Science/BIOS Scientific Publishers.

Jasinska, M., Siucinska, E., Jasek, E., Litwin, J. A., Pyza, E., and Kossut, M. (2016). Effect of associative learning on memory spine formation in mouse barrel cortex. *Neural Plast.* 2016:9828517. doi: 10.1155/2016/9828517

Johnson, I. P. (2001). Rapid estimates of neuron number in the confocal microscope combined with *in situ* hybridisation and immunocytochemistry. *Brain Res. Protoc.* 8, 113–125. doi: 10.1016/s1385-299x(01)00079-4

Kaalund, S. S., Riise, J., Broberg, B. V., Fabricius, K., Karlsen, A. S., Secher, T., et al. (2013). Differential expression of parvalbumin in neonatal phencyclidine-treated ratsand socially isolated rats. *J. Neurochem.* 124, 548–557. doi: 10.1111/jnc.12061

Kelly, C., and Castellanos, F. X. (2014). Strengthening connections: functional connectivity and brain plasticity. *Neuropsychol. Rev.* 24, 63–76. doi: 10.1007/s11065-014-9252-y

Kelly, J. G., and Hawken, M. J. (2017). Quantification of neuronal density across cortical depth using automated 3D analysis of confocal image stacks. *Brain Struct. Funct.* 222, 3333–3353. doi: 10.1007/s00429-017-1382-6

Kim, H. W., Kim, N., Kim, K. W., and Rhyu, I. J. (2013). Three-dimensional imaging of cerebellar mossy fiber rosettes by ion-abrasion scanning electron microscopy. *Microsc. Microanal.* 19, 172–177. doi: 10.1017/s1431927613012609

Kitahara, Y., Ohta, K., Hasuo, H., Shuto, T., Kuroiwa, M., Sotogaku, N., et al. (2016). Chronic fluoxetine induces the enlargement of perforant path-granule cellsynapses in the mouse dentate gyrus. *PLoS One* 11:e0147307. doi: 10.1371/journal.pone.0147307

Klintsova, A. Y., Matthews, J. T., Goodlett, C. R., Napper, R. M., and Greenough, W. T. (1997). Therapeutic motor training increases parallel fiber synapse number per Purkinje neuron in cerebellar cortex of rats given postnatal binge alcohol exposure: preliminary report. *Alcohol. Clin. Exp. Res.* 21, 1257–1263. doi: 10.1111/j.1530-0277.1997.tb04446.x

Koob, G. F., and Volkow, N. D. (2016). Neurobiology of addiction: a neurocircuitry analysis. *Lancet Psychiatry* 3, 760–773. doi: 10.1016/s2215-0366(16)00104-8

Kubínová, L., and Janáček, J. (2015). Confocal stereology: an efficient tool for measurement of microscopic structures. *Cell Tissue Res.* 360, 13–28. doi: 10.1007/s00441-015-2138-3

Li, M., Liu, J., and Tsien, J. Z. (2016). Theory of connectivity: nature and nurture of cell assemblies and cognitive computation. *Front. Neural Circuits* 10:34. doi: 10.3389/fncir.2016.00034

Luebke, J. I. (2017). Pyramidal neurons are not generalizable building blocks of cortical networks. *Front. Neuroanat.* 11:11. doi: 10.3389/fnana.2017.00011

Lukoyanov, N. V., and Andrade, J. P. (2000). Behavioral effects of protein deprivation and rehabilitation in adult rats: relevance to morphological alterations in the hippocampal formation. *Beh. Brain Res.* 112, 85–97. doi: 10.1016/s0166-4328(00)00164-9

Madeira, M. D., and Paula-Barbosa, M. M. (1993). Reorganization of mossy fiber synapses in male and female hypothyroid rats: a stereological study. *J. Comp. Neurol.* 337, 334–352. doi: 10.1002/cne.903370213

Manaye, K. F., and Mouton, P. R. (2014). "AD-type neuron loss in transgenic mouse models," in *Neurostereology*, ed. P. R. Mouton (Boston, MA: Wiley-Blackwell Press), 177–190.

Manaye, K. F., Mouton, P. R., Xu, G., Drew, A., Lei, D. L., Sharma, Y., et al. (2013). Age- related loss of noradrenergic neurons in the brains of triple transgenic mice. *Age (Dordr)* 35, 139–147. doi: 10.1007/s11357-011-9343-0

Mátyás, F., Lee, J., Shin, H. S., and Acsády, L. (2014). The fear circuit of the mouse forebrain: connections between the mediodorsal thalamus, frontal cortices and basolateral amygdala. *Eur. J. Neurosci.* 39, 1810–1823. doi: 10.1111/ejn.12610

Merchán-Pérez, A., Rodriguez, J. R., Alonso-Nanclares, L., Schertel, A., and Defelipe, J. (2009). Counting synapses using FIB/SEM microscopy: a true revolution for ultrastructural volume reconstruction. *Front. Neuroanat.* 3:18. doi: 10.3389/neuro.05.018.2009

Merrill, D. A., Chiba, A. A., and Tuszynski, M. H. (2001). Conservation of neuronal numberand size in entorhinal cortex of behaviorally characterized aged rats. *J. Comp. Neurol.* 438, 445–456. doi: 10.1002/cne.1327

Mestriner, R. G., Miguel, P. M., Bagatini, P. B., Saur, L., Boisserand, L. S., Baptista, P. P., et al. (2013). Behavior outcome after ischemic and hemorrhagic stroke, with similar brain damage, in rats. *Behav. Brain Res.* 244, 82–89. doi: 10.1016/j.bbr.2013.02.001

Mikula, S. (2016). Progress towards mammalian whole-brain cellular connectomics. *Front. Neuroanat.* 10:62. doi: 10.3389/fnana.2016.00062

Mokin, M., and Keifer, J. (2006). Quantitative analysis of immunofluorescent punctate staining of synaptically localized proteins using confocal microscopy and stereology. *J. Neurosci. Methods* 157, 218–224. doi: 10.1016/j.jneumeth.2006.04.016

Mouton, P. R. (2014). *Neurostereology: Unbiased Stereology of Neural Systems*. New York, NY: United States: John Wiley and Sons Inc.

Mulders, W. H. A. M., West, M. J., and Slomianka, L. (1997). Neuron numbers in the presubiculum, parasubiculum and entorhinal area of the rat. *J. Comp. Neurol.* 385, 83–94. doi: 10.1002/(sici)1096-9861(19970818)385:1<83::aid-cne5>3.0.co;2-8

Mura, A., Murphy, C. A., Feldon, J., and Jongen-Relo, A. L. (2004). The use of stereologicalcounting methods to assess immediate early gene immunoreactivity. *Brain Res.* 1009, 120–128. doi: 10.1016/j.brainres.2004.02.054

Napper, R. M., and West, J. R. (1995). Permanent neuronal cell loss in the cerebellum ofrats exposed to continuous low blood alcohol levels during the brain growth spurt: a stereological investigation. *J. Comp. Neurol.* 362, 283–292. doi: 10.1002/cne.903620210

Nava, N., Chen, F., Wegener, G., Popoli, M., and Nyengaard, J. R. (2014). A new efficient method for synaptic vesicle quantification reveals differences between medial prefrontal cortex perforated and nonperforated synapses. *J. Comp. Neurol.* 522, 284–297. doi: 10.1002/cne.23482

Nestler, E. J., and Hyman, S. E. (2010). Animal models of neuropsychiatric disorders. *Nat. Neurosci.* 13, 1161–1169. doi: 10.1038/nn.2647

Nguyen, H. B., Thai, T. Q., Saitoh, S., Wu, B., Saitoh, Y., Shimo, S., et al. (2016). Conductiveresins improve charging and resolution of acquired images in electron microscopic volume imaging. *Sci. Rep.* 6:23721. doi: 10.1038/srep23721

Oorschot, D. E. (1994). Are you using neuronal densitites, synaptic densities orneurochemical densities as your definitive data? There is a better way to go. *Prog. Neurobiol.* 44, 233–247. doi: 10.1016/0301-0082(94)90040-x

Oorschot, D. E. (1996). Total number of neurons in the neostriatal, pallidal, subthalamic,and substantia nigral nuclei of the rat basal ganglia: a stereological study using the cavalieri and optical disector methods. *J. Comp. Neurol.* 366, 580–599. doi: 10.1002/(sici)1096-9861(19960318)366:4<580::aid-cne3>3.0.co;2-0

Oreland, S., Nylander, I., and Pickering, C. (2010). Prolonged maternal separation decreases granule cell number in the dentate gyrus of 3-week-old male rats. *Int. J. Dev. Neurosci.* 28, 139–144. doi: 10.1016/j.ijdevneu.2009.12.005

Pakkenberg, B., and Gundersen, H. J. G. (1989). New stereological method for obtaining unbiased and efficient estimates of total nerve cell number in human brain areas. Exemplified by the mediodorsal thalamic nucleus in schizophrenics. *APMIS* 97, 677–681. doi: 10.1111/j.1699-0463.1989.tb00462.x

Pakkenberg, B., and Gundersen, H. J. G. (1997). Neocortical neuron number in humans: effect of sex and age. *J. Comp. Neurol.* 384, 312–320. doi: 10.1002/(sici)1096-9861(19970728)384:2<312::aid-cne10>3.3.co;2-g

Park, J., and Ahmad, S. O. (2014). "2D and 3D morphometric analyses comparing three rodent models," in *Neurostereology: Unbiased Stereology of Neural Systems*, ed. P. R. Mouton (Hoboken, NJ: John Wiley and Sons, Inc.), 221–236.

Peddie, C. J., and Collinson, L. M. (2014). Exploring the third dimension: volume electron microscopy comes of age. *Micron* 61, 9–19. doi: 10.1016/j.micron.2014.01.009

Peterson, D. A. (1999). Quantitative histology using confocal microscopy: implementation of unbiased stereology procedures. *Methods* 18, 493–507. doi: 10.1006/meth.1999.0818

Poe, B. H., Linville, C., and Brunso-Bechtold, J. (2001). Age-related decline of presumptive inhibitory synapses in the sensorimotor cortex as revealed by the physical disector. *J. Comp. Neurol.* 439, 65–72. doi: 10.1002/cne.1335

Prasad, K., and Richfield, E. K. (2010). Number and nuclear morphology of TH^+ and TH-neurons in the mouse ventral midbrain using epifluorescence stereology. *Exp. Neurol.* 225, 328–340. doi: 10.1016/j.expneurol.2010.07.004

Puigdellívol-Sánchez, A., Giralt, A., Casanovas, A., Alberch, J., and Prats-Galino, A. (2015). Cryostat slice irregularities may introduce bias in tissue thickness estimation: relevance for cell counting methods. *Microsc. Microanal.* 21, 893–901. doi: 10.1017/s143192761501380x

Rubinow, M. J., and Juraska, J. M. (2009). Neuron and glia numbers in the basolateralnucleus of the amygdala from preweaning through old age in male and female rats: a stereological study. *J. Comp. Neurol.* 512, 717–725. doi: 10.1002/cne.21924

Sadowski, R. N., Wise, L. M., Park, P. Y., Schantz, S. L., and Juraska, J. M. (2014). Early exposure to bisphenol A alters neuron and glia number in the rat prefrontal cortex of adult males, but not females. *Neuroscience* 279, 122–131. doi: 10.1016/j.neuroscience.2014.08.038

Schmitz, C., and Hof, P. R. (2005). Design-based stereology in neuroscience. *Neuroscience* 130, 813–831. doi: 10.1016/j.neuroscience.2004.08.050

Shi, L., Pang, H., Linville, M. C., Bartley, A. N., Argenta, A. E., and Brunso-Bechtold, J. K. (2006). Maintenance of inhibitory interneurons and boutons in sensorimotor cortex between middle and old age in Fischer 344 X Brown Norway rats. *J. Chem. Neuroanat.* 32, 46–53. doi: 10.1016/j.jchemneu.2006.04.001

Siucinska, E., Hamed, A., and Jasinska, M. (2014). Increases in the numerical density of GAT-1 positive puncta in the barrel cortex of adult mice after fear conditioning. *PLoS One* 9:e110493. doi: 10.1371/journal.pone.0110493

Smith, A. M., Pappalardo, D., and Chen, W. J. (2008). Estimation of neuronal numbers in rat hippocampus following neonatal amphetamine exposure: a stereology study. *Neurotoxicol. Teratol.* 30, 495–502. doi: 10.1016/j.ntt.2008.05.001

Spiegel, A. M., Koh, M. T., Vogt, N. M., Rapp, P. R., and Gallagher, M. (2013). Hilar interneuron vulnerability distinguishes aged rats with memory impairment. *J. Comp. Neurol.* 521, 3508–3523. doi: 10.1002/cne.23367

Sterio, D. C. (1984). The unbiased estimation of number and sizes of arbitrary particles using the disector. *J. Microsc.* 134, 127–136. doi: 10.1111/j.1365-2818.1984.tb02501.x

Stranahan, A. M., Jiam, N. T., Spiegel, A. M., and Gallagher, M. (2012). Aging reduces total neuron number in the dorsal component of the rodent prefrontal cortex. *J. Comp. Neurol.* 520, 1318–1326. doi: 10.1002/cne.22790

Swanson, L. W., and Lichtman, J. W. (2016). From cajal to connectome and beyond. *Annu. Rev. Neurosci.* 39, 197–216. doi: 10.1146/annurev-neuro-071714-033954

Thind, K. K., Yamawaki, R., Phanwar, I., Zhang, G., Wen, X., and Buckmaster, P. S. (2010). Initial loss but later excess of GABAergic synapses with dentate granule cells in a rat model of temporal lobe epilepsy. *J. Comp. Neurol.* 518, 647–667. doi: 10.1002/cne.22235

von Bartheld, C. S. (2012). Distribution of particles in the Z-axis of tissue sections: relevance for counting methods. *Neuroquantology* 10, 66–75. doi: 10.14704/nq.2012.10.1.431

Wang, H., Wang, R., Xu, S., and Lakshmana, M. K. (2014). RanBP9 overexpression accelerates loss of pre and postsynaptic proteins in the APDeltaE9 transgenic mouse brain. *PLoS One* 9:e85484. doi: 10.1371/journal.pone.0085484

Waworuntu, R. V., Hanania, T., Boikess, S. R., Rex, C. S., and Berg, B. M. (2016). Early life diet containing prebiotics and bioactive whey protein fractions increased dendritic spine density of rat hippocampal neurons. *Int. J. Dev. Neurosci.* 55, 28–33. doi: 10.1016/j.ijdevneu.2016.09.001

Wernitznig, S., Sele, M., Urschler, M., Zankel, A., Pölt, P., Rind, F. C., et al. (2016). Optimizing the 3D-reconstruction technique for serial block-face scanning electron microscopy. *J. Neurosci. Methods* 264, 16–24. doi: 10.1016/j.jneumeth.2016.02.019

West, M. J. (1993). New stereological methods for counting neurons. *Neurobiol. Aging* 14, 275–285. doi: 10.1016/0197-4580(93)90112-o

West, M. J. (1999). Stereological methods for estimating the total number of neurons and synapses: issues of precision and bias. *Trends Neurosci.* 22, 51–61. doi: 10.1016/s0166-2236(98)01362-9

West, M. J. (2002). Design-based stereological methods for counting neurons. *Prog. Brain Res.* 135, 43–51. doi: 10.1016/s0079-6123(02)35006-4

West, M. J. (2012). *Basic Stereology for Biologists and Neuroscientists.* New York, NY: Cold Spring Harbor, Laboratory Press.

West, M. J. (2013a). Getting started in stereology. *Cold Spring Harb. Protoc.* 2013, 287–297. doi: 10.1101/pdb.top071845

West, M. J. (2013b). Tissue shrinkage and stereological studies. *Cold Spring Harb. Protoc.* 2013:pdb.top071860. doi: 10.1101/pdb.top071860

West, M. J., Slomianka, L., and Gundersen, H. G. J. (1991). Unbiased stereological estimation of the total number of neurons in the subdivisions of the rat hippocampus using the optical fractionator. *Anat. Rec.* 231, 482–497. doi: 10.1002/ar.1092310411

Witter, M. P. (2010). "Connectivity of the hippocampus," in *Hippocampal Microcircuits. A Computational Modeler's Resource Book*, eds V. Cutsuridis, B. Graham, S. Cobb and I. Vida (New York, NY: Springer), 5–26.

Woeffler-Maucler, C., Beghin, A., Ressnikoff, D., Bezin, L., and Marinesco, S. (2014). Automated immunohistochemical method to quantify neuronal density in brain sections: application to neuronal loss after status epilepticus. *J. Neurosci. Methods* 225, 32–41. doi: 10.1016/j.jneumeth.2014.01.009

Wu, Y., Whiteus, C., Xu, C. S., Hayworth, K. J., Weinberg, R. J., Hess, H. F., et al. (2017). Contacts between the endoplasmic reticulum and other membranes in neurons. *Proc. Natl. Acad. Sci. U S A* 114, E4859–E4867. doi: 10.3998/panc.2011.6

Yamawaki, R., Thind, K., and Buckmaster, P. S. (2015). Blockade of excitatory synaptogenesis with proximal dendrites of dentate granule cells following rapamycin treatment in a mouse model of temporal lobe epilepsy. *J. Comp. Neurol.* 523, 281–297. doi: 10.1002/cne.23681

Ye, Y., Xiong, J., Hu, J., Kong, M., Cheng, L., Chen, H., et al. (2013). Altered hippocampal myelinated fiber integrity in a lithium-pilocarpine model of temporal lobe epilepsy: a histopathological and stereological investigation. *Brain Res.* 1522, 76–87. doi: 10.1016/j.brainres.2013.05.026

Zhao, F., Li, J., Mo, L., Tan, M., Zhang, T., Tang, Y., et al. (2016). Changes in neurons and synapses in hippocampus of streptozotocin-induced type 1 diabetes rats: a stereological investigation. *Anat. Rec.* 299, 1174–1183. doi: 10.1002/ar.23344

Zhu, Y., Liu, F., Zou, X., and Torbey, M. (2015). Comparison of unbiased estimation of neuronal number in the rat hippocampus with different staining methods. *J. Neurosci. Methods* 254, 73–79. doi: 10.1016/j.jneumeth.2015.07.022

Conflict of Interest Statement: The author declares that the research was conducted in the absence of any commercial or financial relationships that could be construed as a potential conflict of interest.

frontiers in Neuroanatomy

REVIEW
published: 04 December 2017
doi: 10.3389/fnana.2017.00112

Using the Optical Fractionator to Estimate Total Cell Numbers in the Normal and Abnormal Developing Human Forebrain

Karen B. Larsen [1, 2]*

[1] Department of Pathology, Rigshospitalet, University Hospital of Copenhagen, Copenhagen, Denmark, [2] Department of Neuropathology and Ocular Pathology, John Radcliffe Hospital, Oxford University Hospital, Oxford, United Kingdom

Human fetal brain development is a complex process which is vulnerable to disruption at many stages. Although histogenesis is well-documented, only a few studies have quantified cell numbers across normal human fetal brain growth. Due to the present lack of normative data it is difficult to gauge abnormal development. Furthermore, many studies of brain cell numbers have employed biased counting methods, whereas innovations in stereology during the past 20–30 years enable reliable and efficient estimates of cell numbers. However, estimates of cell volumes and densities in fetal brain samples are unreliable due to unpredictable shrinking artifacts, and the fragility of the fetal brain requires particular care in handling and processing. The optical fractionator design offers a direct and robust estimate of total cell numbers in the fetal brain with a minimum of handling of the tissue. Bearing this in mind, we have used the optical fractionator to quantify the growth of total cell numbers as a function of fetal age. We discovered a two-phased development in total cell numbers in the human fetal forebrain consisting of an initial steep rise in total cell numbers between 13 and 20 weeks of gestation, followed by a slower linear phase extending from mid-gestation to 40 weeks of gestation. Furthermore, we have demonstrated a reduced total cell number in the forebrain in fetuses with Down syndome at midgestation and in intrauterine growth-restricted fetuses during the third trimester.

Keywords: fetal, stereology, neurons, glial cells, IUGR, down syndrome

OPEN ACCESS

Edited by:
Bente Pakkenberg, Research Laboratory for Stereology and Neuroscience, Denmark

Reviewed by:
Charles Vyvyan Howard, Ulster University, United Kingdom
Richard S. Nowakowski, Florida State University College of Medicine, United States

***Correspondence:**
Karen B. Larsen
karen.bonde.larsen.01@regionh.dk

Received: *28 June 2017*
Accepted: *17 November 2017*
Published: *04 December 2017*

Citation:
Larsen KB (2017) Using the Optical Fractionator to Estimate Total Cell Numbers in the Normal and Abnormal Developing Human Forebrain. Front. Neuroanat. 11:112. doi: 10.3389/fnana.2017.00112

INTRODUCTION

The neocortex is the main locus of cognition in the human brain and its expansion relative to that in non-human primates is a main anatomic distinction. Since the number of neocortical neurons is generally accepted to bear some relation with cognitive abilities, several stereological studies have quantified neocortical cell numbers in brains of adult humans and various species (Korbo et al., 1990; Pakkenberg and Gundersen, 1997; Jelsing et al., 2006; Christensen et al., 2007; Eriksen and Pakkenberg, 2007; Walløe et al., 2010; Fabricius et al., 2013). On the other hand, there have been few developmental studies of cell numbers in the human fetal and neonate forebrain (Winick, 1968; Dobbing and Sands, 1973; Rabinowicz et al., 1996), none of which employed stereological methods. This paucity may well reflect technical and ethical issues arising in studies of the fetal human brain. Furthermore, many earlier studies of brain cell numbers have been based upon

assumptions that all cells (counting objects) are of uniform shape and size or are isotropically orientated in the specimen (Weibel and Gomez, 1962; Rose and Rohrlich, 1987). Violation of these assumptions give rise to significant bias in the estimation of cell numbers, but stereological methods accommodate these factors. Stereology is an application of spatial sampling that enables researchers to obtain three-dimensional information about the distribution of objects observed in a slice or section. In general, it is not possible to determine the exact cell numbers in large structures, but estimation of total cell numbers through application of stereological principles is efficient, i.e., "with a low variability after spending a moderate amount of time," and unbiased, that is to say "without systematic deviation from the true value" (Gundersen et al., 1988a,b). Thus, the stereological methods yield reliable and efficient estimates of total cell numbers even in structures as complex and heterogenous as the human fetal brain. In order to support statistical comparison between groups, the stereological sampling frequency can be adjusted to give optimal precision without unwarranted effort (Gundersen et al., 1988a,b; West, 2012).

A series of stereological studies has contributed invaluable knowledge of the proliferation of total neocortical cell numbers in human fetal brain by use of the optical fractionator (Samuelsen et al., 2003, 2007; Larsen et al., 2006, 2008, 2010). The optical fractionator design is an ideal method to obtain total cell numbers in the fragile fetal brain due to the minimum of handling of the tissue. There follows a detailed and critical account of how to apply the optical fractionator scheme for robust estimation of cell numbers in the human fetal forebrain across normal and abnormal intrauterine development. Furthermore, there are some comments upon already published results. Since our histological methods did not distinguish between neurons and glial cells, the total cell numbers is a sum of future neurons and glial cells.

DEVELOPMENT OF THE HUMAN FETAL FOREBRAIN BRAIN AND ITS TRANSIENT FETAL ZONES

Main events in the development of the human brain include neuronal proliferation, migration, differentiation, synaptogenesis, pruning and myelination. Deviations from the normal developmental sequence due to genetic or environmental factors give rise to cerebral malformation. Severe misdevelopment of the brain can be diagnosed by post mortem examination or through macroscopic imaging techniques *in utero*. However, detecting subtle changes in cell numbers requires quantitative measurements by microscopy. We have focused our investigations on the total cell numbers in the maturing neocortex or in transient fetal zones destined to develop into neocortex (Kostovic and Judas, 1995). More than 40 years ago, the Boulder Committee, founded by the American Association of Anatomists, described and named these zones, which have no direct counterpart in the adult brain (The Boulder Committee, 1970). This description was revised by Bystron et al. (2008).

During human fetal weeks 3 and 4, the telencephalic wall contains only *the ventricular zone* (VZ). Neuroepithelial cells then constitute a homogenous cell population in the neural tube, and the major histogenic event is intensive symmetric proliferation where single progenitor cell first give rise to two progenitor cells before the onset of neurogenesis (Kornack, 2000). The first phase of neurogenesis starts at approximately fetal week 5, which occurs in conjunction with differentiation of the primordial neuroepithelial cells into radial progenitor cells. They provide a scaffold for migration of newborn cells to their predetermined position, while also acting as progenitor cells for more neurogensis (Malatesta et al., 2000; Miyata et al., 2001; Noctor et al., 2001; Heins et al., 2002). At fetal week 6, *the subventricular zone* (SVZ) arises on the border of the VZ through accumulation of outer radial glial cells and intermediate progenitors lacking an attachment to the ventricular surface. Even through early human postnatal life, immature neurons continue migrating from the SVZ to specific targets such as the olfactory bulb and prefrontal cortex (Sanai et al., 2011; Khodosevich et al., 2013; Wang et al., 2013; Paredes et al., 2016), but this process declines in early childhood (Sanai et al., 2011; Paredes et al., 2016).

The intensive proliferation in the SVZ leads to formation of the ganglionic eminence in the basoventral part of the telencephalon. The ganglionic eminence later develops into the basal ganglia, but is in rodent also the source of neocortical inhibitory GABAergic interneurons, which migrate dorsally into the neocortex in a process known as tangential migration (Anderson et al., 1997; Tamamaki et al., 1997). Human neocortical interneurons are also derived from the ganglionic eminence (Letinic et al., 2002; Fertuzinhos et al., 2009), but the majority of neocortical interneurons arise in the VZ and SVZ of the dorsal telencephalon itself (Letinic et al., 2002).

The Boulder Committee originally suggested that before any post mitotic cells appear in the prospective cortex, the subpial processes of ventricular cells constitute a cell sparse layer which they termed *the marginal zone* (MZ). Increasing evidence has revealed that no such subpial layer exists prior to the tangential invasion of the first cortical neurons (Bystron et al., 2005, 2006), such that the term MZ is more properly employed after the formation of the cortical plate (Uylings, 2000; Bystron et al., 2008). A compartment consisting of heterogeneous post migratory cells and neuropil lying between the proliferative zones and the pial surface of the dorsal telencephalon before the appearance of the cortical plate is known as the preplate.

During fetal weeks 8 and 9, the first migratory wave of cells form *the cortical plate* (CP), a distinctive layer of tightly packed neurons. The CP divides the preplate into the MZ and the subplate/intermediate zone. *The intermediate zone* (IZ), which contains both radially and tangentially migrating cells together with axons, constitutes the future white matter. *The subplate zone* (SP) transiently appears between the IZ and the CP. The first phase of synaptogenesis is thought to occur in the SP, which is also a target for afferents arising from the brain stem, basal forebrain, thalamus and the ipsi- and contralateral cortices (Kostovic and Rakic, 1990). Together with the neighboring CP and the MZ, the SP will develop into the future cortical gray

matter. The SP undergoes intensive reorganization and reaches its maximum thickness at 22 fetal weeks, begins to regress after fetal week 35, and ultimately disappears by the second postnatal year (Kostović et al., 2014).

METHODS

Optical Fractionator

The optical fractionator combines two stereological tools: the optical disector and the fractionator sampling design (Gundersen, 1986; Gundersen et al., 1988a,b; West et al., 1991). A unique aspect of the optical disector method lies in the lack of any assumptions about size, shape, orientation or distribution of the particles (i.e., cells) to be counted, and that it samples with a probability that is proportional only to their number (Gundersen, 1986). The optical disector in which the cells are counted directly is an unbiased three-dimensional probe with a well-defined volume. In particular, the fractionator is a systematic uniform random sampling (SURS) scheme, which assures that the fraction of the structure of interest is known. The basic principle of the fractionator is quite simple: one investigates a known fraction of the whole structure of interest, for example 1:200, and then counts every cell in that fraction. The total number of cells in the entire structure is the number counted in that fraction multiplied by the inverse sampling fraction, in this case 200.

The optical fractionator entails counting within optical disectors using SURS that constitute a known fraction of the structure to be analyzed. This fraction is obtained by sampling a known fraction of the section thickness, under a known fraction of the area encompassing the structure of interest, and for a known fraction of the total number of sections comprising the structure of interest. The method requires that the whole structure be fully available, and that the structure can be exhaustively cut into sections of a thickness exceeding the height of the dissector and guard zones (West et al., 1991). For unbiased estimation, the sampling design must be based on systematic, uniform, and random sampling with a predetermined periodicity from a random starting position within the first interval of the sectioning (Gundersen and Jensen, 1987). Such a sampling ensures that every part of the structure has a priori the same chance of being included in the final sample. Then an estimate of total cell numbers is obtained, but the volume of the region of interest is not known. The method is insensitive to tissue changes due to fixation or preparation, and neither the volume of the region of interest, the cell density, nor the magnification need be known.

These properties make the optical fractionator design an ideal procedure to estimate total cell numbers in fragile and distorted tissue such as fetal brain. Because fetal brain has low myelin content and high water content, tissue handling and processing almost always results in some fragmentation. Therefore, handling of fetal brain prior to paraffin embedding must be minimized. By using the optical fractionator method, the only handling before paraffin embedding is cutting the chosen hemisphere into either two or three blocks before further treatment, or simply directly embed the chosen hemisphere in paraffin depending upon the size of the brain. Thus, the sampling process begins only after cutting the sections.

Practical Application of the Optical Fractionator to the Fetal Brain

Application of the optical fractionator for fetal tissue entails the following steps:

1. Since the fetal brain is soft and vulnerable, the 10% formalin solution used for postnatal brain is unsuitable. Instead, we harden the tissue by fixation in 25% saturated picric acid/20% formalin for 4 weeks prior to cutting. The left or right hemisphere is chosen systematically at random.
2. Hemispheres are cut into either two or three blocks before further treatment, or are directly embedded in paraffin depending on the size of the brain. Primary blocks are then sectioned coronally on a sledge microtome at 40 μm proceeding from the frontal to the occipital pole. Every sampled section is then mounted on glass slides coated with gelatine-chromepotassium sulfate dodecahydrate and immediately thereafter dried at 40°C for 24 h. Before staining, the section are heated to 60°C for 30 min, hydrated in xylene for 2 × 25 min in a 50:50 mixture of xylene and acetone dimethyl acetyl hydrochloride containing 1 μl hydrochloric acid per ml acetone dimethyl acetate, and then immersed for 2 × 30 min in the acetone dimethyl acetal hydrochloride, followed by washing for 5 min in distilled water.
3. The sections are stained by immersion for 45 min in a modified Giemsa stain containing: 50 ml Giemsa stain stock solution and 200 ml $KHPO_4$, 67 mmol/L, pH 4.5, the mixture being filtered just before use. Then the sections are differentiated and dehydrated by passage through 0.5% acetic acid in 96% alcohol for 1 to 5 min, 5 min in 99% alcohol and 10 to15 min in xylene.
4. Beginning from the frontal pole, sections selected according to a predetermined periodicity are sampled after a random start within the first sampling period. A known fraction, the section sampling fraction, *ssf*, is chosen aiming to achieve about 10 sections per brain. If *ssf* were chosen to be 1/100th, a random start within the first predetermined period could be, for example, section 20, and the next would then be section 120 (**Figure 1A**).
5. For each sampled section, the different zones in the neocortex are delineated (**Figure 2**) by making a fiducial mark in Indian ink "corresponding to the borders histologically verified using a stereo microscope. The neocortex develops a prominent CP and SP, while the archicortex develops an exceptionally wide MZ and a thin convoluted CP without a real SP. Furthermore, the telencephalic wall is slightly curved in this area. The paleocortex never develops a true CP" (Kostovic and Judas, 1995; Samuelsen et al., 2003). It should be noted that gyration patterns and sizes of fetal zones change dramatically with increasing fetal age (**Figure 3**).
6. The borders of the fetal zones are then transferred to the Computer Assisted Stereological Test Grid System (CAST

grid system, Olympus Denmark). The total number of cells is estimated separately in each fetal zone, as in step 7 below. The inclusion line for the CP/MZ is drawn according to the outer pial surface, whereas the exclusion line for the CP/MZ is made at the interface between the CP/MZ and the SP. After the cells in the CP/MZ are counted within optical disectors for this zone, the former exclusion line of the CP/MZ becomes the inclusion line for the underlying SP and a new exclusion line is drawn at the interface between the SP and the IZ. The same procedure is applied to the IZ and the SVZ/VZ, thus ensuring that no areas (and thus no cells) are omitted or counted twice due to inconsistent delineation (**Figure 2**).

7. A computer monitor displays the microscopic view obtained with a 100x oil objective of high numerical aperture. The step length (*x,y* interval) and the size of the counting frame *a*(frame) of the optical disector must be designed to achieve counting of ∼100–200 cells in each fetal zone. Furthermore, for correct counting the area of the counting frame of the optical disector should be set so as to count 2–4 cells per frame. Cells are counted when the nucleus come into focus (**Figure 4**). After random placement of a two-dimensional unbiased counting frame of the optical disector in the first predetermined *x,y* interval, the remaining counting frame positions of the optical disector are displaced in the *x,y* intervals using a stepping motor. The area sampling fraction, *asf*, is then calculated as the ratio between the area of the counting frame, *a*(frame) and the area associated with each displacement in x and y, *a*(*x,y* interval). Thus, $asf = a(\text{frame})/a(x,y \text{ interval})$ (**Figure 1B**).
8. The mean thickness, t_q (the number-weighted mean section thicknesss), should be calculated from measurements made at defined intervals such as every 5th optical disector. This is accomplished by locating the surface of the section and registering 0 in the z-axis when the first feature appears in focus, and then moving to the bottom of the section where features are out of focus, and noting the thickness of the section. The fixed height of the optical disector must be less than the total thickness to avoid artifacts at the top and bottom surfaces of sections (these volumes are known as the guard zones). Since the cells are only counted in *h*, the height sampling fraction, *hsf*, is calculated as:

$$hsf = \frac{h}{\bar{t}_{Q^-}} \quad \text{for} \quad \bar{t}_{Q^-} = \frac{\sum_i (t_i q_i^-)}{\sum_i q_i^-}$$

where t_i is the local section thickness centrally in the i*th* counting frame with a disector cell count of q_i^- (Dorph-Petersen et al., 2001). A Heidenhain microcator measures movement in the z-axis with a precision of 0.5 μm (**Figure 1C**).

9. For one brain hemisphere, the cells counted in a fetal zone is denoted as ΣQ^-. Then the total bilateral number of cells in that particular fetal zone is estimeted as:

$$N := \frac{1}{ssf} x \frac{1}{asf} x \frac{1}{hsf} x \sum Q^- x2$$

The doubling to provide a bilateral estimate is allowed because the hemisphere has been selected according to random choice. The total number of cells in the neocortical part of the telencephalic wall is obtained by summing N of each fetal zone in that specimen.

10. Before committing to the use of valuable samples, it is recommended to perform a pilot study to address the various technical issues raised in the above, aiming to obtain an ideal and efficient sampling design. The final design will, for example, depend upon the extent of shrinkage and if there is an either homogeneous or heterogeneous distribution of the cells in the structure of interest. Furthermore, it is of great importance to calibrate the microscope stage so that the commanded step lengths are correctly executed and to check the staining throughout the tissue.

Precision of the Estimate CE Using the Optical Fractionator

In addition to the practical application of the optical fractionator to cell counting in human fetal brain, certain statistical considerations must be addressed to obtain accurate estimates of cell numbers. The total observed variance (CV^2) is the sum of the biological variance and the mean sampling variance, where CV can be calculated as the standard deviation of the estimate divided by the group mean. The coefficient of error, CE = SEM/mean, which indicates the precision of the estimate for a single brain, depends upon the sampling design, and describes both the variance between sections and the variance within sections from a single brain. In essence, the CE describes the quality of the measurement, which refers to the difference between the estimate and the true value. We estimate CE as follows:

$$\text{CE} = \frac{\sqrt{Var_{surs} + Noise}}{\sum Q^-},$$

Here, noise is the sum of counted particles and Var_{SURS} is the estimated variance according to Systematic Uniform Random Sampling (SURS) (Gundersen and Jensen, 1987; Gundersen et al., 1999). The SURS takes into account the systematic nature of the sampling, and this is superior to and more efficient than independent sampling. The $\text{Var}_{\text{SURS}}(N)$ is obtained from the formula:

$$\text{Var}_{\text{SURS}}(\text{N}) = \frac{(3(A - Noise) - 4B + C)}{240},$$

where the systematic section series of the particle count is denoted $f_1, f_2 \ldots\ldots f_n$ and.

$$\text{A} = \sum_{i=1}^{n} fi^2; \text{B} = \sum_{i=1}^{n-1} fifi + 1 \text{ and C} = \sum_{i=1}^{n-2} fifi + 2$$

These CE calculations are valid when samples are not independent and are systematically chosen in a uniform and random way. The nature of the variation between samples in our studies are believed to be of the smoothness class $m = 1$, as we did not observe any abrupt variation between samples. Thus, the

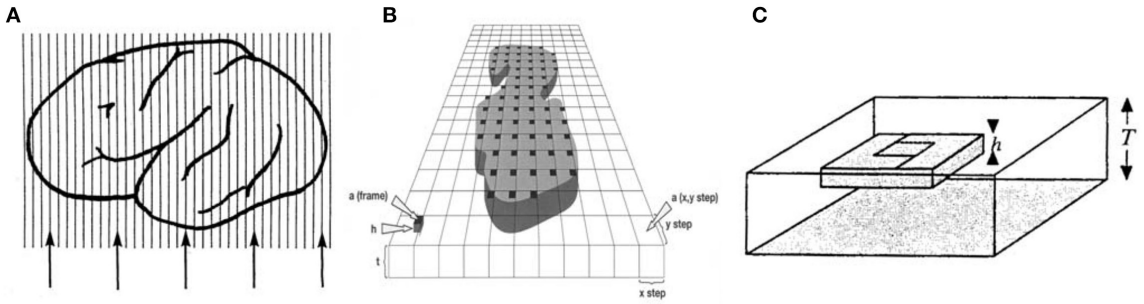

FIGURE 1 | (A) A known fraction, the section sampling fraction, *ssf*, is chosen. In this case five sections (lines are representing sections) are chosen from the object of interest, and **(B)** a step length = (x, y) and a counting frame area = a(frame) are applied. After placement of a 2D unbiased counting frame, a(frame) in the first predetermined x,y interval, the remainder of the positions of the counting frame in the x,y intervals are repositioned using a stepping motor. **(C)** Each black square is an optical disector with a fixed height, *h*. Modified from Figure 5.19 in Howard and Reed (2010).

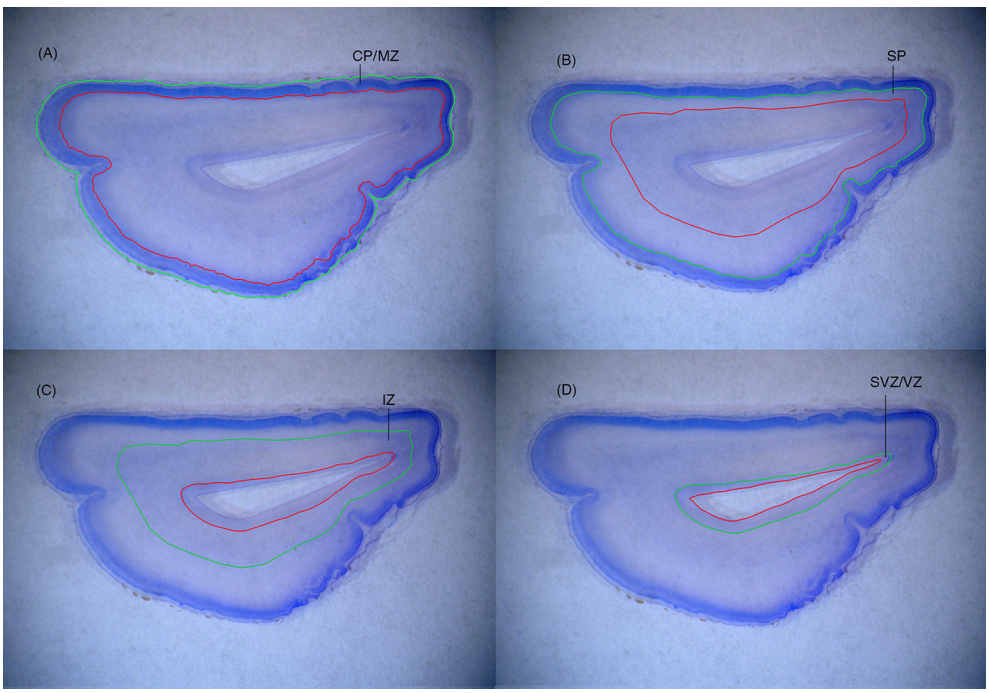

FIGURE 2 | (A) The inclusion line (green line) for the CP/MZ is drawn according to the outer pial surface, whereas the exclusion line (red line) for the CP/MZ is made at the interface between the CP/MZ and the SP. **(B)** After the cells in the CP/MZ are counted within optical disectors for this zone, the former exclusion line of the CP/MZ becomes the inclusion line for the underlying SP and a new exclusion line is drawn at the interface between the SP and the IZ. **(C,D)** The same procedure is applied to the IZ and the SVZ/VZ, thus ensuring that no areas (and thus no cells) are omitted or counted twice due to inconsistent delineation.

numerator in the calculation of Var_{SURS} should be divided by 240 and not 12 (Gundersen et al., 1999).

The biological variance can be calculated when CV and CE are known. The researcher cannot control the biological variance CV_{biol}, which arises from actual differences between individuals, but can determine the mean sampling variance (CE). It is obvious that if the biological variation in cell numbers is high, there is little effect on the total observed variance from adjusting the sampling design whereas the sampling frequency should be increased if the sampling variation is the main contribution to the total observed variance of the estimate.

APPLICATION OF THE OPTICAL FRACTIONATOR TO THE FETAL AND NEONATAL BRAIN IN ORDER TO ESTIMATE TOTAL CELL NUMBERS IN THE NORMAL AND ABNORMAL FETAL AND NEONATAL HUMAN FOREBRAIN

Many recent studies have investigated the molecular background of neurogenesis, patterning of brain regions, and circuit formation in the developing human brain. However, very

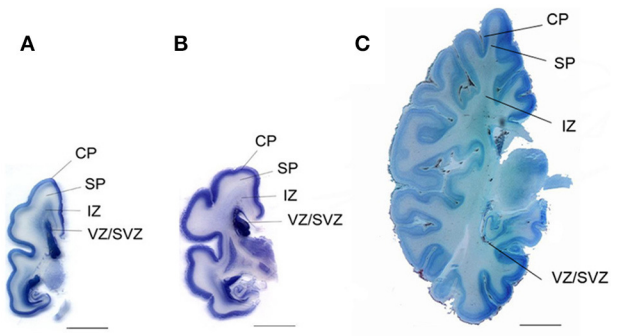

FIGURE 3 | "Coronal sections from a 24-weeks **(A)**, a 25-weeks **(B)**, and a 40-week-old **(C)** human fetus at the level of the basal ganglia. CP, cortical plate; SP, subplate; IZ, intermediatezone; VZ/SVZ, ventricular zone/subventricularzone. Scalebar = 1 cm." Reproduced with permission from Walløe et al. (2014).

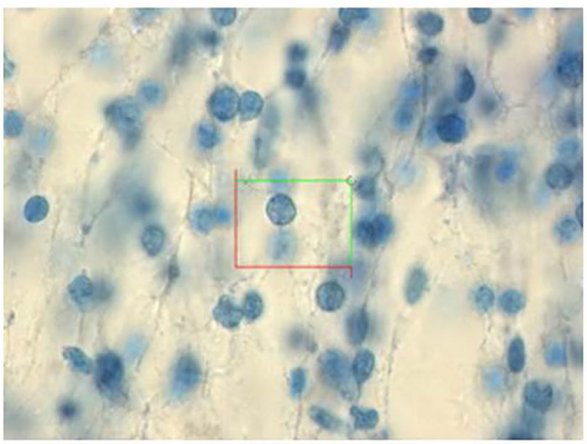

FIGURE 4 | "An optical disector in the neocortex of a 19-week fetus. The cells were counted when the nucleus came into focus in the optical disector. Paraffin, Giemsa—stained section, 40 mm thick, magnification 3100x." Reproduced with permission from Larsen et al. (2008).

little has been known about the prenatal development of the human fetal brain in terms of growth in cell numbers. The first stereological study applying the optical fractionator to cell counting in human fetal brain appeared in 2003 (Samuelsen et al., 2003). In that study we estimated total cell numbers in selected zones of the fetal neocortical cerebral wall in 22 human fetuses aged 13 to 41 gestational weeks. Since our histological methods do not distinguish between neurons and glial cells, we report total cell numbers, i.e. the sum of future neurons and glial cells. We found that the growth in cell numbers in the human fetal forebrain appears to be two-phased, with an initial exponential phase from 13 to 20 gestational weeks, followed by linear phase from 22 weeks of gestation until term. From 13 to 20 weeks of gestation the total number of cells increased four-fold, from 3 $\times$ 10^9 to 13 $\times$ 10^9 cells, and increased by a further factor of 3 to 38 $\times$ 10^9 cells at term (**Figure 5**). During the second half of gestation, we estimated 170 million new brain cells per day in the entire neocortical wall, equivalent to 2,000 new cells each second.

We also estimated the total number of cells in the developing ganglionic eminence in 13 human fetuses aged 22 to 29 fetal weeks with use of the optical fractionator (Larsen, 2010; Larsen et al., 2010). From 11 to 20 fetal weeks, the total number of cells in the ganglionic eminence increased six-fold from 0.47 $\times$ 10^6 to 2.86 $\times$ 10^6, whereafter total cell numbers declined until the structure finally disappeared around term. In that study, we demonstrated that the ganglionic eminence, like the neocortex, exhibits an exponential development of total cell numbers from 10 to 20 fetal weeks. Our stereological data are in agreement with the volumetric data from Huang et al. (2009), who used diffusion tensor imaging of post mortem human fetal brains to chart the increasing volume of the ganglionic eminence during the second trimester. Previous studies have identified the ganglionic eminence as an important source of neocortical inhibitory interneurons and oligodendrocyte progenitor cells (Anderson et al., 1997; Tamamaki et al., 1997; Letinic et al., 2002; Rakic and Zecevic, 2003; Ma et al., 2013), which may well drive the exponential development in total cell numbers lasting until mid-gestation. Although the ganglionic eminence disappears around birth, the production of neocortical inhibitory interneurons continues into early postnatal life (Arshad et al., 2016), and remnants of the SVZ produce cells until early infancy (Del Bigio, 2011).

In the final study to investigate the normal developing brain in term infants, we estimated total cell numbers in 10 normal neonate brains within the CP/MZ, the SP, the IZ and the SVZ/VZ (Larsen et al., 2006) by applying the optical fractionator. The gestational ages ranged from 38 to 42 weeks. In that study, the total number of cells in the entire neocortical part was almost 33 $\times$ 10^9 in the human neonate forebrain, and around 24 $\times$ 10^9 in the CP/MZ. Other studies of the adult neocortex indicate a total of 50 $\times$ 10^9 cells in females and 65 $\times$ 10^9 in males (Pelvig et al., 2008), of which 19 $\times$ 10^9 are neurons in females and 23 $\times$ 10^9 are neurons in males (Pakkenberg and Gundersen, 1997). Compiling these studies indicates that the total number of neurons in neonates equals the total number in adults, whereas glial cells continue to proliferate in postnatal development. Indeed, the first stereological study of total cell numbers during neocortical development of rat pups found similar growth trajectories of neurons and glial cells (Behnam-Rassoli et al., 1991). In agreement with these findings, two recent stereological studies (Kjær et al., 2016; Sigaard et al., 2016) showed linear increases in both oligodendrocyte and astrocyte numbers during the first 3 years of human life in humans, and that the number of neocortical neurons has already attained the adult population at least at term.

The growth in fetal brain cell numbers is so complex and rapid that any disruption is apt to derail the normal growth program away from delicately predetermined interrelationships, likely resulting in anatomic and functional deficits persisting to maturation. With this in mind, we have investigated total cell numbers in the forebrain in fetuses with Down syndrome (DS) and in intrauterine growth-restricted (IUGR) fetuses,

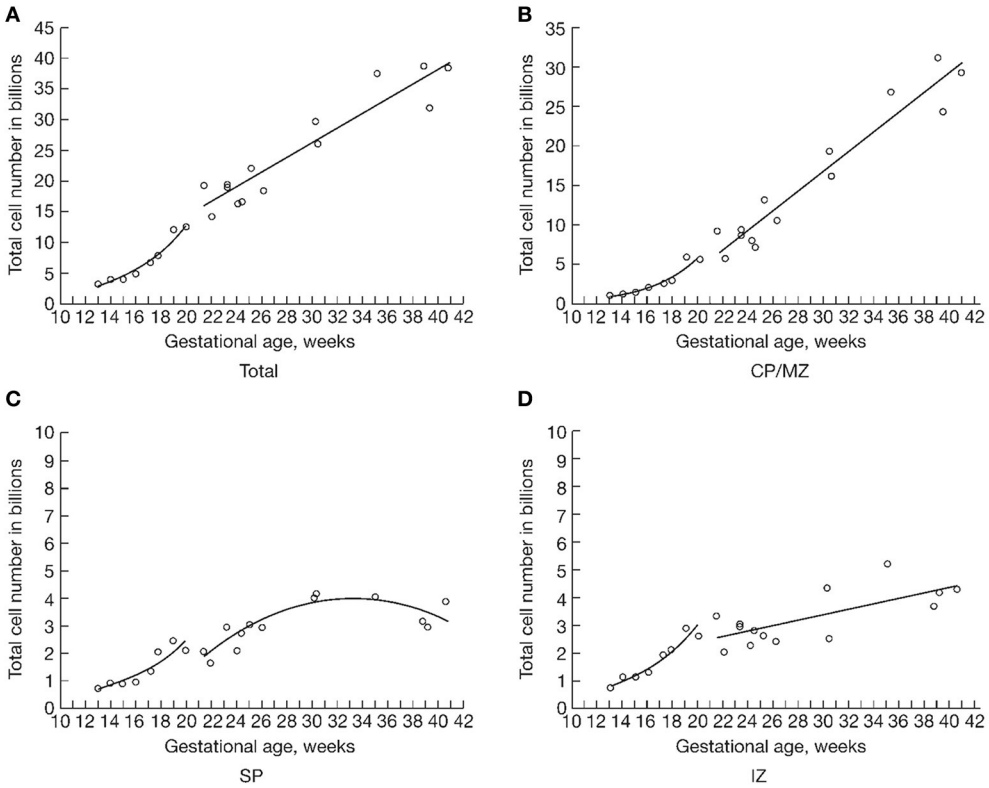

FIGURE 5 | "The total number of cells in billions (10^9) in three major developmental zones of the human fetal forebrain **(B,C,D)** (CP/MZ, SP, IZ) and in the summation of all four zones **(A)** (CP/MZ, SP, IZ, VZ/SVZ), representing the total number of cells in the entire human fetal forebrain. The material has been allocated into two study periods: one from 13 to 20 weeks of gestation and another from 22 weeks of gestation to term. Due to the limited number of cases during the period from 18 to 22 weeks of gestation, we could not determine which of the two mathematical models that gave the best fit in that transitional interval." Reproduced with permission from Samuelsen et al. (2003).

which constitute relative common conditions of abnormal fetal development. Alterations of brain development and intellectual disabilities occur in DS (Schmidt-Sidor et al., 1990; Devenny et al., 1996, 2000; Krinsky-McHale et al., 2002; Nelson et al., 2005). We used the optical fractionator to compare the total cell numbers in forebrain of 4 DS fetuses aged 19 weeks of gestation to 8 normal control fetuses The total cell number was 34% lower in the neocortical part of the cerebral wall of DS fetuses (6.85×10^9) compared to normal controls (10.4×10^9). We suppose that the intellectual disability often occurring in DS may arise from a structural deficit in the human fetal brain already present in the second trimester (Larsen et al., 2008).

We also used the optical fractionator to to estimate the cell numbers in the forbrain of nine severely affected IUGR fetuses and 15 control fetuses with gestational ages ranging from 19 to 41 weeks. The total cell number in the CP/MZ was significantly lower in IUGR fetuses compared to controls, and the daily increase rate in the CP/MZ of IUGR fetuses was only half of the controls; whereas control fetuses acquired an average of 173 million CP/MZ cells per day from midgestation to term, the IUGR fetuses acquire only 86 million new cells per day (Samuelsen et al., 2007).

METHOLOGICAL CONSIDERATIONS USING THE OPTICAL FRACTIONATOR

A large number of stereological studies have used the stereological ratio estimators (density multiplied by reference volume) to quantify total cell numbers in the human brain (Pakkenberg and Gundersen, 1997; Andersen et al., 2003; Pelvig et al., 2008; Karlsen and Pakkenberg, 2011; Karlsen et al., 2014). In that approach, the number of cells is counted in optical disectors, knowing the dimensions of the disector and the total volume (see e.g., Pakkenberg and Gundersen, 1997). The method of multiplying density by the reference volume is obviously a good choice when volume and total cell numbers are both matters of interest. It is then possible to obtain reliable mean estimates of both parameters for making comparisons by group or treatment. The adult brain suffers less unpredictable dimensional change during tissue processing than typically occurs in fetal material.

Due to the unpredictable shrinkage and distoration during fixation of fetal brain, it is of questionable value to attempt an estimation of volumes and densities. However, the optical fractionator method for estimating total cell numbers is the obvious choice for fetal brain studies, because results are robust

to deformation, shrinkage, and swelling of the reference space. Furthermore, it is easier to apply the optical fractionator, because no reference volume estimate is required.

Despite the advantages of the optical fractionator method, some pitfalls should be considered.

- Since only total cell number estimates are obtained with the optical fractionator method, it is sensitive to any errors occuring during the sampling procedure. One such error could be due to incorrect calibration of the microscope stage, resulting in unreliable step lengths. Since the optical fractionator gives only total cell number, neither density nor volume estimates will help to reveal a calibration error.
- If there are many artifacts in the tissue, it is necessary to keep track of the fraction of disectors that are uncountable, so this fraction can be properly included in the final estimation of total numbers.
- Cells in the SVZ/VZ lie very closely together and have a tendency to cluster, intermixed with acellular areas. In such circumstances of heterogeneity of cell distribution, it is important to use a sampling design with relatively small counting frames and small step lengths in order to obtain robust and precise estimates of total cell numbers.
- Often, relatively few (8–12) sections suffice when using the optical fractionator. This is due to low variation in count between sections during the calculation of the CE, since the counts are systematically related. Thus, the numerator can be divided by 240 instead of 12 in the Var_{SURS} (N) equation, see section Precision of the Estimate CE using the Optical Fractionator. The sampling scheme must be strictly systematic if low sampling is to yield the desired amount of precision in the estimate of total cell numbers (West et al., 1991). However, if cell counts between neighboring sections vary considerably, a greater number of sections must be sampled to obtain an acceptable precision.
- When applying the optical disector, it is necessary to introduce guard zones, as noted above. This is due to optical limitations, and also to avoid bias from lost tissue fragments at the cut surface of sections. While especially important in fragile fetal tissue, the use of guard zones can bias total cell number estimates under certain circumstances. This is because the disector placement is not uniformly random within the section thickness, as can happen if there is a heterogeneous cell distribution along the z-axis. In sections thinner than 20 μm, the relative error in measuring the section thickness increases dramatically, so thicker sections are to be preferred. Also, it is recommended to use microscope objectives with high numerical objectives to provide a very shallow depth of focus in the images (West et al., 1991).

If these recommendations and stipulations are satisfied, total cell number estimates with the optical fractionator are indeed "unbiased for all practical purposes" (Gundersen et al., 1988a,b). Correct use of the optical fractionator requires some expertise with stereological tools, and therefore might not be the preferred method for researchers with no access to expert guidance. In such circumstances, multiplying the density by the reference volume method might be more appropriate, as it is more robust and less vulnerable to sampling design. In the present context, there is a particular need to minimize handling of fragile fetal tissue and when all requirements are observed, the optical fractionator method is the perfect choice to estimate total cell numbers in fetal brain.

CONCLUSION

In the three decades since the landmark study showing how to obtain unbiased estimation of individual particle numbers was published (Sterio, 1984), the optical disector method has matured to a general tool for quantifying the number of cells in brain and other organs. Subsequently, the optical fractionator method has made it possible to overcome important methodological problems arising from unpredictable shrinkage during fixation of the fetal brain and furthermore, several user-friendly software programs exist which can assist the un-experienced researcher with the calculations and evaluation of the estimate quality.

Despite the widespread knowledge of the advantages of unbiased stereological methods, many quantitative studies continue to use cell densities in sections. However, the volume/reference trap should be avoided. When using the density multiplied by reference volume, the reference volume and the numerical cell density both contribute to the final readout of total cell counts. To avoid bias, stereologists should always report the numerator and denominator instead of simply reporting cell density. It is better to graph the explicit number or length as a function of the volume. Density, a ratio between two variables, is of limited value unless used to obtain total cell numbers. Alternatively, one may use the optical fractionator to obtain directly the total cell numbers.

Present histological methods do not distinguish between neurons and glial cells until term. Thus, we estimate total cell numbers and net proliferation, although certain transient features can be seen to decline in size and cell counts during late gestation. In future studies the use of an apoptotic marker in combination with stereological methods in the fetal brain could contribute to a more exact knowledge of the growth in cell numbers. Furthermore, other cell-labeling techniques could eventually give separate estimates of neurons and glial cells during human fetal brain development.

In summary, we have applied the optical fractionator to investigate total cell numbers of the developing human fetal and neonate forebrain. Remarkably, the production of billions of cells, many of which are neurons, occurs during a rather brief span of intense and exponential proliferation. Furthermore, we have demonstrated a reduced total cell number in the forebrain in DS fetuses at midgestation and in IUGR fetuses during the third trimester.

AUTHOR CONTRIBUTIONS

The author confirms being the sole contributor of this work and approved it for publication.

ACKNOWLEDGMENTS

The author acknowledges critical reading and editing of the manuscript by Prof. Paul Cumming.

REFERENCES

Andersen, B. B., Gundersen, H. J., and Pakkenberg, B. (2003). Aging of the human cerebellum: a stereological study. *J. Comp. Neurol.* 466, 356–365. doi: 10.1002/cne.10884

Anderson, S. A., Eisenstat, D. D., Shi, L., and Rubenstein, J. L. (1997). Interneuron migration from basal forebrain to neocortex: dependence on Dlx genes. *Science* 278, 474–476. doi: 10.1126/science.278.5337.474

Arshad, A., Vose, L. R., Vinukonda, G., Hu, F., Yoshikawa, K., Csiszar, A., et al. (2016). Extended production of cortical interneurons into the third trimester of human gestation. *Cereb. Cortex* 26, 2242–2256. doi: 10.1093/cercor/bhv074

Behnam-Rassoli, M., Herbert, L. C., Howard, V., Pharoah, P. O., and Stanisstreet, M. (1991). Effect of propylthiouracil treatment during prenatal and early postnatal development on the neocortex of rat pups. *Neuroendocrinology* 53, 321–377. doi: 10.1159/000125736

Bystron, I., Blakemore, C., and Rakic, P. (2008). Development of the human cerebral cortex: boulder Committee revisited. *Nat. Rev. Neurosci.* 9, 110–122. doi: 10.1038/nrn2252

Bystron, I., Molnár, Z., Otellin, V., and Blakemore, C. (2005). Tangential networks of precocious neurons and early axonal outgrowth in the embryonic human forebrain. *J. Neurosci.* 25, 2781–2792. doi: 10.1523/JNEUROSCI.4770-04.2005

Bystron, I., Rakic, P., Molnár, Z., and Blakemore, C. (2006). The first neurons of the human cerebral cortex. *Nat. Neurosci.* 9, 880–886. doi: 10.1038/nn1726

Christensen, J. R., Larsen, K. B., Lisanby, S. H., Scalia, J., Arango, V., Dwork, A. J., et al. (2007). Neocortical and hippocampal neuron and glial cell numbers in the rhesus monkey. *Anat. Rec. (Hoboken).* 290, 330–340. doi: 10.1002/ar.20504

Del Bigio, M. R. (2011). Cell proliferation in human ganglionic eminence and suppression after prematurity-associated haemorrhage. *Brain* 134, 1344–1361. doi: 10.1093/brain/awr052

Devenny, D. A., Krinsky-McHale, S. J., Sersen, G., and Silverman, W. P. (2000). Sequence of cognitive decline in dementia in adults with Down's syndrome. *J. Intellect. Disabil. Res.* 44, 654–665. doi: 10.1046/j.1365-2788.2000.00305.x

Devenny, D. A., Silverman, W. P., Hill, A. L., Jenkins, E., Sersen, E. A., and Wisniewski, K. E. (1996). Normal ageing in adults with Down's syndrome: a longitudinal study. *J. Intellect. Disabil. Res.* 40, 208–221. doi: 10.1111/j.1365-2788.1996.tb00624.x

Dobbing, J., and Sands, J. (1973). Quantitative growth and development of human brain. *Arch. Dis. Child.* 48, 757–767.

Dorph-Petersen, K. A., Nyengaard, J. R., and Gundersen, H. J. (2001). Tissue shrinkage and unbiased stereological estimation of particle number and size. *J. Microsc.* 204, 232–246. doi: 10.1046/j.1365-2818.2001.00958.x

Eriksen, N., and Pakkenberg, B. (2007). Total neocortical cell number in the mysticete brain. *Anat. Rec. (Hoboken).* 290, 83–95. doi: 10.1002/ar.20404

Fabricius, K., Jacobsen, J. S., and Pakkenberg, B. (2013). Effect of age on neocortical brain cells in 90+ year old human females–a cell counting study. *Neurobiol. Aging* 34, 91–99. doi: 10.1016/j.neurobiolaging.2012.06.009

Fertuzinhos, S., Krsnik, Z., Kawasawa, Y. I., Rasin, M. R., Kwan, K. Y., Chen, J. G., et al. (2009). Selective depletion of molecularly defined cortical interneurons in human holoprosencephaly with severe striatal hypoplasia. *Cereb. Cortex* 19, 2196–2207. doi: 10.1093/cercor/bhp009

Gundersen, H. J. (1986). Stereology of arbitrary particles. A review of unbiased number and size estimators and the presentation of some new ones, in memory of William R. Thompson. *J. Microsc.* 143, 3–45. doi: 10.1111/j.1365-2818.1986.tb02764.x

Gundersen, H. J., Bagger, P., Bendtsen, T. F., Evans, S. M., Korbo, L., Marcussen, N., et al. (1988a). The new stereological tools: disector, fractionator, nucleator and point sampled intercepts and their use in pathological research and diagnosis. *APMIS* 96, 857–881. doi: 10.1111/j.1699-0463.1988.tb00954.x

Gundersen, H. J., Bendtsen, T. F., Korbo, L., Marcussen, N., Møller, A., Nielsen, K., et al. (1988b). Some new, simple and efficient stereological methods and their use in pathological research and diagnosis. *APMIS* 96, 379–394. doi: 10.1111/j.1699-0463.1988.tb05320.x

Gundersen, H. J., and Jensen, E. B. (1987). The efficiency of systematic sampling in stereology and its prediction. *J. Microsc.* 147, 229–263.

Gundersen, H. J., Jensen, E. B., Kiêu, K., and Nielsen, J. (1999). The efficiency of systematic sampling in stereology–reconsidered. *J. Microsc.* 193, 199–211. doi: 10.1046/j.1365-2818.1999.00457.x

Heins, N., Malatesta, P., Cecconi, F., Nakafuku, M., Tucker, K. L., Hack, M. A., et al. (2002). Glial cells generate neurons: the role of the transcription factor Pax6. *Nat. Neurosci.* 5, 308–315. doi: 10.1038/nn0502-500c

Huang, H., Xue, R., Zhang, J., Ren, T., Richards, L. J., Yarowsky, P., et al. (2009). Anatomical characterization of human fetal brain development with diffusion tensor magnetic resonance imaging. *J. Neurosci.* 29, 4263–4273. doi: 10.1523/JNEUROSCI.2769-08.2009

Howard, C. V., and Reed, M. G. (2010). *Unbiased Stereology, 2nd Edn.* Liverpool, QTP Publications.

Jelsing, J., Nielsen, R., Olsen, A. K., Grand, N., Hemmingsen, R., and Pakkenberg, B. (2006). The postnatal development of neocortical neurons and glial cells in the Gottingen minipig and the domestic pig brain. *J. Exp. Biol.* 209, 1454–1462. doi: 10.1242/jeb.02141

Karlsen, A. S., Korbo, S., Uylings, H. B., and Pakkenberg, B. (2014). A stereological study of the mediodorsal thalamic nucleus in Down syndrome. *Neuroscience* 279, 253–259. doi: 10.1016/j.neuroscience.2014.08.046

Karlsen, A. S., and Pakkenberg, B. (2011). Total numbers of neurons and glial cells in cortex and basal ganglia of aged brains with Down syndrome–a stereological study. *Cereb. Cortex* 21, 2519–2524. doi: 10.1093/cercor/bhr033

Khodosevich, K., Alfonso, J., and Monyer, H. (2013). Dynamic changes in the transcriptional profile of subventricular zone-derived postnatally born neuroblasts. *Mech. Dev.* 130, 424–432. doi: 10.1016/j.mod.2012.11.003

Kjær, M., Fabricius, K., Sigaard, R. K., and Pakkenberg, B. (2016). Neocortical development in brain of young children-a stereological study. *Cereb. Cortex* 27, 5477–5484. doi: 10.1093/cercor/bhw314

Korbo, L., Pakkenberg, B., Ladefoged, O., Gundersen, H. J., Arlien-Søborg, P., and Pakkenberg, H. (1990). An efficient method for estimating the total number of neurons in rat brain cortex. *J. Neurosci. Methods* 31, 93–100. doi: 10.1016/0165-0270(90)90153-7

Kornack, D. R. (2000). Neurogenesis and the evolution of cortical diversity: mode, tempo, and partitioning during development and persistence in adulthood. *Brain Behav. Evol.* 55, 336–344. doi: 10.1159/000006668

Kostović, I., Jovanov-Milošević, N., Radoš, M., Sedmak, G., Benjak, V., Kostović-Srzentić, M., et al. (2014). Perinatal and early postnatal reorganization of the subplate and related cellular compartments in the human cerebral wall as revealed by histological and MRI approaches. *Brain Struct. Funct.* 219, 231–253. doi: 10.1007/s00429-012-0496-0

Kostovic, I., and Judas, M. (1995). "Prenatal development of the cerebral cortex," in *Ultrasound and the Fetal Brain,* ed K. C. Chervenack (New York, NY: Parthenon), 1–26.

Kostovic, I., and Rakic, P. (1990). Developmental history of the transient subplate zone in the visual and somatosensory cortex of the macaque monkey and human brain. *J. Comp. Neurol.* 297, 441–470. doi: 10.1002/cne.902970309

Krinsky-McHale, S. J., Devenny, D. A., and Silverman, W. P. (2002). Changes in explicit memory associated with early dementia in adults with Down's syndrome. *J. Intellect. Disabil. Res.* 46, 198–208. doi: 10.1046/j.1365-2788.2002.00365.x

Larsen, C. C., Bonde Larsen, K., Bogdanovic, N., Laursen, H., Graem, N., Samuelsen, G. B., et al. (2006). Total number of cells in the human newborn telencephalic wall. *Neuroscience* 139, 999–1003. doi: 10.1016/j.neuroscience.2006.01.005

Larsen, K. B. (2010). *Expression Patterns of PAX6, MEIS2, OTX2 and OTX1 in the Developing Human Central Nervous System and Stereological Quantification of the Ganglionic Eminence in the Forebrain.* Ph.D, thesis, University of Copenhagen, Copenhagen.

Larsen, K. B., Laursen, H., Graem, N., Samuelsen, G. B., Bogdanovic, N., and Pakkenberg, B. (2008). Reduced cell number in the neocortical part of the human fetal brain in down syndrome. *Ann. Anat.* 190, 421–427. doi: 10.1016/j.aanat.2008.05.007

Larsen, K. B., Lutterodt, M. C., Laursen, H., Graem, N., Pakkenberg, B., Møllgård, K., et al. (2010). Spatiotemporal distribution of PAX6 and MEIS2 expression and total cell numbers in the ganglionic eminence in the early developing human forebrain. *Dev. Neurosci.* 32, 149–162. doi: 10.1159/000297602

Letinic, K., Zoncu, R., and Rakic, P. (2002). Origin of GABAergic neurons in the human neocortex. *Nature* 417, 645–649. doi: 10.1038/nature00779

Ma, T., Wang, C., Wang, L., Zhou, X., Tian, M., Zhang, Q., et al. (2013). Subcortical origins of human and monkey neocortical interneurons. *Nat. Neurosci.* 16, 1588–1597. doi: 10.1038/nn.3536

Malatesta, P., Hartfuss, E., and Götz, M. (2000). Isolation of radial glial cells by fluorescent-activated cell sorting reveals a neuronal lineage. *Development* 127, 5253–5263.

Miyata, T., Kawaguchi, A., Okano, H., and Ogawa, M. (2001). Asymmetric inheritance of radial glialfibers by cortical neurons. *Neuron* 31, 727–741. doi: 10.1016/S0896-6273(01)00420-2

Nelson, L., Johnson, J. K., Freedman, M., Lott, I., Groot, J., Chang, M., et al. (2005). Learning and memory as a function of age in Down syndrome: a study using animal-based tasks. *Prog. Neuropsychopharmacol. Biol. Psychiatry* 29, 443–453. doi: 10.1016/j.pnpbp.2004.12.009

Noctor, S. C., Flint, A. C., Weissman, T. A., Dammerman, R. S., and Kriegstein, A. R. (2001). Neurons derived from radial glial cells establish radial units in neocortex. *Nature* 409, 714–720. doi: 10.1038/350 55553

Pakkenberg, B., and Gundersen, H. J. (1997). Neocortical neuron number in humans: effect of sex and age. *J. Comp. Neurol.* 384, 312–320.

Paredes, M. F., James, D., Gil-Perotin, S., Kim, H., Cotter, J. A., Ng, C., et al. (2016). Extensive migration of young neurons into the infant human frontal lobe. *Science* 354:aaf7073. doi: 10.1126/science.aaf7073

Pelvig, D. P., Pakkenberg, H., Stark, A. K., and Pakkenberg, B. (2008). Neocortical glial cell numbers in human brains. *Neurobiol. Aging* 29, 1754–1762. doi: 10.1016/j.neurobiolaging.2007.04.013

Rabinowicz, T., de Courten-Myers, G. M., Petetot, J. M., Xi, G., and de los Reyes, E. (1996). Human cortex development: estimates of neuronal numbers indicate major loss late during gestation. *J. Neuropathol. Exp. Neurol.* 55, 320–328. doi: 10.1097/00005072-199603000-00007

Rakic, S., and Zecevic, N. (2003). Early oligodendrocyte progenitor cells in the human fetal telencephalon. *Glia* 41, 117–127. doi: 10.1002/glia.10140

Rose, R. D., and Rohrlich, D. (1987). Counting sectioned cells via mathematical reconstruction. *J. Comp. Neurol.* 263, 365–386.

Samuelsen, G. B., Larsen, K. B., Bogdanovic, N., Laursen, H., Graem, N., Larsen, J. F., et al. (2003). The changing number of cells in the human fetal forebrain and its subdivisions: a stereological analysis. *Cereb. Cortex* 13, 115–122. doi: 10.1093/cercor/13.2.115

Samuelsen, G. B., Pakkenberg, B., Bogdanović, N., Gundersen, H. J., Larsen, J. F., Graem, N., et al. (2007). Severe cell reduction in the future brain cortex in human growth-restricted fetuses and infants. *Am. J. Obstet. Gynecol.* 197, 56.e1–7. doi: 10.1016/j.ajog.2007.02.011

Sanai, N., Nguyen, T., Ihrie, R. A., Mirzadeh, Z., Tsai, H. H., Wong, M., et al. (2011). Corridors of migrating neurons in the human brain and their decline during infancy. *Nature* 478, 382–386. doi: 10.1038/nature 10487

Schmidt-Sidor, B., Wisniewski, K. E., Shepard, T. H., and Sersen, E. A. (1990). Brain growth in down syndrome subjects 15 to 22 weeks of gestational age and birth to 60 months. *Clin. Neuropathol.* 9, 181–190.

Sigaard, R. K., Kjær, M., and Pakkenberg, B. (2016). Development of the cell population in the brain white matter of young children. *Cereb. Cortex* 26, 89–95. doi: 10.1093/cercor/bhu178

Sterio, D. C. (1984). The unbiased estimation of number and sizes of arbitrary particles using the disector. *J. Microsc.* 134, 127–136. doi: 10.1111/j.1365-2818.1984.tb02501.x

Tamamaki, N., Fujimori, K. E., and Takauji, R. (1997). Origin and route of tangentially migrating neurons in the developing neocortical intermediate zone. *J. Neurosci.* 17, 8313–8323.

The Boulder Committee (1970). Embryonic vertebrate central nervous system: revised terminology. *Anat. Rec.* 166, 257–261. doi: 10.1002/ar.1091660214

Uylings, H. B. (2000). Development of the cerebral cortex in rodents and man. *Eur. J. Morphol.* 38, 309–312. doi: 10.1076/0924-3860(200012)38:51-HFT309

Walløe, S., Eriksen, N., Dabelsteen, T., and Pakkenberg, B. (2010). A neurological comparative study of the harp seal (*Pagophilus groenlandicus*) and harbor porpoise (*Phocoena phocoena*) brain. *Anat. Rec. (Hoboken).* 293, 2129–2135. doi: 10.1002/ar.21295

Walløe, S., Pakkenberg, B., and Fabricius, K. (2014). Stereological estimation of total cell numbers in the human cerebral and cerebellar cortex. *Front. Hum. Neurosci.* 8:508. doi: 10.3389/fnhum.2014.00508

Wang, X., Chang, L., Guo, Z., Li, W., Liu, W., Cai, B., et al. (2013). Neonatal SVZ EGFP-labeled cells produce neurons in the olfactory bulb and astrocytes in the cerebral cortex by *in-vivo* electroporation. *Neuroreport* 24, 381–387. doi: 10.1097/WNR.0b013e328360f7ef

Weibel, E. R., and Gomez, D. M. (1962). A principle for counting tissue structures on random sections. *J. Appl. Physiol.* 17, 343–348.

West, M. J. (2012). Introduction to stereology. *Cold Spring Harb Protoc.* 2012, pdb.top070623. doi: 10.1101/pdb.top070623

West, M. J., Slomianka, L., and Gundersen, H. J. (1991). Unbiased stereological estimation of the total number of neurons in the subdivisions of the rat hippocampus using the optical fractionator. *Anat. Rec.* 231, 482–497. doi: 10.1002/ar.1092310411

Winick, M. (1968). Changes in nucleic acid and protein content of the human brain during growth. *Pediatr. Res.* 2, 352–355.

Conflict of Interest Statement: The author declares that the research was conducted in the absence of any commercial or financial relationships that could be construed as a potential conflict of interest.

frontiers in Neuroanatomy

PROTOCOLS
published: 30 October 2018
doi: 10.3389/fnana.2018.00073

Maximizing Explanatory Power in Stereological Data Collection: A Protocol for Reliably Integrating Optical Fractionator and Multiple Immunofluorescence Techniques

Anna Kreutz[1] *and Nicole Barger*[2,3]*

[1] Neuroscience Graduate Program, University of California, Davis, Davis, CA, United States, [2] Department of Psychiatry and Behavioral Sciences, University of California, Davis, Sacramento, CA, United States, [3] MIND Institute, University of California, Davis, Sacramento, CA, United States

With the promise of greater reliability and replicability of estimates, stereological techniques have revolutionized data collection in the neurosciences. At the same time, improvements in immunohistochemistry and fluorescence imaging technologies have facilitated easy application of immunofluorescence protocols, allowing for isolation of multiple target proteins in one tissue sample. Combining multiple immunofluorescence labeling with stereological data collection can provide a powerful tool to maximize explanatory power and efficiency, while minimizing tissue use. Multiple cell classes, subtypes of larger populations, or different cell states can be quantified in one case and even in one sampling run. Here, we present a protocol integrating stereological data collection and multiple immunofluorescence using commonly employed widefield epifluorescence filter sets, optimized for blue (DAPI), green (FITC), and far red (CY5) channels. Our stereological protocol has been designed to accommodate the challenges of fluorescence imaging to overcome limitations like fixed filter sets, photobleaching, and uneven immunolabeling. To enhance fluorescence signal for stereological sampling, our immunolabeling protocol utilizes both high temperature antigen retrieval to improve primary antibody binding and secondary antibodies conjugated to optimally stable fluorophores. To illustrate the utility of this approach, we estimated the number of Ctip2 immunoreactive subcerebral projection neurons and NeuN immunoreactive neurons in rat cerebral cortex at postnatal day 10. We used DAPI (blue) to define the neocortex, anti-NeuN (far red) to identify neurons, and co-labeling of anti-Ctip2 (green) and anti-NeuN (far red) to isolate only subcerebral projection neurons. Our protocol resulted in estimates with low sampling error (CE $<$ 0.05) and high intrarater reliability (ICC $>$ 0.98) that fall within the range of published values, attesting to its efficacy. We show our immunofluorescence techniques can be used to reliably identify other cell types, e.g., different glial cell classes, to highlight the broader applications of our approach. The flexibility of the technique, increasingly reduced costs of fluorescence technologies, and savings in experimental time and tissue use make this approach valuable for neuroscientists interested in incorporating stereology to ask precise neurophysiological and neuroanatomical questions.

Keywords: optical fractionator, photobleaching, Ctip2, NeuN, neurons, microglia, oligodendrocytes, astrocytes

OPEN ACCESS

Edited by:
Karl-Anton Dorph-Petersen, Aarhus University, Denmark

Reviewed by:
Carlos Avendaño, Universidad Autónoma de Madrid, Spain
Miguel Angel García-Cabezas, Boston University, United States

***Correspondence:**
Nicole Barger
nbarger@ucdavis.edu

Received: *30 March 2018*
Accepted: *20 August 2018*
Published: *30 October 2018*

Citation:
Kreutz A and Barger N (2018) Maximizing Explanatory Power in Stereological Data Collection: A Protocol for Reliably Integrating Optical Fractionator and Multiple Immunofluorescence Techniques. Front. Neuroanat. 12:73. doi: 10.3389/fnana.2018.00073

INTRODUCTION

The introduction of stereological methods to neuroscientific questions has provided novel and, more importantly, reliable tools for quantitative data collection, rapidly becoming the gold standard in the field. The optical fractionator technique, specifically, is used to obtain numerical estimates of cell number (Gundersen, 1986; West, 1993a). Of particular utility for neuroscientists, it is not reliant on structure volume, circumventing potential confounds that can be introduced by a variety of tissue processing artifacts (West et al., 1991). The optical fractionator has been applied in diverse contexts. In the human brain, work by modern neurostereologists has revealed important insights into the number of neurons and glia in a variety of cortical and subcortical brain structures (West, 1993b; Pakkenberg and Gundersen, 1997; Semendeferi et al., 1998, 2001; Uylings et al., 2006; Pelvig et al., 2008), as well as cellular variation in diverse mental disorders (Berretta et al., 2007; Kreczmanski et al., 2007; Camacho et al., 2014; Morgan et al., 2014). Rigorous stereological methods provide a means to estimate biological effects in experimental research and have been used to characterize neuronal variation in animal models of autism, fetal alcohol syndrome, and schizophrenia (Karlsen et al., 2013; Karacay et al., 2015; Lauber et al., 2016). Many analyses use morphological criteria to discriminate between cell types as revealed by traditional stains, like Nissl. While generally useful, morphological criteria cannot always be used to identify every cell type or process of interest in the brain and alternative approaches may be warranted.

To address a broader array of questions, neurostereology can be performed in conjunction with immunohistochemistry to label specific, biologically meaningful "markers" indicative of particular cell types, subclasses, or even states. Employing multiple immunolabeling can further refine and increase the breadth of experimental questions addressed with stereological analysis. A variety of stereological studies have used a single antibody, e.g., against a protein associated with cortical interneurons or serotonergic fibers, to quantify functionally relevant variation in neuronal subtypes across diverse species (Raghanti et al., 2008; Sherwood et al., 2010; Hou et al., 2011; Stimpson et al., 2016). However, protein markers are not always cell specific, limiting the precision and scope of single-labeling approaches. For example, while expression of the transcription factor Ctip2 can be used as a marker to identify subcerebral projection neurons, a small population of other cells are also immunoreactive for Ctip2 (Arlotta et al., 2005). To ensure only neurons expressing Ctip2 are sampled, an additional neuronal marker, like NeuN, is needed (Mullen et al., 1992; Lyck et al., 2007). In such cases, employing multiple immunolabeling with a combination of markers enhances diagnostic precision, improving internal validity. An obvious additional advantage of multiple labeling is the ability to quantify multiple cell types in one tissue series or even stereological sampling run. In rare cases, this can be accomplished with one antibody. For example, we previously reported that we could use nuclear volume to simultaneously stereologically quantify neurons and all glial cell types, if we used a single antibody to segregate microglia whose nuclear volumes overlap with other glia (Morgan et al., 2014). However, most cell types cannot be identified with traditional counterstains. With a standard four-channel epifluorescence setup, up to four separate markers can be used in the same tissue section to quantify diverse cell types and/or clarify markers with complicated expression patterns.

For multiple labeling, fluorescence provides many advantages over enzymatic immunohistochemistry. Generally, they include: a quicker staining protocol, lower reagent cost, and elimination of toxic chemicals commonly used in chromogenic staining, such as DAB (Griswold et al., 1968; Egilsson et al., 1979; Konopaske et al., 2008; Prasad and Richfield, 2010). Although multiple chromogens can be used in enzymatic techniques, fluorophores emitting in individual fluorescence channels provide more distinct and consistent labeling, improving discrimination between antibodies. For stereology, this helps to ensure that the correct cell types are sampled during data collection. Unlike the relatively uniform signal produced by individual fluorophores with standardized spectral properties, labeling in enzymatic immunohistochemistry is highly dependent on incubation conditions during color development. It is particularly sensitive to timing, resulting in variable labeling if consistent parameters are not maintained. This can complicate identification of markers that are naturally variably expressed, e.g., some transcription factors like Ctip2. Because it eliminates dehydration steps and requires briefer section drying time (∼15 min), immunofluorescence labeling results in substantially increased final section thickness compared with enzymatic techniques (Prasad and Richfield, 2010). Thicker sections are preferred for optical fractionator sampling, while it is easier to identify single cells during sampling when tissue height is less compressed. These advantages of immunofluorescence can be harnessed to benefit stereological investigation.

At the same time, immunofluorescence does introduce challenges. Fluorophore selection will likely be limited by the availability of only a few fixed filter sets, as most labs will find it cost prohibitive to have more than a standard set. Inappropriate fluorophore choices could result in "bleed-through" between fluorescence channels that could be interpreted as false positives and reduce the amount of signal that could be visualized. Thus, fluorescence labeling schemes must be optimized to suit fixed spectra, which requires more initial planning than brightfield microscopy. Secondary antibodies can bind to "sticky" regions of tissue, increasing background signal and making it difficult to discriminate low expressing markers. Most importantly, signal can be rapidly lost during data collection as fluorophores photobleach. Some researchers also favor enzymatic immunohistochemistry for stereology as the labeling is maintained nearly indefinitely. To overcome these challenges, we have tested several experimental procedures and fluorophores to develop a reliable working protocol for the stereological quantification of diverse cell types using immunofluorescence.

Here, we present an optimized protocol that is designed to circumvent major issues with immunofluorescence that could impact stereological quantification of cell population estimates with the optical fractionator. To increase epitope availability and

enhance fluorescence signal, it uses antigen retrieval (Ramos-Vara and Miller, 2014). To reduce collapse in tissue height during processing and allow for more complete antibody penetration, immunolabeling is performed on free-floating tissue. To avoid excessive photobleaching during data collection, we tested several fluorophores to choose the most photostable fluorophore. As a test of our protocol, we present an optical fractionator study of rat cortex at postnatal day 10 that estimates: (1) the number of subcerebral projection neurons, defined by co-labeling of the established markers Ctip2 and NeuN (Arlotta et al., 2005; Lyck et al., 2007), and (2) the total population of $NeuN^+$ neurons. We selected Ctip2 because, as mentioned, it makes for a particularly difficult test case, slowing data collection and increasing the potential for photobleaching. Attesting to the efficacy of our protocol, we found that it facilitated the unambiguous identification of $Ctip2^+/NeuN^+$ subcortical projection neurons, yielded low error rates, and produced estimates of $NeuN^+$ neurons consistent with published data, even in a small sample of animals ($N = 5$). To show that our protocol could be extended to address diverse neurobiological questions, we additionally illustrate that various cell types, like microglia, oligodendrocytes, and astroglia, as well as cell states, like "activated" or "quiescent" microglia, can be identified using our immunofluorescence protocol.

MATERIALS AND EQUIPMENT

Multiple Immunolabeling

Equipment

Cryostat or microtome
Rotator (Barnstead Lab-Line, 4630).
Stir plate (VWR, 12365-382).
6 qt. rice steamer (Oster, model 5712).

Reagents and Solutions

Cryoprotectant
30% sucrose in 0.1M PBS (phosphate buffered saline).

Refrigerator storage solution
0.01% sodium azide (Acros, 19038-1000) in 0.1M PBS.

Tissue collecting solution for freezer storage
Glycerol (Fisher, G33-1).
ddH_2O (double distilled water).
Ethylene glycol (Fisher, E178-1).
0.2 M PBS.

Fluorescence labeling
2–3 primary antibodies from host species with no cross-reactivity (e.g., chicken, goat, and rabbit).
2–3 secondary antibodies from one host species directed against the primary antibody hosts and conjugated to a green, red, or far red fluorophore (e.g., donkey anti-rabbit conjugated to AF-488).
DAPI.

10 mM citrate buffer, pH 6.0
Citric Acid, Anhydrous (Affymetrix, AAJ1372936).
Tween20 (Acros, AC233360010).
ddH_2O.

Antibody dilution buffer
Serum matched to secondary antibody host species (e.g., donkey serum: Millipore, 566460).
Triton X-100 (Acros, AC327372500).
0.1 M PBS.

Mounting medium
Glycerol (Fisher, G33-1).
Mowiol (Calbiochem, 475904).
ddH_2O.
0.2 M Tris Buffer, pH 8.5.

Materials

24-well plates or Eppendorf tubes for tissue storage.
Netwells in 12-well plates (Corning, 3478).
Heat-resistant plastic jars (Histoplex).
Superfrost Plus Glass Slides (Fisher, 12-550-15).
Coverslips, 0.13–0.17 mm (Fisher, 12-548-5p).
Optimal Cutting Temperature (Fisher, 23-730-571).
Hooked glass rod or brush to manipulate tissue.
Brain tissue previously fixed with 4% Paraformaldehyde or 10% Formalin.

Optical Fractionator

Equipment

Stereology software suite (Stereo Investigator: MBF Bioscience, Williston, VT, United States).
Computer.
Microscope (Olympus BX61 microscope: Olympus, Tokyo, Japan).
High magnification oil lens, numerical aperture > 1.0 (60× PlanApo: Olympus, Tokyo, Japan).
Low magnification air lens (2× PlanApo: Olympus, Tokyo, Japan).
Fluorescence illumination system (Prior, Rockland, MA, United States).
Filter Cubes (DAPI, FITC, TRITC, and Cy5 filter sets: Chroma, Bellows Falls, VT, United States).
Monochrome video camera with high sensitivity in visible and near infra-red wavelengths (e.g., Hamamatsu, ORCA-ER-1394).
Automated stage (Prior, Rockland, MA, United States).
Microcator (Heidenhain, Plymouth, MN, United States).

Reagents and Solutions

Immersion oil, refraction index matched to mounting medium (e.g., Olympus, MOIL-30).

Materials

Immunolabeled tissue series.

STEPWISE PROCEDURES

Sectioning

For the optical fractionator, tissue should be cut in a consistent manner, maintaining a common section thickness. While

the optimal sectioning method is debated, measures can be incorporated into stereological study design to buffer against biases introduced by specific processing techniques (Dorph-Petersen et al., 2001; Gardella et al., 2003; Schmitz and Hof, 2005). Especially, application of the estimators introduced by Dorph-Petersen et al. (2001) and described in Section 3.3 will produce the most reliable estimates across sectioning techniques. We choose to cryosection tissue at 50 μm to ensure tissue thickness after shrinkage does not fall below the recommended minimum of 15 μm for counting neurons (Howard and Reed, 2005). Our immunofluorescence protocol can mitigate the influence of potential sources of bias reported for cryosectioned tissue, namely, poor cell morphology and considerable collapse in thickness (Dorph-Petersen et al., 2001; Ward et al., 2008). Cell identification is enhanced by fluorescent-tagged antibodies and shrinkage is reduced by omitting dehydration steps and minimizing exposure to air. As alternatives, celloidin embedding is impractical for multiple immunolabeling and paraffin embedded tissue requires considerably more processing, although they are reported to produce good numerical estimates with Nissl stains (Gardella et al., 2003; Ward et al., 2008). Additional processing steps can introduce more opportunities for failed or inconsistent immunolabeling across individual tissue series. Vibratome sectioning has been indicated to produce some of the most extreme artifacts but may be used with appropriate corrections (Dorph-Petersen et al., 2001; Gardella et al., 2003; Ward et al., 2008). Prior to sectioning, whole brains or tissue blocks should be fixed by immersion or perfusion in accordance with laboratory protocol and university Institutional Animal Care and Use Committee (IACUC) guidelines (for more detail on our perfusion protocol see Cunningham et al., 2013). All brains used in this study (N = 5) were perfused. Our study was performed in compliance with the NIH Guide for Care and Use of Laboratory Animals and the University of California at Davis IACUC. Our protocol proceeds as follows.

Tissue Processing

(A) Transfer a whole brain or tissue block to a cryoprotectant solution containing 30% sucrose in 0.1 M PBS. The brain is ready for freezing when it is saturated with cryoprotectant and has sunk to the bottom of the solution.

- For small brains or tissue blocks, this can take 24 h. For larger brains, it can take longer. In the latter case, solutions should be changed every 3–5 days or 0.01% sodium azide should be added to the solution to prevent contamination.

(B) Freeze brains to prepare for cryosectioning.

- We freeze small brains in a container housing a glass dish containing 2-methylbutane cooled on dry ice. Enough 2-methylbutane should be added to cover most, but not all, of the cryomold. We extract the specimen from the cryoprotectant and gently dab it on a Kimwipe to remove excess liquid before placing the brain in a cryomold and covering in Optimal Cutting Temperature (OCT). Note the orientation, the front, and the back of the specimen on the cryomold prior to freezing. Once tissue has frozen to a white solid, usually ∼10 min, brains can be stored at −80°C or cut immediately.

(C) Cryosection brains coronally at 50 μm on a cryostat or sliding microtome.

(D) Collect sections, systematically, in a numbered well plate or Eppendorf tubes, ensuring the rostrocaudal order of sectioning is maintained.

- Well plates and tubes can be filled with 0.01% sodium azide for short term storage at 4°C or tissue collecting solution (TCS) for longer storage at −20 or −80°C.

Solutions

Cryoprotectant solutions can be used for storing tissue at −20 or −80°C to prevent freezing. This is particularly advantageous for longer term storage. We use the following TCS as our cryoprotectant.

TCS protocol

(A) Prepare a solution containing:

500 mL Glycerol.
400 mL ddH_2O.
600 mL Ethylene glycol.
500 mL 0.2 M PBS.

(B) Mix well.

(C) Store at 4°C.

Immunolabeling

For immunolabeling, we employ several modifications intended to increase signal, reduce background fluorescence, and preserve section thickness to support stereological data collection. We

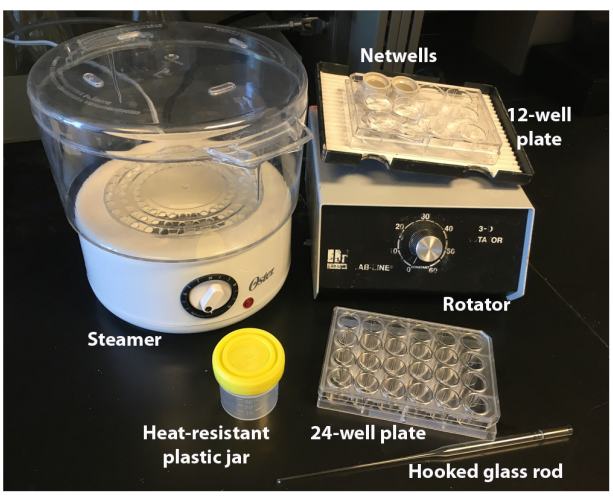

FIGURE 1 | Immunolabeling equipment. Equipment necessary for our antigen-retrieval immunolabeling procedure. Netwells and 12-well plate are used for PBS rinses, steamer and plastic jars for antigen-retrieval, 24-well plate for blocking and antibody steps, and glass rod for manipulating tissue.

use a variant of common heat induced epitope retrieval (HIER) techniques that incorporates a neutral pH Citrate Buffer and rice steamer (**Figure 1**). Compared with other heating methods, like microwaving tissue, the steamer provides steady, high temperature heating, is inexpensive, produces robust labeling of our antigens of interest, and reduces tissue deformation (Tang et al., 2007; Ramos-Vara and Miller, 2014; Vinod et al., 2016). This allows us to stain tissue free-floating to improve antibody penetration. While high heat antigen retrieval increases the availability of many epitopes, it is important to note that some epitopes are sensitive to heat. In these cases, it may be best to omit the antigen retrieval step or use an alternative, lower temperature, method. We also include TritonX-100 in many solutions to increase membrane permeability, which proves especially beneficial for antibodies targeting epitopes localized to the nucleus like Ctip2 and NeuN. Additionally, using fluorophores conjugated to secondary antibodies, rather than directly to primary antibodies, amplifies the signal and provides greater flexibility, increasing the array of commercial fluorophores available for selection and the combination of primary antibodies that can be used in different channels. One drawback is the potential for higher background fluorescence resulting from non-specific binding of secondary antibodies. To reduce false signal, we incorporate serum from the host of the secondary antibodies into our blocking and antibody dilution buffers at high concentrations. This step improves cell discrimination during stereological data collection.

Several considerations need to be taken into account when deciding which secondary antibody conjugated fluorophores to use for multiple labeling. Choosing stable fluorophores with a high quantum efficiency and yield is especially important in widefield epifluorescence microscopy which produces greater light scatter and does not easily filter out of focus photons compared with confocal microscopy (Murphy and Davidson, 2013). Determining which markers to place in which channel is another important consideration. Because they cannot be optimized for every fluorophore, fixed filter sets increase the possibility of fluorescence signal bleed-through between channels. This is particularly problematic when primary antibodies co-localize, increasing the likelihood that bleed-through from adjacent fluorescence channels could be misinterpreted as true co-labeling. It may be necessary to separate these markers into non-adjacent fluorescence channels that would not be excited by the same wavelengths. For our two overlapping markers, NeuN and Ctip2, we were unable to avoid some degree of bleed-through between the green (FITC) and red (TRITC) channels, even after trying multiple combinations of fluorophores. Consequently, we minimized the possibility of spectral overlap by placing them in the green and far red (Cy5) channels, omitting the red channel entirely (**Figure 2**). Green and red fluorophores tend to be brighter than those in far red and ultraviolet wavelengths (Murphy and Davidson, 2013). To maximize signal from the variably expressed Ctip2 antibody, we used a secondary antibody conjugated to the bright green fluorophore, AF-488, while we labeled the robustly expressed NeuN primary with a dimmer far red secondary, AF-647. All four fluorescence channels could be utilized in cases where antibody targets are easier to discriminate, e.g., when different antibodies label separate, non-overlapping cellular components. For example, we used anti-Olig2 to label oligodendrocyte nuclei in the far red channel with AF-647, anti-Iba1 to label the cell bodies and the fine processes of microglia in the green channel with AF-488, and anti-S100β to label astrocyte cytoplasm and processes in the red channel with AF-594 (**Figure 3**), finding them to all to be morphologically discriminable (Dyck et al., 1993; Ito et al., 1998; Zhou and Anderson, 2002).

A primary disadvantage of fluorescence stereology is photobleaching. In order to overcome this issue, a number

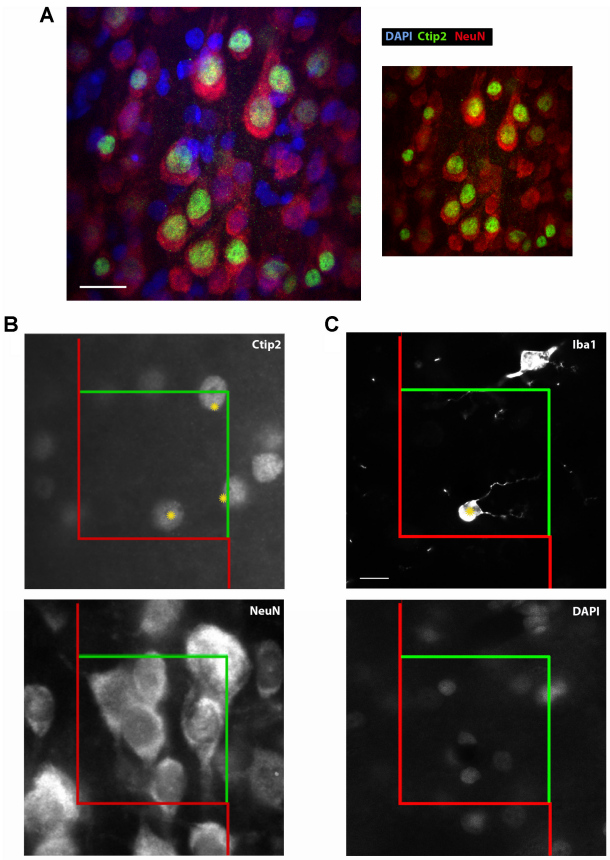

FIGURE 2 | Ctip2 and NeuN labeling. Postnatal day 10 rat cortex immunolabeled with DAPI (blue), Ctip2 (green), and NeuN (far red, colored red here), imaged on our confocal microscope, 60× **(A)**. The transcription factor Ctip2 shows its characteristic nuclear labeling pattern, whereas NeuN labeling is appropriately nuclear and extra-nuclear. Ctip2 is variably expressed in the nuclei of neurons labeled with NeuN. Where Ctip2 expression is low, co-labeling of NeuN, Ctip2, and the nuclear marker DAPI is clear. Ctip2 and NeuN IR in monochrome images at the same sampling site from our epifluorescent setup **(B)**. Ctip2 is in the green channel and NeuN is in the far red channel. Ctip2 and NeuN signals are discrete with no spectral overlap between green and far red channels. Microglia can also be readily quantified using our protocol **(C)**. Microglia can be counted if the widest point of the nucleus, confirmed with DAPI, comes into focus within the counting frame. Scale bar = 20 μm **(A)**, 10 μm **(C)**. Yellow asterisks (*) indicate $Ctip2^{+}$/$NeuN^{+}$ neurons and $Iba1^{+}$ microglia that meet criteria necessary to be sampled in the disector.

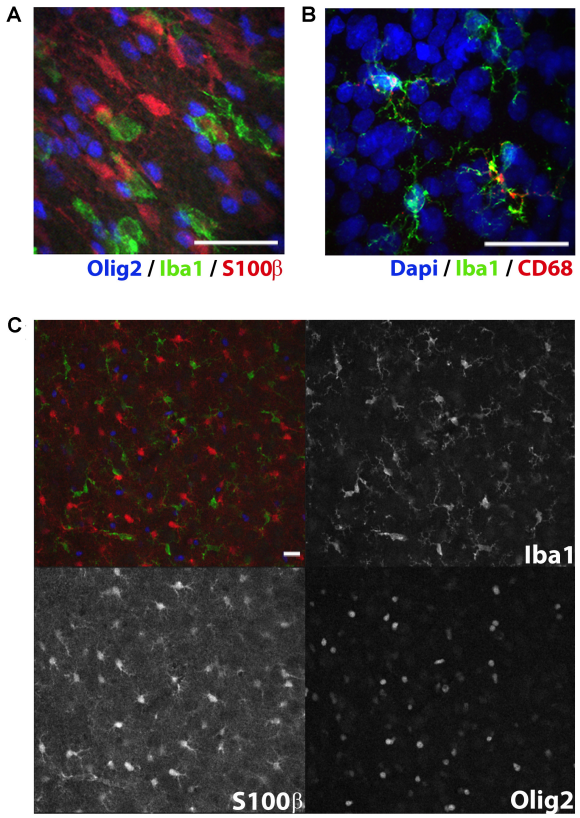

FIGURE 3 | Immunolabeling of glial subtypes in postnatal day 10 rat white matter. Olig2 (far red, colored blue here), Iba1 (green), and S100β (red) clearly label oligodendrocytes, microglia, and astrocytes, respectively **(A)**. Punctate CD68 (red) expression was observed in some but not all Iba1+ microglia (green) in the cerebral cortex **(B)**. Expression pattern of CD68 appropriately reflects the endosomal and lysosomal distribution of this glycoprotein. Expression indicates particularly activated microglia. Low magnification image showing individual channel expression **(C)**. Image acquired with a confocal microscope. Scale bar = 20 μm.

of parameters can be optimized, most critically the specific fluorophores used. Prior to running the stereological analysis, we suggest verifying the robustness of labeling through photobleaching experiments to identify which fluorophores would be sufficiently stable. We tested secondary antibodies conjugated to green, Cy2 (Jackson) and AF-488 (Life Technologies), and far red, AF-647 (Jackson) and NL-637 (R&D Systems), fluorophores directed against our primary antibody, rabbit-anti Ctip2, each at a dilution of 1:500. Another parameter that can be optimized to minimize photobleaching is mounting media. We prepared slides with one fluorophore, AF-488, coverslipping with either our own mounting medium, Mowiol, or one sold as being particularly stable, Prolong Gold. All slides were allowed to dry overnight. We stimulated each fluorophore with the appropriate filter for up to 15 min, taking images of fluorescence emission after 0.5, 2, 3, 4, 5, 6, 8, 10, 12, and 15 min. Exposure time was set at 250 ms to give a relatively bright, even image of Ctip2 across samples. Using images from our set exposure times, we then determined the mean gray values in Fiji (ImageJ) and calculated the percent reduction in signal intensity. We subsequently chose to label Ctip2 with AF-488 and NeuN with AF-647 and to coverslip with Mowiol because emission of these fluorophores lasted well past the time we anticipated it would take to complete sampling at one probe site during stereological quantification (∼2 min).

All antibodies should be tested on a few sections prior to running the whole series for the analysis, employing proper positive and/or negative controls. Once the appropriate labeling scheme has been established, a series of 10 or more sections through the entire region of interest should be selected from each case for immunolabeling and stereological sampling. According to the fractionator principle (Gundersen et al., 1988), sections should be sampled at evenly spaced intervals with the starting section randomly selected from the first interval for each individual in the analysis. For example, if 40 sections span the region of interest in an individual, immunohistochemistry could be performed on every 4th section to yield 10 sections for stereological analysis. If the random number 2 is chosen as the starting point in the first interval, the sections sampled would include 2, 6, 10, 14, etc. Choosing an even section interval is advantageous because, if the first staining run does not yield a sufficient number of sections through the region of interest, an additional intermediate series can be run to add to existing counts. Our immunolabeling protocol is described below, followed by a step by step protocol for mixing solutions. **Table 1** lists concentrations for the primary and secondary antibodies used to test our protocol.

Antigen Retrieval

(A) Transfer selected sections to netwells in 12 well plates (**Figure 1**), being careful to track brains run in parallel with careful labeling throughout.
(B) Fill reservoir of the rice steamer with ddH_20, replace steamer basket, and rotate knob to 45 min mark.
(C) While waiting for steamer to warm, rinse tissue 3 times for 5 mins in fresh 0.1 M PBS (3 × 5 mins) on a rotator using netwells in plastic 12 well plates.
(D) With a glass hook, transfer tissue to heat-resistant plastic jars filled with 20 mL of 10 mM Citrate Buffer. Cap lids loosely to prevent pressure buildup and place jars around the edges inside the steamer to ensure more even heating.
(E) Heat sections in the steamer for 8–15 min, depending on tissue integrity.
(F) Remove jars, uncap, and allow to cool for 5 min or until room temperature is reached.
(G) Rinse tissue 3 × 5 min in PBS using netwells and 12 well plates on a rotator.

Blocking

(A) Rinse tissue 3 × 5 min in PBS using netwells and 12 well plates on a rotator.
(B) Pipette 500 μl of the Blocking Buffer into each well of a 24 well plate.
(C) Transfer sections to well plates with a glass hook being careful to maintain section order.
(D) Place well plate on a rotator at room temperature for 1 h.

TABLE 1 | Overview of primary and secondary antibodies.

Antibody	Dilution	Supplier	Cat. No.
Rabbit anti-Ctip2	1:400	Abcam	ab28448
Rabbit anti-Iba1	1:500	Wako	019-19741
Mouse anti-NeuN	1:400	Millipore	MAB377
Mouse Anti-CD68	1:500	Bio-Rad	MCA341GA
Mouse Anti-S100ß	1:200	Abcam	ab4066
Goat Anti-Olig2	1:500	R&D	AF2418-SP
Donkey anti-rabbit Alexa Fluor-488	1:500	Invitrogen	A-21206
Donkey anti-rabbit Cy2	1:500	Jackson ImmunoResearch	711-225-152
Donkey anti-mouse AF-594	1:500	Jackson ImmunoResearch	715-585-020
Donkey anti-rabbit Alexa Fluor-647	1:500	Jackson ImmunoResearch	711-605-152
Donkey anti-rabbit NL-637	1:500	R&D Systems	NL008
Donkey anti-goat AF-647	1:500	Jackson ImmunoResearch	705-605-147
DAPI	1:1000	Roche	10236276001

Primary Antibodies

(A) Add all primary antibodies (up to four, each from different species) to Antibody Dilution Buffer at room temperature.
(B) Pipette 500 µl of the primary antibody solution into each well of a 24 well plate.
(C) Transfer sections to primary antibody solutions with a glass hook being careful to maintain section order.
(D) Incubate sections overnight at room temperature on a shaker.
(E) Rinse tissue 3 × 5 min in PBS using netwells and 12 well plates on a rotator.

Secondary Antibodies

(A) Add all secondary antibodies for each of the primary antibodies added in 3.2.3A to Antibody Dilution Buffer.
(B) Pipette 500 µl of the secondary antibody solution into each well of a 24 well plate.
(C) Transfer sections to secondary antibody solutions with a glass hook being careful to maintain section order.
(D) Incubate for 2 h at room temperature on a shaker.
(E) Rinse tissue 3 × 5 min in 1/3 PBS diluted in ddH_2O using netwells and 12 well plates on a rotator.
(F) Mount tissue onto glass slides in 1/3 PBS.
(G) Coverslip within 15 min of mounting using Mowiol.

Solutions

Prepare the following prior to immunostaining. Citrate Buffer and Mowiol can be prepared well in advance and stored as indicated. Blocking and antibody dilution solutions can be prepared during the immunostaining protocol in advance of use. They should incorporate serum from the host of the secondary antibodies. We prefer secondary antibodies raised in donkey because they are commonly available conjugated to an array of different fluorophores.

10 mM citrate buffer, pH 6.0

(A) Add 1.92 g Citric Acid Anhydrous to 900 mL ddH_2O.
(B) Stir until dissolved.
(C) Adjust pH to 6.0 with NaOH.
(D) Volumize to 1 L.
(E) Add 0.5 mL Tween20.
(F) Store at 4°C for up to 1 month.

Mowiol mounting medium

(A) Add 19 mL (24 g) Glycerol, 9.6 g Mowiol 4–88, and 48 mL 0.2M Tris Buffer (pH 8.5) to 24 mL ddH_2O.
(B) Stir on hot plate at mid-high setting until combined (∼4–5 h) and do not let boil.
(C) Aliquot into 50 mL Falcon tubes.
(D) Centrifuge at 50,000 × *g* for 15 min.
(E) Discard pellet.
(F) Aliquot supernatant.
(G) Store at 4°C for 1 month or −20°C for 12 months.

Blocking buffer

(A) Thaw donkey serum on ice.
(B) For blocking, prepare a solution that includes 10% donkey serum and 0.3% Triton X-100.
- It is helpful to work with a stock solution of 5–10% Triton X-100 to minimize inaccurate pipetting and facilitate mixing of the viscous stock solution.

(C) Volumize with PBS.
(D) Store on ice until use.

Antibody dilution buffer

(A) Prepare a solution comprising 8% donkey serum, 0.3% Triton X-100, and PBS.
- This buffer is used for primary and secondary antibodies.

(B) Store on ice until use.

Optical Fractionator Data Collection

The optical fractionator is a multi-stage systematic random sampling scheme (Gundersen, 1986; Gundersen et al., 1988; West, 1993a). Decisions about three critical sampling parameters need to be made prior to undertaking the full experimental run: disector volume, grid size, and section sampling interval.

The section sampling interval should be chosen prior to immunolabeling as indicated in the previous section, with sections evenly spaced and the first section chosen randomly from the first interval according to the fractionator principle (Gundersen et al., 1988). The disector is a three-dimensional counting frame (box) used to directly sample cells in conjunction with a precise, "dimensionless" criterion identifiable in a single, thin optical plane (**Figure 4**). Total cell counts are obtained by systematically sampling cells in a series of disectors distributed across all sections in the sample containing the region of interest. These disectors are evenly spaced, located at the intersection of the horizontal and vertical lines of a two-dimensional sampling grid superimposed in a random position over each section. Total cell population (N) estimates are derived using the formula:

$$N = \sum Q^{-} \times \frac{1}{ssf} \times \frac{1}{asf} \times \frac{t}{h} \quad (1)$$

where Q^{-} is the total number of cells sampled, t is the section thickness, and h is the height of the disector. The *asf*, or area sampling fraction, is the ratio of the area (length × width) of the disector to the area of the sampling grid square. The *ssf* is the section sampling fraction, or the interval between sampled sections, e.g., 1/10 for every 10th section. While most measures are straightforward, there is some discussion of the appropriate measure for t. Cut thickness could be used to approximate section thickness. However, because tissue processing often results in shrinkage and/or other distortions in section thickness, using cut thickness in the equation is not recommended. Using the mean tissue thickness measured across sampling sites provides a better estimate for t. In cases where measured tissue thickness within individual sections is highly variable, it should be number-weighted (for calculation see the original formula proposed by Dorph-Petersen et al., 2001). As a rule, it is best to use number-weighted thickness in the calculation because it provides the most accurate estimates across sampling conditions (Dorph-Petersen et al., 2001; Bermejo et al., 2003).

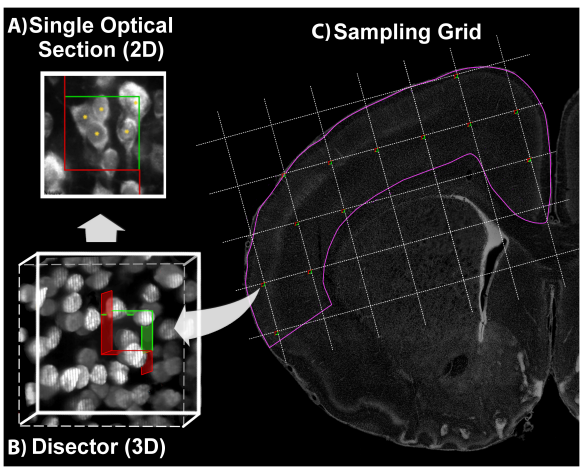

FIGURE 4 | Optical Fractionator. Using a defined criterion (here, the widest point of the Ctip2^{+} nucleus), individual cells in a single optical plane or "section" are marked in the sample (yellow asterisk) if they fall within the disector, touch the green lines of inclusion, and do not touch the red lines of exclusion **(A)**. In the single optical section illustrated here, five cells are counted, including four with nuclei that fall within the disector and one that touches the upper and right green lines of inclusion. One cell is excluded because its lower boundary touches the bottom red line. Cells are sampled in a 3-dimensional disector probe **(B)**. To sample cells, the observer focuses up and down through the entire disector, evaluating each cell that comes into focus in a single optical plane. These 3-dimensional disectors are located at each intersection point on a sampling grid superimposed over each section. This is illustrated on a coronal section of a postnatal day 10 rat brain **(C)**. DAPI was used to delineate the cortical region of interest (pink line). The probe proceeds across the sampling grids from disector to disector in each section until all sections have been sampled.

Guard zones, fixed buffers set above and/or below the disector, should be employed as an additional precaution to mitigate the effects of tissue processing. Processing artifacts at the cut surface, like compression or "lost caps," can bias cell distribution at the outer margins of the tissue, which could, in turn, bias final estimates (Andersen and Gundersen, 1999; Mouton, 2002; Gardella et al., 2003; Howard and Reed, 2005; Ward et al., 2008). Thus, it is often advisable to situate the disector away from the cut surface, where cell distribution in the z-axis is relatively uniform and less affected by processing, to ensure accurate estimates (**Figure 5**). For example, the top of the disector is commonly set at least 2.5 μm below the top of the tissue section, i.e., with a 2.5 μm guard zone. In some cases, complete omission of guard zones has been advocated (Hatton and von Bartheld, 1999; Carlo and Stevens, 2011). We suggest that a preliminary analysis of cell distribution in the z-axis be performed to evaluate these factors.

Our analyses are performed using a widefield epifluorescence Olympus BX61 microscope (Olympus, Tokyo, Japan) and the Stereo Investigator (MBF Bioscience, Williston, VT, United States) software suite. In addition to the standard stereology setup requiring an automated stage (Prior, Rockland, MA, United States) for systematic sampling and microcator for measuring tissue thickness (Heidenhain, Plymouth, MN, United States), the microscope (**Figure 6**) is equipped with a Lumen 200 fluorescence illumination system (Prior, Rockland, MA, United States) with filter cubes optimized for DAPI (blue), FITC (green), TRITC (red), and Cy5 (far red) (Chroma, Bellows Falls, VT, United States). Fluorescence signal is transmitted to a Dell workstation via a monochrome video camera with high sensitivity in visible and near infra-red wavelengths (Hamamatsu, ORCA-ER-1394), which improves visualization and reduces fluorophore fatigue. The light source houses a mercury bulb, but less expensive LED-based units are increasingly popular. We use a 60× Plan Apochromat oil immersion lens (NA, 1.42) for sampling because it is corrected for variation in multiple spectral wavelengths and the high numerical aperture allows for fine optical sectioning (North, 2006; Smith, 2011).

Although the minimum suggested number of counts for stereological estimates is 100–200, we employ a design with an increased sampling intensity because it improves accuracy and can be done without a substantial increase in time spent sampling (Gundersen et al., 1999; Schmitz and Hof, 2000; Slomianka and West, 2005). Moreover, this ensures that cases at the lower end of natural variation will not be thrown out due to insufficient counts from more generous sampling parameters.

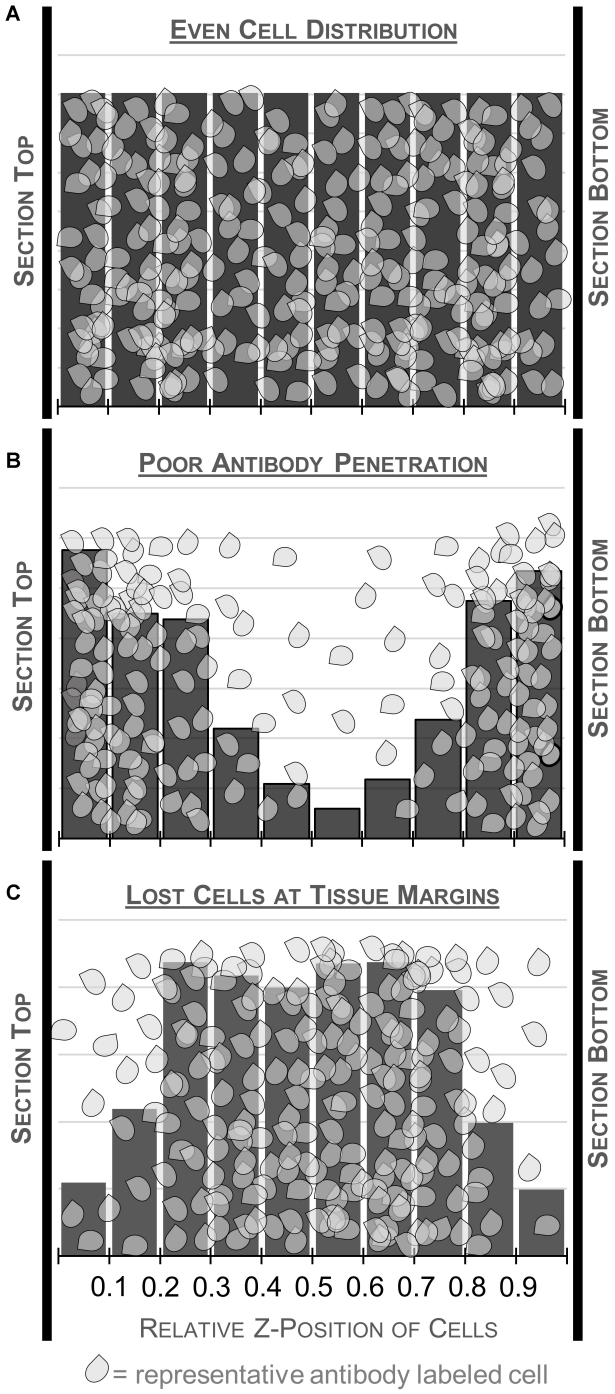

FIGURE 5 | Schematic illustrating different patterns of cell distribution through the tissue thickness as revealed by histograms charting the relative z-position of sampled cells across 10 bins. A relatively even distribution of cells throughout the thickness is ideal and suggests minimal impact of tissue processing (top, **A**). Fewer cells in the middle of the section could indicate poor antibody penetration (middle, **B**). This may warrant processing an additional series from the same case, changing variables that could affect antibody penetration. Histograms with fewer cells at the top and bottom of the tissue suggest cutting artifacts like plucked cells and lost caps may affect the distribution (bottom, **C**). Guard zones can be set to exclude these variable regions.

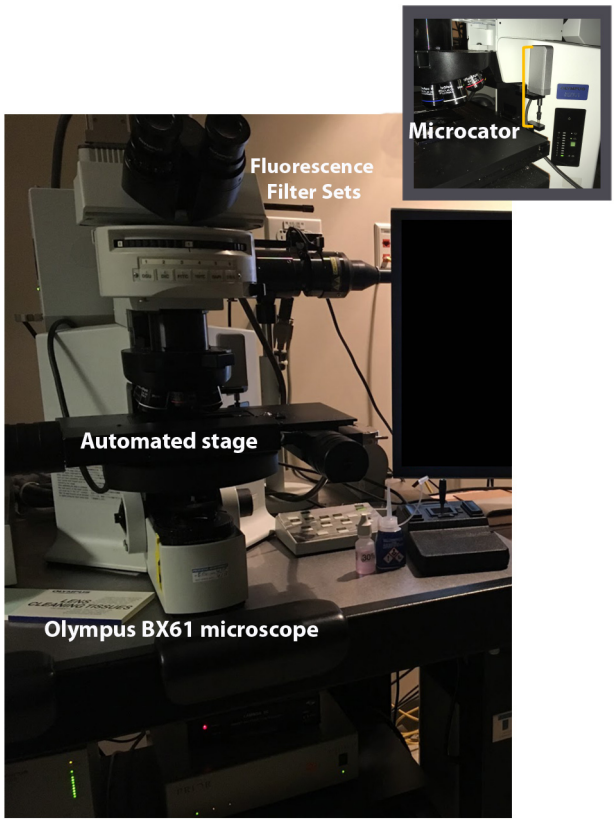

FIGURE 6 | Stereology setup. Computer workstation with Stereo Investigator is attached to the microscope. Microscope includes an automated stage and microcator for measuring *z* depth. Fluorescent filter sets allow for viewing multiple channels. Illumination is provided by an epifluorescent illumination system (not shown).

This buffer is especially important when measuring pathological effects that may produce variation that cannot be anticipated. To produce reliable estimates of cell population number using optical fractionator, we initially determine appropriate sampling parameters on a subsample of cases, attempting to minimize error. Below, we describe our procedure for data collection and illustrate its application on a pilot analysis of neurons, defined as $NeuN^+$ cells labeled with the far red fluorophore AF-647, and subcerebral projection neurons, defined as $NeuN^+/Ctip2^+$ cells additionally co-labeled with the green fluorophore AF-488, in postnatal day 10 rat cerebral cortex ($N = 5$).

Determine Sampling Parameters

(A) Delineate the region of interest at low power (1–4× objective) in 2–3 individual sections each for a small sample of cases (**Figure 4**).

- In multiple immunofluorescence, boundaries can be defined using DAPI to reveal cytoarchitecture or a cell specific marker characteristic of the region. Because our region of interest is the cerebral cortex, we could use the distribution of NeuN labeled neurons in the far-red channel to define this area. However, we chose

to use DAPI because it is equally reliable for our structure of interest and allowed us to preserve the more photosensitive NeuN AF-647 signal for stereological sampling.
- Use a precise anatomical definition to ensure the region is consistently delineated. We defined the neocortices to include all regions of the cerebral cortex except regions comprising four or fewer layers like the hippocampal, olfactory, and amygdalar cortical territories traditionally considered part of the allocortex (Altman et al., 1973; Reep, 1984; Bayer and Altman, 1993; Wise, 2008; Zilles and Amunts, 2012).

(B) Perform a preliminary survey of tissue thickness at several sampling sites within each section delineated in A.

- DAPI can be used for thickness measurements because it is evenly distributed throughout the thickness of the tissue and less critical for stereological analysis.
- A high NA lens (NA > 1) with refractive index matched to the mounting medium should be used for fine optical sectioning and submicron level precision. We use a 60× Plan Apochromat oil immersion lens (NA, 1.42) and final magnification of 600×.
- To measure thickness, set the 0 point as the top of the section, the focal plane where the top of the first visible DAPI labeled cell (or cells) just comes into focus.
- Focus down through the tissue to the plane where the bottom of the last cell (or cells) is visible and record that z-position as the section thickness at that site.
- Continue sampling a few sites (∼5–10) on each delineated section and record thicknesses at each site.
- Data can be recorded in a spreadsheet program to determine average, minimum, and maximum thicknesses and variability across sites.
- We use tools in Stereo Investigator to track our measurements, but these measurements can be done on any microscopy system that includes a *z*-axis depth gauge (microcator) as previously described elsewhere (West et al., 1991; Mouton, 2002; Williams et al., 2003; Howard and Reed, 2005; Schmitz and Hof, 2005).

(C) Some authors advocate measuring the distribution of immunolabeled cells through the depth of the tissue thickness in a representative set of sites (e.g., Ward et al., 2008). This can reveal the impact of processing artifacts at the tissue's margins and also provides a means to check antibody penetration (**Figure 5**) to meet the requirement that every cell has an equal chance of being sampled in the counting frame. Because this exercise can be time consuming and is not considered standard practice in every lab, we present it as an optional step intended to provide additional information for initially determining the sampling scheme. It does not necessarily need to be performed before every stereology experiment (Williams et al., 2003), but instead should be performed judiciously, for example, when using a new sectioning method or antibody.

- This can be easily accomplished in Stereo Investigator by starting an optical fractionator probe run with the section thickness set at the maximum measured thickness from Step B and a large grid size to produce a small number of sampling sites per section. See Data Collection C-F for sampling method. If the file is exported to Excel, *z*-axis values, thickness, and *z* distribution are computed in the exported spreadsheet. For a detailed protocol for sampling without Stereo Investigator see Williams et al. (2003).
- Using the same setup as in B, find the top and bottom of the section using DAPI and record section thickness.
- Switch channels and focus on the top of the first visible immunolabeled cell in the counting frame and mark its position.
- Continue focusing down through the tissue and mark the *z*-position of each labeled cell as it comes into focus.
- Switch fluorescence channels and perform the same exercise for the next set of labeled cells.
- Continue to sample 5–10 sites in each section delineated in A.
- Once a representative sample (∼200–300 cells) is taken for each antibody, enter the results into a spreadsheet or statistical software program.
- For each site, calculate the relative *z*-position of each cell by dividing the *z*-position by the total tissue thickness measured at that site. For example, if a cell is located 2 μm below the top of a 20 μm section, its relative position would be 0.10.
- With these standardized values, a frequency distribution can then be calculated with the pooled relative thickness measures across sites, e.g., using the histogram function in Excel across 10 bins of relative tissue depth (**Figure 5**). Graphing the frequency distribution can help to identify processing artifacts that may influence final results. Cells should be relatively evenly distributed in the histogram, indicated by a flat distribution. Histograms indicating higher densities at the top and bottom of the tissue could suggest tissue compression during processing or poor antibody penetration. Low densities at the section margins likely result from blade artifacts during cutting, like plucked cells and lost caps.

(D) Determine appropriate disector and guard zone height for the sample based on information obtained in steps B and C.

- As a reference, a disector height of 9 μm and guard zone of height 2.5 μm have been recommended as optimal minimum values for neurons and similarly sized cells (Howard and Reed, 2005) but values should be evaluated empirically. Disector height plus upper and lower guard zone height should not exceed the thickness of the thinnest sampling site measured in B.
- Guard zones should be set to exclude any exceptionally dense or sparse areas at the margins of the tissue revealed in the frequency distribution graph from C.

- When step C is performed, the best effort should be made to set guard zones so that the disector is situated where cell distribution is most even, i.e., by manipulating guard zone height, to avoid sectioning artifacts.

(E) Set disector length and width to ensure approximately 1–3 particles, usually cells, are counted per disector.

- This parameter will vary by cell density. It can be determined experimentally by starting an optical fractionator run and testing different dimensions on a few sections. See Data Collection C-F for sampling method.

(F) Set up the sampling grid, aiming for a grid size (step size) that yields approximately 200–500 sampled particles per run.

- Recommendations for the appropriate sample size range between 100 (West, 1993a) and 1000 (Slomianka and West, 2005). 200 particles (cells) is a commonly recommended standard. Statistically, increasing sample size should increase accuracy but sampling efficiency must also be considered in the stereological design. We find aiming for 500 cells per region per case yields very low error rates and can be done without adding excessively to time spent sampling.
- Assuming 1–3 cells per sampling site per disector, determine the grid size needed to produce a total of 100–200 sampling sites across an entire case based on the traced sections.

Data Collection

(A) In Stereo Investigator, we first create a new case using the Optical Fractionator Workflow function. Sections are set up in the serial section manager, indicating the cut section thickness and interval between sections.

(B) Delineate the region of interest at low magnification on the first slide as in Determine Sampling Parameters A.

- A small, unique reference point (e.g., a distinct blood vessel) can be traced on each section at high magnification to facilitate proper alignment for sampling later.

(C) Set criteria for inclusion in the sample.

- With immunofluorescence, the primary criterion for inclusion is relatively straightforward—antibody reactivity and fluorescent signal in the dedicated channel. Fluorescence signal should be clearly higher than background and should not be present in unlabeled channels, in our case the red channel. Signal with the same pattern in all channels would indicate autofluorescence.
- Consider co-labeling. We took advantage of fluorescence co-labeling to improve identification of subcerebral projection neurons, counting only Ctip2$^+$ cells that were also NeuN$^+$.

(D) Once general criteria are set, a unique, "dimensionless" feature that has a high likelihood of only being sampled in one z-plane should be established *a priori*.

- Both Ctip2 and NeuN antibodies clearly label the nucleus, so we used the nucleus's widest point as our criterion for inclusion. The single point where the top or bottom of the counting unit come into focus are additional, commonly used criteria. Caution should be taken to determine the influence of overprojection in the *z*-axis on the chosen criterion when working with fluorescent material.

(E) Start the optical fractionator probe run, progressing along the grid from disector to disector to collect sampling data. Each cell type can be counted in the same run using different markers or each in its own run, if the densities are substantially different.

- In the first disector, mark only cells that meet the above criteria and that come into focus within the disector or intersecting the green lines of inclusion (**Figures 2**, **4**). If they touch the red lines of exclusion, they should not be counted.
- Ideally, section thickness measurements will be taken at all sites or at even intervals across sampling sites to allow for estimates based on number weighted thickness. Using a ubiquitous nuclear marker like DAPI will ensure the most accurate measurements. In cases where it is not practical to use a nuclear marker, it has been recommended to cross-check readings for the tissue top and bottom under both epifluorescence and low transmitted visible light (Negredo et al., 2004).

(F) Continue until all sections have been sampled.

(G) Determine numerical estimates using Eq. 1 and the appropriate thickness measure.

- In Stereo Investigator, this is done by selecting all sampled sections in the serial section manager and exporting results for that case to Excel. The output provides a record of the number of cells sampled, number of sampling sites visited, and stereological parameters in addition to population estimates based on multiple alternative thickness measures and error values.

Error Estimates

(A) It is also advisable to perform intraobserver reliability tests on a small number of cases to assess the effectiveness of the defined parameters and to reduce experimenter error from inconsistent application of stereological criteria.

- Prior to the full run, we sample 2–3 cases that are subsequently resampled 2 times by the same rater.
- To assess reliability, we use the intraclass correlation statistic, comparing total cells counted in each section for each of the three independent runs.

- We aim for a single measures coefficient of 0.95 or greater, reflecting a high degree of correspondence between counts performed by one rater.
- Criteria for inclusion are refined until the criterion can be consistently applied to meet this level of reliability.

(B) It has become common practice to report the Gundersen Coefficient of Error (CE) (Gundersen et al., 1999) as a measure of the error in the sampling scheme, although alternative calculations of experimental error are available. Estimators proposed by Geiser et al. (1990), Scheaffer et al. (1995), Cruz-Orive (1999), Schmitz and Hof (2000), and Cruz-Orive and Geiser (2004) are automatically calculated in Stereo Investigator and included with the standard output, while the original calculations can be explored in the cited literature.

- Two variants of the Gundersen CE have been proposed to assess error, incorporating smoothness measures $m = 1$ or $m = 0$ when sampling regularly or irregularly distributed objects, respectively (Gundersen and Jensen, 1987; Gundersen et al., 1999). A maximum Gundersen CE of 0.10 is commonly accepted as the standard in publication, indicating no more than 10% of total variation is contributed by the stereological design. Our approach produces very low Gundersen CEs, generally under 0.05.
- While this 10% criterion is commonly employed pragmatically, in theory, acceptable CEs may vary by experiment. It has been suggested that the error introduced by the stereological design (CE) should comprise only a "negligible" amount (Gundersen et al., 1999) and not more than 50% of the total variance in the group analyzed (CV), i.e., $CE^2/CV^2 < 0.5$ (Gundersen and Jensen, 1987), although dynamics in variance within and between sample groups should be considered when applying this rule (Slomianka and West, 2005). In their empirical test of alternative error measures, Slomianka and West (2005) found that a Gundersen CE, $m = 0$, performed well when estimating particle numbers with irregular distribution across a range of sampling frequencies, but also suggest comparing these error rates with Cruz-Orive's split-sample estimator, as it more directly reflects variability within the sample. They recommended to increase sampling intensity if these two measures disagree. This more stringent test may be particularly warranted in the pilot phase, when determining initial sampling parameters. Also useful in the planning stage, Cruz-Orive et al. (2004) present a method for determining acceptable CEs in the broader experimental context, addressing their relationship to other critical aspects of study design like population variance, statistical power of the overall design, and sample size.
- An additional measure suggested to reduce sampling error is the smooth fractionator design, an alternative sampling scheme intended to minimize error resulting from abrupt changes in particle distribution between sampled sections (Gundersen, 2002). In this method, sections are rank-ordered based on a proxy variable, like volume, that could be used to estimate the relative numbers of the objects to be counted. Every other section is removed from the rank ordered series and added to the end of the series in reverse rank order. This will ideally increase the smoothness of the distribution for sampling, providing a relatively symmetric distribution around the midpoint. Especially when considering irregular objects, sampling from a series of sections arranged in this manner, rather than by their biological order, makes it less likely that final counts will be biased by selection of sections with unusually high or low particle densities.

ANTICIPATED RESULTS

Immunolabeling

Our immunofluorescence protocol produced robust labeling of all our antigens of interest in the appropriate fluorescence channels. As most fixed tissue requires some degree of antigen retrieval, steamer-mediated antigen retrieval is arguably the most reliable, accessible technique (Ramos-Vara and Miller, 2014). All six primary antibodies tested followed their well-characterized labeling patterns. The markers used in our stereological analysis, Ctip2 and NeuN (**Figure 2**), were visible in the green and far red channels, respectively. Ctip2 labeling was predominant in neuronal nuclei in layer V but also evident in other layers, as might be anticipated particularly at this early developmental timepoint (Arlotta et al., 2005). We compared our fluorescence labeling of Ctip2 to enzymatic labeling with DAB using the same Ctip2 primary antibody. Fluorescence labeling resulted in reduced background relative to enzymatic techniques, making it easier to discriminate (**Figure 7**). NeuN expression followed its standard labeling patterning, localized to neuronal nuclei and immediately surrounding neuronal cytoplasm (Mullen et al., 1992). The majority of $Ctip2^+$ cells were co-labeled with NeuN. In a different series, we were able to use all four channels with antibodies to S100β, Iba1, and Olig2, with DAPI in the blue channel, without worrying about bleed-through affecting cell identification due to the distinct labeling patterns of these markers (**Figures 3A,C**). In the far red channel, Olig2 expression in oligodendrocytes was nuclear and seen predominantly in the white matter, where the majority of oligodendrocytes reside (Zhou and Anderson, 2002). Antibodies to Iba1, in the green channel, and S100β, in the red channel, revealed cell bodies and processes of microglia and astrocytes, respectively—labeling cells that were tiled across the cortex and showed distinct cellular morphologies between gray and white matter (Dyck et al., 1993; Ito et al., 1998). In a separate series, tissue labeled with Iba1 in the green channel and CD68 in the red (**Figure 3B**) showed only a subset of microglia were $CD68^+$; this was primarily along white matter tracts, where microglia are consistently reported to show higher expression of markers of activation (Harry and Kraft, 2012; Ling and Tan, 1974). CD68 expression was

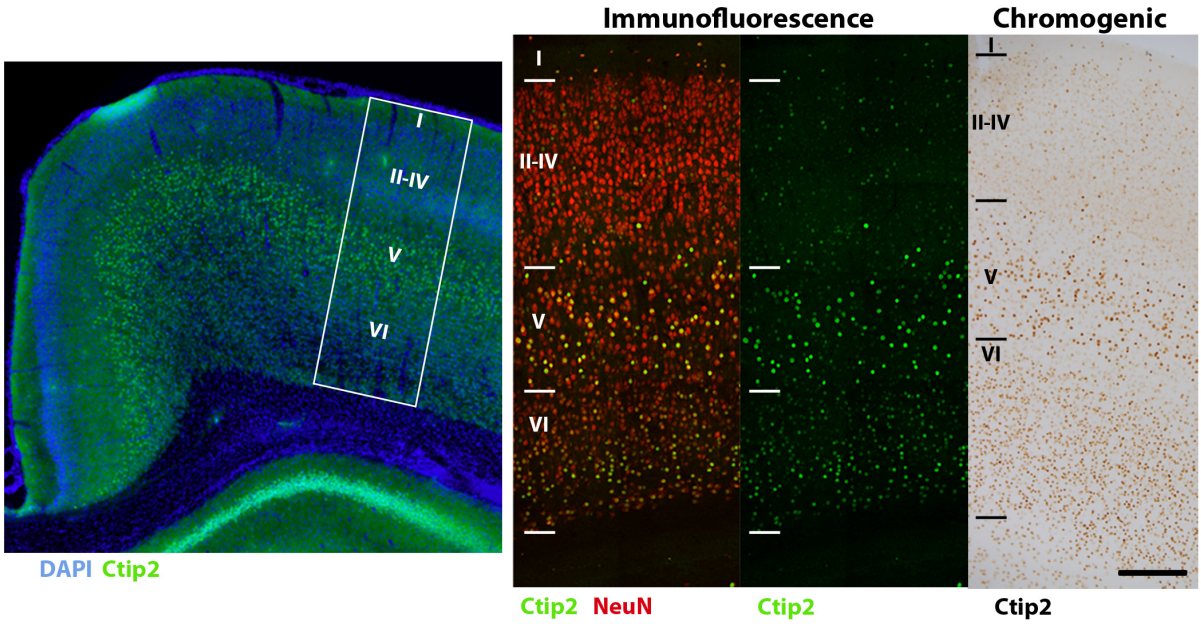

FIGURE 7 | Comparison of Ctip2 labeling with immunofluorescence and chromogenic immunohistochemistry. Subcortical projection neurons of the neocortex (left) can be identified by labeling Ctip2 with AF-488 (green), NeuN with AF-647 (red), and nuclei with DAPI (blue) using immunofluorescence. White box demarcates representative location of Ctip2 and NeuN labeled panels to the right. Immunofluorescence produces clearer and more precise labeling than using the brown chromogen DAB (DAB Peroxidase Substrate Kit, Vector, SK-4100) to label the same rabbit anti-Ctip2 antibody for brightfield microscopy. Fluorophore signal was clearer and easier to discriminate from background labeling and co-labeling with NeuN helped to more clearly identify this neuronal subclass. Scale bar, 100 μm.

punctate, characteristic of its standard endosomal and lysosomal localization pattern. In all cases, background was low and cells were easily distinguishable.

Choosing the right fluorescence secondary antibody label is critical for stereological analysis. In our pilot study, we placed our two nuclear labels in the green, FITC, and far red, Cy5, channels which minimized bleed-through. However, the process of sampling cells induces photobleaching which could, additionally, bias final counts. Before starting the optical fractionator, we tested the resistance of several fluorophores to photobleaching using donkey anti-rabbit secondary antibodies conjugated to fluorophores expressing in green, Cy2 (Jackson) and AF-488 (Life Technologies), or far red, AF-647 (Jackson) and NL-637 (R&D Systems), channels (**Figure 8**). We found significant bleaching of Cy2 even within 30 s. AF-647 was also unstable, bleaching 72% after 2 min of exposure. AF-488 was much more stable, bleaching 36% over this same interval, and NL-637 was the most stable, bleaching

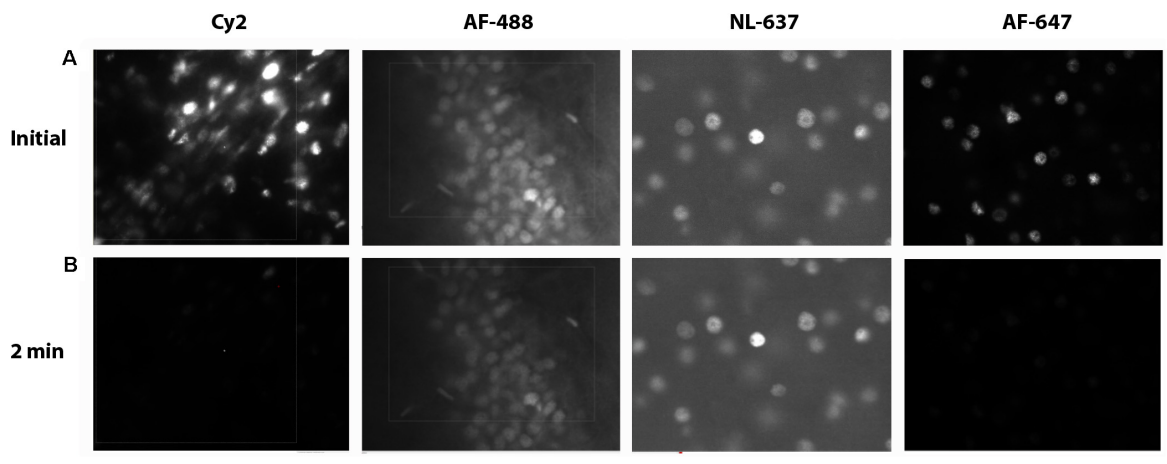

FIGURE 8 | Fluorophore bleaching. Epifluorescent images of Ctip2^{+} cells at 60× at an initial exposure after ~0.1 min **(A)** and after 2 min of exposure **(B)** with Cy2, AF-488, NL-637, and AF-647 secondary antibodies.

TABLE 2 | Photobleaching experiments.

	Mountant	Exposure duration (min)	Mean gray value	Signal reduction (%)
AF-647	*Mowiol*	0.1	6.1	–
		2	1.7	72.1
		15	0.0	100.0
NL-637	*Mowiol*	0.1	78.3	–
		2	76.0	2.9
		15	58.5	25.3
Cy2	*Mowiol*	0.1	33.8	–
		2	2.8	91.8
		15	0.0	100.0
AF-488	*Mowiol*	0.1	61.8	–
		2	39.5	36.1
		15	22.0	64.3
AF-488	*Prolong Gold*	0.1	56.7	–
		2	44.8	20.9
		15	31.8	43.9

Various fluorophores and mounting media were tested for rates of photobleaching by measuring pixel intensity initially, at 2 min after exposure to replicate a sampling run, and at 15 min to attempt to measure total signal quenching.

only 2.9% (**Table 2**). In addition to fluorophore stability, the choice of mounting medium can help to minimize photobleaching. We compared bleaching of the less stable AF-488 fluorophore when coverslipping with Mowiol, a commonly used medium, and Prolong Gold (Thermo Fisher, P10144), developed to reduce bleaching (**Figure 9**). After 2 min of exposure, there was a 36% reduction in signal with Mowiol and 21% reduction with Prolong Gold (**Table 2**). Additionally, we find our fluorescent labeling to last for more than a year when stored in the dark at 4°C, allowing sufficient time for subsequent data collection or reliability testing.

Balancing cost, availability, and efficacy, we found the best strategy was to use the common AlexaFlour (AF) line of fluorophores and the mountant Mowiol. This combination produced a green signal strong enough to reliably quantify our most difficult label, Ctip2. Because NeuN is robustly expressed and can be rapidly quantified, AF-647 was sufficient, despite its more rapid photobleaching. Of course, we did confirm that anti-fade mounting media and extremely stable fluorophores, such as the Northern Lights (NL) antibodies, exhibit decreased photobleaching rates. For some epitopes, it may be advisable to use the newer fluorophores which are marketed as being particularly photostable like the NL line. Prior to data acquisition, investigators should always perform pilot studies to ensure they are adequately familiar with the labeling patterns of the antigens of interest and the optimal fluorophores are chosen for their sampling scheme to minimize bias and time spent at each counting site. While our protocol was tested on perfusion-fixed tissue, we have found it to be effective using immersion-fixed tissue as well. Although immunolabeling may have to be optimized for variation in fixation and individual antibodies, we were able to identify diverse cell types with our protocol and anticipate it would reveal most epitopes.

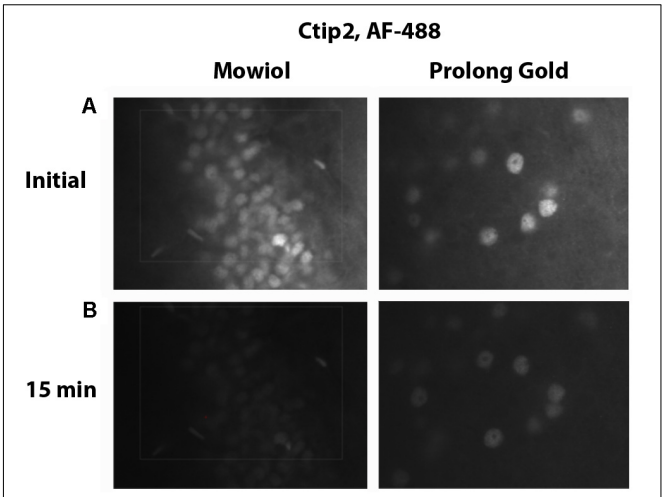

FIGURE 9 | Mounting media bleaching. Tissue immunostained for Ctip2 with an AF-488 secondary antibody was mounted with Mowiol or Prolong Gold. Images show initial fluorescence **(A)**, and fluorescence after 15 min of exposure **(B)**.

Stereology

To validate our protocol, we performed a stereological assessment of the numbers of neurons, defined by NeuN expression, and subcerebral projection neurons, defined by the additional expression of Ctip2, in rat cerebral cortex at postnatal day 10. The stereological parameters from our pilot study are summarized in **Table 3**, a representative table illustrating the minimum criteria necessary to report for optical fractionator analysis per Schmitz and Hof (2005). Tissue series produced with our immunolabeling protocol met the expectations of stereological analysis. Labeling was sufficiently bright and distinct from background to facilitate reliable identification of our criterion for inclusion, the nucleus

TABLE 3 | Stereological analysis parameters.

Variable	Ctip2	NeuN
Mean number of investigated sections	16	16
Mean number of investigated microscopic fields	328	159
Mean actual section thickness after histologic processing (μm)	21.3	18.3
Grid size (μm)	690 × 665	1005 × 925
Disector area (μm^2)	1600	900
Disector height (μm)	11	9
Guard zone height (μm)	4.5	4.5
Mean number of counted cells	447	525
CE	0.05	0.04

Summarized are the parameters that should be reported for all stereological studies. We have listed our final parameters for Ctip2 and NeuN from our pilot study (N = 5).

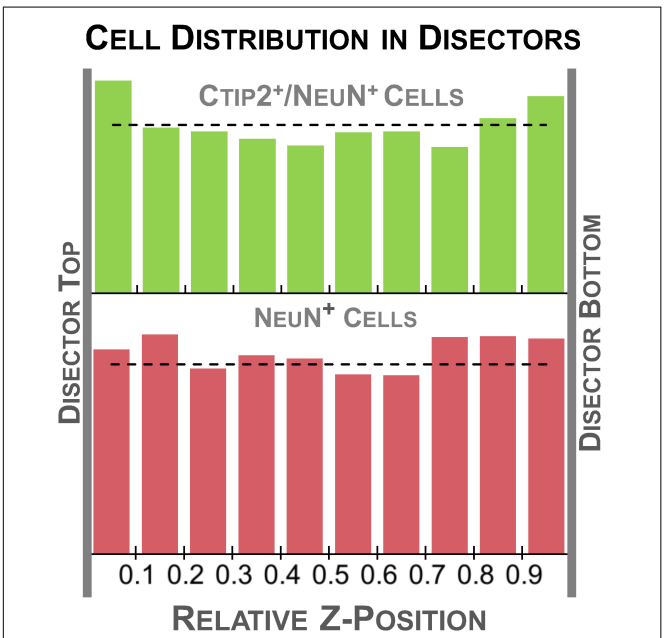

FIGURE 10 | Histogram of relative z-depth in the disector for each cell type sampled. The dashed line indicates the average number of cells expected for each bin (total cells sampled/10 bins), representing a perfectly even distribution. Cells were relatively evenly distributed through the thickness of the tissue, suggesting good penetration of both our Ctip2 and NeuN antibodies. A slight U-shaped distribution can be observed in the Ctip2 graph. The higher density regions at the tissue margins could be avoided by decreasing the height of the disector and increasing the height of the guard zone.

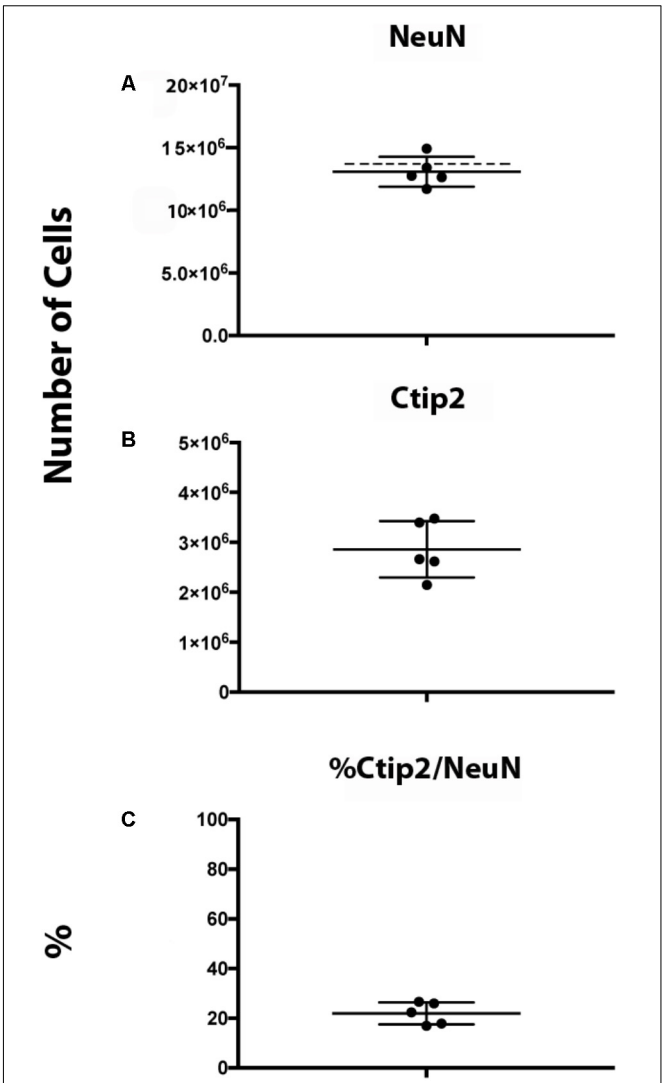

FIGURE 11 | Ctip2 and NeuN quantification in postnatal day 10 rat neocortex. Dot plots show total numbers of $NeuN^+$ **(A)** and $Ctip2^+$ **(B)** neurons based on number-weighted section thickness. Dashed line shows estimate of $NeuN^+$ neurons in postnatal day 11 rat cortex obtained by Bandeira et al. (2009). Percent of $NeuN^+$ cells that are $Ctip2^+$ is shown in **(C)**. Data represent mean and standard deviation (*N* = 5).

at its widest point, in all sampled cells (**Figure 2**). The final average section thickness was ∼20 μm, preserving 40% of tissue height. This increased post-processing tissue thickness provides an advantage over enzymatic immunohistochemical techniques which produce more extensive shrinkage due to multiple dehydration steps. It allowed us to add generous 4.5 μm guard zones to either end of our disectors. Disectors were well within the standard range, 9 μm for neurons and 11 μm for subcerebral projection neurons. Analysis of the *z*-distribution within our disectors indicates even antibody penetration throughout its height (**Figure 10**). However, our pilot data suggest cells may be clustered more at the top and bottom of our larger 11 μm disector. This could reflect compression artifacts and might warrant decreasing the disector height and increasing guard zones for subsequent analyses to ensure a more even distribution.

We obtained an estimate of 13.1 ± 1.2 million $NeuN^+$ neurons and 2.8 ± 0.6 million $Ctip2^+/NeuN^+$ subcerebral projection neurons using our protocol (**Figure 11**). An average of 447 (325–553) neurons and 525 (413–590) subcerebral projection neurons were sampled. Our neuronal estimate correlates well with prior estimates obtained in rat of 14.4 ± 0.6 million

neurons at P11 (Bandeira et al., 2009). The similarity in estimates is particularly notable considering the dynamic nature of this developmental period, when neuron production, maturation, and elimination cause rapid fluctuation in numbers (Lyck et al., 2007; Bandeira et al., 2009), and that Bandeira and colleagues employed a different method, the isotropic fractionator. Neuron numbers in mice at a similar developmental stage are lower, ∼6 million, as can be expected based on evolutionary scaling in brain size and neuron proportions (Lyck et al., 2007; Herculano-Houzel et al., 2010; Karacay et al., 2015). To our knowledge, this is the first quantification of Ctip2^{+} neurons that has been performed in the postnatal rat brain. Subcerebral projection neurons comprised 22% of total neurons. Across the sample, we found that the variance in this percentage was low, indicating strong internal consistency. For both markers, our estimates yielded low Gundersen CEs (m = 1), 0.042 for NeuN and 0.050 for Ctip2, indicating low sampling error. In comparison, the CV was higher, 0.091 for NeuN and 0.20 for Ctip2, making the error introduced by stereological design (CE) less than 50% of the total variance, as recommended (Gundersen et al., 1999). In addition, our intrarater reliability was high, 0.997 for NeuN and for 0.977 Ctip2, attesting to the ease of identifying cellular subtypes with this protocol.

CONCLUSION

We hope that the high reliability estimates we have obtained through application of a relatively simple immunostaining protocol illustrate the accessibility of this gold standard cell quantification technique to researchers in neuroscience. It is increasingly easy to obtain high quality, well vetted antibodies, and an array of fluorophores have been and continue to be designed for enhanced stability. Modification of existing stereology systems for immunofluorescence can be accomplished on relatively modest budgets, especially given the advent of newer systems using inexpensive and long-lasting LED light sources. These factors make it increasingly feasible to incorporate multiple immunofluorescence into stereological design to answer more complex questions more precisely, substantially increasing the explanatory power of individual experiments. Combining the statistical rigor of stereological sampling with the increased precision of immunofluorescence can provide the technical improvements needed to explore novel questions and refine existing ones.

AUTHOR CONTRIBUTIONS

NB and AK designed the experiments, wrote the manuscript, collected the images, and revised the manuscript. AK executed experiments.

FUNDING

This work was conducted in the laboratory of Dr. Stephen Noctor (SCN) in the UC Davis MIND Institute and funded by NIH grant MH101188 to SCN. Additional support was provided by the NIGMS-funded Pharmacology T32 Training Program (T32-GM099608), and by the Wenner-Gren Foundation's Hunt Postdoctoral Fellowship.

ACKNOWLEDGMENTS

We thank SCN for supporting this work and reviewing drafts. We thank Dr. Verónica Martínez Cerdeño, Jeanelle Ariza, and the Shriners Hospitals for Children, Sacramento, for assistance with stereological equipment.

REFERENCES

Altman, J., Brunner, R. L., and Bayer, S. A. (1973). The hippocampus and behavioral maturation I. *Behav. Biol.* 8, 557–596. doi: 10.1016/S0091-6773(73)80144-0

Andersen, B. B., and Gundersen, H. J. G. (1999). Pronounced loss of cell nuclei and anisotropic deformation of thick sections. *J. Microsc.* 196, 69–73. doi: 10.1046/j.1365-2818.1999.00555.x

Arlotta, P., Molyneaux, B. J., Chen, J., Inoue, J., Kominami, R., and Macklis, J. D. (2005). Neuronal subtype-specific genes that control corticospinal motor neuron development in vivo. *Neuron* 45, 207–221. doi: 10.1016/j.neuron.2004.12.036

Bandeira, F., Lent, R., and Herculano-Houzel, S. (2009). Changing numbers of neuronal and non-neuronal cells underlie postnatal brain growth in the rat. *Proc. Natl. Acad. Sci. U.S.A.* 106, 14108–14113. doi: 10.1073/pnas.0804650106

Bayer, S. A., and Altman, J. (1993). *Neocortical Development*. New York, NY: Raven Press.

Bermejo, P. E., Jiménez, C. E., Torres, C. V., and Avendaño, C. (2003). Quantitative stereological evaluation of the gracile and cuneate nuclei and their projection neurons in the rat. *J. Comp. Neurol.* 463, 419–433. doi: 10.1002/cne.10747

Berretta, S., Pantazopoulos, H., and Lange, N. (2007). Neuron numbers and volume of the amygdala in subjects diagnosed with bipolar disorder or schizophrenia. *Biol. Psychiatry* 62, 884–893. doi: 10.1016/j.biopsych.2007.04.023

Camacho, J., Ejaz, E., Ariza, J., Noctor, S. C., and Martínez-Cerdeño, V. (2014). RELN-expressing neuron density in layer I of the superior temporal lobe is similar in human brains with autism and in age-matched controls. *Neurosci. Lett.* 579, 163–167. doi: 10.1016/j.neulet.2014.07.031

Carlo, C. N., and Stevens, C. F. (2011). Analysis of differential shrinkage in frozen brain sections and its implications for the use of guard zones in stereology. *J. Comp. Neurol.* 519, 2803–2810. doi: 10.1002/cne.22652

Cruz-Orive, L. M., Insausti, A., Insausti, R., and Crespo, D. (2004). *"A Case Study from Neuroscience Involving Stereology and Multivariate Analysis," in Quantitative Methods in Neuroscience*. Oxford: Oxford University Press, 16–64.

Cruz-Orive, L. M. (1999). Precision of Cavalieri sections and slices with local errors. *J. Microsc.* 193, 182–198. doi: 10.1046/j.1365-2818.1999.00460.x

Cruz-Orive, L. M., and Geiser, M. (2004). Estimation of particle number by stereology: an update. *J. Aerosol. Med.* 17, 197–212. doi: 10.1089/jam.2004.17.197

Cunningham, C. L., Martinez-Cerdeno, V., and Noctor, S. C. (2013). Microglia regulate the number of neural precursor cells in the developing cerebral cortex. *J. Neurosci.* 33, 4216–4233. doi: 10.1523/JNEUROSCI.3441-12.2013

Dorph-Petersen, K.-A., Nyengaard, J. R., and Gundersen, H. J. G. (2001). Tissue shrinkage and unbiased stereological estimation of particle number and size. *J. Microsc.* 204, 232–246. doi: 10.1046/j.1365-2818.2001.00958.x

Dyck, R. H., Van Eldik, L. J., and Cynader, M. S. (1993). Immunohistochemical localization of the S-100 beta protein in postnatal cat visual cortex: spatial and temporal patterns of expression in cortical and subcortical glia. *Brain Res. Dev. Brain Res.* 72, 181–192. doi: 10.1016/0165-3806(93)90183-B

Egilsson, V., Evans, I. H., and Wilkie, D. (1979). Toxic and mutagenic effects of carcinogens on the mitochondria of Saccharomyces cerevisiae. *Mol. Gen. Genet.* 174, 39–46. doi: 10.1007/BF00433303

Gardella, D., Hatton, W. J., Rind, H. B., Rosen, G. D., and Von Bartheld, C. S. (2003). Differential tissue shrinkage and compression in the z-axis: implications for optical disector counting in vibratome-, plastic- and cryosections. *J. Neurosci. Methods* 124, 45–59. doi: 10.1016/S0165-0270(02)00363-1

Geiser, M., Cruz-Orive, L. M., Hof, V. I., and Gehr, P. (1990). Assessment of particle retention and clearance in the intrapulmonary conducting airways of hamster lungs with the fractionator. *J. Microsc* 160, 75–88. doi: 10.1111/j.1365-2818.1990.tb03049.x

Griswold, D. P., Casey, A. E., Weisburger, E. K., and Weisburger, J. H. (1968). The carcinogenicity of multiple intragastric doses of aromatic and heterocyclic nitro or amino derivatives in young female sprague-dawley rats. *Cancer Res.* 28, 924–933.

Gundersen, H. J. G. (1986). Stereology of arbitrary particles. *J. Microsc.* 143, 3–45. doi: 10.1111/j.1365-2818.1986.tb02764.x

Gundersen, H. J. G. (2002). The smooth fractionator. *J. Microsc.* 207, 191–210. doi: 10.1046/j.1365-2818.2002.01054.x

Gundersen, H. J. G., Bagger, P., Bendtsen, T. F., Evans, S. M., Korbo, L., Marcussen, N., et al. (1988). The new stereological tools: disector, fractionator, nucleator and point sampled intercepts and their use in pathological research and diagnosis. *APMIS* 96, 857–881. doi: 10.1111/j.1699-0463.1988.tb00954.x

Gundersen, H. J. G., and Jensen, E. B. (1987). The efficiency of systematic sampling in stereology and its prediction. *J. Microsc.* 147, 229–263. doi: 10.1111/j.1365-2818.1987.tb02837.x

Gundersen, H. J. G., Jensen, E. B., Kiêu, K., and Nielsen, J. (1999). The efficiency of systematic sampling in stereology–reconsidered. *J. Microsc.* 193, 199–211. doi: 10.1046/j.1365-2818.1999.00457.x

Harry, G. J., and Kraft, A. D. (2012). Microglia in the developing brain: a potential target with lifetime effects. *Neurotoxicology* 33, 191–206. doi: 10.1016/j.neuro.2012.01.012

Hatton, W. J., and von Bartheld, C. S. (1999). Analysis of cell death in the trochlear nucleus of the chick embryo: calibration of the optical disector counting method reveals systematic bias. *J. Comp. Neurol.* 409, 169–186. doi: 10.1002/(SICI)1096-9861(19990628)409:2<169::AID-CNE1>3.0.CO;2-O

Herculano-Houzel, S., Mota, B., and Lent, R. (2010). How to build a bigger brain: cellular scaling rules for rodent brains. *Evol. Nerv. Syst* 3, 155–166.

Hou, J., Eriksen, N., and Pakkenberg, B. (2011). The temporal pattern of postnatal neurogenesis found in the neocortex of the Gottingen minipig brain. *Neuroscience* 195, 176–179. doi: 10.1016/j.neuroscience.2011.08.025

Howard, V., and Reed, M. G. (2005). *Unbiased stereology: three-dimensional measurement in microscopy*. Milton Park: Garland Science.

Ito, D., Imai, Y., Ohsawa, K., Nakajima, K., Fukuuchi, Y., and Kohsaka, S. (1998). Microglia-specific localisation of a novel calcium binding protein, Iba1. *Mol. Brain Res* 57, 1–9. doi: 10.1016/S0169-328X(98)00040-0

Karacay, B., Mahoney, J., Plume, J., and Bonthius, D. J. (2015). Genetic absence of nNOS worsens fetal alcohol effects in mice. *II: microencephaly and neuronal losses*. *Alcohol. Clin. Exp. Res.* 39, 221–231. doi: 10.1111/acer.12615

Karlsen, A. S., Kaalund, S. S., Møller, M., Plath, N., and Pakkenberg, B. (2013). Expression of presynaptic markers in a neurodevelopmental animal model with relevance to schizophrenia. *Neuroreport* 24, 928–933. doi: 10.1097/WNR.0000000000000030

Konopaske, G. T., Dorph-Petersen, K.-A., Sweet, R. A., Pierri, J. N., Zhang, W., Sampson, A. R., et al. (2008). Effect of chronic antipsychotic exposure on astrocyte and oligodendrocyte numbers in macaque monkeys. *Biol. Psychiatry* 63, 759–765. doi: 10.1016/j.biopsych.2007.08.018

Kreczmanski, P., Heinsen, H., Mantua, V., Woltersdorf, F., Masson, T., Ulfig, N., et al. (2007). Volume, neuron density and total neuron number in five subcortical regions in schizophrenia. *Brain* 130, 678–692. doi: 10.1093/brain/awl386

Lauber, E., Filice, F., and Schwaller, B. (2016). Prenatal valproate exposure differentially affects parvalbumin-expressing neurons and related circuits in the cortex and striatum of mice. *Front. Mol. Neurosci.* 9:150. doi: 10.3389/fnmol.2016.00150

Ling, E. A., and Tan, C. K. (1974). Amoeboid microglial cells in the corpus callosum of neonatal rats. *Arch. Histol. Jpn.* 36, 265–280. doi: 10.1679/aohc1950.36.265

Lyck, L., Krøigård, T., and Finsen, B. (2007). Unbiased cell quantification reveals a continued increase in the number of neocortical neurones during early post-natal development in mice. *Eur. J. Neurosci* 26, 1749–1764. doi: 10.1111/j.1460-9568.2007.05763.x

Morgan, J. T., Barger, N., Amaral, D. G., and Schumann, C. M. (2014). Stereological study of amygdala glial populations in adolescents and adults with autism spectrum disorder. *PLoS One* 9:e110356. doi: 10.1371/journal.pone.0110356

Mouton, P. R. (2002). *Principles and practices of unbiased stereology: an introduction for bioscientists*. Baltimore, MD: Johns Hopkins University Press.

Mullen, R. J., Buck, C. R., and Smith, A. M. (1992). NeuN, a neuronal specific nuclear protein in vertebrates. *Development* 116, 201–211.

Murphy, D. B., and Davidson, M. W. (2013). *Fundamentals of Light Microscopy and Electronic Imaging*. Hoboken: Wiley-Blackwell. doi: 10.1002/9781118382905

Negredo, P., Castro, J., Lago, N., Navarro, X., and Avendaño, C. (2004). Differential growth of axons from sensory and motor neurons through a regenerative electrode: a stereological, retrograde tracer, and functional study in the rat. *Neuroscience* 128, 605–615. doi: 10.1016/j.neuroscience.2004.07.017

North, A. J. (2006). Seeing is believing? A beginners' guide to practical pitfalls in image acquisition. *J. Cell Biol.* 172, 9–18. doi: 10.1083/jcb.200507103

Pakkenberg, B., and Gundersen, H. J. G. (1997). Neocortical Neuron Number in Humans. *J. Comp. Neurol.* 320, 312–320. doi: 10.1002/(SICI)1096-9861(19970728)384:2<312::AID-CNE10>3.0.CO;2-K

Pelvig, D. P., Pakkenberg, H., Stark, A. K., and Pakkenberg, B. (2008). Neocortical glial cell numbers in human brains. *Neurobiol. Aging* 29, 1754–1762. doi: 10.1016/j.neurobiolaging.2007.04.013

Prasad, K., and Richfield, E. K. (2010). Number and nuclear morphology of TH+ and TH- neurons in the mouse ventral midbrain using epifluorescence stereology. *Exp. Neurol.* 225, 328–340. doi: 10.1016/j.expneurol.2010.07.004

Raghanti, M. A., Stimpson, C. D., Marcinkiewicz, J. L., Erwin, J. M., Hof, P. R., and Sherwood, C. C. (2008). Differences in cortical serotonergic innervation among humans, chimpanzees, and macaque monkeys: a comparative study. *Cereb. Cortex* 18, 584–597. doi: 10.1093/cercor/bhm089

Ramos-Vara, J. A., and Miller, M. A. (2014). When tissue antigens and antibodies get along. *Vet. Pathol.* 51, 42–87. doi: 10.1177/0300985813505879

Reep, R. (1984). Relationship between prefrontal and limbic cortex: a comparative anatomical review. *Brain Behav. Evol.* 25, 5–80. doi: 10.1159/000118849

Scheaffer, R. L., Mendenhall, W., and Ott, L. (1995). *Elementary Survey Sampling*. Belmont: Duxbury Press.

Schmitz, C., and Hof, P. R. (2000). Recommendations for straightforward and rigorous methods of counting neurons based on a computer simulation approach. *J. Chem. Neuroanat.* 20, 93–114. doi: 10.1016/S0891-0618(00)00066-1

Schmitz, C., and Hof, P. R. (2005). Design-based stereology in neuroscience. *Neuroscience* 130, 813–831. doi: 10.1016/j.neuroscience.2004.08.050

Semendeferi, K., Armstrong, E., Schleicher, A., Zilles, K., and Van Hoesen, G. W. (1998). Limbic frontal cortex in hominoids: a comparative study of area 13. *Am. J. Phys. Anthropol.* 106, 129–155. doi: 10.1002/(SICI)1096-8644(199806)106:2<129::AID-AJPA3>3.0.CO;2-L

Semendeferi, K., Armstrong, E., Schleicher, A., Zilles, K., and Van Hoesen, G. W. (2001). Prefrontal cortex in humans and apes: a comparative study of area 10. *Am. J. Phys. Anthropol.* 114, 224–241. doi: 10.1002/1096-8644(200103)114:3<224::AID-AJPA1022>3.0.CO;2-I

Sherwood, C. C., Raghanti, M. A., Stimpson, C. D., Spocter, M. A., Uddin, M., Boddy, A. M., et al. (2010). Inhibitory interneurons of the human prefrontal cortex display conserved evolution of the phenotype and related genes. *Proc. Biol. Sci.* 277, 1011–1020. doi: 10.1098/rspb.2009.1831

Slomianka, L., and West, M. J. (2005). Estimators of the precision of stereological estimates: an example based on the CA1 pyramidal cell layer of rats. *Neuroscience* 136, 757–767. doi: 10.1016/j.neuroscience.2005.06.086

Smith, C. L. (2011). Basic confocal microscopy. *Curr. Protoc. Neurosci.* 81, 14–11. doi: 10.1002/0471142301.ns0202s56

Stimpson, C. D., Barger, N., Taglialatela, J. P., Gendron-Fitzpatrick, A., Hof, P. R., Hopkins, W. D., et al. (2016). Differential serotonergic innervation of the amygdala in bonobos and chimpanzees. *Soc. Cogn. Affect. Neurosci.* 11, 413–422. doi: 10.1093/scan/nsv128

Tang, X., Falls, D. L., Li, X., Lane, T., and Luskin, M. B. (2007). Antigen-retrieval procedure for bromodeoxyuridine immunolabeling with concurrent labeling of nuclear dna and antigens damaged by HCl pretreatment. *J. Neurosci.* 27, 5837–5844. doi: 10.1523/JNEUROSCI.5048-06.2007

Uylings, H. B. M., Jacobsen, A. M., Zilles, K., and Amunts, K. (2006). Left-right asymmetry in volume and number of neurons in adult Broca's area. *Cortex* 42, 652–658. doi: 10.1016/S0010-9452(08)70401-5

Vinod, K. R., Jones, D., and Udupa, V. (2016). A simple and effective heat induced antigen retrieval method. *MethodsX* 3, 315–319. doi: 10.1016/j.mex.2016.04.001

Ward, T. S., Rosen, G. D., and von Bartheld, C. S. (2008). Optical disector counting in cryosections and vibratome sections underestimates particle numbers: effects of tissue quality. *Microsc. Res. Tech.* 71, 60–68. doi: 10.1002/jemt

West, M., Slomianka, L., and Gundersen, H. J. G. (1991). Unbiased stereological estimation of the total number of neurons in the subdivisions of the rat hippocampus using the optical fractionator. *Anat. Rec.* 231, 482–497. doi: 10.1002/ar.1092310411

West, M. J. (1993a). New stereological methods for counting neurons. *Neurobiol. Aging* 14, 275–285. doi: 10.1016/0197-4580(93)90112-O

West, M. J. (1993b). Regionally specific loss of neurons in the aging human hippocampus. *Neurobiol. Aging* 14, 287–293. doi: 10.1016/0197-4580(93)90113-P

Williams, R. W., von Bartheld, C. S., and Rosen, G. D. (2003). Counting cells in sectioned material: a suite of techniques, tools, and tips. *Curr. Protoc. Neurosci.* 24, 1.11.1–1.11.29. doi: 10.1002/0471142301.ns0111s24

Wise, S. P. (2008). Forward frontal fields: phylogeny and fundamental function. *Trends Neurosci.* 31, 599–608. doi: 10.1016/j.tins.2008.08.008

Zhou, Q., and Anderson, D. J. (2002). The bHLH Transcription Factors OLIG2 and OLIG1 Couple Neuronal and Glial Subtype Specification. *Cell* 109, 61–73. doi: 10.1016/S0092-8674(02)00677-3

Zilles, K., and Amunts, K. (2012). "Architecture of the Cerebral Cortex," in *The Human Nervous System*, eds P. George, J. K. Mai, and K. M. Juergen (New York, NY: Elsevier Science), 836–895.

Conflict of Interest Statement: The authors declare that the research was conducted in the absence of any commercial or financial relationships that could be construed as a potential conflict of interest.

frontiers in Neuroanatomy

REVIEW
published: 09 January 2018
doi: 10.3389/fnana.2017.00131

Stereological Assessments of Neuronal Pathology in Auditory Cortex in Schizophrenia

Emily M. Parker[1] *and Robert A. Sweet*[1,2,3]*

[1]Department of Psychiatry, University of Pittsburgh, Pittsburgh, PA, United States, [2]Department of Neurology, University of Pittsburgh, Pittsburgh, PA, United States, [3]VISN 4 Mental Illness Research, Education and Clinical Center (MIRECC), VA Pittsburgh Healthcare System, Pittsburgh, PA, United States

It has long been known that auditory processing is disrupted in schizophrenia. More recently, postmortem studies have provided direct evidence that morphological alterations to neurons in auditory cortex are implicated in the pathophysiology of this illness, confirming previous predictions. Potential neural substrates for auditory impairment and gray matter loss in auditory cortex in schizophrenia have been identified, described, and are the focus of this review article. Pyramidal cell somal volume is reduced in auditory cortex, as are dendritic spine density and number in schizophrenia. Pyramidal cells are not lost in this region in schizophrenia, indicating that dendritic spine reductions reflect fewer spines per pyramidal cell, consistent with the reduced neuropil hypothesis of schizophrenia. Stereological methods have aided in the proper collection, reporting and interpretation of this data. Mechanistic studies exploring relationships between genetic risk for schizophrenia and altered dendrite morphology represent an important avenue for future research in order to further elucidate cellular pathology in auditory cortex in schizophrenia.

Keywords: auditory cortex, neurostereology, schizophrenia, postmortem, dendritic spine

OPEN ACCESS

Edited by:
Bente Pakkenberg, Research Laboratory for Stereology and Neuroscience, Denmark

Reviewed by:
Maria Medalla, Boston University, United States
Hisayuki Ojima, Tokyo Medical and Dental University, Japan

***Correspondence:**
Robert A. Sweet
sweetra@upmc.edu

Received: *02 August 2017*
Accepted: *18 December 2017*
Published: *09 January 2018*

Citation:
Parker EM and Sweet RA (2018) Stereological Assessments of Neuronal Pathology in Auditory Cortex in Schizophrenia. Front. Neuroanat. 11:131. doi: 10.3389/fnana.2017.00131

INTRODUCTION

Schizophrenia is a chronic illness that besets approximately 1% of the global population (Wong and Van Tol, 2003) and auditory impairment is a fundamental characteristic of schizophrenia psychopathology. Most commonly, individuals with schizophrenia present with auditory hallucinations (Insel, 2010). Further, many individuals with this illness experience auditory sensory processing deficits that can manifest, for instance, in impaired ability to distinguish between auditory tones (Pekkonen et al., 2002; O'Donnell et al., 2004; Kantrowitz et al., 2011, 2014). Auditory sensory processing deficits in turn contribute to socio-cognitive dysfunction (Leitman et al., 2005, 2007, 2010; Javitt and Sweet, 2015; Kantrowitz et al., 2015, 2016). Unlike the positive symptoms of schizophrenia, socio-cognitive dysfunction is not targeted by available pharmacological interventions. Among individuals with schizophrenia, those with prominent socio-cognitive dysfunction have the poorest functional outcomes (Green et al., 2004, 2015; Fett et al., 2011).

Auditory sensory processing deficits typically emerge in schizophrenia around the time of the first psychotic episode and persist over the course of the illness (McCarley et al., 1991; Holcomb et al., 1995; Strous et al., 1995; Javitt et al., 1997; Wexler et al., 1998; Leitman et al., 2005, 2010; Kantrowitz et al., 2011; Gold et al., 2012; Jahshan et al., 2013). Electroencephalography studies reveal that individuals with schizophrenia exhibit reduced auditory mismatch negativity (MMN) responses (Shelley et al., 1991; Javitt, 1993; Catts et al., 1995; Michie et al., 2000; Kasai et al., 2002).

MMN is an event-related potential recorded immediately following a stimulus that differs in characteristic from preceding stimuli (for example a tone of a deviant pitch among a series of tones of the same pitch) and, in the auditory system, reflects pre-attentive auditory sensory processes. In schizophrenia, reduced auditory MMN is correlated with impaired auditory tone discrimination (Javitt et al., 1994, 1996, 2000; Leitman et al., 2010). Electroencephalography methods likewise indicate that individuals with schizophrenia exhibit impaired auditory steady-state response (aSSR) entrainment, predominantly in the gamma frequency range (Brenner et al., 2009; Hamm et al., 2011, 2015). Altered fast GABAergic inhibition in auditory circuits is presumed to underlie impaired aSSR entrainment in this illness (Kwon et al., 1999; Light et al., 2006; Krishnan et al., 2009).

Cortical gray matter loss is a hallmark anatomical feature of schizophrenia (Zipursky et al., 1992; Schlaepfer et al., 1994; see this review, Shenton et al., 2001). The most pronounced gray matter loss is observed in frontal and temporal regions (Wong and Van Tol, 2003), most notably in the superior temporal gyrus (STG; McCarley et al., 1999; Shenton et al., 2001; Honea et al., 2005). Gray matter volume reduction in the STG ranks among the most consistent findings from studies reporting gray matter loss in schizophrenia (McCarley et al., 1999). Gray matter loss is apparent around the time of schizophrenia onset (Hirayasu et al., 1998, 2000; Kubicki et al., 2002; Kasai et al., 2003) and in the years following first episode psychosis (Menon et al., 1995; van Haren et al., 2007; see this review, Vita et al., 2012). Gray matter reductions occur within the STG in Heschl's gyrus (Hirayasu et al., 2000) and the planum temporale (Barta et al., 1997; Kwon et al., 1999; Hirayasu et al., 2000), where the primary auditory cortex (A1) and auditory association cortex are located, respectively.

Functional MRI studies reveal that auditory MMN reductions in schizophrenia subjects are correlated with gray matter loss in Heschl's gyrus (Salisbury et al., 2007). Similarly, auditory MMN and tone discrimination are thought to depend on the integrity of cells in supragranular layers (I–III) of the A1 (Javitt et al., 1994). Thus, we have hypothesized that neurons within the supragranular layers of A1 are altered in schizophrenia (Lewis and Sweet, 2009; Javitt and Sweet, 2015). Electroencephalography and *in vivo* imaging approaches do not have the resolution to test this prediction directly, requiring human postmortem studies to assess gray matter alterations at the neuronal level. In theory, a wide array of neuronal aberrations could lead to reduced gray matter volumes in schizophrenia, as gray matter has multiple constituents, including, neurons, glia and endothelial cells, the cell bodies of these cells and their neuropil, which is made up of the unmyelinated portions of axons, dendrites and the processes of glia. Therefore, it is conceivable that auditory cortical neurons could be altered in schizophrenia due to: (1) reduced neuron somal size; (2) reduced number of axon boutons; (3) reduced number of dendritic spines; (4) fewer total cells; or (5) a combination of any two or more of these possibilities.

The following review is a synopsis of human postmortem studies conducted by our lab that reveal neuronal abnormalities in auditory cortex in schizophrenia. These studies provide direct evidence that morphological features of neurons in the human auditory cortex are implicated in the pathology of this illness. Likewise, these findings provide potential neural correlates for auditory sensory processing deficits and cortical gray matter loss in primary and secondary auditory regions in schizophrenia. Descriptions of the brain regions, predominant feedforward circuit and principal cells in the ascending auditory pathway are provided as background. Next, morphometric findings revealing neuronal pathology in auditory cortex in schizophrenia are detailed. Finally, stereological methods are emphasized in this review that: (1) aided in the collection and interpretation of schizophrenia auditory cortex data; (2) advanced the field at each step; and (3) significantly strengthened the validity of the published results.

ANATOMICAL CONSTITUENTS, CIRCUITS AND CELLS OF THE ASCENDING AUDITORY PATHWAY

The STG is located in the bilateral temporal lobe, just below the Sylvian fissure. The posterior half of the STG in human is often further categorized into two sub-regions, Heschl's gyrus, and the region posterolateral to Heschl's gyrus, the planum temporale. These sub-regions contain the human auditory cortex, which is comprised of the A1 and auditory association cortex (A2). A1 is located in Heschl's gyrus and was historically referred to as Brodmann area 41 (BA41). A2 is located posterolateral to A1 in the STG in an area that spans portions of both Heschl's gyrus and the planum temporale. A2 is also known as Brodmann area 42 (BA42; Garey, 1909/1994; Rivier and Clarke, 1997; Nakahara et al., 2000; Hackett et al., 2001; Wallace et al., 2002; Sweet et al., 2005).

Auditory information travels in a feedforward circuit through several structures in the ascending auditory pathway before reaching the auditory cortex in the STG. Human and non-human primate auditory regions exhibit significant cytoarchitectural and functional homology (Hackett et al., 2001; Dick et al., 2012), thus, findings from non-human primate studies have been used to infer the functional organization of the human ascending auditory pathway. Briefly, auditory information travels from hair cells in the inner ear to the cochlear nucleus, superior olive, inferior colliculus and then to the medial geniculate nucleus (MGN) in the thalamus (Hackett, 2011). MGN thalamic axons synapse onto the dendrites of pyramidal cells and interneurons located in deep layer III and layer IV (Pandya and Rosene, 1993; Hashikawa et al., 1995; Molinari et al., 1995; Pandya, 1995), the major recipient layers of feedforward projections in A1 (Hackett, 2011). From there, intralaminar projections from deep layer III pyramidal cells activate A1 pyramidal cells in layer III (Mitani et al., 1985; Ojima et al., 1991; Wallace et al., 1991), to complete what is generally known as the ascending auditory pathway (**Figure 1**).

Layer III A1 pyramidal cells project to pyramidal cells in other layers within A1 and to pyramidal cells in layer III

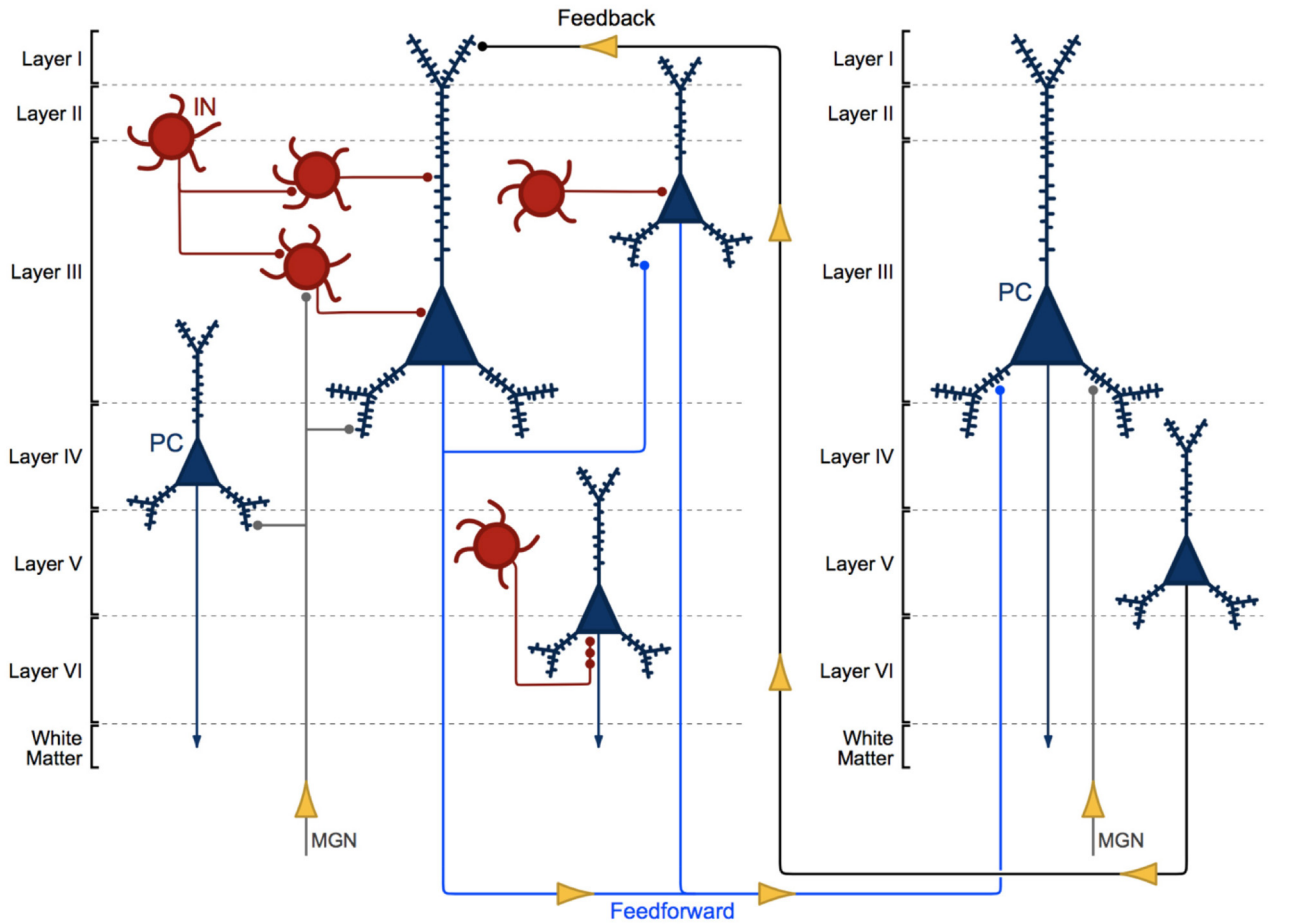

FIGURE 1 | Cytoarchitecture of feedforward and feedback auditory circuits. Thalamic projections from the medial geniculate nucleus (MGN) synapse onto pyramidal cells (PCs, blue) and interneurons (INs, red). Layer III PCs in primary auditory cortex (A1) send local intralaminar projections to other layer III PCs in this region and longer-range feedforward projections to PCs in layer III of auditory association cortex (A2). Layer V PCs in A2 in turn send excitatory feedback projections to neurons in layer I in A1.

of A2. Layer III and V pyramidal cells in A2 send feedback projections to layer I in A1 (Pandya and Sanides, 1973; Galaburda and Pandya, 1983; Pandya and Rosene, 1993; **Figure 1**). The molecular and morphological properties and axonal targeting patterns of cortical GABAergic inhibitory interneurons are diverse. Calbindin and somatostatin expressing interneurons provide inhibitory input to the distal dendrites of pyramidal cells. Calretinin and vasoactive intestinal polypeptide expressing interneurons modulate the activity of other cortical interneurons. Parvalbumin expressing basket cell interneurons provide inhibitory input to the somas and proximal dendrites of nearby pyramidal cells (Kepecs and Fishell, 2014). Finally, parvalbumin expressing chandelier cells provide GABAergic inhibitory input to the axon initial segment of pyramidal cells (Somogyi, 1977; Fairén and Valverde, 1980; DeFelipe et al., 1985; **Figure 1**; A1, bottom right).

Pyramidal cells are the principal cells of the auditory cortex and are recognized by their characteristic pyramid-shaped soma, distinctive radially oriented apical dendrite and multiple basilar dendrites. The dendrites of pyramidal cells have small protrusions, known as dendritic spines, which are the major recipient sites for excitatory synaptic transmission in the brain (Gray, 1959). Excitatory inputs to pyramidal cells almost exclusively synapse onto dendritic spines (Spacek and Harris, 1998; Arellano et al., 2007; Chen et al., 2012), interneurons primarily synapse onto the dendritic shaft of pyramidal cells and less frequently synapse onto spines (Somogyi and Cowey, 1981; DeFelipe et al., 1989; Yuste, 2011; Chen et al., 2012). Spines are rapidly motile structures (Fischer et al., 1998; Dunaevsky et al., 1999) that often undergo morphological alterations in an activity-dependent manner. Dendritic spine form and function are inextricably linked, and altered spine morphology impacts both synaptic transmission and plasticity. The role of dendritic spines in shaping neuronal system function has been extensively debated (Yuste, 2011). One view holds that spiny synapses are altered, and the morphology and molecular profile of spines are tuned, to regulate the gain of pyramidal

cell input/output properties toward the reorganization of neural networks.

Studies of Pyramidal Cell Somal Volume (Sweet et al., 2003, 2004)

Stereologic Methods

Initial studies of the morphometric properties of auditory cortex neurons (Sweet et al., 2003, 2004) did not fully implement uniform random sampling, but did make use of components of a stereologic sampling scheme to select brain tissue from schizophrenia and unaffected comparison cases. Brain specimens were acquired at the time of autopsy and assigned consensus diagnoses by a panel of experienced clinicians using DSM-IV criteria as described previously (Glantz and Lewis, 2000). Following brain extraction, the left temporal lobe was cut into 1–2 cm thick coronal slabs. From these slabs, a single slab containing STG with a visible Heschl's gyrus and planum temporale was selected, a non-uniform random approach, for each case. STG slabs were cut into 40 μm thick sections on a cryostat. Next, tissue sections were selected using a systematic uniformly random sampling (SURS) approach, and stained for Nissl substance. The Nissl-stained sections were examined, and a subset of three Nissl-stained sections were selected using a set of pre-defined criteria (non-uniform random). These criteria required that: (1) each section contain A1 and A2 oriented perpendicular to the pial surface to allow clear visualization of cortical layers and identification of pyramidal cells; and (2) each successive section selected must be no less than 1600 μm away from any other selected section (Sweet et al., 2003).

Pyramidal cells within the deepest 1/3 of layer III of auditory cortex were the focus of these studies. Pyramidal cells in layer V were also assessed. The deepest 1/3 of layer III or layer V was delineated for each section, and pyramidal cells within these regions were sampled systematic uniformly random (within sections) using the optical dissector (Gundersen, 1986), as implemented in Stereo Investigator software (Microbrightfield Inc., Colchester, VT, USA). Images of cell bodies were captured using a 1.4 numerical aperture, 100× oil immersion objective. Somal volumes of pyramidal cells were then estimated using the nucleator (Gundersen, 1988), with one exception, as implemented within Stereo Investigator software. The nucleator is a stereological method that uses isotropic test lines to estimate number-weighted mean particle (in this case somal) volume. This approach requires isotropic tissue sections, which have been, by definition, systematically and randomly sampled in three planes (x, y, z; Gundersen et al., 1988). As is evident from the above description of tissue preparation, the use of the nucleator employed by the authors did not ensure the requirement for isotropic orientation of the sampled neurons. Statistical tests were performed on pairs of subject cases in these studies as well as in each study described in this review article. In this study and in each of the studies detailed in this review, specimens were assessed in pairs, comprising tissue from each diagnostic group. Thus, each pair consisted of one schizophrenia case and one unaffected comparison case matched for age, sex, postmortem interval and, to the extent possible, handedness.

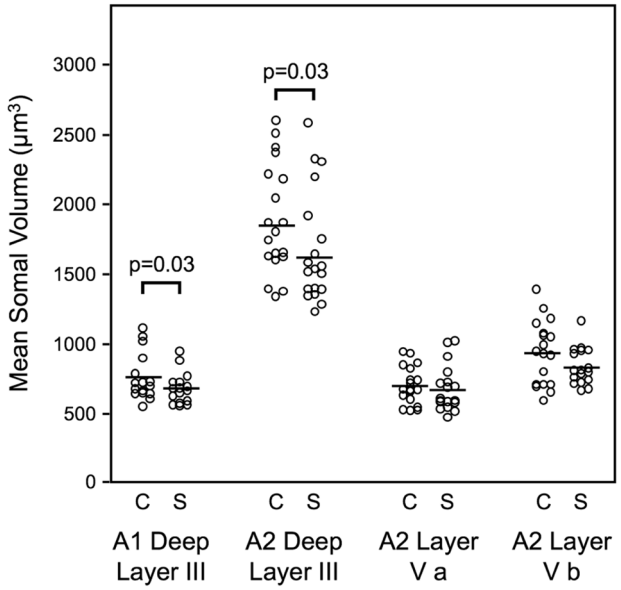

FIGURE 2 | Reduced pyramidal cell somal volume in schizophrenia (Sweet et al., 2004). Summary of findings of mean pyramidal cell somal volume in schizophrenia including in deep layer III of A1, deep layer III, layer V a and layer V b of A2. Studies of auditory cortical pyramidal cell somal volume (Sweet et al., 2003, 2004) revealed significantly reduced pyramidal cell somal volume in deep layer III of A1, and in deep layer III of A2 in schizophrenia.

Results

Mean somal volume of deep layer III pyramidal cells was reduced in schizophrenia by 13.1% in auditory association cortex (Sweet et al., 2003). Similarly, mean pyramidal cell somal volume was decreased in schizophrenia by 10.4% in deep layer III of A1, with no change in the somal volume of layer V pyramidal cells in A2 (Sweet et al., 2004; **Figure 2**). These data implicated feedforward but not feedback auditory circuits in schizophrenia and provided evidence for neuronal morphological abnormalities consistent with gray matter loss in auditory cortex in schizophrenia. Importantly, these studies provided the first direct demonstration of human auditory cortex pathology in schizophrenia.

Studies of Axon Boutons

Study of Synaptophysin-Immunoreactive Boutons (Sweet et al., 2007)

Stereologic methods

Brain specimens were acquired and sampled using the approaches used for studies of pyramidal cell somal volume detailed above. The sections adjacent to those used in the prior studies were selected and processed for immunolabeling with an antibody for synaptophysin. Synaptophysin is a presynaptically located synaptic vesicle glycoprotein that labels approximately 95% of cortical axon boutons (Jahn et al., 1985; Navone et al., 1986). Synaptophysin immunoreactivity (SYP-IR) was visualized

with a diaminobenzidine reaction product followed by osmium tetroxide stabilization. Layer I of A1 and deep layer III of A1 and A2 were delineated in adjacent sections stained for Nissl substance and the outlined regions were then aligned with the SYP-IR sections using surface fiduciaries. Because the sampling of auditory cortex deviated from uniform random, it was not possible to estimate the volume of the regions of interest or determine SYP-IR object number. Instead, only a biased estimate of SYP-IR object density was determined.

Poor antibody penetration and the potential for loss of structures at the cut surface are two issues that should be addressed when using thick tissue sections for immunohistochemistry. Thus, pilot studies using the optical dissector (Gundersen, 1986) to sample SYP-IR objects in z-axis depths of 0.5 μm intervals were conducted to assess antibody penetration and to sample cases in a zone of z-axis depth with uniformly high penetration across cases, and free from artifactual loss of labeled boutons (Sweet et al., 2007).

Results

Putative bouton density (SYP-IR object density) was decreased 13.6% in deep layer III in A1 in schizophrenia, relative to unaffected comparison cases. In contrast, SYP-IR density in layer III of A2 and in layer I of A1 were both not significantly altered in schizophrenia. Putative bouton density reductions did not correlate with reduced somal volume in either region (Sweet et al., 2007), suggesting that the input/output properties of pyramidal cells in auditory feedforward and feedback circuits exhibit more nuanced properties than originally expected, although, this may only be true in the context of pathology.

It must be pointed out that the above study was limited by the biased nature of the sampling. Neither A1 nor A2 reference volume could be estimated using the approaches employed. Without total reference volume, density estimations suffer from the reference trap (Braendgaard and Gundersen, 1986). Thus, the finding of reduced axon bouton density in A1 deep layer III could reflect either reduced number of SYP-IR structures or expanded tissue volume of the sampled region with no change in number of SYP-IR structures. The former interpretation was viewed as more likely given the evidence of auditory cortical gray matter reduction in schizophrenia (Shenton et al., 2001), but could not be established by the current study. For the same reason, it is also conceivable that unchanged SYP-IR object densities in layer I of A1 and in layer III of A2 could reflect modestly lower numbers of SYP-IR structures in schizophrenia.

Study of Vesicular Glutamate Transporter-Immunoreactive Boutons (Moyer et al., 2013)

Stereologic methods

Brain specimens were collected and assigned consensus diagnoses as described in previous studies (Sweet et al., 2003, 2004, 2007). Two cohorts, each with one schizophrenia group and one unaffected comparison group, were assessed. Cohorts 1 and 2 are distinguished by the cutting and sampling methods employed. The subjects included in Cohort 1 were the same as in "Study of Synaptophysin-Immunoreactive Boutons (Sweet et al., 2007)" section above, and the tissue sections for this cohort were cut and sampled using the procedures detailed above (Sweet et al., 2003, 2004, 2007). In contrast, new cases in Cohort 2, comprising the two diagnostic groups, were processed using a rigorous, unbiased SURS method (Dorph-Petersen et al., 2009). The entire left STG was dissected out of coronal blocks of brain specimens for the generation of Cohort 2 tissue. Pial surfaces of STG blocks were then painted with hematoxylin and reassembled in 7% low-melt agarose based on original *in vivo* orientation. Next, STG blocks were cut into 3 mm slabs orientated orthogonal to Heschl's gyrus. From these SURS slabs, every other slab with a random start was selected for A1 mapping and processed using a Nissl protocol to reveal the cytoarchitectural features of the tissue. The sections adjacent to each Nissl section were processed with AChE or parvalbumin to reveal chemoarchitectural characteristics of the tissue. Cyto- and chemoarchitectural sections were used to identify the boundaries of the primary and secondary auditory cortices. Finally, total volume of A1 was estimated according to the Cavalieri method, which uses the sum of the areas of systematic, random parallel sections through an object (in this case A1) to calculate an estimate the volume of the object (Gundersen and Jensen, 1987).

It is impossible to generate uniformly random sections consistently orthogonal to the pial surface to ensure clear definition of cortical layers using the SURS approach above. Thus, slabs interleaved with those used to generate mapping sections were selected, and the boundaries of A1 were extended from the mapping sections into adjacent, uncut slabs of tissue. A1 was dissected out of these slabs using cuts perpendicular to the pial surface, and further separated into smaller blocks. Blocks containing A1 from the most rostral, and caudal slabs were each assigned a weight of 1/3, whereas A1 blocks not at the rostral or caudal ends were each assigned a weight of 1. 1/3 was chosen because the boundary of A1 has a positive curvature that is best fit by a cone or pyramid, which is roughly 1/3 the volume of an A1 block not located at a rostral or caudal boundary (Dorph-Petersen et al., 2009), as such blocks are prismoids. Block weights were used during subsequent determination of axon bouton number. SURS was employed to select blocks for additional processing. Each selected block was processed using the Fixed Axis Vertical Rotator (FAVeR) approach, with the central axis of rotation oriented orthogonal to the pial surface, to generate a FAVeR section from the center of the block (Dorph-Petersen and Gundersen, 2003). FAVeR sections were next processed for Nissl substance. Volume of each cortical layer in A1 was derived by multiplying the estimate of the volume fraction of each cortical layer obtained from the FAVeR section with the A1 total volume estimate.

Tissue sections were processed using fluorescence immunohistochemistry for confocal imaging. Vesicular glutamate transporter 1 (VGluT1) protein is present in boutons of cortico-cortical neurons and VGluT2 in boutons of thalamocortical neurons (Fremeau et al., 2001, 2004a,b; Hackett et al., 2011). Thus, anti-VGluT1 (guinea pig, AB5905, Millipore, Billerica, MA, USA) and anti-VGluT2 (rabbit, V2514,

HY-19, Sigma-Aldrich, St. Louis, MO, USA) antibodies were used as markers of cortico-cortical and thalamocortical axon boutons, respectively. As expected, VGluT1-IR and VGluT2-IR did not colocalize, whereas VGluT1-IR and VGluT2-IR objects significantly overlapped with the axon bouton marker synaptophysin (Synaptophysin-IR). Neither VGluT1-IR nor VGluT2-IR colocalized with fluorescent objects labeling GAD65-containing inhibitory boutons.

Images were captured with a 1.42 NA 60× oil objective on an Olympus BX51 upright microscope with a DSU spinning disk confocal (Olympus, Center Valley, PA, USA) and collected with SlideBook software (Intelligent Imaging Innovations, Denver, CO, USA). Nevertheless, even with this approach, the resolution was below that necessary to fully separate individual axon boutons, especially in the z-axis of the imaging stack. Therefore, prior to quantification, image stacks were deconvolved. Image stacks were then processed using an iterative masking approach that coupled intensity segmentation with morphological selection (Fish et al., 2008). VGluT1- and VGluT2-IR objects were counted using the associated point rule (Baddeley and Jensen, 2004), with the centroid of each bouton mask serving as the associated point allowing selection of those boutons within an optical dissector.

Results

Neither VGluT1-IR nor VGluT2-IR density (Cohort 1 and Cohort 2) nor number (Cohort 2) were altered in deep layer III of A1 in schizophrenia. Similarly, mean VGluT1-IR and VGluT2-IR fluorescence intensity were unchanged in both cohorts. This latter finding indicates not only that bouton VGluT protein levels are unchanged in schizophrenia, but also that the lack of difference in bouton numbers between groups was not due to differences in bouton detectability (Moyer et al., 2013).

Study of Glutamate Decarboxylase 65-Immunoreactive Boutons (Moyer et al., 2012)

Stereologic methods

Brain specimen acquisition, cutting, sampling and imaging were performed as described in "Study of Vesicular Glutamate Transporter-Immunoreactive Boutons (Moyer et al., 2013)" section, above, in the same two cohorts of cases. As in "Study of Vesicular Glutamate Transporter-Immunoreactive Boutons (Moyer et al., 2013)" section, cases were selected using a combined immunohistochemical-confocal imaging approach. Glutamate decarboxylase 65 (GAD65) synthesizes GABA in axon boutons in response to demand for GABA and during sustained neuronal activity (Kaufman et al., 1991; Esclapez et al., 1994; Tian et al., 1999). A mouse anti-GAD65 antibody (MAB351, Millipore, Billerica, MA, USA) was used to visualize and quantify GAD65 levels in boutons. Image stacks were acquired and processed, and boutons selected for quantification also as described in "Study of Vesicular Glutamate Transporter-Immunoreactive Boutons (Moyer et al., 2013)" section.

Results

GAD65 immuno-reactive (GAD65-IR) bouton density (Cohort 1 and Cohort 2) and number (Cohort 2) were unaltered in schizophrenia (**Figures 3A,B**). In contrast, mean bouton GAD65 fluorescence intensity was reduced 40.5% in deep layer III in A1 in schizophrenia (**Figures 3C,D**; Moyer et al., 2012).

Summary of Axon Bouton Studies

In summary, layer III bouton density was significantly reduced in A1 in schizophrenia based on SYP-IR (Sweet et al., 2007). Synaptophysin is found in approximately 95% of cortical boutons (Jahn et al., 1985; Navone et al., 1986) and does not distinguish between excitatory and inhibitory axon boutons (Navone et al., 1986), thus the use of more descriptive markers for boutons were used in subsequent studies. Excitatory bouton density did not appear to be altered in A1 in schizophrenia based on assessments of VGluT1- and VGluT2-IR in two independent cohorts of cases (Moyer et al., 2013). Further, GAD65-IR bouton density was also not altered in two independent cohorts, but GAD65-IR fluorescent intensity was significantly reduced, suggesting that within-bouton GAD65 levels are reduced in A1 in schizophrenia (Moyer et al., 2012). Lower GAD65 levels could indicate decreased GABA synthesis, and thereby contribute to altered fast GABAergic inhibition in auditory circuits which is thought to underlie impaired aSSR entrainment in schizophrenia (Kwon et al., 1999; Light et al., 2006; Krishnan et al., 2009). Future studies are needed to directly test this hypothesis.

Several other bouton types that are SYP-IR have not yet been specifically evaluated in A1 in schizophrenia. These include boutons of chandelier cell inhibitory neurons, sub-populations of somatostatin-expressing and vasoactive intestinal peptide-expressing interneurons that do not express GAD65 (Fish et al., 2011; Rocco et al., 2015), and non-glutamatergic/non-GABAergic boutons (e.g., cholinergic, serotonergic, or dopaminergic boutons). Reduced density of these boutons could contribute to the reduced density of layer III putative axon boutons in schizophrenia, revealed by the assessment of SYP-IR. Finally, published results indicate that synaptophysin itself may be reduced in schizophrenia (Glantz and Lewis, 1997). Thus, it is conceivable that the reduction in SYP-IR bouton density observed in the original article assessing boutons in A1 in schizophrenia (Sweet et al., 2007) could represent reduced detectability of these structures due to lower protein levels in auditory cortex in schizophrenia.

Studies of Dendritic Spines

Study of Spine Quantification Based on Spinophilin Labeling (Sweet et al., 2009)

Stereologic methods

A1 and A2 sections adjacent to those previously studied (Cohort 1 as described above in Sections "Study of Synaptophysin-Immunoreactive Boutons (Sweet et al., 2007)", "Study of Vesicular Glutamate Transporter-Immunoreactive Boutons (Moyer et al., 2013)", "Study of Glutamate Decarboxylase

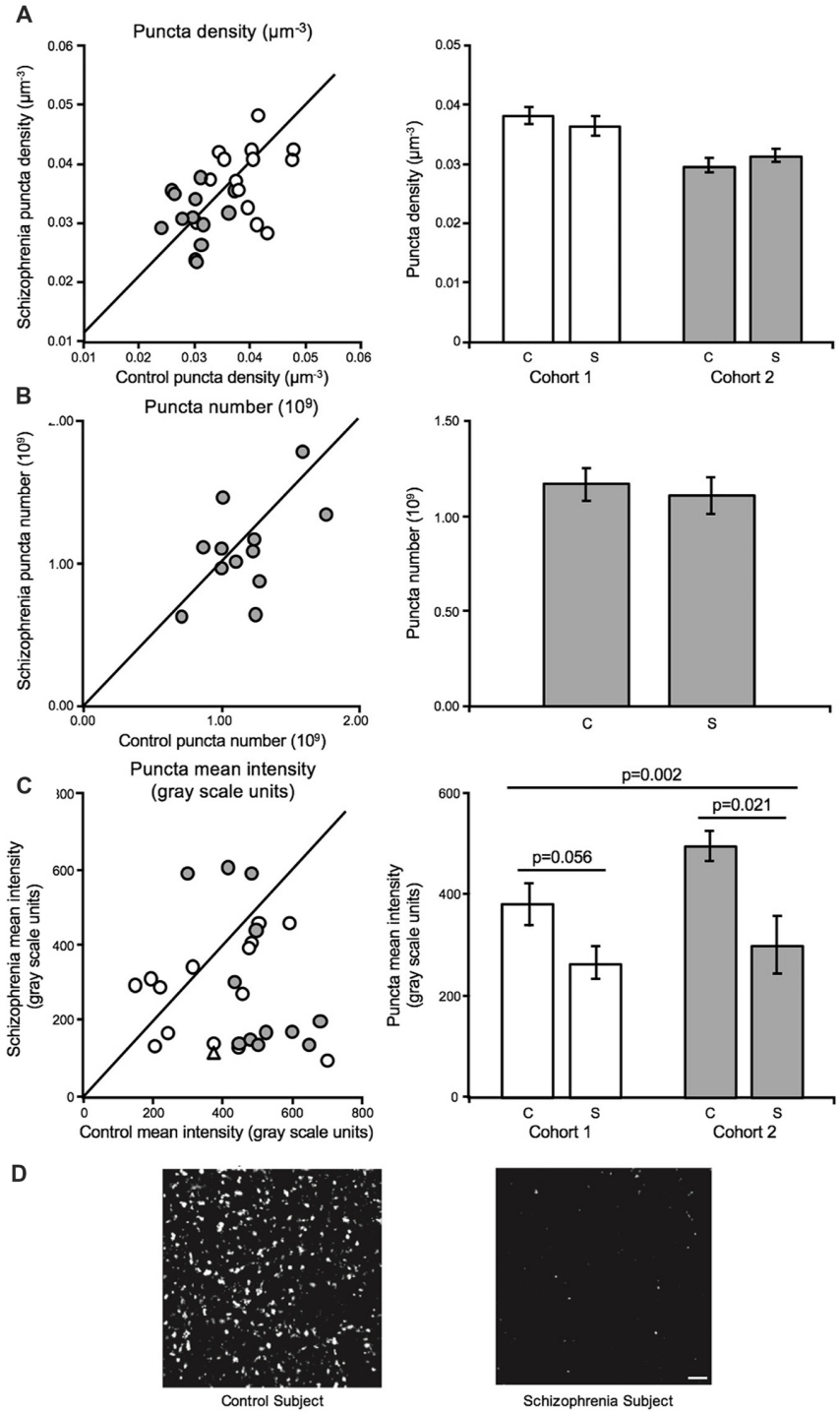

FIGURE 3 | Inhibitory boutons in deep layer III in A1 in schizophrenia (Moyer et al., 2012). For scatterplots: Cohort 1 is denoted by open circles, Cohort 2 is denoted by closed gray circles, and the line represents schizophrenia = unaffected comparison subject values. For bar graphs: C denotes unaffected comparison group, S denotes schizophrenia, and error bars are ± SEM. **(A)** Assessment of biased (Cohort 1) and unbiased (Cohort 2) cohorts revealed putative inhibitory bouton density in deep layer III in A1 is unchanged in schizophrenia. **(B)** Assessment of an unbiased cohort of schizophrenia and unaffected comparison subjects (Cohort 2, closed gray circles) revealed that inhibitory bouton number was also not altered in A1 in schizophrenia. **(C)** Mean intensity of Glutamate decarboxylase 65 immuno-reactive (GAD65-IR) objects was significantly reduced in deep layer III in A1 in schizophrenia in both cohorts. Open triangle in the scatterplot denotes the Cohort 1 subject pair included in the representative micrographs of reduced GAD65-IR in schizophrenia in A1 in **(D)**. Scale bar = 10 μm.

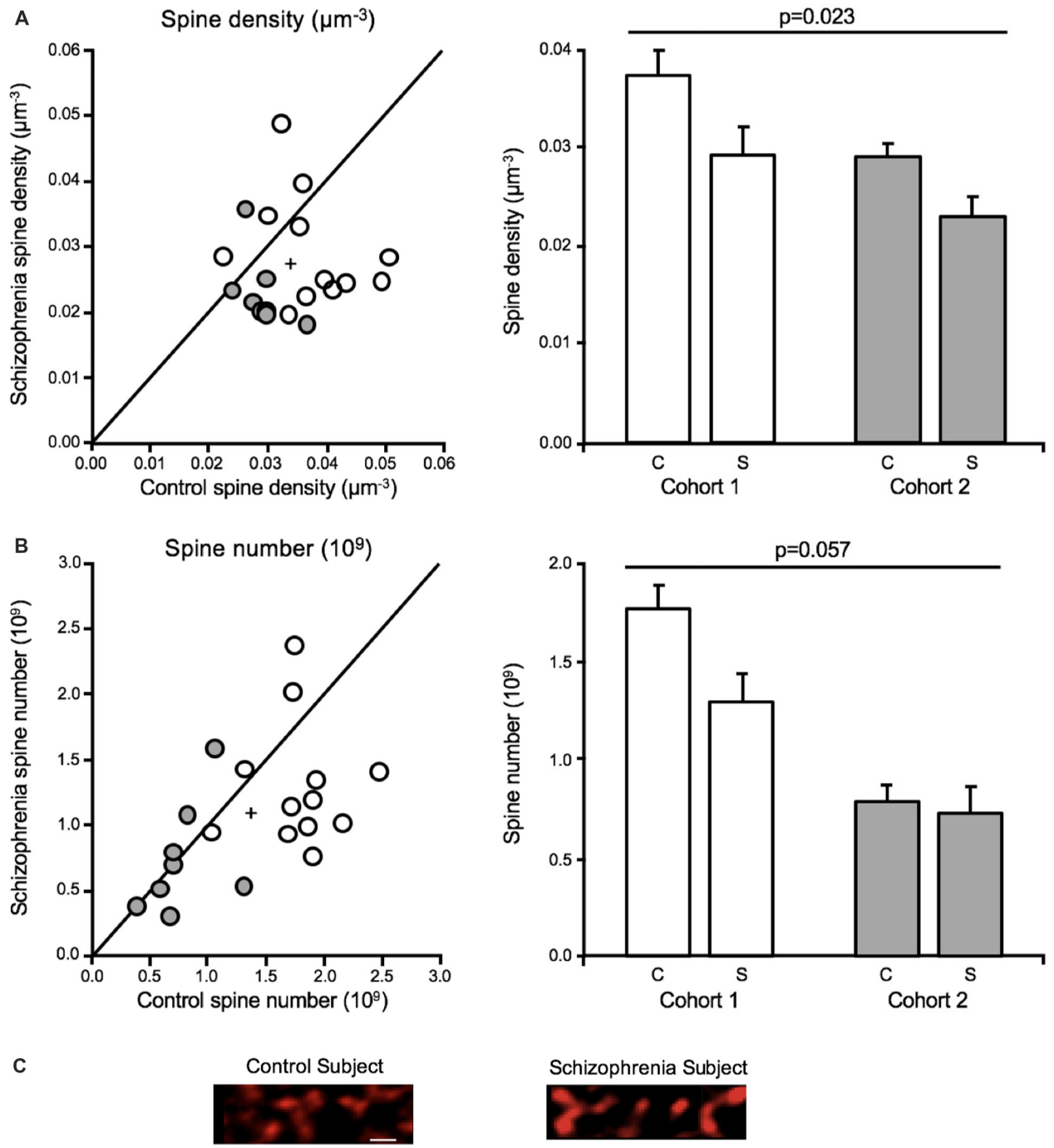

FIGURE 4 | Dendritic spine alterations in deep layer III in A1 in schizophrenia (Shelton et al., 2015; MacDonald et al., 2017). For scatterplots: Cohort 1 is denoted by open circles, Cohort 2 is denoted by closed gray circles, the group mean is indicated by the cross, and the line represents schizophrenia = unaffected comparison subject values. For bar graphs: C denotes unaffected comparison group, S denotes schizophrenia, and error bars are ± SE. **(A)** Assessment of cohorts 1 and 2 revealed mean dendritic spine density was reduced in deep layer III in A1 in schizophrenia. **(B)** Mean spine number was also found to be significantly reduced in deep layer III in A1 in schizophrenia. **(C)** Representative micrographs of phalloidin-labeled objects from one pair comprising one unaffected comparison case and one schizophrenia case revealing putative dendritic spine loss in A1 in schizophrenia. Scale bar = 1 µm.

65-Immunoreactive Boutons (Moyer et al., 2012)"; Sweet et al., 2007) were selected for processing and assessment of dendritic spine density. Tissue sampling and imaging were performed as described in section "Study of Synaptophysin-Immunoreactive Boutons (Sweet et al., 2007)", with a few exceptions. Spinophilin is a protein phosphatase 1-binding

protein found in dendritic spines (Allen et al., 1997; Muly et al., 2004). A selective affinity-purified polyclonal rabbit antibody raised against a peptide from rat spinophilin (Chemicon, Temecula, CA, USA, AB5669; Amateau and McCarthy, 2002) was used to visualize dendritic spines in deep layer III of A1 and A2 in schizophrenia and unaffected comparison subjects. Evaluation of antibody penetration revealed that this antibody labeled the tissue uniformly, except at each tissue surface (Dorph-Petersen et al., 2001). Spinophilin-immunoreactive (SP-IR) objects were manually counted after capture using a 1.4 numerical aperture 100× oil immersion objective and an optical dissector with x and y dimensions of 3.5 μm and a z height of 50% of the final tissue thickness and guard zones of 25% of the final tissue thickness at each sampling site.

Results

The density of SP-IR puncta was reduced by 27.2% in deep layer III of A1 in schizophrenia. Similarly, SP-IR puncta density was also reduced by 22.2% in deep layer III of A2 in schizophrenia. Further, SP-IR density was correlated with density of synaptophysin-immunoreactive axon boutons (Sweet et al., 2009).

These findings were consistent with previous results reporting reduced dendritic spine density in regions of neocortex and of the hippocampal formation implicated in schizophrenia (Moyer et al., 2015). As described in section "Study of Synaptophysin-Immunoreactive Boutons (Sweet et al., 2007)", because of the *in vivo* imaging evidence of reduced gray matter volume of auditory cortex in schizophrenia, the reduced density of dendritic spines was interpreted to reflect a reduction in spine number, despite the fact that A1 volume was not estimated in these subjects. Previous studies using Golgi methods revealed reduced numbers of dendritic spines per dendritic length in PFC (Glantz and Lewis, 2000) and in another region of temporal cortex, Brodmann area 38, in schizophrenia (Garey et al., 1998). Similar to other regions, dendritic spine number was predicted to be decreased in A1 in this illness. Reduced number of dendritic spines in layer III of A1 in schizophrenia could reflect fewer spines per dendrite, reduced total dendritic length of pyramidal cells, reduced numbers of pyramidal cells, or their combination.

A further comment is warranted regarding the potentially conflicting findings of: (1) correlated reductions in dendritic spine density and in density of SYP-IR boutons; and (2) no reduction in excitatory (VGluT1- and VGluT2-IR) boutons. Dendritic spine density is shaped by activity-dependent glutamate signaling (Nägerl et al., 2004; Zhou et al., 2004; Xie et al., 2005). Spine density has been shown to be reduced when glutamatergic signaling is disrupted (Matthews et al., 1976; Cheng et al., 1997; McKinney et al., 1999). Because reduced synaptophysin protein levels can impair glutamate signaling (Kwon and Chapman, 2011), it is plausible that synaptophysin levels are reduced within VGluT1- or VGluT2-positive boutons. Therefore, reduced synaptophysin may contribute to dendritic spine reductions in auditory cortex in schizophrenia. In a future study, this hypothesis could be readily tested using a multi-label immunohistochemistry design with anti-VGluT1, -VGluT2, and -synaptophysin antibodies, in combination with SURS sampling and quantitative fluorescence microscopy.

Study of Spine Quantification Based on Spinophilin-Phalloidin Double Labeling (Shelton et al., 2015)

Stereologic methods

Two cohorts, each comprised of one schizophrenia and one unaffected comparison group, were assessed. The first cohort consisted of the same subjects, and used the same methods of tissue sampling as described for Cohort 2 in sections "Study of Vesicular Glutamate Transporter-Immunoreactive Boutons (Moyer et al., 2013)" and "Study of Glutamate Decarboxylase 65-Immunoreactive Boutons (Moyer et al., 2012)" above. Cases in the second cohort were sampled using a simpler SURS approach. In brief, the left STG was dissected, reassembled in low-melt agarose, and cut into 3 mm slabs orientated orthogonal to Heschl's gyrus. Every other slab with a random start was selected and A1 mapped using adjacent sections stained for Nissl substance, AChE, and parvalbumin. The sections adjacent to the mapping sections were selected for assay SURS. A1 tissue sections were incubated in an anti-spinophilin antibody (polyclonal, AB5669; EMD Millipore, Billerica, MA, USA), to visualize spine heads (Allen et al., 1997; Muly et al., 2004). Additionally, the tissue sections were incubated in phalloidin conjugated to AlexaFluor568 (A12380; Invitrogen Corp., Carlsbad, CA, USA). Phalloidin is a mushroom toxin that binds filamentous actin which is enriched in dendritic spines (Capani et al., 2001). Colocalized SP-IR and phalloidin-labeled fluorescent objects closely resemble dendritic spines in human postmortem A1 tissue (Shelton et al., 2015). A spinophilin + phalloidin dual-labeling approach was used in the current study to identify and exclude potential off-target phalloidin-labeled and SP-IR objects. Two labels were used to detect putative spines because each label separately emits non-spine fluorescence. For example, phalloidin-labeling is sometimes observed in dendrites (presumably labeling filopodia outgrowths; Willig et al., 2014). Images were captured using a 1.42 numerical aperture 60× oil supercorrected objective on an Olympus BX51 upright microscope with a DSU spinning disk confocal (Olympus, Center Valley, PA, USA) with stage x- and y-axis movement controlled by Stereo Investigator (Microbrightfield Inc., Natick, MA, USA). Image stacks were collected using SlideBook software (Intelligent Imaging Innovations, Denver, CO, USA) which controlled z-axis movement. After collection, images of fluorescently labeled objects were processed as described in sections "Study of Vesicular Glutamate Transporter-Immunoreactive Boutons (Moyer et al., 2013)" and "Study of Glutamate Decarboxylase 65-Immunoreactive Boutons (Moyer et al., 2012)" with one addition. After deconvolution, object edges were sharpened by taking the difference between images convolved at different 2 SD of the Gaussian distribution ($\sigma1 = 0.7$; $\sigma2 = 2.0$; Kirkwood et al., 2013), after which point the images underwent iterative masking via intensity segmentation with morphological selection. Dendritic spines were defined as

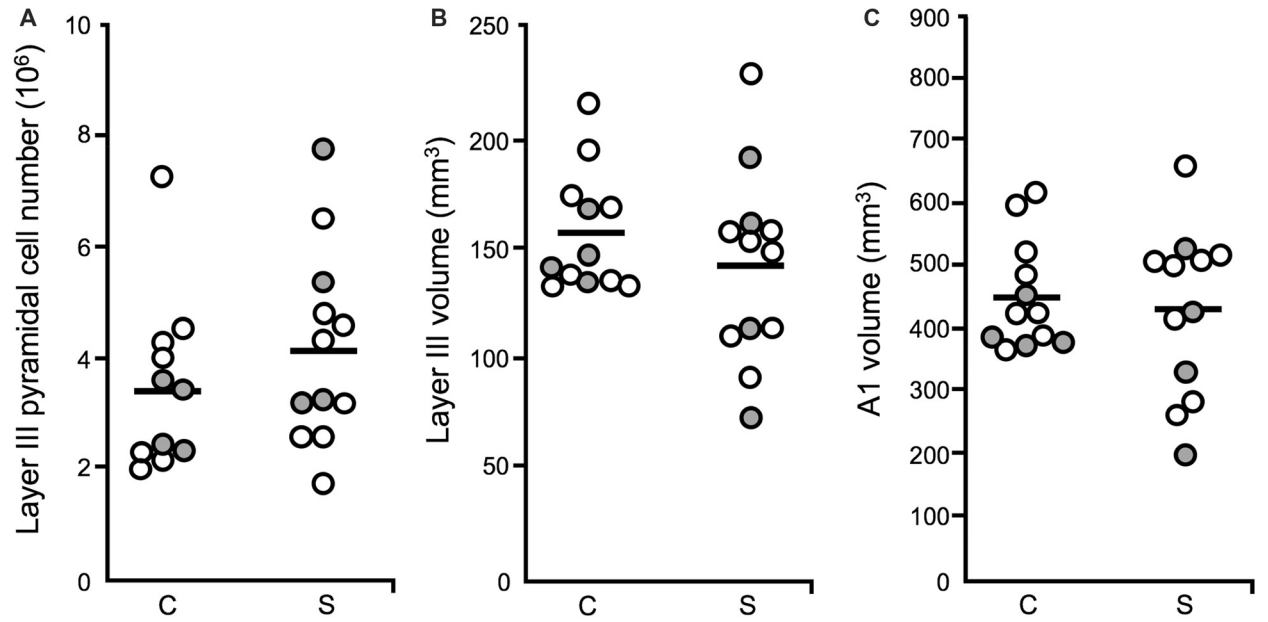

FIGURE 5 | Layer III pyramidal cell number, layer III volume and total A1 volume (Dorph-Petersen et al., 2009). For all plots: diagnostic subject pairs with one member diagnosed with schizophrenia are denoted by open circles and subject pairs with one member diagnosed with schizoaffective disorder are denoted by closed gray circles. **(A)** The number of pyramidal cells in layer III in A1 was unchanged in schizophrenia. **(B)** The volume of layer III in A1 in schizophrenia was not significantly different across diagnostic groups. **(C)** Total A1 volume did not significantly differ in schizophrenia relative to unaffected comparison cases.

phalloidin masked objects overlapping by one or more voxels of a spinophilin masked object. Spines were counted if the centroid of the phalloidin masked object fell inside the dissector, consistent with the associated point rule (Baddeley and Jensen, 2004).

Results

Both dendritic spine density and number were significantly reduced in deep layer III in A1 in schizophrenia (**Figures 4A–C**), consistent with the earlier report that found decreased spine density in this region in schizophrenia (Sweet et al., 2009). The earlier report found a reduction in SP-IR density of 27.2%, whereas the current study reported a 19.2% reduction in mean spine density in deep layer III in A1 in schizophrenia. Off-target labeling of the anti-spinophilin antibody could explain the discrepancy in the magnitude of spine density reductions observed across studies. Significantly, the current study provided for the estimation of dendritic spine number in addition to density (Shelton et al., 2015). Thus, this study showed, for the first time in any brain region, that dendritic spine number is reduced in schizophrenia.

Study of Pyramidal Cell Number (Dorph-Petersen et al., 2009)

Stereologic methods

The current study was conducted using the Cohort 2 subjects described above in sections "Study of Vesicular Glutamate Transporter-Immunoreactive Boutons (Moyer et al., 2013)" and "Study of Glutamate Decarboxylase 65-Immunoreactive Boutons (Moyer et al., 2012)" and detailed in the *Stereological methods* portion of section "Study of Vesicular Glutamate Transporter-Immunoreactive Boutons (Moyer et al., 2013)", above, with a minor adjustment. A FAVeR (weighted) sampling scheme was used to estimate pyramidal cell number in layer III in A1. Pyramidal cells were identified in the FAVeR sections stained for Nissl substance, and counted using an optical dissector in Stereo Investigator (Microbrightfield; Gundersen, 1986).

Volume by cortical layer in A1 and total A1 volume were estimated for postmortem schizophrenia and unaffected comparison cases. With total reference volume estimations, the authors of the current study were able to estimate pyramidal cell number in A1 in schizophrenia, for the first time.

Results

A1 layer III pyramidal cell density was increased in schizophrenia, relative to unaffected comparison cases. In contrast, pyramidal cell number did not differ significantly across diagnostic groups (**Figure 5A**), in agreement with previous reports that found no change in neuron number in cerebral cortex (Pakkenberg, 1993), PFC (Thune et al., 2001) nor anterior cingulate (Stark et al., 2004) in schizophrenia. Neither layer III A1 volume (**Figure 5B**), nor total A1 volume were found to be significantly reduced in schizophrenia (**Figure 5C**). Increased pyramidal cell density, with no change in pyramidal cell number, was interpreted to mean that STG gray matter loss in schizophrenia is due to the loss of neuropil components such as dendritic spines, rather than to the loss of the number of pyramidal cells.

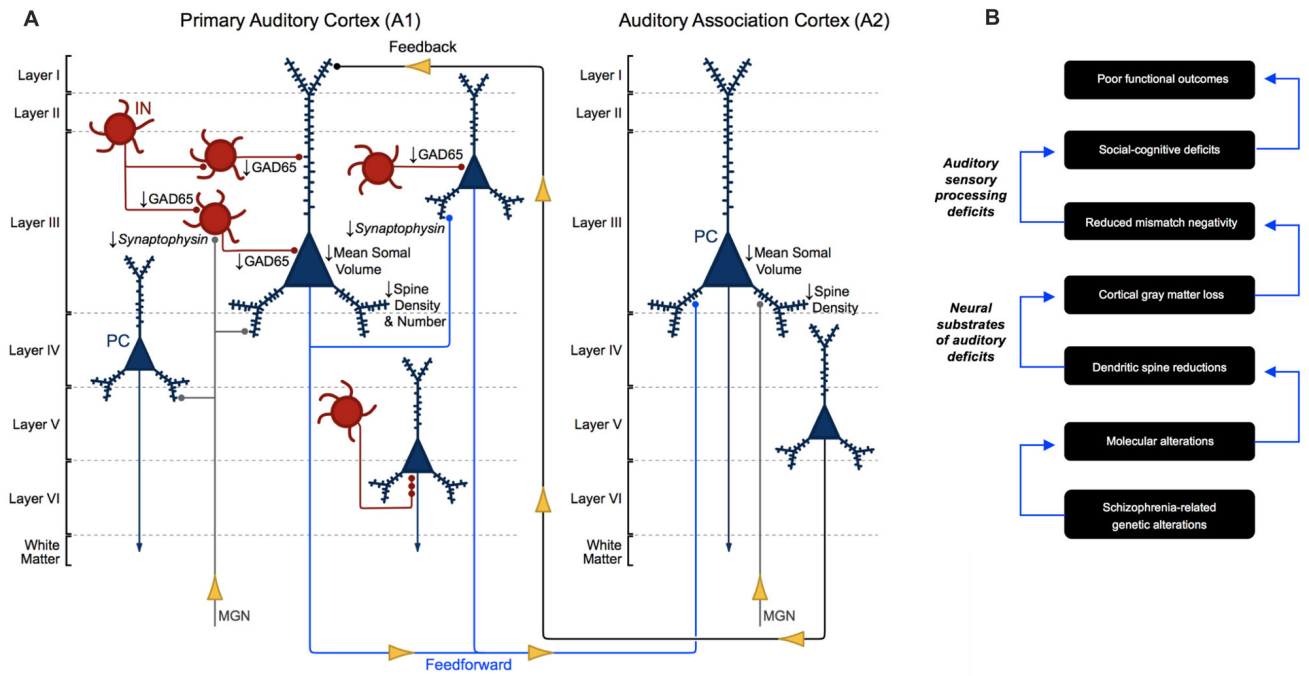

FIGURE 6 | Morphometric alterations in auditory cortex in schizophrenia. **(A)** Neuron pathology in schizophrenia as revealed by human postmortem studies of auditory cortex. Mean somal volume of PCs in deep layer III in A1 and A2 in schizophrenia were found to be significantly reduced. Dendritic spine density was reduced in deep layer III of A1 and A2, reflecting reduced number of dendritic spines in deep layer III of A1 in schizophrenia. GAD65 levels were reduced in deep layer III boutons in A1 in schizophrenia, although the specific interneuron cell types affected are not currently known. **(B)** Proposed model for auditory cortex related dysfunction in schizophrenia, linking genetic risk to anatomical alterations, auditory sensory processing deficits and poor functional outcomes.

DISCUSSION

Auditory sensory processing deficits correlate with gray matter loss in Heschl's gyrus in schizophrenia (Salisbury et al., 2007) and are now understood to reflect structural alterations, in particular, altered neuron morphology in A1 in schizophrenia (Leitman et al., 2007, 2010; Petkova et al., 2014; Javitt and Sweet, 2015). To date, human postmortem studies have revealed several important neuronal morphological aberrations in auditory cortex in schizophrenia (**Figure 6A**). Pyramidal cells in A1 and A2 deep layer III exhibit reduced somal volume (Sweet et al., 2003, 2004). Findings regarding axon boutons in deep layer III in auditory cortex in schizophrenia are mixed. An earlier report found reduced putative bouton density (Sweet et al., 2007), while later publications reported no change in the density of excitatory and inhibitory boutons (Moyer et al., 2012, 2013). Consistent with the reduced neuropil hypothesis of schizophrenia (Selemon and Goldman-Rakic, 1999; Glausier and Lewis, 2013), the number and density of dendritic spines were found to be reduced in deep layer III of A1 in schizophrenia in three independent cohorts of subjects (Sweet et al., 2009; Shelton et al., 2015).

Unlike in other diseases, such as Alzheimer's disease (Penzes et al., 2011), in A1 in schizophrenia dendritic spine loss is not accompanied by neuron loss. Specifically, layer III pyramidal cell number was confirmed to be unaltered in A1 in this illness (Dorph-Petersen et al., 2009), indicating that spine loss in this region likely reflects fewer spines per pyramidal cell. Finally, gray matter loss in auditory regions in schizophrenia has been shown to progressively worsen over time in subjects with schizophrenia, raising concerns that progressive gray matter loss is a consequence of damage to cellular structures from long-term antipsychotic use (Vita et al., 2012). Importantly, postmortem studies of long-term haloperidol exposed non-human primates have found no significant evidence that the morphology of auditory cortical neurons change as a function of antipsychotic exposure, indicating that gray matter alterations in auditory cortex in schizophrenia are not simply a result of effects of long-term antipsychotic use on these structures (Sweet et al., 2007; Moyer et al., 2012, 2013; Shelton et al., 2015).

Unique among studies of auditory-related deficits in schizophrenia, postmortem studies provide the resolution needed to identify anatomical alterations at the neuron level. The studies detailed in this review revealed several important morphometric alterations in auditory cortex in schizophrenia, and in doing so advanced the field. However, two limitations of these studies must be noted. First, all of the studies detailed in this review examined auditory cortical tissue from the left hemisphere, only (Sweet et al., 2003, 2004, 2007, 2009;

Dorph-Petersen et al., 2009; Moyer et al., 2012, 2013; Shelton et al., 2015) whereas the basic auditory processing deficits measured using *in vivo* methods from human subjects with schizophrenia are bilateral (Leitman et al., 2010). Follow up studies are needed to assess neuropathology in auditory cortex in schizophrenia in the right hemisphere. Second, these data suggest as a whole that the function of layer III pyramidal cells are altered in auditory cortex in schizophrenia. However, the immunolabeling strategies used, for example, in the dendritic spine studies could not indicate the laminar location of the cell bodies that corresponded to the altered spines (Sweet et al., 2009; Shelton et al., 2015). Therefore, although most dendritic spines in layer III arise from layer III pyramidal cells, reduction of dendritic spine on auditory cortex layer III pyramidal cells in schizophrenia has not been specifically demonstrated.

Incorporating stereological methods into postmortem studies has been instrumental in revealing neuronal morphological aberrations in auditory cortex in schizophrenia. These methods have enabled our group to utilize unbiased sampling of tissue as well as the unbiased estimation of the structural features of neurons, including axon bouton density and number, dendritic spine density and number, and pyramidal cell number. Likewise, rigorous inclusion of stereological techniques has made it possible for our group (Dorph-Petersen et al., 2009) and others (Smiley et al., 2013) to accurately estimate individual cortical layer volumes within A1 and A1 total volume. In sum, stereological methods have been critical for the collection and publication of a body of work about neuronal alterations in auditory cortex in schizophrenia that provide a strong foundation upon which future studies will rely.

One such study is a recent human postmortem study of dendritic spines in A1 in schizophrenia, which performed a secondary analysis of the data described in section "Study of Spine Quantification Based on Spinophilin-Phalloidin Double Labeling (Shelton et al., 2015)" which revealed that reduced dendritic spine density in A1 in schizophrenia is restricted to the smallest dendritic spines (MacDonald et al., 2017). *In vivo* imaging of dendritic spine dynamics in animal models indicate that small spines are largely new and/or transient, whereas large spine are typically mature/persistent (Holtmaat et al., 2005). Selective reduction of nascent dendritic spines could indicate that altered spine morphology in schizophrenia is due to aberrant spinogenesis or spine stabilization, rather than, as was historically assumed, over-pruning of mature spines during adolescent development (Boksa, 2012).

Reduced dendritic spine density may function as an intermediate, anatomical phenotype for schizophrenia, a key component in a hierarchical model that could link genetics, at one extreme, to functional outcomes, at the other (**Figure 6B**). Many schizophrenia risk genes encode synaptic proteins and those involved in excitatory (Ca^{2+}) signaling in dendrites (Purcell et al., 2014; Schizophrenia Working Group of the Psychiatric Genomics Consortium, 2014; Heyes et al., 2015). Thus, one promising future direction for the assessment of A1 cellular pathology in schizophrenia involves investigating potential mechanisms associated with known genetic risk for schizophrenia, that could lead to reduced small dendritic spine density, as is observed in A1 in this disease. Our group recently showed that levels of a peptide shared among voltage-gated calcium channel (VGCC) β subunits ($Ca_V\beta$) was inversely correlated with the density of small spines. Overexpressing *CACNB4*, the gene that encodes $Ca_V\beta4$, which is present in the temporal cortex, and is a critical regulator of VGCC activity (Dolphin, 2012), in primary neuronal culture resulted in reduced density of small, but not large, dendritic spines (MacDonald et al., 2017). Future studies should observe the effects of overexpressing *CACNB4* in a model organism during adolescence, a period that is associated with schizophrenia onset as well as system-wide spine number changes in normative development (Penzes et al., 2011). The functional outcomes of individuals with schizophrenia have remained largely unchanged since the introduction of antipsychotics, likely due in part to the fact that we do not fully understand the pathophysiology of this illness (Insel, 2010). Probing relationships between $Ca_V\beta4$ (and other proteins like it) and dendritic spine morphology has the potential to elucidate an important, anatomical phenotype of schizophrenia, which may be a final common pathway for auditory impairment in schizophrenia. Finally, examining such relationships could lead to the identification of drug targets or provide other critical information for the development of superior strategies to treat or prevent auditory sensory processing deficits in schizophrenia.

AUTHOR CONTRIBUTIONS

All studies reviewed took place in the lab of RAS. EMP did not contribute to any of the studies reviewed (hence, lack of authorship on the published works). EMP drafted the current review with significant direction from and revision by RAS. EMP and RAS approve the version to be published. The content is solely the responsibility of the authors and does not necessarily represent the official views of the National Institute of Mental Health, the National Institutes of Health, the Department of Veterans Affairs, or the United States Government.

FUNDING

This study was supported by the following federal grants (National Institutes of Health): T32-DC011499 (EMP) and MH071533 (RAS).

ACKNOWLEDGMENTS

We would like to thank Dr. Karl-Anton Dorph-Petersen for providing comments for this manuscript and Mary L. Brady for her help with **Figures 1–6** in this review article.

REFERENCES

Allen, P. B., Ouimet, C. C., and Greengard, P. (1997). Spinophilin, a novel protein phosphatase 1 binding protein localized to dendritic spines. *Proc. Natl. Acad. Sci. U S A* 94, 9956–9961. doi: 10.1073/pnas.94.18.9956

Amateau, S. K., and McCarthy, M. M. (2002). A novel mechanism of dendritic spine plasticity involving estradiol induction of prostaglandin-E2. *J. Neurosci.* 22, 8586–8596.

Arellano, J. I., Espinosa, A., Fairén, A., Yuste, R., and DeFelipe, J. (2007). Non-synaptic dendritic spines in neocortex. *Neuroscience* 145, 464–469. doi: 10.1016/j.neuroscience.2006.12.015

Baddeley, A., and Jensen, E. B. V. (2004). *Stereology for Statisticians.* Boca Raton, FL: CRC Press.

Barta, P. E., Pearlson, G. D., Brill, L. B. II., Royall, R., McGilchrist, I. K., Pulver, A. E., et al. (1997). Planum temporale asymmetry reversal in schizophrenia: replication and relationship to gray matter abnormalities. *Am. J. Psychiatry* 154, 661–667. doi: 10.1176/ajp.154.5.661

Boksa, P. (2012). Abnormal synaptic pruning in schizophrenia: urban myth or reality? *J. Psychiatry Neurosci.* 37, 75–77. doi: 10.1503/jpn.120007

Braendgaard, H., and Gundersen, H. J. G. (1986). The impact of recent stereological advances on quantitative studies of the nervous system. *J. Neurosci. Methods* 18, 39–78. doi: 10.1016/0165-0270(86)90112-3

Brenner, C. A., Krishnan, G. P., Vohs, J. L., Ahn, W.-Y., Hetrick, W. P., Morzorati, S. L., et al. (2009). Steady state responses: electrophysiological assessment of sensory function in schizophrenia. *Schizophr. Bull.* 35, 1065–1077. doi: 10.1093/schbul/sbp091

Capani, F., Deerinck, T. J., Ellisman, M. H., Bushong, E., Bobik, M., and Martone, M. E. (2001). Phalloidin-eosin followed by photo-oxidation: a novel method for localizing F-actin at the light and electron microscopic levels. *J. Histochem. Cytochem.* 49, 1351–1361. doi: 10.1177/002215540104901103

Catts, S. V., Shelley, A.-M., Ward, P. B., Liebert, B., McConaghy, N., Andrews, S., et al. (1995). Brain potential evidence for an auditory sensory memory deficit in schizophrenia. *Am. J. Psychiatry* 152, 213–219. doi: 10.1176/ajp.152.2.213

Chen, J. L., Villa, K. L., Cha, J. W., So, P. T., Kubota, Y., and Nedivi, E. (2012). Clustered dynamics of inhibitory synapses and dendritic spines in the adult neocortex. *Neuron* 74, 361–373. doi: 10.1016/j.neuron.2012.02.030

Cheng, H.-W., Rafols, J. A., Goshgarian, H. G., Anavi, Y., Tong, J., and McNeill, T. H. (1997). Differential spine loss and regrowth of striatal neurons following multiple forms of deafferentation: a golgi study. *Exp. Neurol.* 147, 287–298. doi: 10.1006/exnr.1997.6618

DeFelipe, J., Hendry, S., and Jones, E. (1989). Synapses of double bouquet cells in monkey cerebral cortex visualized by calbindin immunoreactivity. *Brain Res.* 503, 49–54. doi: 10.1016/0006-8993(89)91702-2

DeFelipe, J., Hendry, S. H. C., Jones, E. G., and Schmechel, D. (1985). Variability in the terminations of GABAergic chandelier cell axons on initial segments of pyramidal cell axons in the monkey sensory-motor cortex. *J. Comp. Neurol.* 231, 364–384. doi: 10.1002/cne.902310307

Dick, F., Tierney, A. T., Lutti, A., Josephs, O., Sereno, M. I., and Weiskopf, N. (2012). *In vivo* functional and myeloarchitectonic mapping of human primary auditory areas. *J. Neurosci.* 32, 16095–16105. doi: 10.1523/JNEUROSCI.1712-12.2012

Dolphin, A. C. (2012). Calcium channel auxiliary α2δ and β subunits: trafficking and one step beyond. *Nat. Rev. Neurosci.* 13, 542–555. doi: 10.1038/nrn3311

Dorph-Petersen, K.-A., Delevich, K. M., Marcsisin, M. J., Zhang, W., Sampson, A. R., Gundersen, H. J. G., et al. (2009). Pyramidal neuron number in layer 3 of primary auditory cortex of subjects with schizophrenia. *Brain Res.* 1285, 42–57. doi: 10.1016/j.brainres.2009.06.019

Dorph-Petersen, K.-A., and Gundersen, H. J. G. (2003). Fixed axis vertical rotator: a method for unbiased stereological estimation from central vertical sections. *FASEB* 17:A771.

Dorph-Petersen, K.-A., Nyengaard, J. R., and Gundersen, H. J. G. (2001). Tissue shrinkage and unbiased stereological estimation of particle number and size. *J. Microsc.* 204, 232–246. doi: 10.1046/j.1365-2818.2001.00958.x

Dunaevsky, A., Tashiro, A., Majewska, A., Mason, C., and Yuste, R. (1999). Developmental regulation of spine motility in the mammalian central nervous system. *Proc. Natl. Acad. Sci. U S A* 96, 13438–13443. doi: 10.1073/pnas.96.23.13438

Esclapez, M., Tillakaratne, N., Kaufman, D. L., Tobin, A., and Houser, C. (1994). Comparative localization of two forms of glutamic acid decarboxylase and their mRNAs in rat brain supports the concept of functional differences between the forms. *J. Neurosci.* 14, 1834–1855.

Fairén, A., and Valverde, F. (1980). A specialized type of neuron in the visual cortex of cat: a Golgi and electron microscope study of chandelier cells. *J. Comp. Neurol.* 194, 761–779. doi: 10.1002/cne.901940405

Fett, A.-K. J., Viechtbauer, W., Dominguez, M.-G., Penn, D. L., van Os, J., and Krabbendam, L. (2011). The relationship between neurocognition and social cognition with functional outcomes in schizophrenia: a meta-analysis. *Neurosci. Biobehav. Rev.* 35, 573–588. doi: 10.1016/j.neubiorev.2010.07.001

Fischer, M., Kaech, S., Knutti, D., and Matus, A. (1998). Rapid actin-based plasticity in dendritic spines. *Neuron* 20, 847–854. doi: 10.1016/s0896-6273(00)80467-5

Fish, K. N., Sweet, R. A., Deo, A. J., and Lewis, D. A. (2008). An automated segmentation methodology for quantifying immunoreactive puncta number and fluorescence intensity in tissue sections. *Brain Res.* 1240, 62–72. doi: 10.1016/j.brainres.2008.08.060

Fish, K. N., Sweet, R. A., and Lewis, D. A. (2011). Differential distribution of proteins regulating GABA synthesis and reuptake in axon boutons of subpopulations of cortical interneurons. *Cereb. Cortex* 21, 2450–2460. doi: 10.1093/cercor/bhr007

Fremeau, R. T. Jr., Kam, K., Qureshi, T., Johnson, J., Copenhagen, D. R., Storm-Mathisen, J., et al. (2004a). Vesicular glutamate transporters 1 and 2 target to functionally distinct synaptic release sites. *Science* 304, 1815–1819. doi: 10.1126/science.1097468

Fremeau, R. T. Jr., Voglmaier, S., Seal, R. P., and Edwards, R. H. (2004b). VGLUTs define subsets of excitatory neurons and suggest novel roles for glutamate. *Trends Neurosci.* 27, 98–103. doi: 10.1016/j.tins.2003.11.005

Fremeau, R. T. Jr., Troyer, M. D., Pahner, I., Nygaard, G. O., Tran, C. H., Reimer, R. J., et al. (2001). The expression of vesicular glutamate transporters defines two classes of excitatory synapse. *Neuron* 31, 247–260. doi: 10.1016/s0896-6273(01)00344-0

Galaburda, A. M., and Pandya, D. N. (1983). The intrinsic architectonic and connectional organization of the superior temporal region of the rhesus monkey. *J. Comp. Neurol.* 221, 169–184. doi: 10.1002/cne.902210206

Garey, L. J. (1909/1994). *Brodmann's 'Localisation in the Cerebral Cortex'.* London: Smith-Gordon.

Garey, L., Ong, W., Patel, T., Kanani, M., Davis, A., Mortimer, A., et al. (1998). Reduced dendritic spine density on cerebral cortical pyramidal neurons in schizophrenia. *J. Neurol. Neurosurg. Psychiatry* 65, 446–453. doi: 10.1136/jnnp.65.4.446

Glantz, L. A., and Lewis, D. A. (1997). Reduction of synaptophysin immunoreactivity in the prefrontal cortex of subjects with schizophrenia: regional and diagnostic specificity. *Arch. Gen. Psychiatry* 54, 943–952. doi: 10.1001/archpsyc.1997.01830220065010

Glantz, L. A., and Lewis, D. A. (2000). Decreased dendritic spine density on prefrontal cortical pyramidal neurons in schizophrenia. *Arch. Gen. Psychiatry* 57, 65–73. doi: 10.1001/archpsyc.57.1.65

Glausier, J. R., and Lewis, D. A. (2013). Dendritic spine pathology in schizophrenia. *Neuroscience* 251, 90–107. doi: 10.1016/j.neuroscience.2012.04.044

Gold, R., Butler, P., Revheim, N., Leitman, D. I., Hansen, J. A., Gur, R. C., et al. (2012). Auditory emotion recognition impairments in schizophrenia: relationship to acoustic features and cognition. *Am. J. Psychiatry* 169, 424–432. doi: 10.1176/appi.ajp.2011.11081230

Gray, E. (1959). Electron microscopy of synaptic contacts on dendrite spines of the cerebral cortex. *Nature* 183, 1592–1593. doi: 10.1038/1831592a0

Green, M. F., Horan, W. P., and Lee, J. (2015). Social cognition in schizophrenia. *Nat. Rev. Neurosci.* 16, 620–631. doi: 10.1038/nrn4005

Green, M. F., Kern, R. S., and Heaton, R. K. (2004). Longitudinal studies of cognition and functional outcome in schizophrenia: implications for MATRICS. *Schizophr. Res.* 72, 41–51. doi: 10.1016/j.schres.2004.09.009

Gundersen, H. J. G. (1986). Stereology of arbitrary particles. *J. Microsc.* 143, 3–45. doi: 10.1111/j.1365-2818.1986.tb02764.x

Gundersen, H. J. G. (1988). The nucleator. *J. Microsc.* 151, 3–21. doi: 10.1111/j.1365-2818.1988.tb04609.x

Gundersen, H. J. G., Bagger, P., Bendtsen, T. F., Evans, S. M., Korbo, L., Marcussen, N., et al. (1988). The new stereological tools: disector, fractionator, nucleator and point sampled intercepts and their use in pathological research and diagnosis. *APMIS* 96, 857–881. doi: 10.1111/j.1699-0463.1988.tb00954.x

Gundersen, H. J. G., and Jensen, E. B. (1987). The efficiency of systematic sampling in stereology and its prediction. *J. Microsc.* 147, 229–263. doi: 10.1111/j.1365-2818.1987.tb02837.x

Hackett, T. A. (2011). Information flow in the auditory cortical network. *Hear. Res.* 271, 133–146. doi: 10.1016/j.heares.2010.01.011

Hackett, T. A., Preuss, T. M., and Kaas, J. H. (2001). Architectonic identification of the core region in auditory cortex of macaques, chimpanzees, and humans. *J. Comp. Neurol.* 441, 197–222. doi: 10.1002/cne.1407

Hackett, T. A., Takahata, T., and Balaram, P. (2011). VGLUT1 and VGLUT2 mRNA expression in the primate auditory pathway. *Hear. Res.* 274, 129–141. doi: 10.1016/j.heares.2010.11.001

Hamm, J. P., Bobilev, A. M., Hayrynen, L. K., Hudgens-Haney, M. E., Oliver, W. T., Parker, D. A., et al. (2015). Stimulus train duration but not attention moderates γ-band entrainment abnormalities in schizophrenia. *Schizophr. Res.* 165, 97–102. doi: 10.1016/j.schres.2015.02.016

Hamm, J. P., Gilmore, C. S., Picchetti, N. A., Sponheim, S. R., and Clementz, B. A. (2011). Abnormalities of neuronal oscillations and temporal integration to low-and high-frequency auditory stimulation in schizophrenia. *Biol. Psychiatry* 69, 989–996. doi: 10.1016/j.biopsych.2010.11.021

Hashikawa, T., Molinari, M., Rausell, E., and Jones, E. G. (1995). Patchy and laminar terminations of medial geniculate axons in monkey auditory cortex. *J. Comp. Neurol.* 362, 195–208. doi: 10.1002/cne.903620204

Heyes, S., Pratt, W. S., Rees, E., Dahimene, S., Ferron, L., Owen, M. J., et al. (2015). Genetic disruption of voltage-gated calcium channels in psychiatric and neurological disorders. *Prog. Neurobiol.* 134, 36–54. doi: 10.1016/j.pneurobio.2015.09.002

Hirayasu, Y., McCarley, R. W., Salisbury, D. F., Tanaka, S., Kwon, J. S., Frumin, M., et al. (2000). Planum temporale and Heschl gyrus volume reduction in schizophrenia: a magnetic resonance imaging study of first-episode patients. *Arch. Gen. Psychiatry* 57, 692–699. doi: 10.1001/archpsyc.57.7.692

Hirayasu, Y., Shenton, M. E., Salisbury, D. F., Dickey, C. C., Fischer, I. A., Mazzoni, P., et al. (1998). Lower left temporal lobe MRI volumes in patients with first-episode schizophrenia compared with psychotic patients with first-episode affective disorder and normal subjects. *Am. J. Psychiatry* 155, 1384–1391. doi: 10.1176/ajp.155.10.1384

Holcomb, H. H., Ritzl, E. K., Medoff, D. R., Nevitt, J., Gordon, B., and Tamminga, C. A. (1995). Tone discrimination performance in schizophrenic patients and normal volunteers: impact of stimulus presentation levels and frequency differences. *Psychiatry Res.* 57, 75–82. doi: 10.1016/0165-1781(95)02270-7

Holtmaat, A. J. G. D., Trachtenberg, J. T., Wilbrecht, L., Shepherd, G. M., Zhang, X., Knott, G. W., et al. (2005). Transient and persistent dendritic spines in the neocortex *in vivo*. *Neuron* 45, 279–291. doi: 10.1016/j.neuron.2005.01.003

Honea, R., Crow, T. J., Passingham, D., and Mackay, C. E. (2005). Regional deficits in brain volume in schizophrenia: a meta-analysis of voxel-based morphometry studies. *Am. J. Psychiatry* 162, 2233–2245. doi: 10.1176/appi.ajp.162.12.2233

Insel, T. R. (2010). Rethinking schizophrenia. *Nature* 468, 187–193. doi: 10.1038/nature09552

Jahn, R., Schiebler, W., Ouimet, C., and Greengard, P. (1985). A 38,000-dalton membrane protein (p38) present in synaptic vesicles. *Proc. Natl. Acad. Sci. U S A* 82, 4137–4141. doi: 10.1073/pnas.82.12.4137

Jahshan, C., Wynn, J. K., and Green, M. F. (2013). Relationship between auditory processing and affective prosody in schizophrenia. *Schizophr. Res.* 143, 348–353. doi: 10.1016/j.schres.2012.11.025

Javitt, D. C. (1993). Neurophysiological approaches to analyzing brain dysfunction in schizophrenia. *Psychiatric Ann.* 23, 144–150. doi: 10.3928/0048-5713-19930301-10

Javitt, D. C., Shelley, A.-M., and Ritter, W. (2000). Associated deficits in mismatch negativity generation and tone matching in schizophrenia. *Clin. Neurophysiol.* 111, 1733–1737. doi: 10.1016/s1388-2457(00)00377-1

Javitt, D. C., Steinschneider, M., Schroeder, C. E., and Arezzo, J. C. (1996). Role of cortical N-methyl-D-aspartate receptors in auditory sensory memory and mismatch negativity generation: implications for schizophrenia. *Proc. Natl. Acad. Sci. U S A* 93, 11962–11967. doi: 10.1073/pnas.93.21.11962

Javitt, D. C., Steinschneider, M., Schroeder, C. E., Vaughan, H. G. Jr., and Arezzo, J. C. (1994). Detection of stimulus deviance within primate primary auditory cortex: intracortical mechanisms of mismatch negativity (MMN) generation. *Brain Res.* 667, 192–200. doi: 10.1016/0006-8993(94)91496-6

Javitt, D. C., Strous, R. D., Grochowski, S., Ritter, W., and Cowan, N. (1997). Impaired precision, but normal retention, of auditory sensory ("echoic") memory information in schizophrenia. *J. Abnorm. Psychol.* 106, 315–324. doi: 10.1037/0021-843x.106.2.315

Javitt, D. C., and Sweet, R. A. (2015). Auditory dysfunction in schizophrenia: integrating clinical and basic features. *Nat. Rev. Neurosci.* 16, 535–550. doi: 10.1038/nrn4002

Kantrowitz, J. T., Epstein, M. L., Beggel, O., Rohrig, S., Lehrfeld, J. M., Revheim, N., et al. (2016). Neurophysiological mechanisms of cortical plasticity impairments in schizophrenia and modulation by the NMDA receptor agonist D-serine. *Brain* 139, 3281–3295. doi: 10.1093/brain/aww262

Kantrowitz, J. T., Hoptman, M. J., Leitman, D. I., Moreno-Ortega, M., Lehrfeld, J. M., Dias, E., et al. (2015). Neural substrates of auditory emotion recognition deficits in schizophrenia. *J. Neurosci.* 35, 14909–14921. doi: 10.1523/JNEUROSCI.4603-14.2015

Kantrowitz, J. T., Hoptman, M. J., Leitman, D. I., Silipo, G., and Javitt, D. C. (2014). The 5% difference: early sensory processing predicts sarcasm perception in schizophrenia and schizo-affective disorder. *Psychol. Med.* 44, 25–36. doi: 10.1017/S0033291713000834

Kantrowitz, J. T., Leitman, D. I., Lehrfeld, J. M., Laukka, P., Juslin, P. N., Butler, P. D., et al. (2011). Reduction in tonal discriminations predicts receptive emotion processing deficits in schizophrenia and schizoaffective disorder. *Schizophr. Bull.* 39, 86–93. doi: 10.1093/schbul/sbr060

Kasai, K., Nakagome, K., Itoh, K., Koshida, I., Hata, A., Iwanami, A., et al. (2002). Impaired cortical network for preattentive detection of change in speech sounds in schizophrenia: a high-resolution event-related potential study. *Am. J. Psychiatry* 159, 546–553. doi: 10.1176/appi.ajp.159.4.546

Kasai, K., Shenton, M. E., Salisbury, D. F., Hirayasu, Y., Onitsuka, T., Spencer, M. H., et al. (2003). Progressive decrease of left Heschl gyrus and planum temporale gray matter volume in first-episode schizophrenia: a longitudinal magnetic resonance imaging study. *Arch. Gen. Psychiatry* 60, 766–775. doi: 10.1001/archpsyc.60.8.766

Kaufman, D. L., Houser, C. R., and Tobin, A. J. (1991). Two forms of the γ-aminobutyric acid synthetic enzyme glutamate decarboxylase have distinct intraneuronal distributions and cofactor interactions. *J. Neurochem.* 56, 720–723. doi: 10.1111/j.1471-4159.1991.tb08211.x

Kepecs, A., and Fishell, G. (2014). Interneuron cell types: Fit to form and formed to fit. *Nature* 505, 318–326. doi: 10.1038/nature12983

Kirkwood, C. M., Ciuchta, J., Ikonomovic, M. D., Fish, K. N., Abrahamson, E. E., Murray, P. S., et al. (2013). Dendritic spine density, morphology, and fibrillar actin content surrounding amyloid-β plaques in a mouse model of amyloid-β deposition. *J. Neuropathol. Exp. Neurol.* 72, 791–800. doi: 10.1097/NEN.0b013e31829ecc89

Krishnan, G. P., Hetrick, W. P., Brenner, C. A., Shekhar, A., Steffen, A. N., and O'Donnell, B. F. (2009). Steady state and induced auditory γ deficits in schizophrenia. *Neuroimage* 47, 1711–1719. doi: 10.1016/j.neuroimage.2009.03.085

Kubicki, M., Shenton, M. E., Salisbury, D. F., Hirayasu, Y., Kasai, K., Kikinis, R., et al. (2002). Voxel-based morphometric analysis of gray matter in first episode schizophrenia. *Neuroimage* 17, 1711–1719. doi: 10.1006/nimg.2002.1296

Kwon, S. E., and Chapman, E. R. (2011). Synaptophysin regulates the kinetics of synaptic vesicle endocytosis in central neurons. *Neuron* 70, 847–854. doi: 10.1016/j.neuron.2011.04.001

Kwon, J. S., O'Donnell, B. F., Wallenstein, G. V., Greene, R. W., Hirayasu, Y., Nestor, P. G., et al. (1999). Gamma frequency-range abnormalities to auditory stimulation in schizophrenia. *Arch. Gen. Psychiatry* 56, 1001–1005. doi: 10.1001/archpsyc.56.11.1001

Leitman, D. I., Foxe, J. J., Butler, P. D., Saperstein, A., Revheim, N., and Javitt, D. C. (2005). Sensory contributions to impaired prosodic processing in schizophrenia. *Biol. Psychiatry* 58, 56–61. doi: 10.1016/j.biopsych.2005.02.034

Leitman, D. I., Hoptman, M. J., Foxe, J. J., Saccente, E., Wylie, G. R., Nierenberg, J., et al. (2007). The neural substrates of impaired prosodic detection in

schizophrenia and its sensorial antecedents. *Am. J. Psychiatry* 164, 474–482. doi: 10.1176/appi.ajp.164.3.474

Leitman, D. I., Sehatpour, P., Higgins, B. A., Foxe, J. J., Silipo, G., and Javitt, D. C. (2010). Sensory deficits and distributed hierarchical dysfunction in schizophrenia. *Am. J. Psychiatry* 167, 818–827. doi: 10.1176/appi.ajp.2010.09030338

Lewis, D. A., and Sweet, R. A. (2009). Schizophrenia from a neural circuitry perspective: advancing toward rational pharmacological therapies. *J. Clin. Invest.* 119, 706–716. doi: 10.1172/JCI37335

Light, G. A., Hsu, J. L., Hsieh, M. H., Meyer-Gomes, K., Sprock, J., Swerdlow, N. R., et al. (2006). Gamma band oscillations reveal neural network cortical coherence dysfunction in schizophrenia patients. *Biol. Psychiatry* 60, 1231–1240. doi: 10.1016/j.biopsych.2006.03.055

MacDonald, M. L., Alhassan, J., Newman, J. T., Richard, M., Gu, H., Kelly, R. M., et al. (2017). Selective loss of smaller spines in schizophrenia. *Am. J. Psychiatry* 174, 586–594. doi: 10.1176/appi.ajp.2017.16070814

Matthews, D. A., Cotman, C., and Lynch, G. (1976). An electron microscopic study of lesion-induced synaptogenesis in the dentate gyrus of the adult rat. II. Reappearance of morphologically normal synaptic contacts. *Brain Res.* 115, 23–41. doi: 10.1016/0006-8993(76)90820-9

McCarley, R. W., Faux, S. F., Shenton, M. E., Nestor, P. G., and Adams, J. (1991). Event-related potentials in schizophrenia: their biological and clinical correlates and new model of schizophrenic pathophysiology. *Schizophr. Res.* 4, 209–231. doi: 10.1016/0920-9964(91)90034-o

McCarley, R. W., Wible, C. G., Frumin, M., Hirayasu, Y., Levitt, J. J., Fischer, I. A., et al. (1999). MRI anatomy of schizophrenia. *Biol. Psychiatry* 45, 1099–1119. doi: 10.1016/S0006-3223(99)00018-9

McKinney, R. A., Capogna, M., Dürr, R., and Gähwiler, B. H. (1999). Miniature synaptic events maintain dendritic spines via AMPA receptor activation. *Nat. Neurosci.* 2, 44–49. doi: 10.1038/4548

Menon, R. R., Barta, P. E., Aylward, E. H., Richards, S. S., Vaughn, D. D., Tien, A. Y., et al. (1995). Posterior superior temporal gyrus in schizophrenia: grey matter changes and clinical correlates. *Schizophr. Res.* 16, 127–135. doi: 10.1016/0920-9964(94)00067-i

Michie, P., Budd, T., Todd, J., Rock, D., Wichmann, H., Box, J., et al. (2000). Duration and frequency mismatch negativity in schizophrenia. *Clin. Neurophysiol.* 111, 1054–1065. doi: 10.1016/s1388-2457(00)00275-3

Mitani, A., Shimokouchi, M., Itoh, K., Nomura, S., Kudo, M., and Mizuno, N. (1985). Morphology and laminar organization of electrophysiologically identified neurons in the primary auditory cortex in the cat. *J. Comp. Neurol.* 235, 430–447. doi: 10.1002/cne.902350403

Molinari, M., Dell'Anna, M., Rausell, E., Leggio, M., Hashikawa, T., and Jones, E. (1995). Auditory thalamocortical pathways defined in monkeys by calcium-binding protein immunoreactivity. *J. Comp. Neurol.* 362, 171–194. doi: 10.1002/cne.903620203

Moyer, C. E., Delevich, K. M., Fish, K. N., Asafu-Adjei, J. K., Sampson, A. R., Dorph-Petersen, K.-A., et al. (2012). Reduced glutamate decarboxylase 65 protein within primary auditory cortex inhibitory boutons in schizophrenia. *Biol. Psychiatry* 72, 734–743. doi: 10.1016/j.biopsych.2012.04.010

Moyer, C. E., Delevich, K. M., Fish, K. N., Asafu-Adjei, J. K., Sampson, A. R., Dorph-Petersen, K.-A., et al. (2013). Intracortical excitatory and thalamocortical boutons are intact in primary auditory cortex in schizophrenia. *Schizophr. Res.* 149, 127–134. doi: 10.1016/j.schres.2013.06.024

Moyer, C. E., Shelton, M. A., and Sweet, R. A. (2015). Dendritic spine alterations in schizophrenia. *Neurosci. Lett.* 601, 46–53. doi: 10.1016/j.neulet.2014.11.042

Muly, E. C., Smith, Y., Allen, P., and Greengard, P. (2004). Subcellular distribution of spinophilin immunolabeling in primate prefrontal cortex: localization to and within dendritic spines. *J. Comp. Neurol.* 469, 185–197. doi: 10.1002/cne.11001

Nägerl, U. V., Eberhorn, N., Cambridge, S. B., and Bonhoeffer, T. (2004). Bidirectional activity-dependent morphological plasticity in hippocampal neurons. *Neuron* 44, 759–767. doi: 10.1016/j.neuron.2004.11.016

Nakahara, H., Yamada, S., Mizutani, T., and Murayama, S. (2000). Identification of the primary auditory field in archival human brain tissue via immunocytochemistry of parvalbumin. *Neurosci. Lett.* 286, 29–32. doi: 10.1016/s0304-3940(00)01072-7

Navone, F., Jahn, R., Di Gioia, G., Stukenbrok, H., Greengard, P., and De Camilli, P. (1986). Protein p38: an integral membrane protein specific for small vesicles of neurons and neuroendocrine cells. *J. Cell Biol.* 103, 2511–2527. doi: 10.1083/jcb.103.6.2511

O'Donnell, B. F., Vohs, J. L., Hetrick, W. P., Carroll, C. A., and Shekhar, A. (2004). Auditory event-related potential abnormalities in bipolar disorder and schizophrenia. *Int. J. Psychophysiol.* 53, 45–55. doi: 10.1016/j.ijpsycho.2004.02.001

Ojima, H., Honda, C. N., and Jones, E. (1991). Patterns of axon collateralization of identified supragranular pyramidal neurons in the cat auditory cortex. *Cereb. Cortex* 1, 80–94. doi: 10.1093/cercor/1.1.80

Pakkenberg, B. (1993). Total nerve cell number in neocortex in chronic schizophrenics and controls estimated using optical disectors. *Biol. Psychiatry* 34, 768–772. doi: 10.1016/0006-3223(93)90065-l

Pandya, D. N. (1995). Anatomy of the auditory cortex. *Rev. Neurol.* 151, 486–494.

Pandya, D. N., and Rosene, D. (1993). Laminar termination patterns of thalamic, callosal, and association afferents in the primary auditory area of the rhesus monkey. *Exp. Neurol.* 119, 220–234. doi: 10.1006/exnr.1993.1024

Pandya, D. N., and Sanides, F. (1973). Architectonic parcellation of the temporal operculum in rhesus monkey and its projection pattern. *Z. Anat. Entwicklungsgesch.* 139, 127–161. doi: 10.1007/bf00523634

Pekkonen, E., Katila, H., Ahveninen, J., Karhu, J., Huotilainen, M., and Tiihonen, J. (2002). Impaired temporal lobe processing of preattentive auditory discrimination in schizophrenia. *Schizophr. Bull.* 28, 467–474. doi: 10.1093/oxfordjournals.schbul.a006954

Penzes, P., Cahill, M. E., Jones, K. A., VanLeeuwen, J.-E., and Woolfrey, K. M. (2011). Dendritic spine pathology in neuropsychiatric disorders. *Nat. Neurosci.* 14, 285–293. doi: 10.1038/nn.2741

Petkova, E., Lu, F., Kantrowitz, J., Sanchez, J. L., Lehrfeld, J., Scaramello, N., et al. (2014). Auditory tasks for assessment of sensory function and affective prosody in schizophrenia. *Compr. Psychiatry* 55, 1862–1874. doi: 10.1016/j.comppsych.2014.08.046

Purcell, S. M., Moran, J. L., Fromer, M., Ruderfer, D., Solovieff, N., Roussos, P., et al. (2014). A polygenic burden of rare disruptive mutations in schizophrenia. *Nature* 506, 185–190. doi: 10.1038/nature12975

Rivier, F., and Clarke, S. (1997). Cytochrome oxidase, acetylcholinesterase, and NADPH-diaphorase staining in human supratemporal and insular cortex: evidence for multiple auditory areas. *Neuroimage* 6, 288–304. doi: 10.1006/nimg.1997.0304

Rocco, B. R., Sweet, R. A., Lewis, D. A., and Fish, K. N. (2015). GABA-synthesizing enzymes in calbindin and calretinin neurons in monkey prefrontal cortex. *Cereb. Cortex* 26, 2191–2204. doi: 10.1093/cercor/bhv051

Salisbury, D. F., Kuroki, N., Kasai, K., Shenton, M. E., and McCarley, R. W. (2007). Progressive and interrelated functional and structural evidence of post-onset brain reduction in schizophrenia. *Arch. Gen. Psychiatry* 64, 521–529. doi: 10.1001/archpsyc.64.5.521

Schizophrenia Working Group of the Psychiatric Genomics Consortium. (2014). Biological insights from 108 schizophrenia-associated genetic loci. *Nature* 511, 421–427. doi: 10.1038/nature13595

Schlaepfer, T. E., Harris, G. J., Tien, A. Y., Peng, L. W., Lee, S., Federman, E. B., et al. (1994). Decreased regional cortical gray matter volume in schizophrenia. *Am. J. Psychiatry* 151, 843–848. doi: 10.1176/ajp.151.6.842

Selemon, L. D., and Goldman-Rakic, P. S. (1999). The reduced neuropil hypothesis: a circuit based model of schizophrenia. *Biol. Psychiatry* 45, 17–25. doi: 10.1016/s0006-3223(98)00281-9

Shelley, A. M., Ward, P., Catts, S., Michie, P. T., Andrews, S., and McConaghy, N. (1991). Mismatch negativity: an index of a preattentive processing deficit in schizophrenia. *Biol. Psychiatry* 30, 1059–1062. doi: 10.1016/0006-3223(91)90126-7

Shelton, M. A., Newman, J. T., Gu, H., Sampson, A. R., Fish, K. N., MacDonald, M. L., et al. (2015). Loss of microtubule-associated protein 2 immunoreactivity linked to dendritic spine loss in schizophrenia. *Biol. Psychiatry* 78, 374–385. doi: 10.1016/j.biopsych.2014.12.029

Shenton, M. E., Dickey, C. C., Frumin, M., and McCarley, R. W. (2001). A review of MRI findings in schizophrenia. *Schizophr. Res.* 49, 1–52. doi: 10.1016/s0920-9964(01)00163-3

Smiley, J. F., Hackett, T. A., Preuss, T. M., Bleiwas, C., Figarsky, K., Mann, J. J., et al. (2013). Hemispheric asymmetry of primary auditory cortex and Heschl's gyrus in schizophrenia and nonpsychiatric brains. *Psychiatry Res.* 214, 435–443. doi: 10.1016/j.pscychresns.2013.08.009

Somogyi, P. (1977). A specific 'axo-axonal'interneuron in the visual cortex of the rat. *Brain Res.* 136, 345–350. doi: 10.1016/0006-8993(77)90808-3

Somogyi, P., and Cowey, A. (1981). Combined Golgi and electron microscopic study on the synapses formed by double bouquet cells in the visual cortex of the cat and monkey. *J. Comp. Neurol.* 195, 547–566. doi: 10.1002/cne.901950402

Spacek, J., and Harris, K. M. (1998). Three-dimensional organization of cell adhesion junctions at synapses and dendritic spines in area CA1 of the rat hippocampus. *J. Comp. Neurol.* 393, 58–68. doi: 10.1002/(SICI)1096-9861(19980330)393:1<58::AID-CNE6>3.0.CO;2-P

Stark, A. K., Uylings, H. B., Sanz-Arigita, E., and Pakkenberg, B. (2004). Glial cell loss in the anterior cingulate cortex, a subregion of the prefrontal cortex, in subjects with schizophrenia. *Am. J. Psychiatry* 161, 882–888. doi: 10.1176/appi.ajp.161.5.882

Strous, R. D., Cowan, N., Ritter, W., and Javitt, D. C. (1995). Auditory sensory ("echoic") memory dysfunction in schizophrenia. *Am. J. Psychiatry* 152, 1517–1519. doi: 10.1176/ajp.152.10.1517

Sweet, R. A., Bergen, S. E., Sun, Z., Marcsisin, M. J., Sampson, A. R., and Lewis, D. A. (2007). Anatomical evidence of impaired feedforward auditory processing in schizophrenia. *Biol. Psychiatry* 61, 854–864. doi: 10.1016/j.biopsych.2006.07.033

Sweet, R. A., Bergen, S. E., Sun, Z., Sampson, A. R., Pierri, J. N., and Lewis, D. A. (2004). Pyramidal cell size reduction in schizophrenia: evidence for involvement of auditory feedforward circuits. *Biol. Psychiatry* 55, 1128–1137. doi: 10.1016/j.biopsych.2004.03.002

Sweet, R. A., Dorph-Petersen, K.-A., and Lewis, D. A. (2005). Mapping auditory core, lateral belt, and parabelt cortices in the human superior temporal gyrus. *J. Comp. Neurol.* 491, 270–289. doi: 10.1002/cne.20702

Sweet, R. A., Henteleff, R. A., Zhang, W., Sampson, A. R., and Lewis, D. A. (2009). Reduced dendritic spine density in auditory cortex of subjects with schizophrenia. *Brain Res.* 34, 374–389. doi: 10.1038/npp.2008.67

Sweet, R. A., Pierri, J. N., Auh, S., Sampson, A. R., and Lewis, D. A. (2003). Reduced pyramidal cell somal volume in auditory association cortex of subjects with schizophrenia. *Neuropsychopharmacology* 28, 599–609. doi: 10.1038/sj.npp.1300120

Thune, J. J., Uylings, H. B., and Pakkenberg, B. (2001). No deficit in total number of neurons in the prefrontal cortex in schizophrenics. *J. Psychiatr. Res.* 35, 15–21. doi: 10.1016/s0022-3956(00)00043-1

Tian, N., Petersen, C., Kash, S., Baekkeskov, S., Copenhagen, D., and Nicoll, R. (1999). The role of the synthetic enzyme GAD65 in the control of neuronal γ-aminobutyric acid release. *Proc. Natl. Acad. Sci. U S A* 96, 12911–12916. doi: 10.1073/pnas.96.22.12911

van Haren, N. E., Pol, H. E. H., Schnack, H. G., Cahn, W., Mandl, R. C., Collins, D. L., et al. (2007). Focal gray matter changes in schizophrenia across the course of the illness: a 5-year follow-up study. *Neuropsychopharmacology* 32, 2057–2066. doi: 10.1038/sj.npp.1301347

Vita, A., De Peri, L., Deste, G., and Sacchetti, E. (2012). Progressive loss of cortical gray matter in schizophrenia: a meta-analysis and meta-regression of longitudinal MRI studies. *Transl. Psychiatry* 2:e190. doi: 10.1038/tp.2012.116

Wallace, M. N., Johnston, P. W., and Palmer, A. R. (2002). Histochemical identification of cortical areas in the auditory region of the human brain. *Exp. Brain Res.* 143, 499–508. doi: 10.1007/s00221-002-1014-z

Wallace, M. N., Kitzes, L., and Jones, E. (1991). Intrinsic inter-and intralaminar connections and their relationship to the tonotopic map in cat primary auditory cortex. *Exp. Brain Res.* 86, 527–544. doi: 10.1007/bf00230526

Wexler, B. E., Stevens, A. A., Bowers, A. A., Sernyak, M. J., and Goldman-Rakic, P. S. (1998). Word and tone working memory deficits in schizophrenia. *Arch. Gen. Psychiatry* 55, 1093–1096. doi: 10.1001/archpsyc.55.12.1093

Willig, K. I., Steffens, H., Gregor, C., Herholt, A., Rossner, M. J., and Hell, S. W. (2014). Nanoscopy of filamentous actin in cortical dendrites of a living mouse. *Biophys. J.* 106, L01–L03. doi: 10.1016/j.bpj.2013.11.1119

Wong, A. H. C., and Van Tol, H. H. (2003). Schizophrenia: from phenomenology to neurobiology. *Neurosci. Biobehav. Rev.* 27, 269–306. doi: 10.1016/s0149-7634(03)00035-6

Xie, Z., Huganir, R. L., and Penzes, P. (2005). Activity-dependent dendritic spine structural plasticity is regulated by small GTPase Rap1 and its target AF-6. *Neuron* 48, 605–618. doi: 10.1016/j.neuron.2005.09.027

Yuste, R. (2011). Dendritic spines and distributed circuits. *Neuron* 71, 772–781. doi: 10.1016/j.neuron.2011.07.024

Zhou, Q., Homma, K. J., and Poo, M.-M. (2004). Shrinkage of dendritic spines associated with long-term depression of hippocampal synapses. *Neuron* 44, 749–757. doi: 10.1016/j.neuron.2004.11.011

Zipursky, R. B., Lim, K. O., Sullivan, E. V., Brown, B. W., and Pfefferbaum, A. (1992). Widespread cerebral gray matter volume deficits in schizophrenia. *Arch. Gen. Psychiatry* 49, 195–205. doi: 10.1001/archpsyc.1992.01820030027004

Conflict of Interest Statement: The authors declare that the research was conducted in the absence of any commercial or financial relationships that could be construed as a potential conflict of interest.

frontiers in Neuroanatomy

METHODS
published: 12 June 2018
doi: 10.3389/fnana.2018.00049

Space Balls Revisited: Stereological Estimates of Length With Virtual Isotropic Surface Probes

*Mark J. West**

Department of Biomedicine, Aarhus University Faculty of Health Sciences, Aarhus, Denmark

The space ball probe was fully described in the literature 15 years ago by Mouton et al. (2002). Since then, it has been used in a number of studies in the nervous system that focus on axon, dendrite, and capillary length. The length of structural parameters in tissues reflect functional aspects of the tissues. Here, some of the various applications of this methodology will be presented, along with a review of the salient features of the methodology that has resulted in new wave of quantitative morphological studies of length in the nervous system. The validity of the method is discussed in view of its widespread use along with insights into the problems associated with its application to histological tissue and future techniques for applying space balls.

Keywords: stereology, length, unbiased, isotropic probe, space ball

OPEN ACCESS

Edited by:
Bente Pakkenberg, Research Laboratory for Stereology and Neuroscience, Denmark

Reviewed by:
Nuno Miguel M. Amorim Da Costa, Allen Institute for Brain Science, United States
Irmgard Amrein, ETH Zürich, Switzerland

***Correspondence:**
Mark J. West
mjw@biomed.au.dk

Received: *01 June 2017*
Accepted: *23 May 2018*
Published: *12 June 2018*

Citation:
West MJ (2018) Space Balls Revisited: Stereological Estimates of Length With Virtual Isotropic Surface Probes. Front. Neuroanat. 12:49. doi: 10.3389/fnana.2018.00049

INTRODUCTION

Estimates of the length of cellular features can provide quantitative information about various biological functions. Examples using space ball probes include; the length of dopaminergic axons, which can be related to the dopaminergic innervation and function of the striatum (Li et al., 2016); the length of serotoninergic (Liu et al., 2011) and cholinergic axons in cerebral cortex which can be related to cortical function (Nikolajsen et al., 2011) and the length of astrocyte processes, which can be related to immune-reactivity (McNeal et al., 2016). These parameters can be used to evaluate brain hemodynamics (Kubíková et al., 2018), tissue oxygenation (Nikolajsen et al., 2015), and tissue repair (Lee et al., 2005; McConnell et al., 2016) and ultimately used to develop therapeutic approaches to brain disorders. Structural parameters of potential interest and for which quantitative studies of length have yet to be carried out include microtubules, involved in intracellular transport, and neuropil threads, an expression of Alzheimer's disease.

BACKGROUND

The stereological relationship formula for estimating length density, $\widehat{L_V} = 2 \bullet Q_A$

Prior to the introduction of the space ball probe, stereological estimators of length were plagued by the requirement for an isotropic interaction between the area probes and linear features such as axons and capillaries. In this article, the use and application of a virtual isotropic surface probe that readily fulfills this requirement is described.

The formula that relates measurements made on images to length (Smith and Guttman, 1953) is simple and easy to apply (Equation 1). Accordingly, the number of times that a linear structural

feature ($\boldsymbol{Q}$) passes through a probe of known area ($\boldsymbol{A}$) is directly related to the length per unit volume ($\boldsymbol{L_V}$) of the structural feature. In spite of the simplicity of the formula, its' derivation is somewhat deep and the derivation and proof are presented in the original Smith-Guttman paper. Briefly, it is based on a three dimensional version of the Buffon needle problem. Unlike the two dimensional Buffon problem, which involves the probability that a randomly thrown needle intersects a line on the floor, the space ball probe is based on the probability that a surface is hit by a line that is randomly oriented in 3D space.

$$\widehat{L_V} = 2 \bullet Q_A \quad (1)$$

It is important to remember that this formula is applicable only when the linear structural feature has an *isotropic interaction* with the areal probe. This will be the case when the structural feature is truly isotropic. That is, the direction of its linear elements is equal in all three dimensions of space. In this case, the orientation of the 2 dimensional area probe is not important. However, biological structures are seldom if ever isotropic structures. One would prefer to avoid having to make any assumptions about the extent or existence of isotropy in biological tissue in order to avoid potential biases in the estimate that result from anisotropy. Methodological biases of this type lead to estimates that systematically deviate from the true value regardless of the amount of sampling performed.

In order to avoid the problem related to the anisotropy of biological structures a number of techniques have been developed to ensure an isotropic interaction between probe and structural feature. One way to accomplish this would be to section small samples of randomly oriented pieces of tissue and probe these sections with flat 2-D area probes (Nyengaard and Gundersen, 1992; Løkkegaard et al., 2001) or by cutting the tissue in three orthogonal planes (Kubíková et al., 2018). Another would be to use probes with surfaces that were isotropic, such as a sphere (Mouton et al., 2002). In the first case, to fulfill the isotropic interaction requirement, the tissue is randomly oriented. In the latter, the surface of the probe is itself isotropic. Prior to the advent of the space ball probe a number of methods had been developed for estimating length by using combinations of randomness in the orientations of the probe and the structure. For example methods exist in which the tissue is randomly oriented in two dimensions and the probe is oriented randomly in the third dimension (Baddeley et al., 1986), cut in orthogonal planes (Mattfeldt et al., 1985) or in which flat surface probes are randomly oriented in tissue cut arbitrarily (Larsen et al., 1998). Though all of these earlier approaches provide unbiased estimates of length, some are more difficult to implement than others. Area probes with isotropic surfaces (space balls) are generally preferred in view due to the ease with which they can be applied to modern 3D tissue imaging.

THE PREFERRED ISOTROPIC SPHERICAL PROBE OR SPACE BALL

The surface of a sphere is an isotropic probe in that all surface orientations are represented on its surface (see appendix in Mouton et al., 2002). In fact each orientation of a surface element on a sphere is represented twice; at the antipodes. As a consequence, the probe need only consist of a hemisphere, since all orientations of the surface are present on the surface of a hemisphere (see **Figure 1**). By placing a hemisphere, of known area ($\boldsymbol{A = 2\pi \bullet r^2}$, where $\boldsymbol{r}$ is the radius of the hemisphere), in a thick section or stack of aligned sections, the area of the probe can be set to any desired value. One would only have to count the number of times a linear feature passed through the surface of the probe to obtain the $\boldsymbol{Q}$ in Equation (1). Using a hemisphere rather than a sphere also increases the amount of area that the probe can have in a section of a certain thickness.

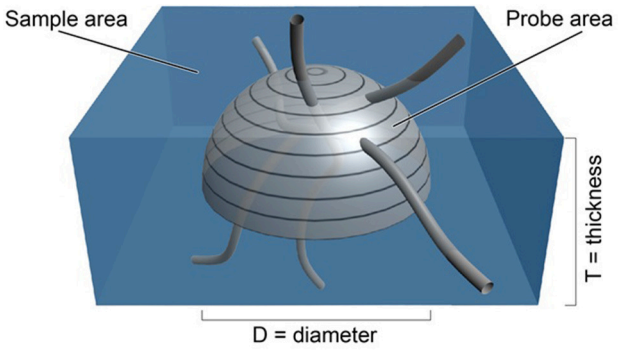

FIGURE 1 | Depiction of an isotropic surface probe shown in light gray in a tissue sample shown in blue. The estimate of the length density, $\widehat{L_V}$, is directly related to the number of times the linear features pass through the surface of the hemi-space ball probe (see Equation 1). The area of the probe is known from the formula for the surface of a sphere of known diameter, D. The volume of tissue sampled is known from the sample area times the thickness of the section (West, 2012, Figure 5.3, with permission).

It is impossible to physically place a 3-D probe into histological material. One can do this in a *virtual* manner, however, by superimposing an image of the surface of the probe (which will appear as a circle of a certain size), at particular depths of a thick section or stack of images. By focusing up and down through the tissue or stack, one would see a series of concentric circles of various diameters that represented the surface of the hemispheric probe. At each level, one would determine whether a linear structural feature of interest intercepted the circle that represented the surface of the probe (See **Figure 2**). This approach is used in commercially available computerized microscope systems that superimpose the surface of the probe, seen as a series of concentric circles, at appropriate focal depths to create a virtual hemispheric probe.

Using thick section light microscopy or stack based confocal and multiphoton microscopy; the choice of using probes with isotropic surfaces is attractive because one can orient the tissue of interest in any convenient plane. This is particularly valuable when one prefers to examine sections that are cut at a particular orientation. This will likely reduce the effort needed to define the borders of the region of interest. The latter is required if one is to

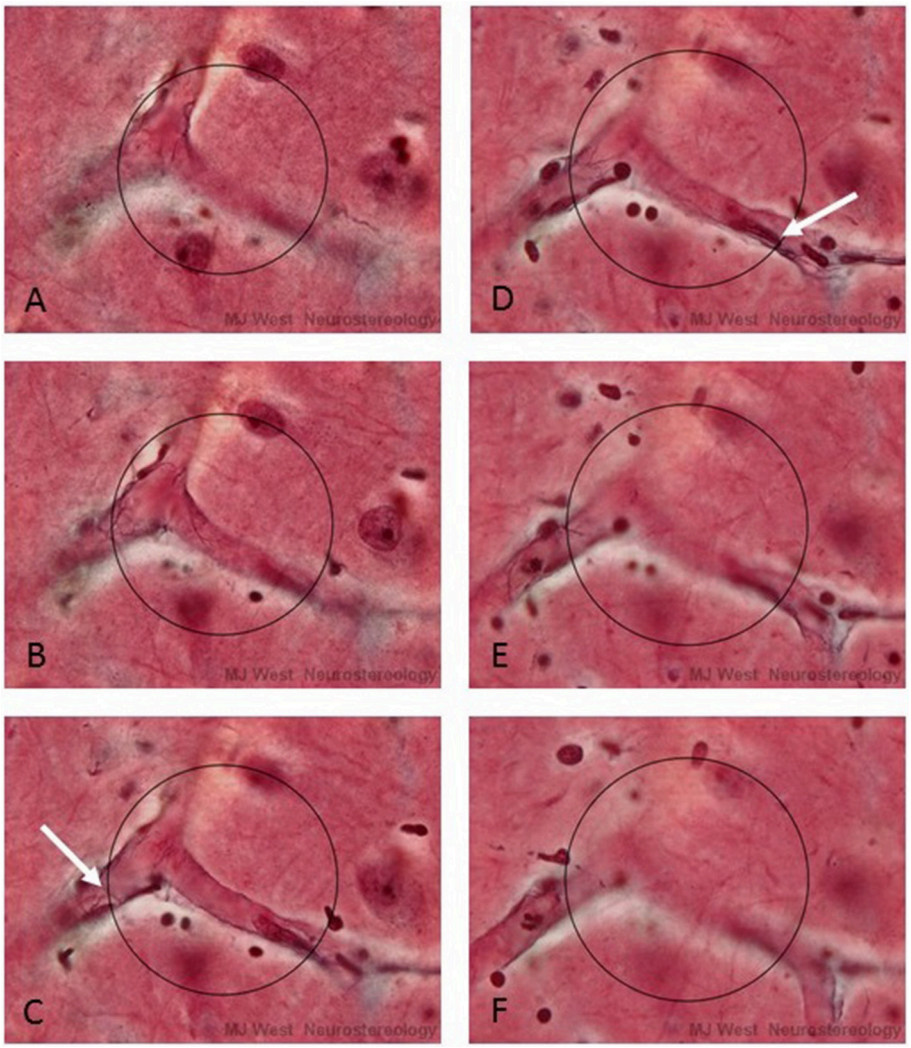

FIGURE 2 | A series of micrographs depicting a virtual hemispheric probe (circles) at six different focal levels **(A–F)** of a thick histological section stained for capillaries. The white arrows in C and D point to interactions, ***Q***, between capillaries and the surface of the probe. In practice the surface of the hemi-space ball appears as an expanding circle as one focuses through the section.

make estimates of total length. This important aspect of modern stereology, total amounts, is discussed further below.

COUNTING INTERACTIONS BETWEEN LINEAR STRUCTURES AND VIRTUAL SPHERICAL PROBES

There are a two important points to be made about counting intercepts of the linear feature with the virtual isotropic hemispheric probe. The first has to do with the fact that a capillary, or any biological linear structural feature, for that matter, is not a true line. Linear biological features have a certain diameter, true lines do not. Linear biological structures are often tubes or cylinders. The Smith-Guttman formula applies only to true lines. The diameter of biological linear features can create problems when determining whether or not a linear structural feature interacts with the surface of the hemispheric surface probe. This is particularly so when the diameter of the hemi-space ball is of the same magnitude as the diameter of the linear feature. If one counts intercepts when any part of the structural feature touches the surface of the probe, one will over count the intercepts.

There is a "correction" for the "over counting" that will occur when one uses the touch counting rule. Briefly, one divides the touch intercept counts ($\boldsymbol{Q}$) by 1 plus the ratio of the square of the diameter of the structural feature, $\boldsymbol{d}$, to the square of the diameter of the space ball probe, $\boldsymbol{D}[\boldsymbol{1 + (d^2/D^2)}]$. From this relationship between the diameters of the probe and structural features, it can be shown that if one used a probe that has 10 times the diameter of the structural feature, there can be expected to be a bias of about 1% in the touch counts. A bias of this magnitude can be

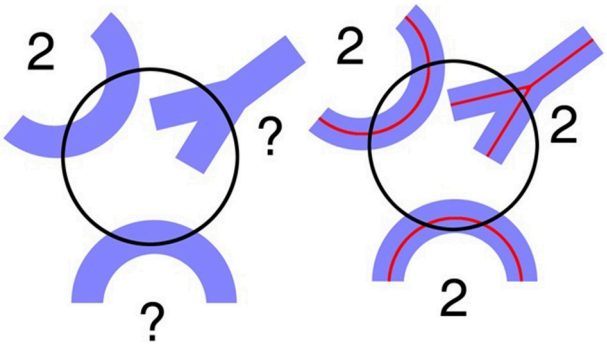

FIGURE 3 | (Left) A circle depicting the virtual space ball probe at a specific depth where the linear morphological feature appears in focus. Problems arise when trying to determine how many interactions occur between the probe and the linear morphological features shown in blue. **(Right)** Using the spline counting rule, the number of probe interactions is clearer. There are two interactions for each blue structure (West, 2012, Figure 5.4, with permission).

considered to be unimportant for all practical purposes. Still, the correction is an approximation of the magnitude of the bias and estimates based on touch counts are not truly unbiased.

The second point is that it may be possible to avoid having to correct for "touch" counts. This approach involves defining a central line or spline in the center of a cross section of the linear feature (**Figure 3** right). In this case one can avoid having to make corrections for touches. One counts intersections with a one dimensional (true line) spline running along the center of the structural feature. In the case of capillaries, one can readily define the position of a spline midway between the top and bottom of the capillary, i.e., half way through the focal depth of the capillary. The half way point will be readily apparent, in that the capillary wall will be in sharp focus when the endothelial cells are viewed on end at the midpoint a shown in **Figure 2**. This approach may be attractive when it is not possible to obtain a section or stack thickness that can accommodate a hemi-space ball probe that is five to 10 times the diameter of the structural feature. When this is the case, the estimate will be unbiased for all practical purposes. In the case of very thin fibers, such as cholinergic fibers which are less than a micron in diameter, the d/D ratio is so small in thick histological sections that one can ignore any bias related to over counting using the touch rule.

TWO WAYS TO MAKE ESTIMATES OF TOTAL LENGTH, L_{TOT}

There are two ways to estimate total length. One is to multiply the length density, L_V, by the volume of the region of interest, the reference volume, V_{REF}. The latter can be readily estimated with point counting techniques.

$$\hat{\mathrm{L}} = L_V \bullet V_{REF} \tag{2}$$

The other way is to estimate L_{TOT} by estimating the length of a structure in a known fraction of the volume of interest and multiplying this by the reciprocal of the fraction of the structure sampled (Mouton et al., 2002). Using the fractionator sampling principle, L_{TOT} would be calculated in the following manner,

$$\begin{aligned}\hat{\mathrm{L}} &= 2 \bullet \Sigma Q \bullet (1/ssf) \bullet (v/a) \\ &= 2 \bullet \Sigma Q \bullet (1/ssf) \bullet ([A_{\mathrm{step}} \bullet t]/a) \\ &= 2 \bullet \Sigma Q \bullet (1/ssf) \bullet ([A_{\mathrm{step}} \bullet t]/(2\pi \bullet r^2))\end{aligned} \tag{3}$$

where v is equal to the volume of tissue sampled by the probe, which is equal to the area associated with the movement from one sampling position to the next, A_{step}, times the thickness of the section, t (see blue area in **Figure 1**). The surface area of the probe, a hemisphere in this case, is equal to a, which is equal to 2π times the radius of the hemisphere, squared r^2.

To date, over 100 peer reviewed research papers have used the space ball probe (Web of Science). The applications involve a wide range of structural features, ranging from peripheral nerve innervation to central axon terminations, capillary innervation of brain tissue, and gliosis. In a recent study of gliosis (McNeal et al., 2016) the authors evaluated different methods for evaluating cerebral injury the authors concluded; "Only modern stereological techniques (i.e., optical fractionator and space balls) and virtual process thickness measurements demonstrated significant changes in astrocyte number, process length, or proximal process thickness in cases with brain injury relative to controls."

Since the introduction of space ball probes, there are few scientific papers that have used other unbiased stereological techniques for estimating unbiased length. One example is the exemplary use of the orthogonal triplet probe in the exhaustive work of Kubíková et al. (2018). A recent alternative proposal involve the use the automatic tracking software for following linear features within 3D preparations. Accordingly, 3D reconstructions of the digitized features can be used to estimate length. This approach may ultimately prove to be useful when high contrast imaging and segmentation routines become more available. At present they require significant amounts of operator intervention and monitoring. Automated segmentation of histological features is not yet able to replace the human visual systems ability to rapidly segment structural features in microscopic preparations that vary in background and intensity. This inability, combined with the fact that only slightly more than 100 interactions between probe and structural feature, the "Q" in $\widehat{\mathrm{L_V}} = 2 \bullet Q_A$, are needed to make useful estimates in one individual (West, 2013) render these approaches impractical at this time.

As pointed out in previous publications (Dorph-Petersen et al., 2001; Nikolajsen et al., 2015), tissue shrinkage is a major problem when analyzing length parameters in conventional light microscopic preparations. This because the absolute or true length of linear features, unlike object number, is sensitive to the volumetric distortions in the tissue The increasing use of *in vivo* 3D imaging of biological tissue can be expected to eliminate these problems. For example, a comparison of estimates of length density, using space ball probes in neocortical tissue of DBA mice that had been fixed for light microscopy, 2,857 mm/mm^3, (Nikolajsen et al., 2015) and in similar mice of the same age,

viewed *in vivo* with 2 photon microscopy, (720 mm/mm$^{3)}$ (Gutiérrez-Jiménez et al., 2018) indicate that the length density estimates in the histological material were about four times those for the *in vivo* estimates. This comparison, although limited to only part of the cortex in the *in vivo* material, indicates that the length density of capillaries in light microscopic preparations, increases roughly in proportion to the reduction in volume of the processed tissue. This may not be the case with histological histological material prepared in a manner different from that used in the Nikolajsen study. Interpreting and comparing density data from substantially (and potentially different) shrunken materials across studies should only be done with great care if at all!

VALIDATION OF THE METHODOLOGY

The validation of the space ball method for estimating length is dependent on the validity of the proof of the formula for the relationship between the length of the structural feature and the number of intercepts that occur per unit area of a surface probe, $\widehat{L_V} = 2 \bullet Q_A$

That is, the estimate of the length per unit volume, $\widehat{L_V}$,is equal to 2 times the number of intercepts per unit area Q_A of probe, with the caveat that the interaction between surface of the areal probe and the linear feature must isotropic. In that this relationship has been proven mathematically (see appendix in Mouton et al., 2002), the relationship itself cannot be validated as such. It is either true or it is not. If proper sampling is used, i.e., the surface of the probes have equal orientations in 3D space and all parts of the region of interest have equal probabilities of being sampled, then the estimate will be unbiased. That is, the estimate will approach the true value of the length without limit, as the amount of sampling is increased (West, 2012).

By definition, the surface of a sphere is isotropic. That is, there are small areas on the surface of a sphere that have all orientations in 3D space (see appendix in Mouton et al., 2002), The use of spherical probes, ensures an isotropic interaction between probe and feature. This will also be so for linear features that are isotropic and anisotropic, so that one does not have to assume anything about the orientation of the feature of interest or the direction along which one sections the material.

The estimation procedure will be assumption free with regard to an isotropic interaction between probe and feature.

If one uses random (unbiased) sampling and isotropic probes, any differences in the results of repeated estimates made with space balls can be related to the amount of sampling performed i.e., the variance of the estimator, or to some inability to meet the other requirements for making an unbiased estimate, i.e., practical issues. The latter might include errors in the delineation of the region of interest, the inability to generate a true spherical probe within a thick section, non-random sampling, histological artifacts, and lack of corrections for tissue shrinkage. Tissue shrinkage is of major concern, in that the length of a structural parameter, unlike object number, is subject to changes if the tissue shrinks. The use of *in vivo* confocal microscopic images removes some of these concerns.

The issue of reproducibility or validity of stereological data obtained with space ball probes is therefore not based on the mathematical relationship equation and the isotropy of the surface of the space ball, but to one's ability to meet the general requirements for making an unbiased estimate. These issues are not trivial and can affect the validity of a particular set of data, but they are not stereological issues. When evaluating the validity of any stereological data, it is essential that one confirms the unbiasedness of the sampling scheme. That is, the unbiased choice of subjects, the unbiased choice of sections, the unbiased choice of the positions on the sections to be probed, and the choice of an unbiased probe. All must be unbiased for the estimate to be valid.

AUTHOR CONTRIBUTIONS

The author confirms being the sole contributor of this work and approved it for publication.

FUNDING

I have been awarded a dispensation for the publishing fee.

REFERENCES

Baddeley, A. J., Gundersen, H. J., and Cruz-Orive, L. M. (1986). Estimation of surface area from vertical sections. *J. Microsc.* 142, 259–276.

Dorph-Petersen, K. A., Nyengaard, J. R., and Gundersen, H. J. (2001). Tissue shrinkage and unbiased stereological estimation of particle number and size. *J. Microsc.* 204, 232–246.

Gutiérrez-Jiménez, E., Angleys, H. H., Rasmussen, P. M., West, M. J., Catalini, L., Iversen, N. K., et al. (2018). Disturbances in the control of capillary flow in an aged APPswe/PS1DE9 model of Alzheimer's disease. *Neurobiol. Aging* 62, 82–94. doi: 10.1016/j.neurobiolaging.2017.10.006

Kubíková, T., Kochová, P., Tomášek, P., Witter, K., and Tonar, Z. (2018). Numerical and length densities of microvessels in the human brain: Correlation with preferential orientation of microvessels in the cerebral cortex, subcortical grey matter and white matter, pons and cerebellum. *J. Chem. Neuroanat.* 88, 22–32. doi: 10.1016/j.jchemneu.2017.11.005

Larsen, J. O., Gundersen, H. J., and Nielsen, J. (1998). Global spatial sampling with isotropic virtual planes: estimators of length density and total length in thick, arbitrarily orientated sections. *J. Microsc.* 191, 238–248.

Lee, G. D., Aruna, J. H., Barrett, P. M., Lei, D. L., Ingram, D. K., and Mouton, P. R. (2005). Stereological analysis of microvascular parameters in a double transgenic model of Alzheimer's disease. *Brain Res. Bull.* 65, 317–322. doi: 10.1016/j.brainresbull.2004.11.024

Li, W., Englund, E., Widner, H., Mattsson, B., van Westen, D., Lätt, J., et al. (2016). Extensive graft-derived dopaminergic innervation is maintained 24 years after transplantation in the degenerating parkinsonian brain. *Proc. Natl. Acad. Sci. U.S.A.* 113, 6544–6549. doi: 10.1073/pnas.1605245113

Liu, Y., Lee, M. K., James, M. M., Price, D. L., Borchelt, D. R., Troncoso, J. C., et al. (2011). Passive (amyloid-β) immunotherapy attenuates monoaminergic axonal degeneration in the AβPPswe/PS1dE9 mice. *J. Alzheimers Dis.* 23, 271–279. doi: 10.3233/JAD-2010-101602

Løkkegaard, A., Nyengaard, J. R., and West, M. J. (2001). Stereological estimates of number and length of capillaries in subdivisions of the human hippocampal region. *Hippocampus* 11, 726–740. doi: 10.1002/hipo.1088

Mattfeldt, T., Möbius, H. J., and Mall, G. (1985). Orthogonal triplet probes: an efficient method for unbiased estimation of length and surface of objects with unknown orientation in space. *J. Microsc.* 39, 279–289.

McConnell, E. D., Wei, H. S., Reitz, K. M., Kang, H., Takano, T., Vates, G. E., et al. (2016). Cerebral microcirculatory failure after subarachnoid hemorrhage is reversed by hyaluronidase. *J. Cereb. Blood Flow Metab.* 36, 1537–1552. doi: 10.1177/0271678X15608389

McNeal, D. W., Brandner, D. D., Gong, X., Postupna, N. O., Montine, T. J., Keene, C. D., et al. (2016). Unbiased stereological analysis of reactive astrogliosis to estimate age-associated cerebral white matter injury. *J. Neuropathol. Exp. Neurol.* 75, 539–554. doi: 10.1093/jnen/nlw032

Mouton, P. R., Gokhale, A. M., Ward, N. L., and West, M. J. (2002). Stereological length estimation using spherical probes. *J. Microsc.* 206, 54–64.

Nikolajsen, G. N., Jensen, M. S., and West, M. J. (2011). Cholinergic axon length reduced by 300 meters in the brain of an Alzheimer mouse model. *Neurobiol. Aging* 32, 1927–1931. doi: 10.1016/j.neurobiolaging.2011.05.006

Nikolajsen, G. N., Kotynski, K. A., Jensen, M. S., and West, M. J. (2015). Quantitative analysis of the capillary network of aged APPswe/PS1dE9 transgenic mice. *Neurobiol. Aging* 36, 2954–2962. doi: 10.1016/j.neurobiolaging.2015.08.004

Nyengaard, J. R., and Gundersen, H. J. G. (1992). The isector: a simple and direct method for generating isotropic, uniform random sections from small specimens. *J. Microsc.* 165, 427–431.

Smith, C. S., and Guttman, L. (1953). Measurement of internal boundaries in three dimensional structures by random sectioning. *Trans. AIME* 197, 81–87.

West, M. J. (2013). Optimizing the sampling scheme for a stereological study: how many individuals, sections, and probes should be used. *Cold Spring Harb. Protoc.* 6, 521–532. doi: 10.1101/pdb.top071852

West, M. J. (2012). "Introduction to stereology," in *Basic Stereology for Biologists and Neuroscientists*, ed M. J. West (New York, NY: Cold Spring Harbor Laboratory Press), 1–14.

Conflict of Interest Statement: The author declares that the research was conducted in the absence of any commercial or financial relationships that could be construed as a potential conflict of interest.

frontiers in Neuroanatomy

METHODS
published: 21 March 2018
doi: 10.3389/fnana.2018.00019

The Automatic Proportionator Estimator Is Highly Efficient for Estimation of Total Number of Sparse Cell Populations

Rogely W. Boyce[1*†] *and Hans J. G. Gundersen*[2]

[1] *Amgen Inc., Comparative Biology and Safety Sciences, Thousand Oaks, CA, United States,* [2] *Aarhus University, Aarhus, Denmark*

Estimation of total number of a population of cells that are sparsely distributed in an organ or anatomically-defined region of interest represents a challenge for conventional stereological methods. In these situations, classic fractionator approaches that rely on systematic uniform random sampling are highly inefficient and, in many cases, impractical due to the intense sampling of the organ and tissue sections that is required to obtain sufficient counts for an acceptable level of precision. The proportionator, an estimator based on non-uniform sampling theory, marries automated image analysis with stereological principles and is the only estimator that provides a highly efficient and precise method to address these challenging quantification problems. In this paper, the practical considerations of the proportionator estimator and its implementation with Proportionator™ software and digital slide imaging are reviewed. The power of the proportionator as a stereological tool is illustrated in its application to the estimation of the total number of a very rare (∼50/vertebrae) and sparsely distributed population of osteoprogenitor cells in mouse vertebral body. The proportionator offers a solution to neuroscientists interested in quantifying total cell number of sparse cell populations in the central and peripheral nervous system where systematic uniform random sampling-based stereological estimators are impractical.

Keywords: proportionator, nonuniform sampling, cell number, image analysis, fractionator

OPEN ACCESS

Edited by:
Bente Pakkenberg, Research Laboratory for Stereology and Neuroscience, Denmark

Reviewed by:
Carlos Avendaño, Universidad Autonoma de Madrid, Spain
Daniel A. Peterson, Rosalind Franklin University of Medicine and Science, United States

****Correspondence:***
Rogely W. Boyce
rogely.w.boyce@gmail.com

†Present Address:
Rogely W. Boyce, Beechy Ridge ToxPath LLC, Clay, WV, United States

Received: *21 August 2017*
Accepted: *05 March 2018*
Published: *21 March 2018*

Citation:
Boyce RW and Gundersen HJG (2018) The Automatic Proportionator Estimator Is Highly Efficient for Estimation of Total Number of Sparse Cell Populations. Front. Neuroanat. 12:19. doi: 10.3389/fnana.2018.00019

INTRODUCTION

The optical and physical fractionators have been the stereological method-of-choice for obtaining unbiased estimates of total cell number for nearly three decades (Gundersen, 1986; West et al., 1991). The statistical robustness of the fractionator principle relies on the precision and efficiency of systematic uniform sampling to obtain an estimate of cell number from a final fraction of the organ/region of interest for cell counting (Gundersen, 1986). The true total population number is inferred in a statistical sense from the subsample which requires the total cell population be of sufficient size such that subsampling can be performed. When the total population of the cell of interest is small and/or sparsely distributed, fractionator sampling becomes laborious and prohibitively inefficient. To obtain sufficient counts for an acceptable level of estimate precision (∼100–200 counts), intense sampling of the organ and tissue sections is required because many sampled fields will not contain the cell of interest.

Gardi (Gardi et al., 2008) introduced the proportionator estimator, a unique application of non-uniform sampling based on automated image analysis-derived features combined with stereological principles. This estimator is the only estimator that provides a solution for estimating sparse cell populations, where a large fraction of the fields of view are devoid of the cell of interest at the magnification used for counting. A sparse population may be a small number of cells in a small organ or may constitute a large number in a large organ but sparsely distributed. The gain in efficiency and precision compared with systematic uniform random sampling (SURS) sampling such as classical fractionators was detailed by Gardi (Gardi et al., 2008) and later by Keller (Keller et al., 2013). The basic sampling unit of the proportionator is the tile: an area of a size and shape and position defined by the unbiased sampling frame. All tiles (or a known fraction when the total cell population is large and/or not sparsely distributed) are assigned a "weight" using automated image analysis. Weight is most commonly the area of the tile occupied by a special or immunohistochemical stain that identifies the cells of interest. The non-uniform sampling intrinsic to the proportionator avoids sampling tiles with low cell number or weight. Although the sampling may appear biased, the probability of sampling is known and is proportional to the weight, and the estimation is therefore unbiased. The tiles are then arranged in a smooth fractionator (Gundersen, 2002) according to weight which reduces variance, and then subsampled for analysis and counting. Total cell number can then be derived with a few straightforward mathematical formulas (Gardi et al., 2008).

The implementation of the proportionator in the laboratory has been facilitated by the development of Proportionator™ software (Visiopharm, Hørsholm, DK) in combination with digital slide imaging, collectively termed the automatic proportionator estimator. In this paper, practical considerations for implementation of the automatic proportionator estimator are reviewed. To illustrate the power of the automatic proportionator estimator as a stereological tool, estimation of total number of a very rare and sparsely distributed population of osteoprogenitor cells in mouse vertebrae where total number ordinarily is below 50 cells/vertebrae was performed. For in-depth presentation of the theory of the proportionator estimator, the reader is referred to additional references (Gardi et al., 2008; Gundersen et al., 2013).

AUTOMATIC PROPORTIONATOR ESTIMATOR: PRACTICAL CONSIDERATIONS FOR IMPLEMENTATION AND THEORY

Section Preparation and Staining

Because the cell population is sparsely distributed, the volume of tissue available for analysis must be maximized. For small organs which can be routinely processed intact in paraffin, a known fraction of the organ is collected during exhaustive sectioning using fractionator sampling. Shrinkage is not a concern because the entire organ is processed in paraffin before any sampling occurs; the total number of cells is available for sampling regardless of deformation caused by shrinkage. These sections are collected as serial section pairs at each sampling interval for counting in physical disectors. Collecting disector pairs on a single slide should be done if possible to reduce the number of slides for subsequent digital scanning. For large organs, subsampling will need to be performed, and if paraffin processing is planned, special sampling designs have to be used to deal with shrinkage of subsamples during paraffin processing. The reader is referred to Gundersen et al. (2013), where numerous sampling designs are presented that account for paraffin processing for large organs where subsampling is required.

For preparation of disector sections (i.e., section pairs separated by a known distance) from paraffin blocks, thermal deformation of paraffin must be avoided. Chilling or "icing" of the block face during sectioning will result in thermal deformation and inconsistent section thickness and hence disector height. In addition, overstretching in the water bath should be avoided as this confounds alignment of the disector section pairs and the matched tile at high magnification used for counting by the software (Autodisector™, Visiopharm, described below). It is recommended sections are first placed on a room temperature water bath to collect section pairs, then transferred on uncharged slides to a warm water bath to briefly allow sections to relax, then picked up on charged slides. Section preparation is discussed in more detail in Gundersen et al. (2013).

Because some type of chromogenic staining will typically be used as the image analysis feature for weighting of the tiles, staining protocols must be optimized. Nonspecific staining or stain trapping must be avoided as the image analysis algorithm will capture staining artifacts and assign a large weight where cell count will not be proportional; this "high weight/low count" increases the variance of the estimate i.e., it decreases estimator precision.

Details of Fractionator Sampling of the Sections of the Organ

True to its name, the fractionator is the uniform sampling of a *fixed, constant fraction* of any series of items (Gundersen, 1986) including but not restricted to that of serial sections. The rational sampling of fractionator sections is performed in a few steps using as an example, an organ of dimensions approximately 3 × 3 × 3 mm with a sparse cell population of interest:

1. Measure the height ($H \sim 3.0\ mm \sim 3000\ \mu m$) of the organ perpendicular to the sectioning plane.
2. Decide upon a total number of section pairs *ns* in the fractionator sample. Although $ns \sim 10$ section pairs are a typically sufficient sample for obtaining acceptable precision, for a sparse cell population which may also be very inhomogeneous, an $ns \sim 15 - 20$ is suggested for the pilot study.
3. Decide upon the section thickness *t*. To avoid several practical problems (and bias) in the disector counting of cells, *t* should be thinner than the smallest particle size if the matrix is not transparent. However, in most histologic preparations, the matrix is transparent. For efficiency reasons, section thickness

should approximate ¼ the height of the particle of interest. In most cases, this would typically be 3 μm. However, for a sparse population with no overprojection problems, i.e., cells are not closely packed and not superimposed in a thicker section, we selected 6 μm for a disector height. Serial sectioning the organ at 6 μm is expected to provide $\frac{H}{t} \sim \frac{3000}{6} \sim 500$ sections.

4. To obtain a sample of $ns \sim 20$ from 500 sections we need to sample every $\frac{500}{ns} = \frac{500}{20} = 25$th section and collect the consecutive section to make a serial section pair, i.e., the sampling interval *si* must be fixed at precisely $si = 25$.
5. Most importantly, the sampling interval *si*, which determines the sampling fraction *sf*, is a known and fixed constant $sf = \frac{1}{si} = \frac{1}{25}$, hence the name of the fractionator.
6. Before cutting, the starting point for sampling in the first period of length 25 must be determined. The first section of the first section pair to be sampled must be taken at a random point, *R*, in the period: $1 \leq R \leq 25$; the random number *R* is looked up in a random number table; a new random number is used for each block. After the first section pair, all further section pairs are sampled 25 sections apart.

When the total number of cells, $N(\frac{cell}{sample})$, is determined in all sampled sections (using the proportionator, discussed below) the estimator of the total number per organ is simply

$$N\left(cell\right) := \frac{1}{sf} * N\left(\frac{cell}{sample}\right) = 25 * N(\frac{cell}{sample}) \qquad (1)$$

If the average cross section of the organ has area $A \sim$10,000,000 μm^2 $\sim 10 mm^2$, the total tissue volume to be investigated is $A^*ns^*2^*t \sim 2,400,000,000 \mu m^3$ (about 2 cubic mm; counting both ways in the disectors is expressed in the factor of 2, described below). The sampled sections constitute $sf = \frac{1}{25}$ of the total organ and contains $\frac{1}{25}$ of the total number of sparse particles (and $\frac{1}{25}$ of the total quantity of anything else in the organ).

Cell Counting Using the Disector

As indicated by its name, the disector, (Sterio, 1984) is two adjacent sections separated by a known distance. On one section, an unbiased sampling and counting frame is superposed; the other section is a look-up section. A cell profile sampled according to the unbiased counting rule as illustrated is looked for in the other section. If the cell is also detected in the look-up section it is not counted. Cells sampled in the frame and not detectable in the look-up section are counted; the count of such real cells is denoted $Q^-(cell)$ to emphasize the negative criterion for counting.

The disector counting rule means it is particle tops that are counted: count 1 if the top is *in* the disector. It is most efficient to count in both directions of the disector: having completed the counting in section 1 (with section 2 as a look-up) use section 2 as the counting section and section 1 as the look-up section (now counting bottoms of other cells).

For the sake of unbiasedness, one should use the smallest and most contrasting cell feature as the counting unit: the nucleolus in the cell types that have strictly one per cell; in most cell types the nucleus is an optimal choice. The counting of polynucleated cells requires very special counting rules that are discussed in more detail in Gundersen et al. (2013).

Counting cells at high magnification in physical disectors has been greatly facilitated by development of the Autodisector™ software. The software provides for alignment of counting and lookup fields of view (FOV) in disector sections at high magnification used for cell counting. This is most efficient when analyses are conducted on whole slide digital images. Many digital slide scanners are compatible with the Visiopharm platform.

The Practical Set-Up of Proportionator Sampling

The above set of fractionator sections with a section sampling fraction of $\frac{1}{25}$ can now be analyzed and subsampled with the proportionator. This can be performed using either a microscope under complete computer control or digital slide images in conjunction with the Proportionator™ software. The example below outlines the general procedure using digital slide images for cell counting.

1. Sections are scanned at high magnification ("40× objective") on a digital slide scanner and imported into the Visiopharm software platform.
2. An image analysis algorithm is created to identify the cells of interest (typically a histochemical or immunohistochemical stain) on high resolution digital image at the magnification the "weighting" of tiles will be done for proportionator sampling.
3. In the Autodisector ™ software, superimages (lower resolution images) of the sections are created for alignment and linking of the sections. If there is a specific region of interest in the sections to which sampling will be restricted, these can be drawn. Note: The Proportionator™ combines all sampling sections or ROIs into one "supersection" of a combined area of $SumA = ns^*A =$ 200,000,000 μm^2. This is the total area which is sampled for estimating $N(\frac{cell}{sample})$, the total number of cells in the supersection, which is $\frac{1}{25}$ of the organ.
4. Proportionator sampling is selected. The size of the unbiased sampling frame *a(fra)* which defines the tile e.g., 200 by 200 μm = 40,000 μm^2 is specified; largest frame possible is typically best. The number of tiles or sample size (22–30 typically) for each independent sampling performed with the proportionator (3 are performed, see below) is also specified.
5. The Proportionator™ applies the image analysis algorithm to the original high resolution digital slide images and assigns a weight to all tiles. The Proportionator™ software sorts these tiles by increasing then decreasing weight modeling a smooth and symmetrical distribution (known as the smooth fractionator (Gundersen, 2002), described further below).
6. The Proportionator™ performs the 3 independent samplings of tiles from the smooth fractionator but presents for examination and counting the total sample of tiles summed for the 3 samplings (e.g., 22 per sampling = 66 tiles are presented for counting). In the end, the tripartition of the complete sample enables the precision of the estimator to be estimated directly and unbiasedly discussed below.

Proportionator Sampling and Determination of the Sampling Probability of Individual Tile

The Proportionator™ automatically scans all possible tiles across the high resolution digital images of all sampled fractionator sections. In the example, the supersection contains *SumA/a(fra)* ∼200,000,000/40,000 ∼5,000 tiles. For each tile, the proportionator automatically records the number of pixels z_i of the specific color.

This is the pivotal step in the proportionator sampling/estimator. The crucial information (presence of specific pixels in tiles) is sampled automatically in all 5,000 tiles. The user only has to examine for example 66 tiles but the information in all 5,000 tiles participated in their selection.

In cases of an exorbitant number of tiles when the section area is large, it is possible to sample a fraction of these, in the final estimation one just takes the tile sampling fraction in consideration. For a sparse population, the sampled number of tiles should not be below 10,000.

For automatic sampling, the 5,000 tiles, each with a known content of specific pixels, are arranged using the smooth fractionator (Gundersen, 2002) in a co-ordinate system in one (long!) staggered column, cf. **Figure 1** which shows the arrangement for just 10 tiles. From the 5,000 tiles, a non-uniform sample of size $n = 22$ for example is drawn 3 times independently and proportional to the pixel content (i.e., weight) and the 66 tiles are presented for cell counting by the expert user.

Each rectangle, i.e., each $Tile_i$, is sampled with probability $p_i = \frac{z_i}{T_z}$. The probability is exact: z_i is the exact number of special pixel in $Tile_i$ and T_z is a large, known constant: $\sum_{5,000} z_i$, the sum of all the individual pixel values. As an example, let $z_i = 17$ pixel and $T_z = 343$ pixel, then $p_i = \frac{17}{343} = 0.0496$. This is the probability that this particular tile was sampled; other tiles are sampled with different probabilities. It is a major advantage of the proportionator that the (many) tiles with no pixels are never sampled for counting because tiles are sampled with a probability proportional to number of special pixels contained in a tile.

From the above example, the probability $p_i = 0.0496$ is the sampling probability of this particular tile (the i'th $Tile_i$) but it is also the sampling probability of any cells in the tile (x_i in $Tile_i$). Therefore, when a count of $x_i = 2$ cells was observed in the disector for this particular tile, that event had probability $p_i = 0.0496$.

The Estimation of the Total Number of Cells, N(Cell), in the Complete Organ

There exists a mathematical theorem, the *Horvitz-Thompson theorem*, which states that the contribution of a count from a tile to total cell number in the supersection is directly proportional to the count divided by the probability of sampling the tile based on weight. This is mathematically defined for the particular tile with a count of 2 and probability of sampling based on weight as 0.0496:

$$X_i = \frac{x_i}{p_i} = \frac{2}{0.0496} = 40.3 \quad (2)$$

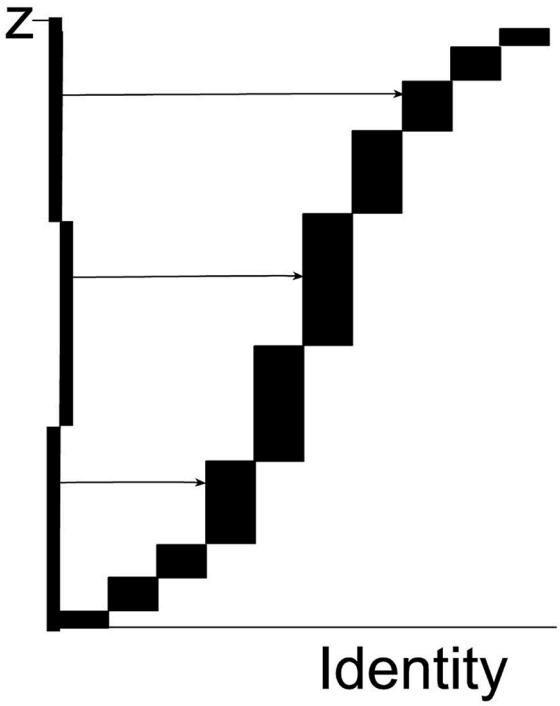

FIGURE 1 | Each rectangle represents one tile. The height of each rectangle is the number z_i of pixels of the specified color in the tile in question; the horizontal axis contains information about the location of the tile in the tessellation of all tile in the supersection. The total height of the abscissa is the total number of all specified pixels in the supersection, $\sum_{5,000} z_i = Z$ (the figure just shows 10 tiles). The ordinate is divided into $n = 22$ equidistant intervals (only 3 are shown in the figure as horizontal lines). The length of each interval on the ordinate is $T_z = Z/22$. A set of 22 horizontal and equidistant lines is drawn, each originating on its own interval (the set of lines is a systematic uniformly random sample on the ordinate). Each line intersects the vertical side of exactly one rectangle and thereby samples that rectangle. Tiles with a relatively large number of pixels have a higher sampling probability, i.e., proportionator sampling among all tiles is non-uniform. There can be hundreds or thousands of tiles with zero specific pixels (e.g., specific immunoreactivity) and they would never be sampled.

where X_i is the contribution from the count of $x_i = 2$ to the total number of cells in the supersection. The computation is performed automatically by the Proportionator™ software. That is, by counting 2 cells in a volume of tissue defined by the area of one random tile with a known probability and the disector height, the contribution of 40.3 from this sample to the total supersection can be computed. By analogy, if a cell is sampled in the tile with probability $\frac{1}{21}$ there must be 21 such cells in the supersection–on average.

This process is repeated for all 22 tiles in one subsample of tiles which then provides the first estimate of the total number of cells $\sum_{22} X_i = X1 = 224$, for example, in the supersection. Two further repetitions of independent samplings for the remaining 44 tiles provide $X2 = 124$ and $X3 = 214$, respectively. Three independent samplings are recommended to achieve a stable CE.

The $mean\,(X) = \frac{X1+X2+X3}{3} = 188$ divided by the fractionator section sampling fraction, $sf = \frac{1}{25}$, is the final

estimate of the global total number of cells

$$N\left(cell\right)\frac{mean\left(X\right)}{2{*}sf} = \frac{188}{2{*}\frac{1}{25}} = 2,950 \quad (3)$$

The factor of 2 compensates for counting both directions in the disector because this doubles the volume in which cells are counted. This is the result of the study of one animal.

The Precision of the Estimator and the Variability of Animals in a Group

The differences between $X1, X2, X3$, estimates from 3 independent samplings of the supersection are indicative of the imprecision of the estimator of total number of cells. If very similar, the precision must be good, and vice versa. In fact, the imprecision of the estimator is simply defined:

$$CE\left(N\right) := \frac{SEM\left(X1, X2, X3\right)}{mean\left(X\right)} = \frac{31.8}{188} = 0.17 \quad (4)$$

This is an extraordinarily simple equation and unbiased estimator of precision of the measurement. This simple mathematical expression for unbiased estimation of precision, *CE* (coefficient of error), is unique to the proportionator.

At the end of the pilot phase (e.g., 3–6 animals per group), compute the average imprecision of the estimator:

$$\overline{CE_{est}}\left(N\right): = \sqrt{\left(\sum\nolimits_4 CE_i^2\right)/4} \sim 0.13 \quad (5)$$

This is the mean CE for a group of 4 animals.

Compute also

$$CV_{obs}\left(N\right) := \frac{SD\left(est1,\ est2,\ est3, est4\right)}{mean\ estimate} \sim 0.32 \quad (6)$$

which is the observed, computed variability among the estimates from four pilot animal; *SD* is the ordinary standard deviation. The numbers in Equations (5, 6) are arbitrary numbers used as examples.

Note that one cannot overestimate the value of a pilot study which provides very valuable information about the precision of the estimation procedure, $\overline{CE_{est}}\left(N\right)$, and the biological variability of the test animals, $CV_{obs}\left(N\right)$. No optimization of the main (large) study design is possible without the pilot study, see below.

EXAMPLE OF APPLICATION OF THE AUTOMATED PROPORTIONATOR: PILOT STUDY FOR ESTIMATION OF TOTAL NUMBER OF OSTEOPROGENITOR CELLS IN MOUSE VERTEBRAE

Material and Methods

Animals

C57BL/6 male mice (6–7 weeks old) carrying the SOX9-creERt and dT-tomato reporter, were used in this pilot study. Lineage tracing studies have demonstrated that early mesenchymal progenitors defined by promoter activity of Sox9 and subsequent expression of tomato protein differentiate into chondrocytes, osteoblasts, stromal cells and adipocytes during endochondral bone development (Ono et al., 2014). Mice were administered subcutaneously either vehicle ($n = 3$) or 50 mg/kg sclerostin antibody ($n = 3$) (r13c7, supplied by Amgen Inc.) on Day 1. On Day 6, mice were administered tamoxifen (2 mg intraperitoneally) and then terminated by cervical dislocation under isoflurane anesthesia on Day 10. Thoracic vertebrae T11-13 were collected, cleaned of soft tissue and fixed in 4% paraformaldehyde (PFA) for 2–3 days at 4°C. Vertebral samples used in this pilot study were graciously provided by Drs. Deepak Balani and Henry Kronenberg, Massachusetts General Hospital, Boston MA. Mice were group-housed in sterile, ventilated microisolator cages on corn cob bedding in a facility accredited by the Association for Assessment and Accreditation of Laboratory Animal Care. All procedures were conducted in compliance with the Guide for the Care and Use of Laboratory Animals approved by Massachusetts General Hospital's Institutional Animal Care and Use Committee. Animals were provided *ad libitum* access to pelleted feed (LabDiet 5010) and water (Standard drinking water of Boston, MA; pH 7.8) via Hydropac. Animals were maintained on a 12-h light/12-h dark cycle in rooms at 64° to 79°F with 30–70% humidity under pathogen-free conditions.

Vertebral segments consisting of 3 thoracic vertebrae/animal were decalcified in 10% EDTA + 2% PFA, then routinely processed in paraffin. Blocks were exhaustively sectioned at 6 μm and using SURS section pairs were collected every 36 micrometers using an automated microtome calibrated to the section thickness (ssf=1/6). Six micron thick sections were chosen for the pilot because the target cell population was expected to be sparse based on qualitative evaluation of sections stained for tomato protein. Number of section pairs ranged from 13 to 18 per animal. Section pairs were mounted on charged slides and immunohistochemically stained for tomato protein using a rabbit polyclonal antibody to Red Fluorescent Protein at 1:500 (Abcam, #ab62341) on a Ventana Discovery Ultra™ (Ventana, Tuscon AZ), an automated immunostaining system. Briefly, sections were incubated with primary antibody for 1 h, followed by anti-rabbit HQ (Ventana, reference no. 760-4815) for 12 min and anti-HQ horseradish peroxidase (Ventana, reference no. 760-4820) for 12 min, developed with diaminobenzadine, then counterstained with hematoxylin.

Stereological Methods

Stained slides were scanned at 40X objective magnification using the Hamamatsu Nanozoomer™ whole slide scanner and imported into the AutoDisector™; superimages were then created by the software. Superimages of disector pairs were linked and aligned, and the region of interest (ROI) was defined. A ROI was drawn around each vertebral body (excluding the cortical bone and growth plate); 3 vertebral bodies were used in analysis for each animal to increase the total tissue volume. An image analysis algorithm was created to identify tomato-positive cells and stored to guide Proportionator™ sampling. Three independent samplings of

60 tiles each were performed for a total of 180 tiles at the "40X magnification" setting. An unbiased counting frame (200 × 200 μm) was applied to define the proportionator tile and the number of tomato-positive osteoprogenitor cells within the bone marrow was counted, which included tomato-positive cells on the bone surface interpreted to be osteoblasts. Occasional tomato-positive cells were observed within the bone matrix (consistent with osteocytes); these cells were not included in the analysis. The nucleus was used as the unique counting feature. Counting was performed on both directions of the disector (**Figure 2**).

The total number of tomato-positive osteoprogenitor cells for each independent sampling was determined by the following calculation: $\frac{\sum X}{2} * \frac{1}{ssf}$, where $\sum X$ is the sum of the weighted counts (divided by 2 to account for counting in both directions of the disector) and *ssf* is the section sampling fraction, which was 1/6. The mean of the 3 independent samplings was calculated for each animal and was divided by the 3 (number of vertebrae used in analysis) to determine the number of tomato-positive cells per vertebra for each animal. CE was calculated per Equation (4). The mean, standard deviation, CE, and coefficient of variation (CV) for each group was calculated.

Results

The results of the pilot study are sumarized in **Table 1**. Total tomato-positive osteoprogenitor counts across 3 vertebral bodies/animal ranged from 19 to 80 and total number/vertebrae ranged from 27 to 187. Sclerostin antibody increased the mean number by approximately 3-fold but with a high CV (∼60%). Mean CE of the proportionator estimator in both groups was ∼9–10%.

Optimizing the Relationship of the Data Quality (Precision) to the Necessary Effort

At the end of the pilot study it is possible to get an answer to the crucial question: is the stereological estimator precise enough for the purpose of the study?

$\overline{CE_{est}}(N)$, the imprecision of the estimator, is under full control of the investigator: the larger the sample the smaller the $\overline{CE_{est}}(N)$. "Sample" can be any or all of (1) the fractionator sections, (2) the area of the counting frame, and (3) the number of tiles sampled. The design outlined above results in a certain precision of the estimator in the organ under study, $\overline{CE_{est}}(N) \sim 0.088$ in the vehicle group and 0.103 in the treatment group. The question is, is that low enough for the purpose of the study.

The variability among animal estimates, $CV_{obs}(N)$, and the estimator imprecision, $\overline{CE_{est}}(N)$, are dependent in a very useful way:

$$CV^2_{obs}(N) = CV^2_{ani}(N) + \overline{CE^2_{est}}(N) \quad (7)$$

which states that the estimator imprecision, $\overline{CE^2_{est}}(N)$, inflates the real (unknown) variability between animals (the biological variation), $CV^2_{ani}(N)$, thus contributing to the observed $CV^2_{obs}(N)$. If two groups show very different $CV^2_{obs}(N)$ but have similar $\overline{CE^2_{est}}(N)$ then their biological variation must be very different, cf. the example in **Table 1**.

Clearly, $\overline{CE^2_{est}}(N)$ should be small compared to $CV^2_{obs}(N)$, cf. Equation (7). The question is how small? The simple answer is provided by the general inequality applicable to each group of the study (and very useful for all stereological estimators) is estimation of the Precision Range of an Optimally Balanced

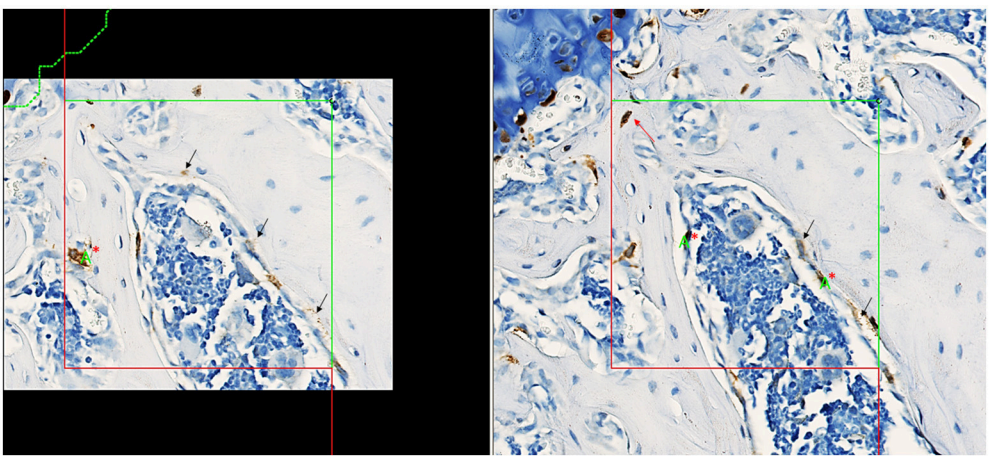

FIGURE 2 | Screenshots captured from the Visiopharm platform of matched fields of view in a disector pair with aligned unbiased counting frames, counting section on left, look-up section on right. Nuclei present in tomato-positive osteoprogenitor cells (brown cytoplasm) in the counting section are counted if it is not present in the look-up section. Counting in the other direction of the disector, nuclei present in tomato-positive osteoprogenitor cells in the look-up section are counted if not present in the counting section. The final total count is divided by 2 to correct for counting in both directions. Counting in both directions increases the count and improves precision of the estimate. The green letter "A" with red "*" denotes a "count"; a total count of 3 was recorded for this tile counting in both directions of the disector. Tomato-positive osteocytes (red arrow) were rare events and were not included in the counts. Staining interpreted as non-specific is denoted by black arrows.

TABLE 1 | Summary of stereological data of tomato-positive osteoprogenitors (OP) labeled with tomato protein in mouse vertebrae.

	Vehicle	Sclerostin antibody
INDIVIDUAL TOTAL COUNT SUMMED FOR 3 SAMPLING		
	36	33
	19	48
	28	80
Mean total count/group	28	54
INDIVIDUAL ESTIMATE OF TOTAL NUMBER OF OP CELLS/VERTEBRAE		
	41	90
	38	58
	27	187
Mean total number of OP cells/group	35	112
SD	7.4	67.2
CV	0.21	0.60
INDIVIDUAL CE		
	0.05	0.11
	0.08	0.14
	0.12	0.01
Mean CE/group	0.088	0.103

Estimator (PROBE) (Gundersen et al., 2013):

$$PROBE: 2 < \frac{CV^2_{obs}(N)}{\overline{CE^2_{est}}(N)} < 4 \quad (8)$$

The above inequalities leads to 1 of 3 possible conclusions:

PROBE larger than 4: the precision of the estimator may be too good for the purpose. If convenient, reduce the workload where it is heaviest.
PROBE between 2 and 4: The precision is adequate for the purpose.
PROBE below 2. The case where the estimator imprecision is too large for the purpose. The question is which part of the estimator should be studied more intensively.

1. If the organ is inhomogeneous at the scale of sections, increase the number of sections (e.g., from 20 to 30–40 in each organ).
2. If the sections are very inhomogeneous at the scale of tile or the total count is too small for the purpose: increase the frame size to its maximum and increase the number of sampled tiles (e.g., from 22*3 to 35*3).

Substituting the values from Equations (5, 6), the PROBE ratio $\frac{CV^2_{obs}(N)}{\overline{CE^2_{est}}(N)}$ in Equation (8) becomes

$$\frac{CV^2_{obs}(N)}{\overline{CE^2_{est}}(N)} = 5.7 \quad (9)$$

for the vehicle group and

$$\frac{CV^2_{obs}(N)}{\overline{CE^2_{est}}(N)} = 34 \quad (10)$$

for the sclerostin antibody group.

Since 5.7 is larger than 4, cf. Equation (8), we may optimize the sampling effort in the main study, probably by moderately reducing the number of fractionator sections from an average of 15 to 12: there is no indication of a pronounced inhomogeneity among the sections, they look mostly the same. Also, the number of tiles sampled may be reduced from 60 *3 to 40 * 3.

The value of 34 is much larger than 4 and one might think of reducing the sampling for sclerostin antibody group by a large measure. However, under ordinary scientific paradigms one must study groups of animals blindly, i.e., one can only use one sampling protocol for the entire study. That just emphasizes the importance of the pilot study and the subsequent optimization of the study estimator.

There are no set rules for performing the optimization, except to use caution and change the sample sizes by a proportion less than that of the PROBE number in relation to the PROBE limit. As an example, the PROBE number of the vehicle group is 5.7 which is roughly a factor 3 larger than the PROBE limit of 2.0. Consequently, we have reduced the sample sizes by a factor less than 3.

Due to the low number of observations in the pilot study the PROBE values are not very precise and one should use common sense in the interpretation. If some of the values are unexpected or counter intuitive, it is worth considering another pilot study.

Note that all of the above pertains to sparse population of cell. For the pilot study of ordinary organs with many cells, it is recommended that 10 fractionator sections and 15 tiles with 3 independent samplings (total 45 tiles for counting) are used for the pilot study.

The Hopeless Case of the Fractionator Estimator of Total Number in Sparse Populations

What would the imprecision be for the good-old, no-nonsense fractionator estimator of total number using uniform sampling provide in this sparse osteoprogenitor population?

One answer is the $CE_{fract\ est}(N)$ when, in the presented example, all 1,900 tiles or unbiased counting frames in all ∼15 sampled sections are studied (the tile sampling fraction is therefore 1.00). The total number of cells in all sampled sections is 35, which is also the fractionator total count. To reach a count of 1 cell, it is necessary to study $\frac{1900}{35} \sim 54$ empty tiles. The imprecision of the fractionator estimator is

$$CE_{fract\ est}(N) = \frac{1}{\sqrt{count}} = \frac{1}{\sqrt{35}} \sim 0.169.$$

Even when studying all 1,900 tiles the fractionator has a PROBE value of $\frac{CV^2_{obs}(N)}{\overline{CE^2_{est}}(N)} = 1.5$, well below the lower limit of 2.0 for acceptable imprecision. In truth, a Herculean effort with a poor outcome.

DISCUSSION

Estimation of the total number of osteoprogenitors with SOX9 promoter activity in the mouse vertebral body is a nice example to illustrate why the automated proportionator is the first ever practical estimator of the total number in sparse cell populations. The automatic proportionator offers many advantages compared with other sampling and estimation strategies, notably the relative immunity of the proportionator to sparseness and inhomogeneity.

The degree of sparseness of these osteoprogenitors in the mouse vertebra has not been properly defined, but one may index this by a ratio of the total number of zero count tiles/tiles with a count (usually a count of 1). On this scale, these osteoprogenitors in the vertebra have a sparseness of 54. It is a remarkable feature of the automatic proportionator that its efficiency does not depend on the degree of sparseness. To a first approximation it is equally efficient in cell populations with the degree of sparseness ranging from 10 to 1,000. Like sparseness, inhomogeneity is difficult to define rigorously, but one may think of a large variability between sampling items with respect to cell density that may exist independently among tiles and among sections. Inhomogeneity makes the fractionator inefficient, whereas the proportionator is largely unaffected. In the raw data, inhomogeneity was evident between sections, but there was also marked inhomogeneity between tiles. Cells were preferentially located near the endplates, notably adjacent to the endocortex, which has been described for these cells using bone clearing techniques and 3-dimensional imaging of whole mouse vertebral bodies (Greenbaum et al., 2017). Inhomogeneity or non-uniform distribution of cell populations, which may or may not be sparse, is a common situation in the neurosciences where proportionator sampling can offer significant improvements in efficiency.

Another unique feature of the proportionator is the relationship between the absolute count $\sum Q^-$ and the weighted estimator imprecision CE (N). Under uniform sampling the imprecision of the vehicle group mean $\sum Q^-$ of 28 is $\frac{1}{\sqrt{28}} = 0.189$. However, under weighted sampling the CE (28) is 0.088, cf. **Table 1**, and is computed from the differences of the three individual estimates based on three independent sampling of 60 tiles.

There are a number of practical details to address for optimal performance of the proportionator. Near perfect sections are required as loss of tissue is evidently a loss of information, i.e., a bias. Near perfect staining is required because the proportionator is particularly sensitive to nonspecific staining of the background and section edges. Moderate staining problems increase the CE, but noteworthy does not result in a bias, but uneven staining of sections leads to reduced efficiency. Bias can be introduced in cases where staining does not detect the cell of interest or staining artifact prevents identification of the cell. Tiles may be encountered with staining or sectioning artifacts that confound performing a count. Appendix details the method to address these non-useable tiles.

Another consideration in regard to efficiency of the proportionator is the amount of computing time required to perform the weighting. In the current version of the Proportionator ™ software, weighting is performed on the high resolution digital images, critically important when weighting on small stained features in a cell, such as the cytoplasm or nucleus. When the section area is small, weighting on 100% of the tiles is not burdensome, as this can be performed unattended by the user. However, when section area is large, some fraction of the tiles may be sampled; this option is currently available in the Proportionator™ software.

Although this paper focused on applications using chromogenic immunophenotyping, immunofluorescent-stained thin sections can be used with the Proportionator™ software and integrated into the automated workflow if an immunofluorescence slide scanner is available. Proportionator sampling of immunofluorescent-stained thick sections combined with the optical disector can be performed with the Visiopharm platform configured with an automated microscope and appropriate camera. Although not an aspect of the present study it is worthy of mention that the proportionator is equally efficient as a sampling and estimation protocol for all stereological modalities: total number, total length, total surface, total volume and all the particle size estimators and size distributions (Gundersen et al., 2013).

In conclusion, the automated proportionator estimator is the only practical stereological solution for obtaining estimates of total number of sparse cell populations.

AUTHOR CONTRIBUTIONS

HJGG and RWB are responsible for the conception and design, analysis and interpretation of the work; drafting, revising and final approval of the manuscript; and accountable for accuracy and integrity of the work.

FUNDING

Funding for the pilot study was provided by Amgen Inc. and UCB Pharma.

ACKNOWLEDGMENTS

The authors are grateful to Dr. Danielle Brown of Charles River Laboratories for performing the proportionator analysis on the pilot study. The authors especially thank Dr. Ruth Lightfoot-Dunn (retired vice president of Amgen) for supporting the continued development and improvement of the Proportionator™ software and Dr. Kim Anders Bjerrum at Visiopharm for his expert implementation of these improvements in the current version of the Proportionator™ software.

REFERENCES

Gardi, J. E., Nyengaard, J. R., and Gundersen, H. J. (2008). Automatic sampling for unbiased and efficient stereological estimation using the proportionator in biological studies. *J. Microsc.* 230, 108–120. doi: 10.1111/j.1365-2818.2008.01963.x

Greenbaum, A., Chan, K. Y., Dobreva, T., Brown, D., Balani, D. H., Boyce, R., et al. (2017). Bone CLARITY: clearing, imaging, and computational analysis of osteoprogenitors within intact bone marrow. *Sci. Transl. Med.* 9:387. doi: 10.1126/scitranslmed.aah6518

Gundersen, H. J. (1986). Stereology of arbitrary particles. A review of unbiased number and size estimators and the presentation of some new ones, in memory of William, R. Thompson. *J. Microsc.* 143, 3–45. doi: 10.1111/j.1365-2818.1986.tb02764.x

Gundersen, H. J. (2002). The smooth fractionator. *J. Microsc.* 207, 191–210. doi: 10.1046/j.1365-2818.2002.01054.x

Gundersen, H. J. G., Mirabile, R., Brown, D., and Boyce, R. W. (2013). "Stereological principles and sampling procedures for toxicologic pathologists," in *Haschek and Rousseaux's Handbook of Toxicologic Pathology, 3rd Edn.*, eds W. M. Haschek, C. G. Rousseaux, and M. A. Wallig (Boston, MA: Academic Press), 215–286.

Keller, K. K., Andersen, I. T., Andersen, J. B., Hahn, U., Stengaard-Pedersen, K., Hauge, E. M., et al. (2013). Improving efficiency in stereology: a study applying the proportionator and the autodisector on virtual slides. *J. Microsc.* 251, 68–76. doi: 10.1111/jmi.12044

Ono, N., Ono, W., Mizoguchi, T., Nagasawa, T., Frenette, P. S., and Kronenberg, H. M. (2014). Vasculature-associated cells expressing nestin in developing bones encompass early cells in the osteoblast and endothelial lineage. *Dev. Cell* 29, 330–339. doi: 10.1016/j.devcel.2014.03.014

Sterio, D. C. (1984). The unbiased estimation of number and sizes of arbitrary particles using the disector. *J. Microsc.* 134, 127–136. doi: 10.1111/j.1365-2818.1984.tb02501.x

West, M. J., Slomianka, L., and Gundersen, H. J. (1991). Unbiased stereological estimation of the total number of neurons in the subdivisions of the rat hippocampus using the optical fractionator. *Anat. Rec.* 231, 482–497. doi: 10.1002/ar.1092310411

Conflict of Interest Statement: RWB is a former Amgen employee and currently a consultant for Amgen through Beechy Ridge ToxPath LLC.

The other author declares that the research was conducted in the absence of any commercial or financial relationships that could be construed as a potential conflict of interest.

APPENDIX

Non-useable Tiles

Unavoidably in practice, technical problems may prevent a sampled tile from being correctly evaluated with respect to the objects under study; simple examples being incorrectly focusing of the image or the local loss of section substance. Since the correct estimate is based on the distinct sampling probability of the tile, p_i, the user cannot instead select a nearby tile: that tile has a genuinely unknown sampling probability, incorporating, among other factors, the probability that the non-useable tile was indeed non-useable! As a result, no contribution to the universe total from the non-useable tile can be generated, and this unequivocally renders the estimator (negatively) biased.

A correct procedure in the face of non-useable tiles (under a critical assumption) at this stage may be as follows.

1. The total number of non-useable tiles in the sample turns out to be $n_{n-u} = 2$ of a sample total of $n = 22$. The biased estimate of the total geometric feature of interest such as total number from the incomplete procedure is X_{n_u}, where the suffix indicates that it is based on a sample size of only $n_u = n - n_{n-u} = 22 - 2 = 20$ tiles.
2. Reusing the tessellation and weights of the incomplete procedure, the user specifies a second sample of precisely $n_{n-u} = 2$ tiles. The software thus resamples the complete set of tiles with a sampling period of Z/n_{n-u} and the user provides the correct count x_i for each tile. The resulting estimate is X_{n-u}. This is an unbiased estimate of the total geometric feature of interest, but evidently rather imprecise, provided n_{n-u} is a small number. If there happens to be non-useable tiles in this complementary sample, the whole sample is discarded and the correction procedure is repeated.
3. The original estimate, X_{n_u}, is biased because it is short by the contribution from $n_{n-u} = 20$ tiles, which were sampled with probabilities $p_i = z_i/[\frac{Z}{n}]$. The second estimate almost fulfills the bill: it is the sum of the contributions from $n_{n-u} = 2$ tiles, but they were sampled with probabilities $p_i = z_i/[\frac{Z}{n_{n-u}}]$, off by just a known constant. It follows that the second estimate may be recomputed to provide the missing contribution: $\Delta X_{n-u} = (n_{n-u}/n) * X_{n-u} = (2/22) * X_{n-u}$.
4. The unbiased estimate of total geometric feature of interest is $X_{n_u} + \Delta X_{n-u}$–now based on the required n tiles.

The correction of X_{n_u} is 0 if $X_{n-u} = 0$, obviously, i. e. in this case X_{n_u} happens to coincide with an unbiased estimate.

In the split-sample procedure, each sample of 22 observations must be corrected separately.

The assumption underlying the correction is that the non-useable tiles are a uniform sample from the total weight (only then does the correction by an extra uniform sample work). Some technical problems are plausibly independent of the objects under study, like incorrect focusing of the image. The really bad news are folds in the section. They are genuinely impossible to correct for completely (the loss of information is 3 times the loss of area) and must be avoided as far as at all possible. They are also quite likely related to the local structure of the tissue and may not be uniformly positioned. The best that can be said in such cases is that the result of the correction is likely to be less biased than the uncorrected estimate–but that is not guaranteed.

Advantages of publishing in Frontiers

OPEN ACCESS
Articles are free to read for greatest visibility and readership

FAST PUBLICATION
Around 90 days from submission to decision

HIGH QUALITY PEER-REVIEW
Rigorous, collaborative, and constructive peer-review

TRANSPARENT PEER-REVIEW
Editors and reviewers acknowledged by name on published articles

Frontiers
Avenue du Tribunal-Fédéral 34
1005 Lausanne | Switzerland

Visit us: www.frontiersin.org
Contact us: info@frontiersin.org | +41 21 510 17 00

REPRODUCIBILITY OF RESEARCH
Support open data and methods to enhance research reproducibility

DIGITAL PUBLISHING
Articles designed for optimal readership across devices

FOLLOW US
@frontiersin

IMPACT METRICS
Advanced article metrics track visibility across digital media

EXTENSIVE PROMOTION
Marketing and promotion of impactful research

LOOP RESEARCH NETWORK
Our network increases your article's readership